CHARACTERIZATION OF ION CONDUCTING SOLID BIOPOLYMER ELECTROLYTES BASED ON STARCH-CHITOSAN BLEND AND APPLICATION IN ELECTROCHEMICAL DEVICES

MUHAMMAD FADHLULLAH BIN ABD. SHUKUR

INSTITUTE OF GRADUATE STUDIES
UNIVERSITY OF MALAYA
KUALA LUMPUR

2015

CHARACTERIZATION OF ION CONDUCTING SOLID BIOPOLYMER ELECTROLYTES BASED ON STARCH-CHITOSAN BLEND AND APPLICATION IN ELECTROCHEMICAL DEVICES

MUHAMMAD FADHLULLAH BIN ABD. SHUKUR

THESIS SUBMITTED IN FULFILMENT OF THE REQUIREMENTS FOR THE DEGREE OF DOCTOR OF PHILOSOPHY

INSTITUTE OF GRADUATE STUDIES
UNIVERSITY OF MALAYA
KUALA LUMPUR

2015

UNIVERSITY OF MALAYA

ORIGINAL LITERARY WORK DECLARATION

Name of Candidate: **Muhammad Fadhlullah bin Abd. Shukur**

Registration/Matric No: **HHC130003**

Name of Degree: **Doctor of Philosophy (Ph.D)**

Title of Project Paper/Research Report/Dissertation/Thesis ("this Work"):

Characterization of Ion Conducting Solid Biopolymer Electrolytes Based on Starch-Chitosan Blend and Application in Electrochemical Devices

Field of Study: **Physics (Advanced Materials)**

I do solemnly and sincerely declare that:

(1) I am the sole author/writer of this Work;
(2) This Work is original;
(3) Any use of any work in which copyright exists was done by way of fair dealing and for permitted purposes and any excerpt or extract from, or reference to or reproduction of any copyright work has been disclosed expressly and sufficiently and the title of the Work and its authorship have been acknowledged in this Work;
(4) I do not have any actual knowledge nor do I ought reasonably to know that the making of this work constitutes an infringement of any copyright work;
(5) I hereby assign all and every rights in the copyright to this Work to the University of Malaya ("UM"), who henceforth shall be owner of the copyright in this Work and that any reproduction or use in any form or by any means whatsoever is prohibited without the written consent of UM having been first had and obtained;
(6) I am fully aware that if in the course of making this Work I have infringed any copyright whether intentionally or otherwise, I may be subject to legal action or any other action as may be determined by UM.

Candidate's Signature Date:

Subscribed and solemnly declared before,

Witness's Signature Date:

Name:

Designation:

ABSTRACT

In this work, the aim is to develop a solid polymer electrolyte (SPE) system based on biopolymer. From X-ray diffraction (XRD) technique, the blend of 80 wt.% starch and 20 wt.% chitosan is found to be the most amorphous blend. This starch-chitosan blend ratio is used as the polymer host in preparation of two SPE systems (salted and plasticized) via solution cast technique. Interaction between the materials is confirmed by Fourier transform infrared (FTIR) spectroscopy analysis. In the salted system, the incorporation of 25 wt.% ammonium chloride (NH_4Cl) has optimized the room temperature conductivity to $(6.47 \pm 1.30) \times 10^{-7}$ S cm^{-1}. In the plasticized system, the conductivity is enhanced to $(5.11 \pm 1.60) \times 10^{-4}$ S cm^{-1} on addition of 35 wt.% glycerol. The conductivity is found to be influenced by the number density (n_d) and mobility (μ) of ions. Conductivity trend is verified by XRD, scanning electron microscopy (SEM) and differential scanning calorimetry (DSC) results. The temperature dependence of conductivity for all electrolytes is Arrhenian. From transference number of ion (t_{ion}) measurement, ion is found as the dominant conducting species. Transference number of cation (t_+) for the highest conducting electrolyte (P7) is found to be 0.56. Linear sweep voltammetry (LSV) result confirms the suitability of P7 electrolyte to be used in the fabrication of an electrochemical double layer capacitor (EDLC) and proton batteries. The EDLC has been characterized using galvanostatic charge-discharge and cyclic voltammetry (CV) measurements. The primary proton batteries have been discharged at different constant currents. The secondary proton battery has been charged and discharged for 40 cycles.

ABSTRAK

Penyelidikan ini bermatlamat untuk membangunkan satu sistem elektrolit polimer pepejal berasaskan biopolimer. Daripada teknik pembelauan sinar-X, campuran yang mengandungi 80% kanji dan 20% kitosan adalah campuran yang paling amorfus. Nisbah campuran kanji-kitosan ini digunakan sebagai perumah untuk penyediaan dua sistem elektrolit (bergaram dan berplastik) dengan menggunakan teknik penuangan larutan. Interaksi antara bahan-bahan disahkan oleh analisis spektroskopi inframerah transformasi Fourier. Dalam sistem bergaram, pencampuran 25% berat amonium klorida telah mengoptimumkan nilai kekonduksian suhu bilik kepada $(6.47 \pm 1.30) \times 10^{-7}$ S cm^{-1}. Dalam sistem berplastik, kekonduksian meningkat kepada $(5.11 \pm 1.60) \times 10^{-4}$ S cm^{-1} dengan pencampuran 35% berat gliserol. Didapati bahawa nilai kekonduksian dipengaruhi oleh kepadatan dan mobiliti ion. Trend kekonduksian disahkan oleh analisis-analisis pembelauan sinar-X, pengimbas mikroskopi elektron dan pengimbas kalorimetri pembezaan. Kebergantungan kekonduksian terhadap suhu untuk semua elektrolit adalah bersifat Arrhenius. Daripada pengukuran nombor pemindahan ion, didapati bahawa ion adalah spesis berkonduksi yang dominan. Nombor pemindahan kation untuk elektrolit berkonduksi tertinggi (P7) adalah 0.56. Dapatan pengimbasan voltametri linear mengesahkan kesesuaian elektrolit P7 untuk digunakan dalam fabrikasi kapasitor elektrokimia dua lapisan dan bateri-bateri proton. EDLC tersebut dicirikan melalui eksperimen-ekesperimen cas-nyahcas galvanostat dan kitaran voltametri. Bateri-bateri proton primer telah dinyahcas pada arus malar yang berbeza. Bateri proton sekunder telah dicas dan dinyahcas sebanyak 40 kitaran.

ACKNOWLEDGEMENTS

I am grateful to express my sincere gratitude and appreciation to my supervisor, Dr. Mohd Fakhrul Zamani bin Abdul Kadir, for his direction, guidance, encouragement and support for completing this thesis. This work would not have been a reality without his sparking ideas and worthy words. I am humbly thankful to him for his remarkable supervision and attention. I am also thankful to my co-supervisor, Associate Prof. Dr. Roslinda binti Ithnin for her guidance and support.

I wish to express my appreciation to all my lab mates for their cooperation, team work and friendship. I would like to thank University of Malaya for financial support and Malaysian Ministry of Education for the scholarship awarded. Finally, and most importantly, I would like to express my special gratitude and thanks to my family especially to my parents for their love, support, prayers and understanding.

TABLE OF CONTENTS

LIST OF FIGURES

LIST OF TABLES

LIST OF SYMBOLS

A	:	Temperature dependent parameter
A_a	:	Area of amorphous region in XRD pattern
A_e	:	Electrode-electrolyte contact area
A_o	:	Pre-exponential factor proportional to the concentration of carriers
A_T	:	Area of total hump in XRD pattern
C	:	Capacitance of CPE
C_1	:	Capacitance at high frequency
C_2	:	Capacitance at low frequency
C_o	:	Vacuum capacitance
C_s	:	Specific capacitance
d	:	Interplanar spacing
dV/dt	:	CV's scan rate
e	:	Electron charge
E_a	:	Activation energy
$E_{f\,peak}$	:	Activation energy of relaxation of M_i
E_{fmax}	:	Activation energy of relaxation of tan δ
E_{VTF}	:	Pseudo activation energy
f_o	:	Pre-exponential factor of relaxation frequency
f_{max}	:	Frequency at tan δ_{max}
f_{peak}	:	Frequency at M_i peak
H^+	:	Proton
i	:	Constant current
I	:	Current
$I(V)$	:	Current at a given potential
I_i	:	Initial current
I_{ss}	:	Steady state current
J	:	Current density
k	:	Boltzmann constant
l	:	Distance between two complexation sites
Li^+	:	Lithium ion
m	:	Mass of active material
m_c	:	Mass of charge carrier
M_i	:	Imaginary part of electrical modulus
M_r	:	Real part of electrical modulus
n	:	Order of reflection
n_d	:	Number density of ion
NH_4^+	:	Ammonium ion
p	:	Deviation of the impedance plot from the axis
p_1	:	Deviation of the radius of the circle from the imaginary axis in impedance plot

p_2	:	Deviation of the inclined adjacent line from the real axis in impedance plot
P	:	Power density
q	:	Charge of ion
Q	:	Discharge capacity of proton battery
Q_s	:	Specific discharge capacity of proton battery
r	:	Internal resistance
R_b	:	Bulk resistance
s	:	Power law exponent
s_d	:	Slope of discharge curve in galvanostatic charge-discharge plot
t	:	Thickness of the electrolyte
t_+	:	Transference number of cation
t_c	:	Charge time of EDLC
t_d	:	Discharge time of EDLC
t_e	:	Transference number of electron
t_{ion}	:	Transference number of ion
t_{Mi}	:	Relaxation time of M_i
$t_{plateau}$	:	Discharge time at the plateau region
$t_{tan\ \delta}$	:	Relaxation time of tan δ
tan δ	:	Loss tangent
tan δ_{max}	:	Maximum of tan δ
T	:	Absolute temperature
T_o	:	Temperature at which the configuration entropy becomes zero
T_g	:	Glass transition temperature
T_m	:	Melting point
v	:	Velocity of mobile ion
$v_{as}(NH_4^+)$	:	Asymmetry vibration of NH_4^+
$v_s(NH_4^+)$	:	Symmetry vibration of NH_4^+
V	:	Potential
V_o	:	OCP
V_1	:	Initial potential during CV measurement
V_2	:	Final potential during CV measurement
V_{drop}	:	Voltage drop upon discharge
Z	:	Valency of conducting species
Z_{CPE}	:	Impedance of CPE
Z_r	:	Real part of impedance
Z_i	:	Imaginary part of impedance
β_{KWW}	:	Kohlrausch exponent
χ_c	:	Degree of crystallinity
ε_o	:	Vacuum permittivity
$\varepsilon_{\text{glycerol}}$	:	Dielectric constant of glycerol
ε_i	:	Dielectric loss
ε_r	:	Dielectric constant
$\phi(t)$	:	Time evolution of the electric field within a material

η	:	Coulombic efficiency	σ_{dc}	:	dc conductivity
λ	:	Wavelength	σ_o	:	Pre-exponential factor
μ	:	Mobility of ion	τ	:	Traveling time of ion
θ	:	Bragg's angle	ω	:	Angular frequency
σ	:	Ionic conductivity	ω_{peak}	:	Angular frequency of the relaxation peak
$\sigma(\omega)$	:	Total conductivity			
σ_{ac}	:	ac conductivity			

LIST OF ABBREVIATIONS

$3CdSO_4.8H_2O$	:	Cadmium sulphate
ac	:	Alternating current
$AgCF_3SO_3$	:	Silver triflate
$AgNO_3$	:	Silver nitrate
Al_2O_3	:	Aluminium oxide
Al_2SiO_5	:	Aluminum silicate
BATS	:	Butyltrimethyl ammonium bis (trifluoromethyl sulfonyl) imide
CBH	:	Correlated barrier hopping
CPE	:	Constant phase element
CV	:	Cyclic voltammetry
DBP	:	Dibutyl phthalate
dc	:	Direct current
DEC	:	Diethyl carbonate
DSC	:	Differential scanning calorimetry
DTAB	:	Dodecyltrimethyl ammonium bromide
EC	:	Ethylene carbonate
EDLC	:	Electrochemical double layer capacitor
EIS	:	Electrochemical impedance spectroscopy
ESR	:	Equivalent series resistance
FTIR	:	Fourier transform infrared spectroscopy
FWHM	:	Full width at half maximum
H_2SO_4	:	Sulfuric acid
H_3PO_4	:	Phosphoric acid
HCl	:	Hydrochloric acid
KIO_4	:	Potassium periodate
LiBOB	:	Lithium bis(oxolato)borate
$LiCF_3SO_3$	:	Lithium triflate
$LiClO_4$	:	Lithium perchlorate
LiI	:	Lithium iodide
$LiN(CF_3SO_2)_2$	:	Lithium trifluoromethane sulfonimide
$LiNO_3$	:	Lithium nitrate
LiOAc	:	Lithium acetate
$LiPF_6$	:	Lithium hexafluorophosphate
LiTFSI	:	Lithium bis(trifluoromethane sulfonyl) imide
LSV	:	Linear sweep voltammetry
Mg	:	Magnesium
MnO_2	:	Manganese (IV) dioxide
$NaClO_4$	:	Sodium perchlorate
$(NH_4)_2SO_4$	:	Ammonium sulfate

$(NH_4)_3PO_4$	:	Ammonium phosphate
NH_4Br	:	Ammonium bromide
$NH_4C_2H_3O_2$	:	Ammonium acetate
$NH_4CF_3SO_3$	:	Ammonium triflate
NH_4Cl	:	Ammonium chloride
NH_4ClO_4	:	Ammonium perchlorate
NH_4F	:	Ammonium fluoride
NH_4I	:	Ammonium iodide
NH_4NO_3	:	Ammonium nitrate
NH_4SCN	:	Ammonium thiocyanate
NMP	:	N-methyl pyrrolidone
OCP	:	Open circuit potential
OLPT	:	Overlapping large polaron tunneling
PAN	:	Polyacrylonitrile
PbO_2	:	Lead oxide
PC	:	Propylene carbonate
PCL	:	Poly ε-caprolactone
PEG	:	Polyethylene glycol
PEMA	:	Polyethyl methacrylate
PEO	:	Polyethylene oxide
PESc	:	Polyethylene succinate
PMMA	:	Polymethyl methacrylate
PMVT	:	Poly(4-methyl-5-vinylthiazole)
p(TMC)	:	Poly(trimethylene carbonate)
PTFE	:	Polytetrafluoroethylene
PVA	:	Polyvinyl alcohol
PVAc	:	Polyvinyl acetate
PVC	:	Polyvinyl chloride
PVdF	:	Polyvinylidene fluoride
PVP	:	Polyvinyl pyrrolidone
PVPh	:	Poly(*p*-vinylphenol)
QMT	:	Quantum mechanical tunneling
SiO_2	:	Silicon dioxide
SEM	:	Scanning electron microscopy
SPE	:	Solid polymer electrolyte
SPH	:	Small polaron hopping
TiO_2	:	Titanium dioxide
TGA	:	Thermogravimetric analysis
V_2O_3	:	Vanadium (III) oxide
V_2O_5	:	Vanadium (V) oxide
VTF	:	Vogel-Tamman-Fulcher
XRD	:	X-ray diffraction
Zn	:	Zinc
$ZnSO_4 \cdot 7H_2O$	:	Zinc sulfate heptahydrate

CHAPTER 1

INTRODUCTION TO THE THESIS

1.1 Research Background

Nowadays, the demand for safer and more efficient electrochemical devices has increased due to the growing interest in electronic devices and electric vehicles. Currently, liquid electrolytes are widely used in commercial devices. However, this type of electrolyte tends to make some devices bulky and heavy, thus lowering the specific energy and specific power densities of these devices (Yap, 2012). Besides, the use of liquid electrolyte also bears the high risk of leakage and can cause corrosion during packaging (Osman, Ghazali, Othman, & Isa, 2012). Due to these drawbacks, solid polymer electrolyte (SPE) is a good candidate to replace liquid electrolyte.

Ion conducting polymer electrolytes have become an interesting area in solid state ionics due to their prospective application in solid state electrochemical devices (Tamilselvi & Hema, 2014). Fenton, Parker, and Wright (as cited in Noor, Ahmad, Rahman, & Talib, 2010) were the first to report on polyethylene oxide (PEO)-inorganic salts complexes as SPEs. Later, Armand, Chabagno, and Duclot (as cited in Schaefer et al., 2012) proved the possibility of PEO-alkali metal salt complexes as commercial electrolytes. Since then many polymers have been investigated, mostly synthetic polymers like polyvinyl alcohol (PVA) (Noor, Majid, & Arof, 2013), polyvinyl chloride (PVC) (Subban & Arof, 2004), polyvinyl pyrrolidone (PVP) (Ravi, Kumar, Mohan, &

Rao, 2014) and poly ε-caprolactone (PCL) (Woo, Majid, & Arof, 2011a, 2011b, 2012, 2013). The works are mainly focused on the improvement in ionic conductivity and mechanical strength, as well as chemical, thermal and electrochemical stabilities of polymer electrolytes to realize their potential application in electrochemical devices (Ramesh, Winie, & Arof, 2007; Sim, Majid, & Arof, 2014).

Natural polymers are worth to be investigated due to their natural abundance, low price and environmentally friendly nature (Noor et al., 2012). These polymers are usually used in the pharmaceutical (Ogaji, Nep, & Audu-Peter, 2011; Kulkarni, Butte, & Rathod, 2012), food (Alp, Mutlu, & Mutlu, 2000; Wang, Yang, Brenner, Kikuzaki, & Nishinari, 2014) and biomedical (Mahoney, Mccullough, Sankar, & Bhattarai, 2012) applications. Natural polymers can also be used to prepare SPEs (Aziz, Abidin, & Arof, 2010a, 2010b; Majid & Arof, 2005). Natural polymers are able to be processed as membranes or films with excellent transparency (Noor et al., 2012).

The choice of polymer blend as an electrolyte host is due to the fact that polymer blending is one of the effective techniques to optimize the ionic conductivity (Buraidah & Arof, 2011; Reddy, Kumar, Rao, & Chu, 2006; Xi et al., 2006). Polymer blends have become commercially and technologically more important than the fabrication of homo-polymers and copolymers because blending allows one to create a new material with specific properties for the desired application at a low cost (Tamilselvi & Hema, 2014). In this work, the blend of corn starch and chitosan is chosen as the polymer host. Report by Xu, Kim, Hanna, and Nag (2005) suggested that starch and chitosan are compatible and can interact with each other. Starch-chitosan blend has been extensively studied for tissue engineering (Nakamatsu, Torres, Troncoso, Min-Lin, & Boccaccini, 2006),

biomedical (Baran, Mano, & Reis, 2004) and food packaging (Tripathi et al., 2008) applications.

Ionic source is one of the main constituents in an electrolyte because of its strong influence on the electrolyte's properties such as conductivity, amorphousness and thermal stability. Alkali metal salts, inorganic acids and ammonium salts are widely used for preparation of SPEs as reported in the literature. Among the alkali metal salts, lithium is the most preferred for polymer electrolyte studies due to the small size of lithium ion (Li^+) which provides high gravimetric Coulombic density (Johansson, 1998). Besides, lithium ion conducting electrolytes have a wide potential window (Ghosh, Wang, & Kofinas, 2010). However, due to the safety issue associated with lithium battery, attention has been given to proton conducting electrolytes to serve as electrolyte in device application.

1.2 Objectives of the Present Work

The objectives of this work are as follow:

1. To develop proton conducting starch-chitosan blend based polymer electrolytes by solution cast technique.
2. To characterize the samples using electrochemical impedance spectroscopy (EIS) to identify the highest conducting electrolyte. Further characterization using various techniques will be done to strengthen the EIS results.
3. To optimize the conductivity by adding glycerol as plasticizer.
4. To fabricate and to test an electrochemical double layer capacitor (EDLC) employing the optimized conducting electrolyte.

5. To fabricate and to test proton batteries employing the optimized conducting electrolyte.

1.3 Scope of the Thesis

This thesis is divided into ten chapters. In Chapter 2, a general introduction and literature review on electrolytes, polymers, polymer blend, plasticization, EDLC and proton battery will be discussed. The details of electrolytes preparation and characterization techniques will be the main focus in Chapter 3. The electrochemical devices fabrication and characterization are also presented in this chapter.

Since starch-chitosan blend host is used in this work, the most suitable ratio of the blend to be chosen as the polymer host will be determined. This is because the amorphousness of the polymer host is a crucial factor for ion conduction (Kadir, Aspanut, Yahya, & Arof, 2011; Kadir, Majid, & Arof, 2010). Thus, Chapter 4 will present the X-ray diffraction (XRD) studies on different ratios of starch-chitosan blend to determine the most amorphous blend, thereby selecting the polymer host.

Chapter 5 discusses the interaction of polymer-polymer, polymer-salt, polymer-plasticizer, salt-plasticizer and polymer-salt-plasticizer, resulted from Fourier transform infrared (FTIR) spectroscopy studies. These are necessary as these interactions can affect the ionic conductivity and conductivity mechanism of the ions (Yap, 2012). The conductivity of the electrolytes will be described in detail in Chapter 6. Further in this chapter, transport analysis as well as XRD, scanning electron microscopy (SEM), differential scanning calorimetry (DSC) and thermogravimetric analysis (TGA) results

will be discussed to strengthen the conductivity result. The other electrical properties of the electrolytes such as dielectric and conduction mechanism will be described in detail in Chapter 7.

The highest conducting electrolyte in this work will be chosen for fabrication of an EDLC and proton batteries. The characteristics of the devices are presented in Chapter 8. Chapter 9 discusses the overall results presented in this thesis and finally Chapter 10 summarizes the thesis with some suggestions for further works.

CHAPTER 2

LITERATURE REVIEW

2.1 Introduction

The science of energy storage is an important branch of technology nowadays, as portable electronic devices such as laptops, mobile phones, digital cameras and tablets are becoming increasingly multifunctional which demands high power energy resources. Electrochemical devices such as batteries (Ali, Subban, Bahron, Yahya, & Kamisan, 2013; Kufian et al., 2012; Noor et al., 2013), solar cells (Arof, Aziz, et al., 2014; Buraidah, Teo, Majid, & Arof, 2010; Jun et al., 2013), EDLCs (Asmara, Kufian, Majid, & Arof, 2011; G.P. Pandey, Kumar, & Hashmi, 2011; Syahidah & Majid, 2013) and fuel cells (Nara, Momma, & Osaka, 2013; Shuhaimi, Alias, Kufian, Majid, & Arof, 2010) have been vigorously studied due to the rise in popularity of the portable electronic devices. The studies include the performance of the devices, electrode materials and ionic conductors.

Ionic conductor or electrolyte is a key component in electrochemical devices since ionic conduction has strong influence on the device performance (Hofmann, Schulz, & Hanemann, 2013; McBreen, Lee, Yang, & Sun, 2000; Park, Zhang, Chung, Less, & Sastry, 2010; Rao, Geng, Liao, Hu, & Li, 2012; Takami, Sekino, Ohsaki, Kanda, & Yamamoto, 2001). Liquid electrolytes are preferable due to their high ionic conductivity (Deepa et al., 2002; Perera & Dissanayake, 2006). However,

electrochemical devices containing liquid electrolyte are exposed to problems such as leakage, corrosion and solvent evaporation at high temperature (P.-Y. Chen, Lee, Vittal, & Ho, 2010; Lee, Chen, Vittal, & Ho, 2010; Lee, Lin, Chen, Vittal, & Ho, 2010). Therefore, SPEs have received wide attention for their thermal stability, ability to eliminate corrosive solvent and harmful gas formation, and low volatility with easy handling (Ramesh, Liew, & Arof, 2011). The study on polymer electrolytes was disclosed by Fenton et al. (as cited in Noor et al., 2010). However, their work did not receive much attention until Armand et al. (as cited in Periasamy et al., 2002; Schaefer et al., 2012) reported the possibility of PEO-alkali metal salt complexes as commercial electrolytes. Their work has encouraged further studies on the new polymer electrolyte systems. The examples of SPE systems with their room temperature conductivity are listed in Table 2.1.

Table 2.1: Examples of solid polymer electrolyte systems.

Electrolytes	**Conductivity (S cm^{-1})**	**Reference**
PEO-$(NH_4)_2SO_4$	9.3×10^{-7}	Maurya, Hashmi, & Chandra, 1992
Chitosan-$LiNO_3$	2.7×10^{-4}	Mohamed, Subban, & Arof, 1995
PEO-NH_4SCN	$\sim 10^{-6}$	Srivastava, Chandra, & Chandra, 1995
PEO-$3CdSO_4.8H_2O$	5.5×10^{-7}	Zain & Arof, 1998
PVC-PMMA-$LiCF_3SO_3$	2.06×10^{-6}	Ramesh, Yahaya, & Arof, 2002
Starch-NH_4NO_3	2.83×10^{-5}	Khiar & Arof, 2010
Chitosan/PVA-NH_4I	1.77×10^{-6}	Buraidah & Arof, 2011
PVP-KIO_4	1.42×10^{-4}	Ravi et al., 2014

Where;
$3CdSO_4.8H_2O$ = cadmium sulphate
KIO_4 = potassium periodate
$LiCF_3SO_3$ = lithium triflate
$LiNO_3$ = lithium nitrate
NH_4I = ammonium iodide
NH_4NO_3 = ammonium nitrate
NH_4SCN = ammonium thiocyanate
$(NH_4)_2SO_4$ = ammonium sulfate
PMMA = polymethyl methacrylate

2.2 Polymers

A polymer is a macromolecule composed of repeated subunits, i.e. monomers. Polymers already have a wide range of applications in our daily life including plastic bags, contact lenses, plastic bottles and electronic components. The ability of polymers to host ionic conduction has lead towards the development of polymer electrolytes. Generally, polymers are insulators since their conductivity is very low (Shuhaimi, 2011). To form a complexation with salt, a polymer should have polar groups on the polymer chain to solvate the salt effectively (Sadhukhan, 2011).

There are two types of polymers:-

- synthetic polymers, and
- natural polymers.

2.2.1 Synthetic Polymers

Synthetic polymers are chemically manufactured from separate materials through the polymerization. Most of them are derived from petrochemicals and regarded as non-biodegradable (Lu, Xiao, & Xu, 2009). Examples of synthetic polymers are Teflon, polyethylene, epoxy, polyester and nylon. Although synthetic polymers possesss advantages like predictable properties, batch-to-batch uniformity and easily tailored, the widespread use of non-biodegradable polymers is a contributor to environmental problems (Lu et al., 2009). This is because the solid waste from these materials take up a thousand years to degrade (Azahari, Othman, & Ismail, 2011). Besides, the non-

biodegradable polymers are quite expensive, not suitable for temporary use and insoluble in most solvents (Lu, et al., 2009; Ma, Yu, He, & Wang, 2007). Hence reseachers have turned their attention to natural polymers to overcome problems encountered by synthetic polymers.

2.2.2 Natural Polymers

Natural polymers or biopolymers are produced from raw materials found in nature. They are usually biocompatible and biodegradable (Kucinska-Lipka, Gubanska, & Janik, 2014; Yu, Dean, & Li, 2006). Therefore the use of natural polymers gives lesser negative impact on the environment than synthetic polymer (Rodrigo, 2012). Three major classes of natural polymers are proteins, polyesters and polysaccharides (Aravamudhan, Ramos, Nada, & Kumbar, 2014). For the use in electrolyte, proteins and polysaccharides are best candidates to replace synthetic polymers due to their abundance in environment (Varshney & Gupta, 2011). The examples of polysaccharides are starch, cellulose, chitin, carrageenan, chitosan, agarose and pectin. Polysaccharides are polymers composed of many monosaccharide units linked by glycosidic bonds.

2.3 Starch

Starch is a mixture of linear amylose (poly-α-1,4-D-glucopyranoside) (molecular weight of 10^4-10^6 g mol^{-1}) and branched amylopectin (poly-α-1,4-D-glucopyranoside and α-1,6-D-glucopyranoside) (molecular weight of 10^6-10^8 g mol^{-1}), where it is regenerated from carbon dioxide and water via photosynthesis in plants (Averous &

Pollet, 2012; Ghoshal, 2012; Teramoto, Motoyama, Mosomiya, & Shibata, 2003). About 70% of the mass of a starch granule is amorphous, which consist mainly of amylose, while ~ 30% is crystalline, which contain primarily of amylopectin (Ochubiojo & Rodrigues, 2012; Sajilata, Singhal, & Kulkarni, 2006). The chemical structures of amylose and amylopectin are depicted in Figure 2.1.

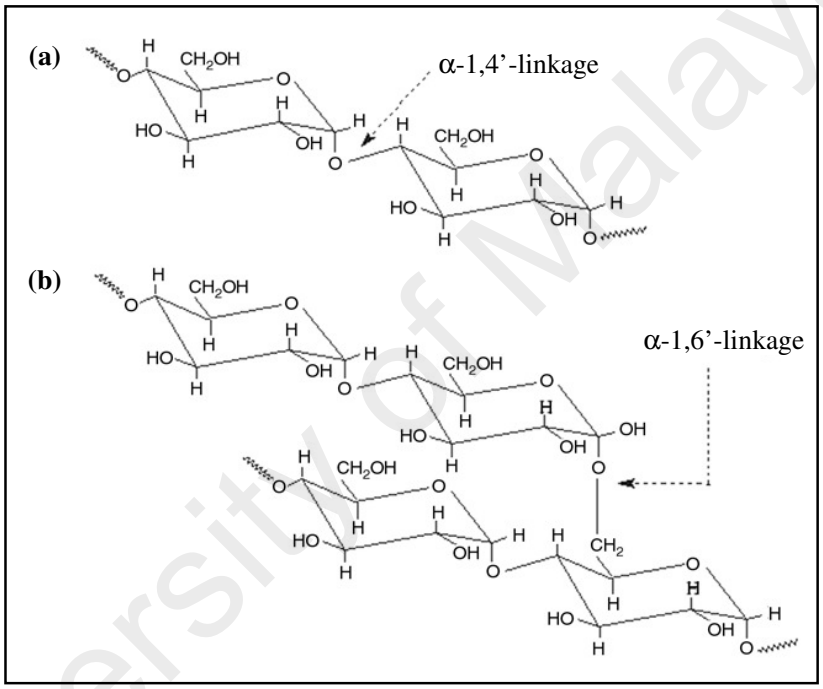

Figure 2.1: Structure of (a) amylose and (b) amylopectin (Lu et al., 2009)**.**

Starch is biodegradable, renewable and inexpensive material (Araujo, Cunha, & Mota, 2004; Zhang & Sun, 2004). Starch is the main material in industries such as coatings and sizing in paper, carpets and textiles (Biswas, Willet, Gordon, Finkenstadt, & Cheng, 2006; Neelam, Vijay, & Lalit, 2012). Starch is sourced from corn, potato, rice, wheat, cassava, tapioca and other staple foods (Agudelo, Varela, Sanz, & Fiszman, 2014; Luk, Sandoval, Cova, & Muller, 2013; Singh, Singh, Kaur, Sodhi, & Gill, 2003).

Starch is a hydrophilic material and can form mechanically poor film (Guohua et al., 2006; Hejri, Seifkordi, Ahmadpour, Zebarjad, & Maskooki, 2013). The mechanical strength and hydrophobicity of starch film can be improved by using acetic acid as the solvent (Gonzalez & Perez, 2002; Xu & Hanna, 2005). It is reported that when starch reacts with an acid, the water solubility of the starch granules is enhanced (Ochubiojo & Rodrigues, 2012).

The preparation of starch based polymer electrolytes is initiated by gelatinization of starch powder in the solvent (Teoh, 2012). Gelatinization of starch is a process that breaks down the intermolecular bonds of starch molecules in the presence of water and heat, allowing the hydrogen bonding sites to engage more water (Ubwa, Abah, Asemave, & Shambe, 2012). The gelatinization temperature varied from 55-82 °C, depending on its source (Ubwa et al., 2012, Shelton & Lee, 2000).

2.3.1 Starch Based Polymer Electrolytes

The use of starch as a host in electrolyte has been widely reported as shown in Table 2.2. Starch-salt complexation is expected to occur at the functional groups in amylose. This is because the cations of salt would be more easily attached to the amylose compound rather than the amylopectin since the α-1,4-D-glucosidic linkages of amylose are more stable and less steric than the α-1,6-D-glucosidic linkages of amylopectin (Khiar & Arof, 2010). Besides, ions are preferably mobile in amorphous region, which is mainly composed of amylose in starch. Different starches contain different proportion of amylose as shown in Table 2.3.

Table 2.2: Examples of starch based solid polymer electrolytes with their room temperature conductivity.

Electrolytes	Conductivity (S cm^{-1})	Reference
Starch-NH_4NO_3	2.83×10^{-5}	Khiar & Arof, 2010
Starch-$LiPF_6$	~ 10^{-7}	Ramesh et al., 2011
Starch-NH_4I	2.4×10^{-4}	M. Kumar, Tiwari, & Srivastava, 2012
Starch-LiI	4.68×10^{-5}	Khanmirzaei & Ramesh, 2013
Starch-$NaClO_4$	7.19×10^{-6}	Tiwari, Srivastava, & Srivastava, 2013
Starch-$AgNO_3$	1.03×10^{-9}	Shukur, Sonsudin, et al., 2013
Starch-$LiClO_4$	1.55×10^{-5}	Teoh, Ramesh, & Arof, 2012

Where;
$AgNO_3$ = silver nitrate
LiI = lithium iodide
$LiPF_6$ = lithium hexafluorophosphate
$LiClO_4$ = lithium perchlorate
$NaClO_4$ = sodium perchlorate

Table 2.3: Some starches and their amylose content.

Sources of starch	Amylose content (%)	Reference
Corn	25-28	Corn Refiners Association, 2006; Hegenbart, 1996; Jane, Xu, Radosavljevic, & Seib, 1992; Ning, Xingxiang, Haihui, & Jianping, 2009
Potato	20	Corn Refiners Association, 2006; Hegenbart, 1996; Jane et al., 1992
Tapioca	15-18	Corn Refiners Association, 2006; Hegenbart, 1996
Rice	20	Hegenbart, 1996
Wheat	25	Hegenbart, 1996; Maningat, Seib, Bassi, Woo, & Lasater, 2009

2.4 Chitosan

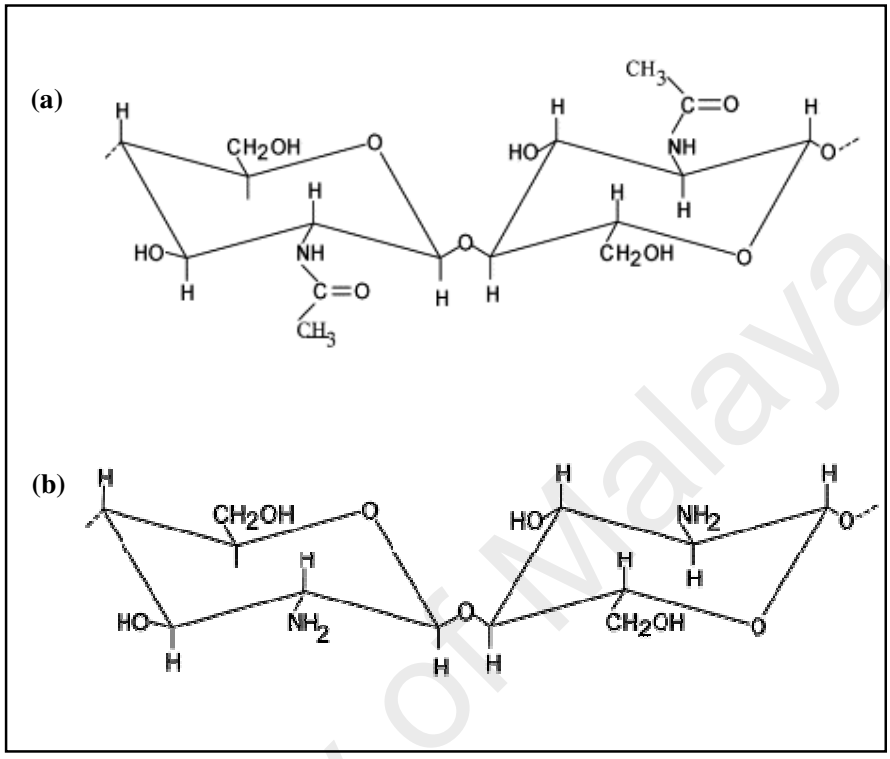

Figure 2.2: Structure of (a) chitin and (b) chitosan (Hejazi & Amiji, 2003)**.**

Chitosan consists of 1,4 linked-2-deoxy-2-aminoglucose obtainable by N-deacetylation of chitin (Xu et al., 2005). Both polysaccharides are sourced from shrimp, lobster and crab shells. The deacetylation process removes the acetyl groups from the molecular chain of chitin, thus leaving an amino group (Samar, El-Kalyoubi, Khalaf, & El-Razik, 2013). Chitosan has been studied as a food packaging material (Schreiber, Bozell, Hayes, & Zivanovis, 2013), dietary fiber (Muzzarelli, 1996) and potential carrier for drugs (Sinha et al., 2004). The properties of chitosan are influenced by the degree of deacetylation, the distribution of acetyl groups, chain length and molecular weight distribution (Li, Lin, & Chen, 2014; Park, Marsh, & Rim, 2002). Chitosan is highly

soluble in acidic solution (Jones, 2010). The chemical structures of chitin and chitosan are depicted in Figure 2.2.

2.4.1 Chitosan Based Polymer Electrolytes

Chitosan has been widely developed as a host in electrolyte. Chitosan-salt interaction can occur between the conducting charge species with the oxygen or nitrogen atoms which contain lone pair electrons (Arof, Morni, & Yarmo, 1998; Yahya & Arof, 2003). FTIR studies on chitosan-NH_4NO_3 electrolytes by Majid and Arof (2005, 2008) revealed that cation of the salt attached to the polymer based on the shifting of the carboxamide, amine and hydroxyl bands in the spectra (Majid & Arof, 2005, 2008). Examples of SPEs based on chitosan with their room temperature conductivity are listed in Table 2.4.

Table 2.4: Examples of chitosan based solid polymer electrolytes with their room temperature conductivity.

Electrolytes	Conductivity (S cm^{-1})	Reference
Chitosan-NH_4NO_3	2.53×10^{-5}	Majid & Arof, 2005
Chitosan-NH_4Br	4.38×10^{-7}	Shukur, Azmi, et al., 2013
Chitosan-$AgCF_3SO_3$	4.25×10^{-8}	Aziz et al., 2010a
Chitosan-$LiN(CF_3SO_2)_2$	5.1×10^{-8}	Ali et al., 2005
Chitosan-$NH_4CF_3SO_3$	~ 10^{-6}	Khiar, Puteh, & Arof, 2006
Chitosan-$AgNO_3$	2.6×10^{-5}	Morni, Mohamed, & Arof, 1997

Where;
$AgCF_3SO_3$ = silver triflate
$LiN(CF_3SO_2)_2$ = lithium trifluoromethane sulfonimide
NH_4Br = ammonium bromide
$NH_4CF_3SO_3$ = ammonium triflate

2.5 Polymer Blend

A blend is formed when different polymers are mixed together without covalent bond formation. Polymer blending is usually cheaper and less time consuming for the production of materials (Marsano, Corsini, Canetti, & Freddi, 2008). This method is a versatile or an alternative way to develop new materials with a desirable combination of properties (Lu & Weiss, 1991). Besides, the resulting blend often exhibit better properties than any one of the component polymers. For example, the blending of chitosan-PEO has decreased the tendency to spherulitic crystallization of PEO (Zivanovic, Li, Davidson, & Kit, 2007). Kadir et al. (2010) reported that PVA-chitosan blend film is more amorphous than the pure PVA film and pure chitosan film. The ionic transference number of starch-methyl cellulose blend film is higher than pure starch and pure methyl cellulose films (El-Kader & Ragab, 2013). Conductivity of polymer electrolytes has been reported to be improved by using polymer blend host (Kim, Park, & Rhee, 1996; Rajendran & Mahendran, 2001). Examples of polymer blend based electrolytes are listed in Table 2.5.

Table 2.5: Examples of polymer blend based electrolytes with their room temperature conductivity.

Electrolytes	Conductivity (S cm^{-1})	Reference
Chitosan-PEO-NH_4NO_3	1.02×10^{-4}	Kadir, Aspanut, Yahya, & Arof, 2011
PVC-PMMA-$LiCF_3SO_3$	2.06×10^{-6}	Ramesh et al., 2002
Chitosan-PVA-NH_4I	1.77×10^{-6}	Buraidah & Arof, 2011
Starch-PEO-NH_4NO_3	2.81×10^{-7}	Ramly, Isa, & Khiar, 2011
Methyl cellulose-chitosan-$NH_4CF_3SO_3$	4.99×10^{-6}	Hamdan & Khiar, 2014
PVA-chitosan-NH_4NO_3	2.07×10^{-5}	Kadir et al., 2010

2.5.1 Starch-Chitosan Blend

Starch based products were reported to possess many disadvantages, such as brittleness, sensitive to water and low in mechanical strength (Kampeerapappun, Aht-ong, Pentrakoon, & Srikulkit, 2007; Mathew, Brahmakumar, & Abraham, 2006; Wu & Zhang, 2001). In order to overcome these problems, starch has been blended with other polymers (Miyamoto, Yamane, Seguchi, & Okajima, 2009; Ramly et al., 2011; Xu et al., 2005).

Salleh, Muhamad, and Khairuddin (2009) reported that the interactions between hydroxyl groups of starch and amino groups of chitosan in starch-chitosan blend results a good miscibility between both polymers. The existence of starch provides more transparent films while chitosan can reinforce the mechanical strength of the films (Salleh & Muhamad, 2010; Salleh et al., 2009). Zhai, Zhao, Yoshii, and Kume (2004) state that the addition of chitosan into starch film improved the formation condition and ductility of the films. The conductivity of starch-NH_4NO_3 had been increased from 2.83×10^{-5} S cm^{-1} to 3.89×10^{-5} S cm^{-1} when starch was blended with chitosan (Khiar & Arof, 2010, 2011). Starch-chitosan-$LiClO_4$ obtained a conductivity of 3.7×10^{-4} S cm^{-1}, which is higher compared to 1.55×10^{-5} S cm^{-1} by using starch as a single polymer host (Sudhakar & Selvakumar, 2012; Teoh et al., 2012).

2.6 Proton Conducting Polymer Electrolytes

In proton conducting SPEs, H^+ ions (or proton) are the cations responsible for the ionic conduction. Proton conducting SPEs have been recognized for their suitability

in the application of low energy density devices (Pratap, Singh, & Chandra, 2006). Strong inorganic acids such as phosphoric acid (H_3PO_4) (Yan et al. 2011; Prajapati, Roshan, & Gupta; 2010) and sulfuric acid (H_2SO_4) (Raj & Varma, 2010) have been used as proton provider in SPEs. However, polymer electrolytes employing inorganic acid suffer from chemical degradation and mechanical integrity making them not suitable for practical applications (Hema, Selvasekarapandian, Sakunthala, Arunkumar, & Nithya, 2008).

From a report by Srivastava and Chandra (2000), two different methods, alternating current (ac)-direct current (dc) combination technique and coulometric investigation had been used to determine the positive charge carrier responsible for ionic conduction in polyethylene succinate (PESc)-NH_4ClO_4 electrolyte. The authors concluded that the transporting cation is found to be H^+ ion. In PEO-NH_4SCN electrolyte, H^+ ion is found to be the charge carrier in the electrical transport from coulometric investigation (Srivastava et al., 1995). Shuhaimi, Alias, Majid and Arof (2008) inferred that the conducting charge species in κ-carrageenan-chitosan-NH_4NO_3 electrolyte is H^+ ion. Reports from the literature concluded that in polymer-ammonium salt complexes, the cation responsible for ionic conduction is H^+ ion. The ammonium ion (NH_4^+) has an ideal tetrahedral structure as shown in Figure 2.3.

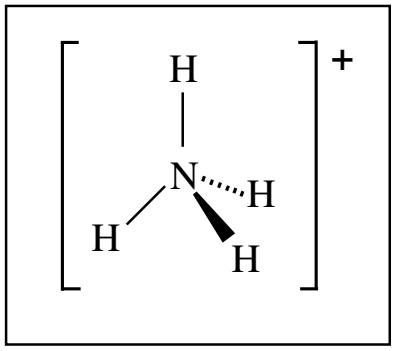

Figure 2.3: Structure of NH_4^+ ion.

As shown in Figure 2.3, four hydrogen atoms are bonded to a nitrogen atom. Under the influence of an electric field, the most weakly bounded hydrogen atom in NH_4^+ can be easily dissociated. The dissociated H^+ ion can move from one site to another. The vacancy left by the ion will be filled by another H^+ ion from the neighbouring site. This kind of protonic conduction is known as Grotthuss mechanism (Buraidah, Teo, Majid & Arof, 2009; Kadir, Aspanut, Majid, & Arof, 2011; Kreuer, 1996; Majid & Arof, 2005).

Many ammonium salts have been employed in SPEs, for example $NH_4CF_3SO_3$ (Deraman, Mohamed, & Subban, 2013), NH_4SCN (Woo et al., 2012), ammonium fluoride (NH_4F) (Aziz, Idris, & Isa, 2010) and ammonium chloride (NH_4Cl) (Vijaya et al., 2013). Table 2.6 lists the examples of proton conducting SPE systems with their room temperature conductivity.

Table 2.6: Examples of proton conducting solid polymer electrolytes with their room temperature conductivity.

Electrolytes	**Conductivity (S cm^{-1})**	**Reference**
Starch-NH_4NO_3	2.83×10^{-5}	Khiar & Arof, 2010
PVA-chitosan-NH_4NO_3	2.07×10^{-5}	Kadir et al., 2010
Methyl cellulose-NH_4F	6.4×10^{-7}	Aziz et al., 2010
PCL-NH_4SCN	1.01×10^{-4}	Woo et al., 2011a
Starch-NH_4I	2.4×10^{-4}	M. Kumar et al., 2012
PVC-$NH_4CF_3SO_3$	~ 10^{-7}	Deraman et al., 2013

In the present work, NH_4Cl has been chosen as the dopant. Hema, Selvasekarapandian, Arunkumar, Sakunthala, and Nithya (2009) have doped PVA with

15 mol% NH_4Cl and reported a conductivity value of 1.0×10^{-5} S cm^{-1} at ambient temperature. PVP-NH_4Cl polymer electrolyte system obtained a room temperature conductivity of 2.51×10^{-5} S cm^{-1} (Vijaya et al., 2012). A system of polyethylene glycol (PEG) doped NH_4Cl obtained an optimum room temperature conductivity of 9.58×10^{-7} S cm^{-1} (Polu & Kumar, 2011).

2.7 Plasticization

The conductivity of SPEs can be enhanced by using plasticization method (Buraidah & Arof, 2009; Woo et al., 2013). Plasticizer with low viscosity and high dielectric constant can increase the mobility of carriers as well as improve salt dissociation (Rajendran, Sivakumar, & Subadevi, 2004). When more salt is dissociated, the number of charge carriers will increase hence improves the conductivity (Yap, 2012). Addition of plasticizers can increase the amorphous content of the electrolytes as well as lower the glass transition temperature (T_g) (Ibrahim, Yasin, Nee, Ahmad, & Johan, 2012; Pradan, Choudhary, Samantaray, Karan, & Katiyar, 2007). When the polymer interacts with plasticizer, the dipole-dipole interactions between the polymer chains can be weakened (Ramesh & Ling, 2010). The amorphous phase is then become more flexible thus increases the segmental motion of polymer (Osman, Ibrahim, & Arof, 2001; Ramesh & Ling, 2010). This phenomenon reduces the T_g.

The use of plasticizer in polymer electrolyte is one of the easiest and practical ways to maximize the conductivity. Table 2.7 shows the effect of plasticizer on room temperature conductivity of various SPE systems.

Table 2.7: Examples of plasticized solid polymer electrolytes with their room temperature conductivity.

Electrolytes	Conductivity (S cm^{-1})	Reference
PEO-$LiCF_3SO_3$ PEO-$LiCF_3SO_3$-DBP	3.3×10^{-6} 6.0×10^{-5}	Johan & Ting, 2011
Chitosan-PVA-NH_4NO_3 Chitosan-PVA-NH_4NO_3-EC	2.07×10^{-5} 1.60×10^{-3}	Kadir et al., 2010
PCL-NH_4SCN PCL-NH_4SCN-EC	4.6×10^{-8} 3.8×10^{-5}	Woo et al., 2013
Methyl cellulose-NH_4NO_3 Methyl cellulose-NH_4NO_3-PEG	2.10×10^{-6} 1.14×10^{-4}	Shuhaimi et al., 2010

Where;
DBP = dibutyl phthalate **EC = ethylene carbonate**

2.7.1. Glycerol

Glycerol (molecular formula, $C_3H_8O_3$) is a low toxicity alcohol and virtually nontoxic to both human and environment (Tan, Aziz, & Aroua, 2013). Glycerol has a wide range of applications in pharmaceutical (Breslin & Stephenson, 1985), cosmetics (Polaskova et al., 2012) and microbiology (da Silva, Mack, & Contiero, 2009) industries. Glycerol has a dielectric constant ($\varepsilon_{glycerol}$) of 42.5. The chemical structure of glycerol is depicted in Figure 2.4.

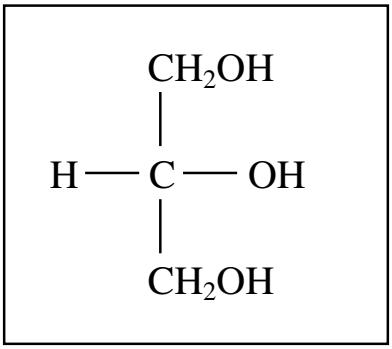

Figure 2.4: Chemical structure of glycerol.

In this work, the use of glycerol as plasticizing agent is due to the fact that glycerol is the most compatible plasticizer for starch based film (Curvelo, de Carvalho, & Agneli, 2001; Marcondes et al., 2010). Besides, glycerol has high boiling point of 290 °C and low melting point of 18 °C (Speight, 2002). Low melting point of glycerol ensures that it will not solidify at room temperature, which may limit the ion mobility. High boiling point ensures that glycerol will not boil in the temperature range of present study. Table 2.8 shows the examples of SPE systems with glycerol as plasticizer.

Table 2.8: Examples of solid polymer electrolytes with glycerol as plasticizer with their room temperature conductivity.

Electrolytes	Conductivity (S cm^{-1})	Reference
Starch-$LiClO_4$-glycerol	5.05×10^{-5}	Dragunski & Pawlicka, 2002
Chitosan-HCl-glycerol	9.5×10^{-4}	Pawlicka, Danczuk, Wieczorek, & Zygadlo-Monikowska, 2008
Gelatin-acetic acid-glycerol	4.5×10^{-5}	Vieira, Avellaneda, & Pawlicka (2007)
Starch-LiOac-glycerol	1.04×10^{-3}	Shukur, Ithnin, & Kadir, 2014
Chitosan-HCl-$LiCF_3SO_3$-glycerol	2.2×10^{-5}	Pawlicka et al., 2008
Chitosan-NH_4Br-glycerol	2.15×10^{-4}	Shukur, Azmi, et al., 2013

Where;
HCl = hydrochloric acid

2.8 Ionic Conductivity

Ionic conductivity is one of the crucial characteristics in the study of ionic conductor. In principle, ionic conductivity (σ) is related to the number density (n_d), mobility (μ) and charge (q) of ion as shown in Equation (2.1).

$$\sigma = n_d \mu q \quad (2.1)$$

From Equation (2.1), the conductivity can be increased when the number density and mobility of ion increase. To ensure the increment of the number density and mobility of ion, the concentration of ionic source in an electrolyte should be increased as depicted in Figure 2.5.

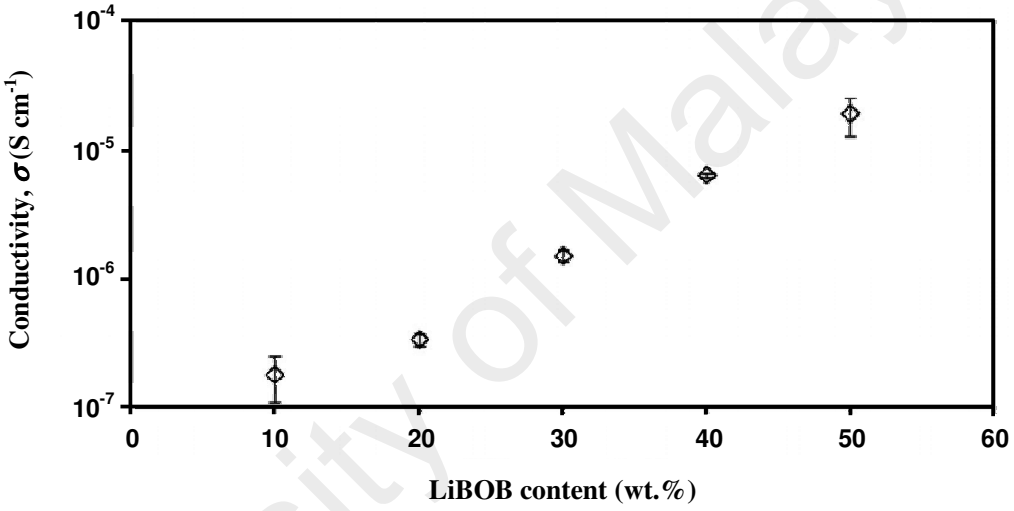

Figure 2.5: Room temperature conductivity of PAN-LiBOB electrolytes as a function of LiBOB concentration (Arof, Amirudin, Yusof, & Noor, 2014)**.**

From Figure 2.5, the conductivity of polyacrylonitrile (PAN)-lithium bis(oxolato)borate (LiBOB) electrolyte increases as the concentration of LiBOB increases. According to Arof, Amirudin, et al. (2014), the increasing conductivity with increasing LiBOB concentration is a result of either an increase in number density and/or mobility of ion. Using a method based on impedance spectroscopy, the authors proved that the increasing conductivity could be attributed to the increase in those parameters.

2.8.1 Rice and Roth Model

The Rice and Roth model (as cited in Idris, Majid, Khiar, Hassan, & Arof, 2005; Kadir et al., 2010; Majid & Arof, 2005) can be employed to evaluate the number density and mobility of ion. This model expresses the conductivity as:

$$\sigma = \frac{2}{3}\left[\frac{(Ze)^2}{kTm_c}\right] n_d E_a \tau \exp\left(\frac{-E_a}{kT}\right) \tag{2.2}$$

where, Z is the valency of conducting species, e is electron charge, T is absolute temperature, k is Boltzmann constant, m_c is mass of charge carrier, E_a is activation energy and τ is travelling time of ion. In this work, since H^+ ions are the positive charge carriers, the values of Z and m_c are +1 and 1.67×10^{-27} kg, respectively. The value of τ can be calculated using Equation (2.3).

$$\tau = \frac{l}{v} \tag{2.3}$$

Here, l is the distance between two coordination sites and v is velocity of mobile ion. The velocity of mobile ion can be obtained using:

$$v = \sqrt{\frac{2E_a}{m_c}} \tag{2.4}$$

The mobility of ion can be calculated using Equation (2.5):

$$\mu = \frac{\sigma}{n_d e} \tag{2.5}$$

Samsudin, Khairul, and Isa (2012) have estimated the number density and mobility of ion for carboxy methylcellulose-dodecyltrimethyl ammonium bromide (DTAB) electrolytes using the Rice and Roth model. The authors inferred that the conductivity is governed by those parameters. The conductivity of chitosan-NH_4Br-glycerol electrolytes have been reported to be affected by the number density and mobility of ion, where those parameters are reported to be 10^{17}-10^{18} cm^{-3} and 10^{-6}-10^{-4} cm^2 $V^{-1}s^{-1}$, respectively, using Rice and Roth model (Shukur, Azmi, et al., 2013).

2.9 Electrochemical Double Layer Capacitor (EDLC)

EDLC is an energy storage device with better power density during charge-discharge process, higher charging-discharging rate and longer cycle life compared to conventional secondary batteries (Kim & Mitani, 2006; Mitani, Lee, Saito, Korai, & Mochida, 2006). EDLC can be used as a complementary or alternative power source in many applications e.g. portable electronic devices , telecommunication devices, electric hybrid vehicles and standby power systems (Lei, Markoulidis, Ashitaka, & Lekakou, 2013). Basically, the charge storage mechanism in an EDLC is based on the Helmholtz double-layers formation through the ionic migration within the electrolyte without any electrode-electrolyte interaction (Lim, Teoh, Liew, & Ramesh, 2014a). Various materials have been used as EDLC electrode active material e.g. graphite (Ka & Oh, 2008; Shukur, Ithnin, Illias, & Kadir, 2013), carbon aerogel (Ling & Qing-Han, 2005;

Zeng, Wu, Fu, & Lai, 2008), activated carbon (Arof et al., 2012; Lei, Wilson, & Lekakou, 2011; Shuhaimi, Teo, Woo, Majid, & Arof, 2012) and manganese oxide (MnO_2) (Subramanian, Zhu, & Wei, 2008). However, activated carbon is preferred as electrode for its high surface area, good chemical stability, high conductivity and low cost (Syahidah & Majid, 2013).

The application of SPE in the fabrication of EDLCs can lead to thin film cells and high reliability without leakage of liquid components (Lee et al., 2012). Table 2.9 lists the examples of EDLCs using proton conducting SPEs.

Table 2.9: Examples of EDLCs using proton conducting solid polymer electrolyte.

Electrolytes	Electrode materials	Reference
Cellulose-PVA-H_3PO_4	Activated carbon	Hashim, Majid, Ibrahim, & Arof, 2005
PVA-chitosan-NH_4NO_3-EC	Activated carbon	Kadir & Arof, 2011
Chitosan-H_3PO_4-NH_4NO_3-Al_2SiO_5	Activated carbon	Arof & Majid, 2008
PVA-H_3PO_4	Graphite and activated carbon	Hashmi, Latham, Linford, & Schlindwein, 1997
Methyl cellulose-NH_4NO_3-PEG	Activated carbon	Shuhaimi et al., 2012
Chitosan-PEO-NH_4NO_3-EC	Graphite	Shukur, Ithnin, et al., 2013

Where;
Al_2SiO_5 = aluminum silicate

2.10 Proton Battery

Proton conducting electrolytes have long been recognized as the reputable initiative to lithium ion conductors in electrochemical device applications (Nasef, Saidi,

& Dahlan, 2007; Panero, Ciuffa, D'Epifano, & Scrosati, 2003). This is because the ionic radii of H^+ (~ 0.84 fm) is smaller than Li^+ ion (0.90 Å), makes it suitable for better intercalation into the layered structure of electrodes (Antognini et al., 2013; Mishra, 2013; Wongsaenmai, Ananta, & Yimnirun, 2012). For battery application, most of the proton conducting electrolytes are electrochemically decomposed at 1 to 2 V compare to Li^+ electrolytes (~4 V) (Kufian & Majid, 2010; Kufian et al., 2012; Ng & Mohamad, 2008; Samsudin, Lai, & Isa, 2014; Shukur, Ithnin, et al., 2013). However, due to the low cost of electrode and electrolyte materials used for proton batteries as well as no safety issues associated with them, proton batteries have become an alternative for application in low energy density devices (Mishra, 2013; Pratap et al., 2006).

A lot of cathode materials have been used in the development of proton batteries, such as lead oxide (PbO_2) (Ali, Mohamed, & Arof, 1998), vanadium (V) oxide (V_2O_5) (Agrawal, Hashmi, & Pandey, 2007), vanadium (III) oxide (V_2O_3) (Ali et al., 1998) and manganese (IV) oxide (MnO_2) (Ng & Mohamad, 2006). Study by Alias, Chee, and Mohamad (2014) shows that proton battery with MnO_2 cathode obtain a better performance and higher power density compared to proton battery with V_2O_5 cathode. According to the authors, V_2O_5 undergoes structural conversion due to mechanical stress, thus reduces the specific capacity of the battery. Bansod, Bhoga, Singh, and Tiwari (2007) have reported the performance of proton batteries using different cathode materials. The authors concluded that MnO_2 cathode is the most promising cathode for H^+ intercalation.

In this work, MnO_2 will be used as the cathode material while the combination of zinc (Zn) and zinc sulfate heptahydrate ($ZnSO_4 \cdot 7H_2O$) will be used as the anode material to sandwich the highest conducting electrolyte for proton batteries fabrication.

Table 2.10 shows some of reported proton batteries with their configuration from the literature.

Table 2.10: Examples of proton batteries with their configuration.

Electrolytes	Cathode	Anode	Reference
PEO-$(NH_4)_2SO_4$	$PbO_2 + MnO_2$	$Zn + ZnSO_4 \cdot 7H_2O$	Ali et al., 1998
Cellulose acetate-$NH_4CF_3SO_3$-EC	MnO_2	Zn	Saaid, Kudin, Ali, Ahmad, & Yahya, 2009
PVA-chitosan-NH_4NO_3-EC	MnO_2	$Zn + ZnSO_4 \cdot 7H_2O$	Kadir et al., 2010
Chitosan-NH_4CH_3COO-EC	V_2O_5	$Zn + ZnSO_4 \cdot 7H_2O$	Alias et al., 2014
Carboxymethyl cellulose-NH_4Br	MnO_2	$Zn + ZnSO_4 \cdot 7H_2O$	Samsudin et al., 2014
PVC-$NH_4CF_3SO_3$-BATS	MnO_2	$Zn + ZnSO_4 \cdot 7H_2O$	Deraman et al., 2013

Where;
BATS = butyltrimethyl ammonium bis (trifluoromethyl sulfonyl) imide

2.11 Summary

In this chapter, background and knowledge on starch, chitosan and polymer electrolytes have been reviewed. Brief discussions on proton batteries and EDLCs have also been presented. From the knowledge gained in this literature review, it is expected that the polymer electrolyte in this work can be used for application in proton batteries and EDLC.

CHAPTER 3

METHODOLOGY

3.1 Introduction

In this work, starch-chitosan blend was used as the electrolyte's polymer host, NH_4Cl salt as the ion provider and glycerol as the plasticizer. The preparation and characterization of the electrolytes were done using the techniques discussed in this chapter. Three systems have been prepared:

- starch-chitosan,
- starch-chitosan-NH_4Cl and
- starch-chitosan-NH_4Cl-glycerol.

The starch-chitosan system was prepared to determine the most amosphous blend to serve as the polymer host. The best ratio of starch-chitosan blend was then used in the preparation of starch-chitosan-NH_4Cl and starch-chitosan-NH_4Cl-glycerol systems. The electrolytes were characterized using XRD, SEM, FTIR, TGA, DSC, electrochemical impedance spectroscopy (EIS), transference number measurements and linear sweep voltammety (LSV). The highest conducting electrolyte was used in an EDLC and proton batteries applications.

3.2 Samples Preparation

3.2.1 Starch-Chitosan System

Different weight percentages (*x* wt.%) of corn starch (Brown & Polson) were dissolved in 100 mL of 1% acetic acid (SYSTERM) separately at 80 °C for 20 min. At this point, starch was not fully gelatinized since gelatinization is a multistage process and starch will completely gelatinized over a temperature range below the boiling point of water (Knorr, Heinz, & Buckow, 2006; Zarillo, Pearsall, Raymond, Tisdale, & Quon, 2008). After the starch solutions were cooled to room temperature (25 °C or 298 K), (100-*x*) wt.% of chitosan [viscosity: 800-2000 cP, 1 wt.% in 1% acetic acid (25 °C), molecular weight of approximately 310000-375000 Da with degree of deacetylation >75% (Moutzouri & Athanassiou, 2014), Sigma-Aldrich] were then added to the solutions. The composition and designation of various starch-chitosan blends are listed in Table 3.1. The starch-chitosan blend solutions were stirred until homogeneous solutions were obtained. All homogenous solutions were cast onto plastic Petri dishes and left to dry at room temperature for 2-3 days to form film. The dry films were then kept in desiccators filled with silica gel desiccants for further drying before being characterized to avoid any trace of moisture.

Table 3.1: Composition and designation of starch-chitosan blend system.

Starch : chitosan composition (wt.%)	Starch (g)	Chitosan (g)	Designation
100 : 0	1.000	0	S10C0
90 : 10	0.900	0.100	S9C1
80 : 20	0.800	0.200	S8C2

Table 3.1, continued

70 : 30	0.700	0.300	S7C3
60 : 40	0.600	0.400	S6C4
50 : 50	0.500	0.500	S5C5
40 : 60	0.400	0.600	S4C6
30 : 70	0.300	0.700	S3C2
20 : 80	0.200	0.800	S2C8
10 : 90	0.100	0.900	S1C9
0 : 100	0	1.000	S0C10

The physical appearance of starch-chitosan films is demonstrated in Figure 3.1.

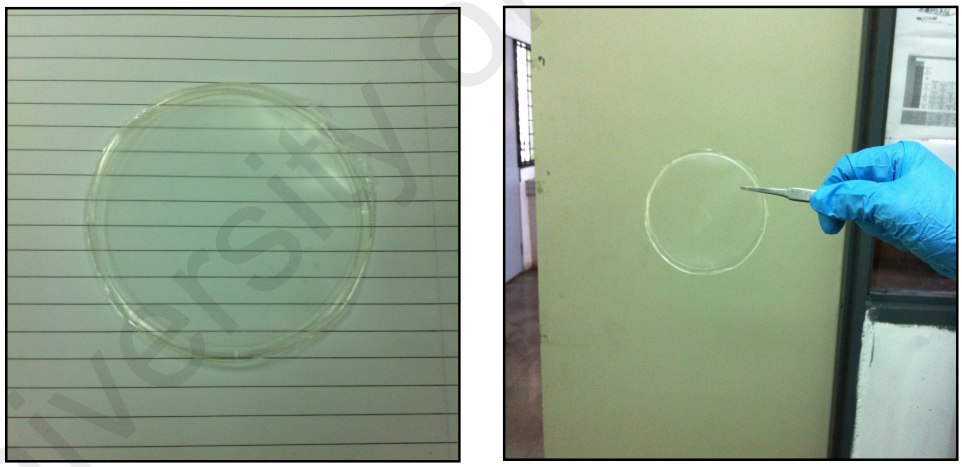

Figure 3.1: Transparent and free standing starch-chitosan based film.

3.2.2 Starch-Chitosan-NH_4Cl (Salted) System

For preparation of salted system, 0.8 g starch was dissolved in 100 mL of 1% acetic acid at 80 °C for 20 min. After the solution was cooled to room temperature, 0.2 g chitosan was added. Different amounts of NH_4Cl (R&M Chemicals) were added to the

solutions separately and stirred until homogenous solutions were obtained. The composition and designation of electrolytes in salted system are listed in Table 3.2. All homogenous solutions were cast onto plastic Petri dishes and left to dry at room temperature for 2-3 days to form film (Figure 3.2). The dry films were then kept in desiccators filled with silica gel desiccants for further drying before being characterized to avoid any trace of moisture.

Table 3.2: Composition and designation of electrolytes in salted system.

S8C2 : NH_4Cl composition (wt.%)	**Starch (g)**	**Chitosan (g)**	**NH_4Cl (g)**	**Designation**
95 : 5	0.800	0.200	0.053	S1
90 : 10	0.800	0.200	0.111	S2
85 : 15	0.800	0.200	0.177	S3
80 : 20	0.800	0.200	0.250	S4
75 : 25	0.800	0.200	0.333	S5
70 : 30	0.800	0.200	0.429	S6
65 : 35	0.800	0.200	0.538	S7
60 : 40	0.800	0.200	0.667	S8

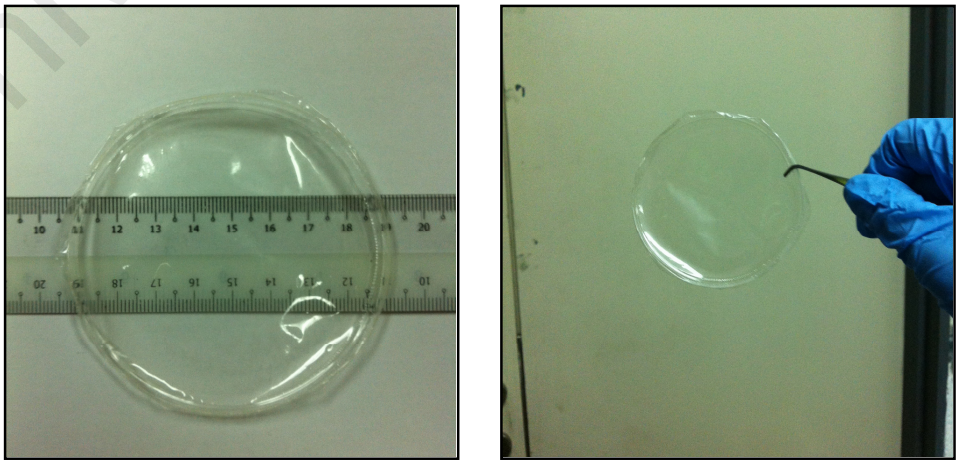

Figure 3.2: Transparent and free standing starch-chitosan-NH_4Cl based electrolyte.

3.2.3 Starch-Chitosan-NH_4Cl-Glycerol (Plasticized) System

For the preparation of plasticized system, different amounts of glycerol (SYSTERM) were added to the highest conducting salted electrolyte solutions separately. All homogenous solutions were cast onto plastic Petri dishes and left to dry at room temperature for 2-3 days to form film. The dry films were then kept in desiccators filled with silica gel desiccants for further drying before being characterized to avoid any trace of moisture. The composition and designation of electrolytes in plasticized system are listed in Table 3.3.

Table 3.3: Composition and designation of electrolytes in plasticized system.

S5 : glycerol composition (wt.%)	Starch (g)	Chitosan (g)	NH_4Cl (g)	Glycerol (g)	Designation
95 : 5	0.800	0.200	0.333	0.070	P1
90 : 10	0.800	0.200	0.333	0.148	P2
85 : 15	0.800	0.200	0.333	0.235	P3
80 : 20	0.800	0.200	0.333	0.333	P4
75 : 25	0.800	0.200	0.333	0.444	P5
70 : 30	0.800	0.200	0.333	0.571	P6
65 : 35	0.800	0.200	0.333	0.718	P7
60 : 40	0.800	0.200	0.333	0.889	P8
55 : 45	0.800	0.200	0.333	1.091	P9

The physical appearance of starch-chitosan-NH_4Cl-glycerol electrolytes is demonstrated in Figure 3.3.

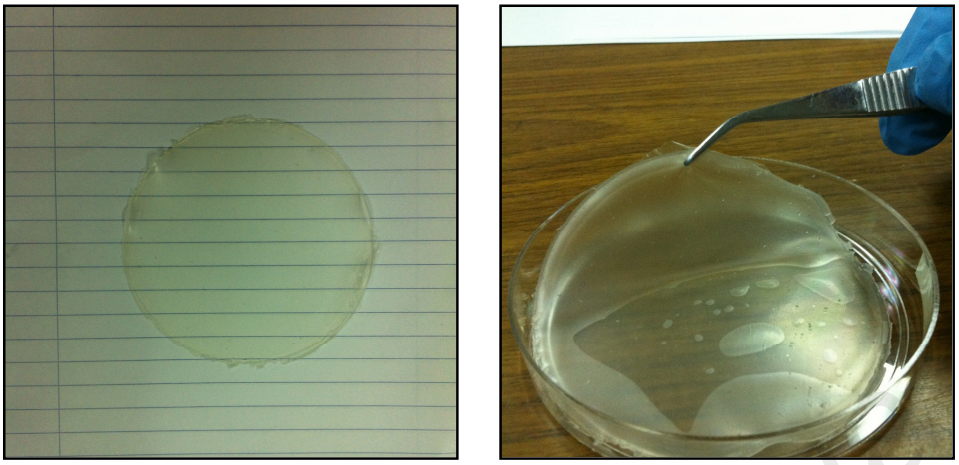

Figure 3.3: Transparent and flexible starch-chitosan-NH_4Cl-glycerol based electrolyte.

3.3 Electrolytes Characterization

3.3.1 X-ray Diffraction

XRD method is a well established technique to determine the crystallinity and amorphousness of samples. In the present work, XRD measurements were carried out by Siemens D5000 X-ray diffractometer in the range of $5° \leq 2\theta \leq 80°$ at a resolution of 0.1°. X-rays of 1.5406 Å wavelength were generated by a Cu Kα source. When the monochromatic X-ray beam hits a sample, scattered X-rays with the same wavelength as the incident beam will be generated (Aziz, 2012). The angle between the incident beam and the normal to the sample will change as the sample rotates (Kadir, 2010). Reflection of X-rays will only occur when the following Bragg's law is fulfilled:

$$n\lambda = 2d \sin\theta \tag{3.1}$$

where n is the order of reflection, λ is the wavelength, d is the interplanar spacing and θ is the angle between incident beam and the planes, which is also known as Bragg's angle.

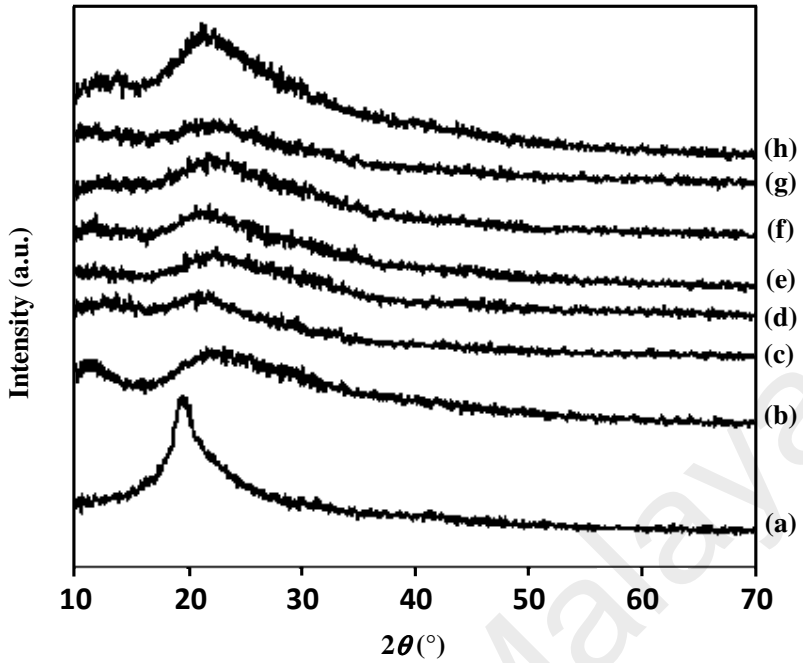

Figure 3.4: XRD patterns of (a) pure PVA, (b) pure PVP, (c) PVA-PVP blend, (d) PVA-PVP-5 wt.% $NH_4C_2H_3O_2$, (e) PVA-PVP-15 wt.% $NH_4C_2H_3O_2$, (f) PVA-PVP-20 wt.% $NH_4C_2H_3O_2$, (g) PVA-PVP-30 wt.% $NH_4C_2H_3O_2$ and (h) PVA-PVP-35 wt.% $NH_4C_2H_3O_2$ (Rajeswari et al., 2013)**.**

Figure 3.4 shows the XRD patterns of pure PVA, pure PVP, PVA-PVP blend and PVA-PVP blend doped with various concentration of ammonium acetate ($NH_4C_2H_3O_2$) by Rajeswari et al. (2013). The authors explained the XRD results on the basis of amorphousness of the electrolyte. The authors added that the addition of $NH_4C_2H_3O_2$ salt to the PVA-PVP blend has decreased the crystallinity of the electrolytes.

3.3.2 Scanning Electron Microscopy

The surface morphology of the polymer blend films in starch-chitosan system at room temperature was studied using Leica S440 scanning electron microscope at 1000×

magnification. The surface morphology of the electrolytes in salted and plasticized systems at room temperature was studied using ZEISS EVO MA10 scanning electron microscope at 2000× magnification. Prior to the SEM studies, all samples were coated with a thin layer of gold using SC7620 mini sputter coater to prevent electrostatic charging on the films.

In SEM technique, the image of a sample is produced by scanning it with a focused beam of electrons. The interaction between these electrons and the atoms in the sample produces detected signals that contain information about the sample's surface (Khan, 2014). Morphology studies can shed some light to the variation in conductivity of the electrolytes (Kadir et al., 2010; Woo et al., 2012). Figure 3.5 depicts the surface morphology of PVA-NH_4SCN electrolyte as reported by Bhad and Sangawar (2013). The authors stated that the particles observed on the electrolyte's surface performed as the channels for proton conduction through the electrolyte.

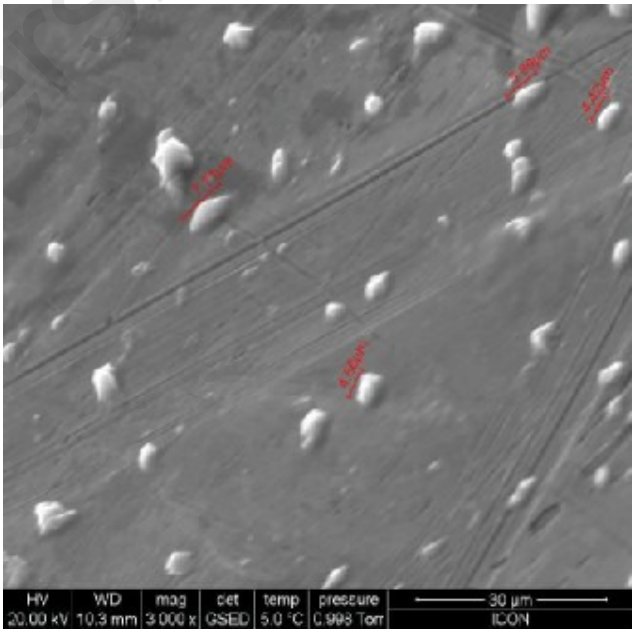

Figure 3.5: SEM image of PVA-NH_4SCN electrolyte (Bhad & Sangawar, 2013)**.**

3.3.3 Fourier Transform Infrared Spectroscopy

In order to study the interaction between the electrolyte materials, FTIR studies were recorded using Spotlight 400 Perkin-Elmer spectrometer in the wavenumber range of 450-4000 cm^{-1} at a resolution of 1 cm^{-1}. FTIR method is based on the fact that different bonds and groups of bonds vibrate at characteristic frequencies (Buraidah, 2012). The interaction between the materials induces changes in the position and shape intensity of the bands' peak. In the present work, FTIR studies were carried out to determine the interaction of starch-chitosan, starch-chitosan-NH_4Cl and starch-chitosan-NH_4Cl-glycerol. Another two systems; starch-chitosan-glycerol and NH_4Cl-glycerol were prepared in order to gain understanding on the interaction between these materials. The compositions of starch-chitosan-glycerol and glycerol-NH_4Cl samples are listed in Tables 3.4 and 3.5, respectively.

Table 3.4: Composition of starch-chitosan-glycerol samples.

S8C2 : glycerol composition (wt.%)	Starch (g)	Chitosan (g)	Glycerol (g)
95 : 5	0.800	0.200	0.053
85 : 15	0.800	0.200	0.177
75 : 25	0.800	0.200	0.333
65 : 35	0.800	0.200	0.538

Table 3.5: Composition of glycerol-NH_4Cl samples.

Glycerol : NH_4Cl composition (wt.%)	Glycerol (g)	NH_4Cl (g)
99 : 1	18.000	0.182
96 : 4	18.000	0.750
93 : 7	18.000	1.355

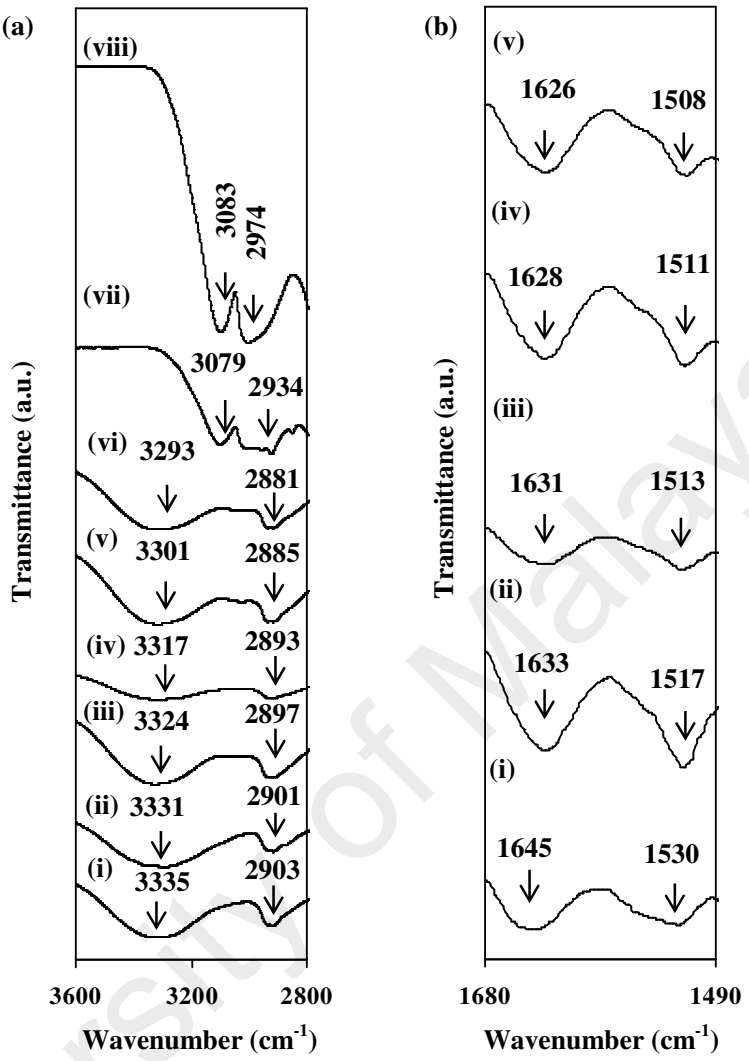

Figure 3.6: FTIR spectra of PVA-chitosan electrolyte with (i) 0, (ii) 10, (iii) 20, (iv) 30, (v) 40, (vi) 50 and (vii) 60 wt.% NH_4Br and (viii) pure NH_4Br salt in the region of 2800-3600 cm^{-1}. (b) FTIR spectra of PVA-chitosan electrolyte with (i) 0, (ii) 20, (iii) 30, (iv) 40 and (v) 50 wt.% NH_4Br in the region of 1490-1680 cm^{-1} (Yusof et al., 2014).

Figure 3.6 shows the FTIR spectra of chitosan-PVA-NH_4Br complexes (Yusof, Illias, & Kadir, 2014). It can be observed that the peak of different functional groups of the polymer host shifts to lower wavenumbers and thus proves the interaction between the salt and the polymer host. The authors also discussed the occurrence of excess salt and ion recombination using the FTIR result.

3.3.4 Electrochemical Impedance Spectroscopy

EIS is a non-destructive and powerful technique to study ionic conductors (Arof, Amirudin, et al., 2014; Hamdy, El-Shenawy, & El-Bitar, 2006). The usefulness of impedance spectroscopy lies in its ability to distinguish the electric and dielectric properties of a sample (Khaled & Al-Mhyawi, 2013). In this technique, measurements were carried out by applying an alternating voltage across the sample in a wide range of frequencies (Buraidah, 2012).

In the present work, the electrolytes were sandwiched between two stainless steel blocking disc electrodes of 1.6 cm diameter of a conductivity holder. The electrolyte and electrodes were held under spring pressure. The impedance measurements of the electrolytes were conducted using HIOKI 3532-50 LCR HiTESTER from room temperature to 343 K in the frequency range of 50 Hz to 5 MHz. The conductivity of the electrolytes was calculated using the equation below:

$$\sigma = tR_b^{-1}A_e^{-1} \tag{3.2}$$

where t is the thickness of electrolyte, R_b is bulk resistance and A_e is the electrode-electrolyte contact area. A digital thickness gauge (Mitutoyo Corp.) was employed to measure the thickness of the electrolytes. The value of R_b was determined from the Cole-Cole plot obtained from impedance measurements of the electrolytes. Figure 3.7 depicts the Cole-Cole plot for PCL-NH_4SCN electrolyte at room temperature as reported by Woo et al. (2011a), where the R_b is taken from the intercept of the semi circle with the tilted spike.

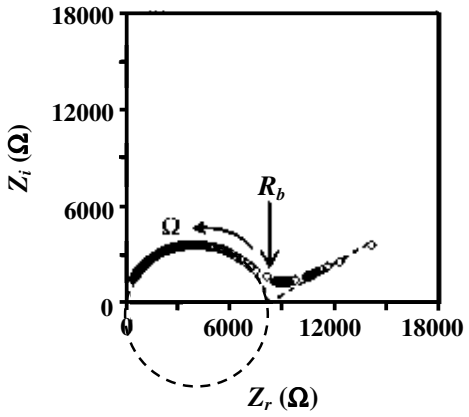

Figure 3.7: Cole-Cole plot of PCL-5 wt.% NH_4SCN electrolyte at room temperature (Woo et al., 2011a).

3.3.5 Transference Number Measurements

Ionic and electronic transference numbers are important in explaining the conductivity of polymer electrolytes (Sekhar, Kumar, & Sharma, 2012a). Since polymer electrolytes are ionic conductor, ionic transference number (t_{ion}) of the electrolyte should be higher than the electronic transference number (t_e) (Aziz, Majid, & Arof, 2012; Shukur & Kadir, 2015; Woo et al., 2011b). In the present work, the value of t_{ion} was determined using Wagner's dc polarization technique (Agrawal, 1999; Wagner & Wagner, 1957). A cell consists of the electrolyte sandwiched by two stainless steel electrodes was polarized using V&A Instrument DP3003 digital dc power supply at 0.20 V at room temperature. The dc current was monitored as a function of time.

Table 3.6 summarizes the value of t_{ion} of polyvinyl acetate (PVAc)-NH_4SCN electrolytes as reported by Selvasekarapandian, Baskaran, and Hema (2005). Based on the result, the authors concluded that the charge transport in PVAc-NH_4SCN electrolytes is mainly due to ions.

Table 3.6: Ionic transference number of PVAc-NH_4SCN electrolytes (Selvasekarapandian et al., 2005).

PVAc : NH_4SCN composition (mol%)	t_{ion}
95 : 5	0.92
90 : 10	0.93
85 : 15	0.94
80 : 20	0.94
75 : 25	0.94

Wagner's dc polarization technique has also been used to determine the transference number of cation (t_+). The electrodes were prepared by mixing 0.40 g MnO_2 (Sigma-Aldrich), 0.04 g activated carbon (RP20, manufactured by Kuraray, Japan) and 0.08 g polytetrafluoroethylene (PTFE). The mixture was grounded and pressed using hydraulic pressing for 15 min. A cell consists of the electrolyte sandwiched by two MnO_2 electrodes was polarized using V&A Instrument DP3003 digital dc power supply at 0.20 V at room temperature.

3.3.6 Thermogravimetric Analysis

TGA technique can be used to measure the thermal stability and thermal degradation of a sample due to the simplicity of the weight loss method (Lee, Lee, Cho, Kim, & Ha, 2007). By knowing the thermal properties of present electrolytes, their thermal stability in the temperature range of present studies can be ensured. TGA measurements were carried out using TA Instruments QA500 from room temperature to

480 °C at a heating rate of 20 °C min^{-1}. Apart from the decomposition temperature, information on the water content of the electrolytes also can be determined.

Figures 3.8 shows the TGA curves of poly(trimethylene carbonate), p(TMC) based electrolytes doped with $LiPF_6$ as reported by Barbosa, Rodrigues, Silva, and Smith (2011). According to the authors, the increasing salt concentration decreases the thermal stability of polymer electrolyte confirming the destabilizing influence from the salt on the matrix host.

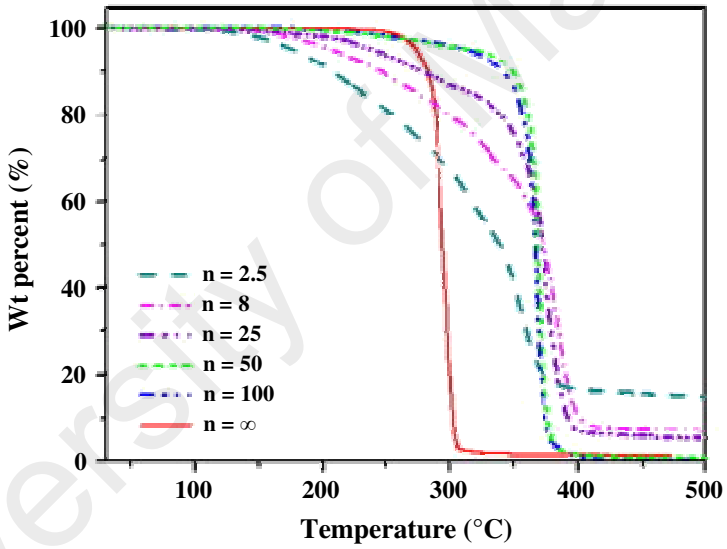

Figure 3.8: TGA curves of selected $p(TMC)_nLiPF_6$ electrolytes (Barbosa et al., 2011).

3.3.7 Differential Scanning Calorimetry

In a polymer electrolyte, ionic conduction occurs predominantly in the amorphous region, where the transport properties are associated with the polymer's segmental motion (Money, Hariharan, & Swenson, 2012). The increase in segmental motion results in an increase in conductivity (Aravindan & Vickraman, 2007; Bhad,

Sangawar, Maldhure, Tayade, & Yerawar, 2012). According to Woo et al. (2013), by lowering the glass transition temperature (T_g), the polymer segmental mobility can be enhanced. Thus the determination of T_g may further enhance the understanding in conductivity trend on addition of salt and plasticizer.

DSC technique is commonly used to measure the value of T_g of polymer electrolyte (Liew, Ramesh, & Arof, 2014; Lim et al., 2014a; Zainal, Mohamed, & Idris, 2013). In this technique, the difference in the amount of heat required to increase the temperature of a sample and reference are measured as a function of temperature (Isa, 2010). In the present studies, DSC measurements were carried out using TA Instruments Q200. The samples were sealed in aluminium pans and heated at a heating/cooling rate of 10 °C min^{-1} from -80 °C to 120 °C. A nitrogen flow (50 ml min^{-1}) was maintained throughout the experiment.

Figure 3.9 shows the DSC curves of PVA-LiBOB based electrolytes as reported by Noor et al. (2013). The authors reported that the addition of 40 wt.% LiBOB decreases the T_g value.

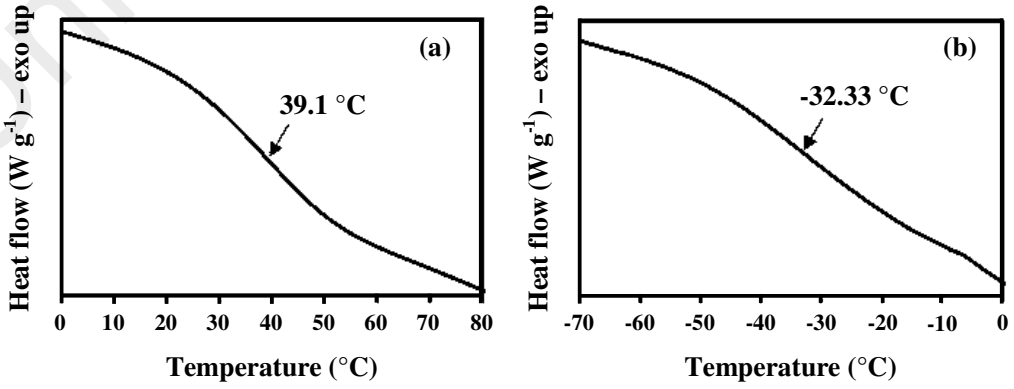

Figure 3.9: DSC thermograms of PVA electrolytes with (a) 0 and (b) 40 wt.% LiBOB (Noor et al., 2013).

3.3.8 Linear Sweep Voltammetry

Before using the electrolyte in any electrochemical devices, it is important to know the voltage limit that can be applied on the electrolyte. In this work, LSV measurements were carried out by Digi-IVY DY2300 potentiostat to know the electrochemical stability window of the electrolytes at room temperature. Stainless steel foils were used as reference, working and counter electrodes. LSV measurements were done at 5 mV s^{-1} scan rate. In LSV technique, the current at the working electrode is measured while the potential between the working electrode and the reference electrode is swept linearly in time.

Figure 3.10 depicts the LSV results of chitosan-iota carrageenan based electrolytes with different weight ratio of H_3PO_4 and PEG (Arof, Shuhaimi, Alias, Kufian, & Majid, 2010). The authors stated that there is no appreciable current flow in the electrolytes up to ~ 1.6 V. The authors then employed the highest conducting electrolyte in the fabrication of an EDLC.

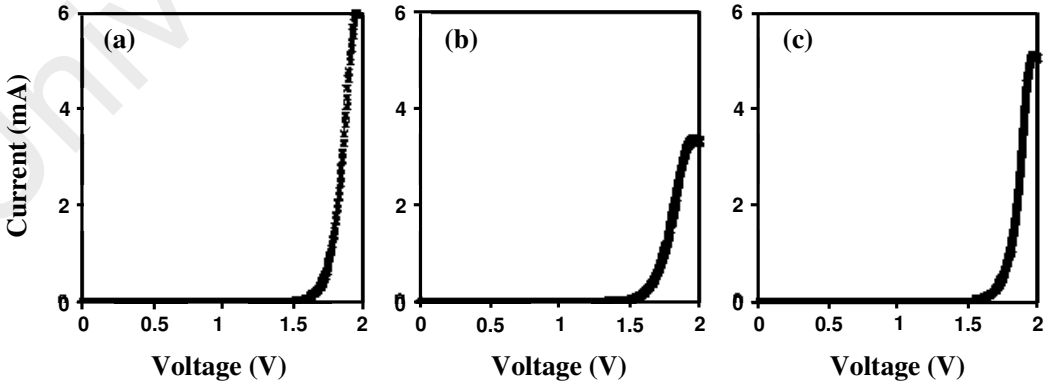

Figure 3.10: LSV curves of chitosan-iota carrageenan based electrolytes with (H_3PO_4:PEG) weight ratio of (a)1:1, (b) 1:3 and (c) 3:1 (Arof et al., 2010).

3.4 Fabrication and Characterization of EDLC

3.4.1 Electrode Preparation

For the preparation of EDLC electrode, 13 g activated carbon (RP20, manufactured by Kuraray, Japan), 1 g carbon black (Super P) and 2 g polyvinylidene fluoride (PVdF) were mixed together in 60 mL N-methyl pyrrolidone (NMP) (EMPLURA) and stirred until homogenous. The mixture was then doctor-bladed on an aluminium foil, which serves as the current collector, and heated at 60 °C for drying process. The thickness of electrode before drying was 0.25 mm. After heating, the electrode thickness was reduced to 0.10 mm. The dried electrode was kept in a desiccator containing silica gel before being used.

3.4.2 Fabrication of EDLC

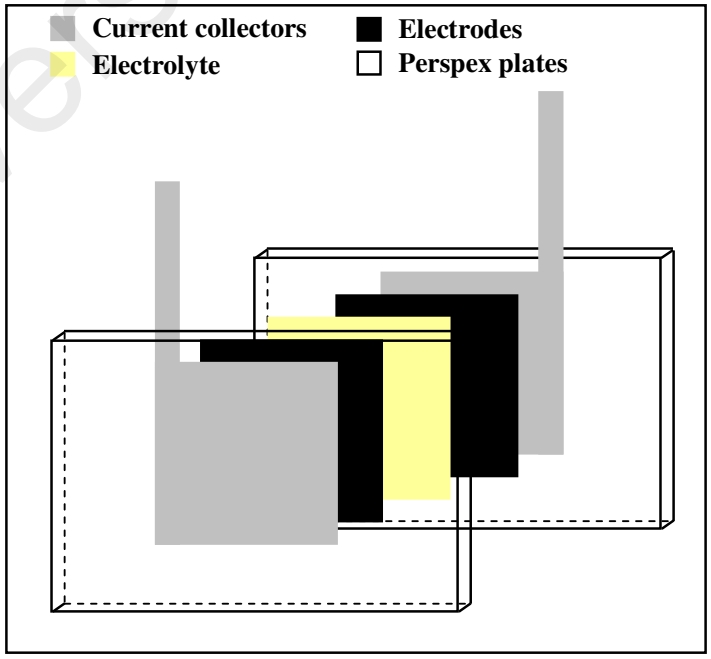

Figure 3.11: Illustration of EDLC fabrication.

EDLC was fabricated by sandwiching the highest conducting electrolyte with two electrodes as illustrated in Figure 3.11. The area of the electrode is 1.26 cm^2. Perspex (made of PMMA) plates were used to hold the EDLC.

3.4.3 Cyclic Voltammetry (CV)

CV measurement of the EDLC at room temperature was performed using Digi-IVY DY2300 potentiostat in the potential range of 0-0.85 V at different scan rates. Figure 3.12 shows the cyclic voltammogram of EDLC using PMMA-LiBOB electrolyte as reported by Arof et al. (2012). According to the authors, the EDLC is scan rate dependent, which is a characteristic of capacitor cells.

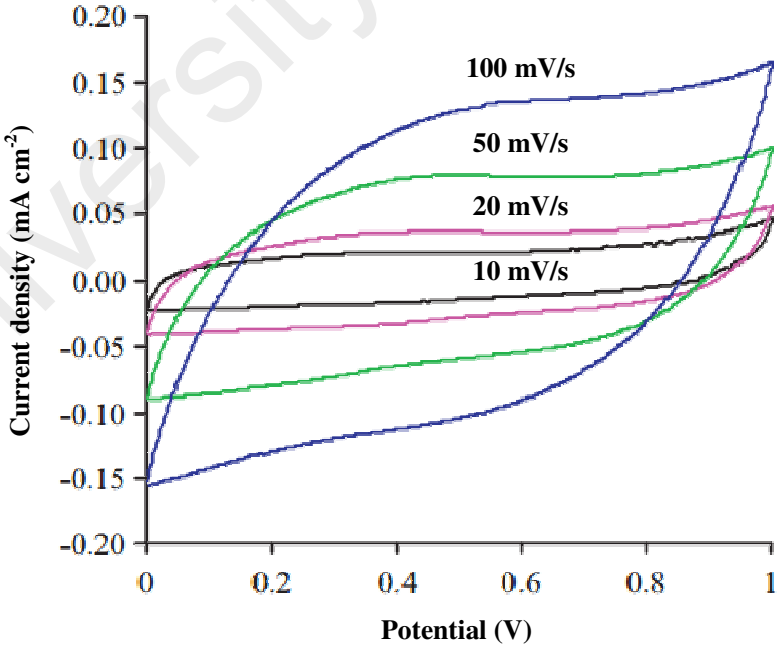

Figure 3.12: Cyclic voltammogram of EDLC using PMMA-LiBOB electrolyte at different scan rates (Arof et al., 2012).

From the CV measurement, the specific capacitance (C_s) of the EDLC at each scan rate will be calculated. The result will be shown in Chapter 8.

3.4.4 Galvanostatic Charge-Discharge

The galvanostatic charge-discharge cycling of the EDLC was carried out using Neware battery cycler at a constant current density of 0.063 mA cm^{-2} for 500 cycles. From the EDLC's charge-discharge cycling, the C_s value and Coulombic efficiency (η) at selected cycles will be calculated. The result will be discussed in Chapter 8.

Galvanostatic charge-discharge of EDLC employing chitosan-H_3PO_4 electrolyte as reported by Arof and Majid (2008) is shown Figure 3.13. The capacitance of the EDLC is reported to be between 80 and 96 mF g^{-1} and quite constant for 100 cycles as shown in Figure 3.14.

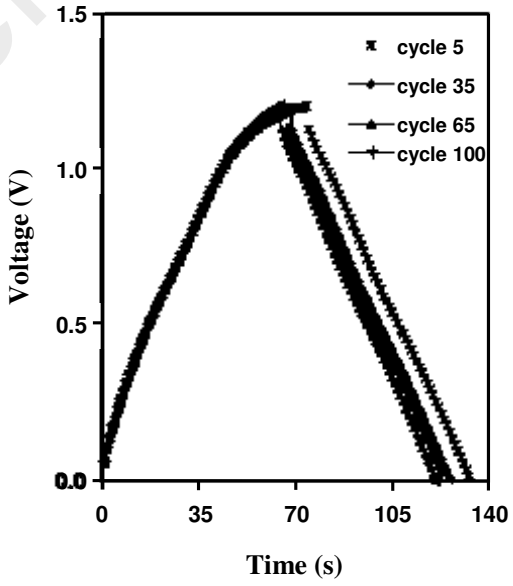

Figure 3.13: The charge-discharge curves for EDLC using chitosan-H_3PO_4 electrolyte (Arof & Majid, 2008).

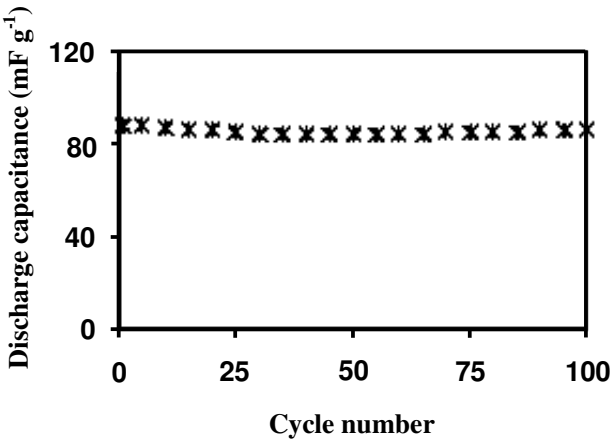

Figure 3.14: Variation of the discharge capacitance as a function of number of cycle for EDLC using chitosan-H_3PO_4 electrolyte (Arof & Majid, 2008).

3.5 Fabrication and Characterization of Proton Batteries

3.5.1 Primary Proton Batteries

For the preparation of cathode pellet for primary proton batteries, a mixture of 0.44 g MnO_2, 0.04 g carbon black and 0.02 g PTFE was grounded and pressed using hydraulic pressing for 15 min. For the preparation of anode pellet, the same procedure was done on the mixture of 0.31 g zinc (Merck), 0.15g $ZnSO_4 \cdot 7H_2O$ (Univar), 0.02 g carbon black and 0.02 g PTFE. The primary proton batteries were fabricated by sandwiching P7 electrolyte with the cathode and anode pellets. The batteries were then packed in CR2032 coin cells. The schematic diagram of the fabricated EDLC is shown in Figure 3.15.

Open circuit potential (OCP) is the potential difference between two terminals of a battery without connected to any circuit, which means no external electric current

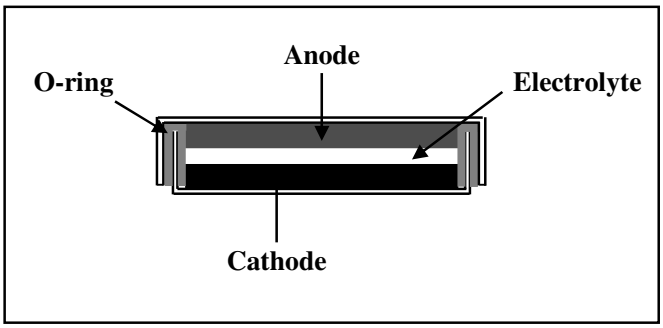

Figure 3.15: Battery configuration in a CR2032 coin cell.

flows through the battery. OCP value represents the full potential of a battery since the potential does not share any of its potential with a load. In the present work, OCP of the batteries was monitored for 48 h using Neware battery cycler at room temperature. The OCP characteristic of proton batteries employing chitosan-NH_4NO_3-EC electrolyte as reported by Ng and Mohamad (2006) is shown in Figure 3.16. According to the authors, the voltage was observed to be higher at the first 2 h and later stabilized at (1.56 ± 0.06) V until the 24th hour.

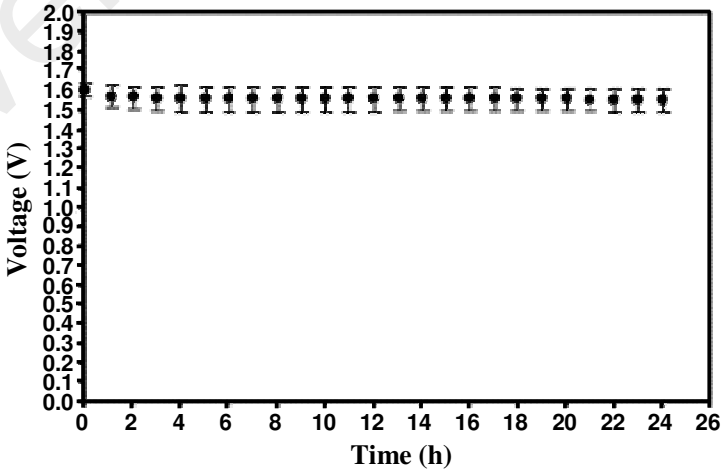

Figure 3.16: OCP of proton battery employing chitosan-NH_4NO_3-EC electrolyte (Ng & Mohamad, 2006).

To study the discharge characteristic of the batteries, the primary batteries were discharged at different constant currents (0.10, 0.25, 0.40 and 0.60 mA) using Neware battery cycler at room temperature. Figure 3.17 shows the discharge profiles of proton batteries using carboxymethyl cellulose-NH_4Br electrolyte at different constant currents as reported by Samsudin et al. (2014). The authors found that the discharge capacity is lower at higher discharge current.

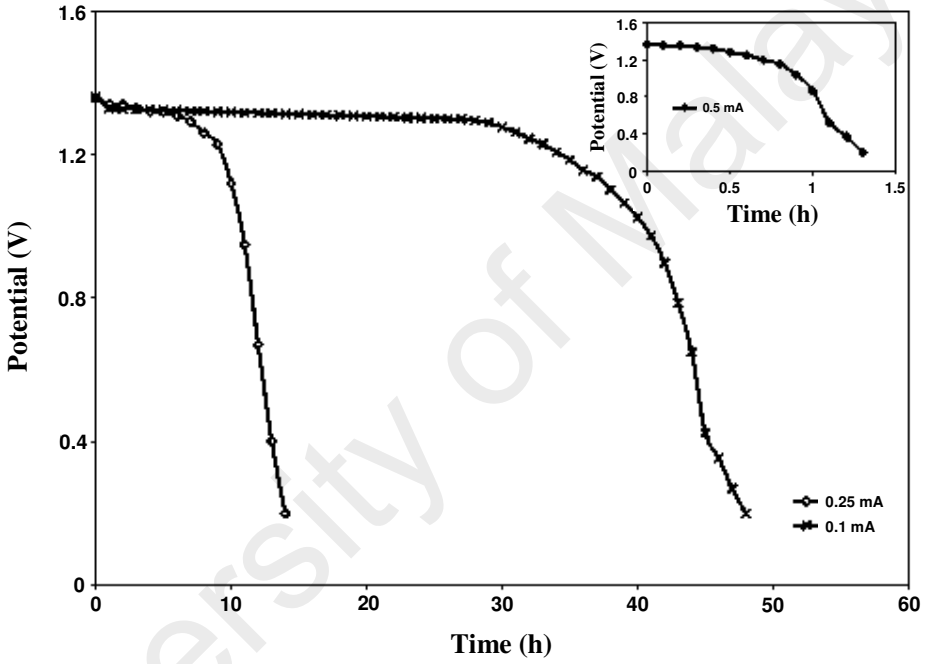

Figure 3.17: Discharge profiles of proton batteries using carboxymethyl cellulose-NH_4Br electrolyte at different constant currents (Samsudin et al., 2014).

The current-potential (*I-V*) and current density-power density (*J-P*) characteristics of the batteries at room temperature were determined by monitoring the potential while draining the current from 1.6 μA to 35 mA. The plot of *I-V* and *J-P* of the proton batteries employing chitosan-PEO-NH_4NO_3-EC electrolyte as reported by Shukur, Ithnin, et al. (2013) is represented in Figure 3.18.

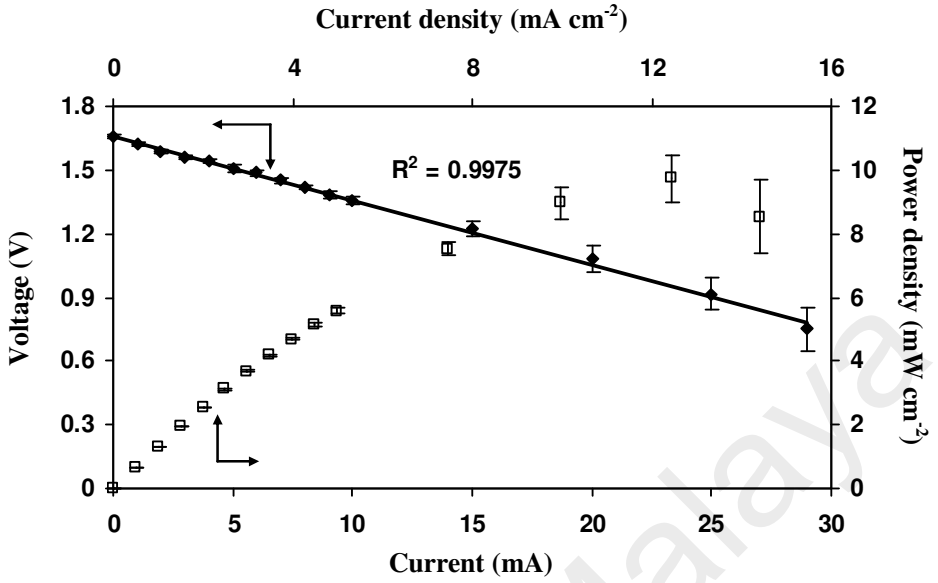

Figure 3.18: Plot of *I-V* and *J-P* of the primary proton batteries employing chitosan-PEO-NH_4NO_3-EC electrolyte (Shukur, Ithnin, et al., 2013).

3.5.2 Secondary Proton Batteries

For the preparation of cathode pellet for secondary proton battery, a mixture of 0.42 g MnO_2, 0.03 g carbon black, 0.02 g PTFE and 0.03 g P7 electrolyte solution was grounded and pressed using hydraulic pressing for 15 min. The anode pellet remained the same as the anode used in primary battery. The secondary proton battery was fabricated by sandwiching P7 electrolyte with the cathode and anode pellets. The battery was then packed in a CR2032 coin cell as shown in Figure 3.15. The OCP was monitored for 48 h using Neware battery cycler. The secondary battery was charged and discharged at 0.35 mA using Neware battery cycler at room temperature. Figure 3.19 depicts the charge-discharge curves of secondary proton battery using chitosan-PVA-NH_4NO_3-EC electrolyte at a constant current of 0.3 mA as reported by Kadir et al. (2010). The secondary battery can perform up to nine cycles.

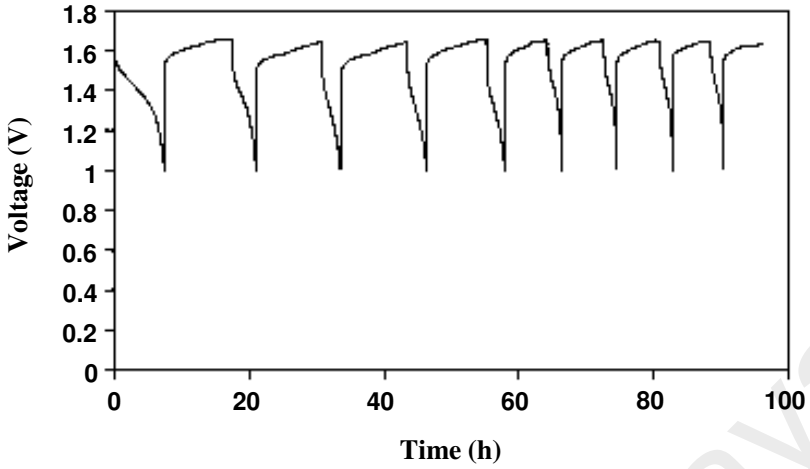

Figure 3.19: Charge-discharge curves of proton battery using chitosan-PVA-NH_4NO_3-EC electrolyte at 0.3 mA (Kadir et al., 2010).

3.6 Summary

This chapter has presented the preparation method of solid polymer electrolytes based on starch-chitosan blend in detail. Characterization techniques employed in this work has been clearly described. Fabrication of electrochemical devices has been presented step by step. Results from experiments conducted using the techniques described in this chapter will be discussed in the next five chapters.

CHAPTER 4

DETERMINATION AND CHARACTERIZATION OF POLYMER BLEND HOST

4.1 Introduction

The amorphousness of a polymer host is a crucial factor for ionic conduction since ions are preferably mobile in the amorphous region (Agrawal, Sahu, Mahipal, & Ashrafi, 2013; Gadjourova, Andreev, Tunstall, & Bruce, 2001; Johan & Ting, 2011). For a polymer blend, the crystallinity and amorphousness of the blend are affected by the ratio of the polymer components (Kadir et al., 2010; Kadir, Teo, Majid, & Arof, 2009; Shibayama, Uenoyama, Oura, Nomura, & Iwamoto, 1995). This is because the presence of an amorphous component affects the crystallization process of the other polymer component (Pereira, Paulino, Rubira, & Muniz, 2010). Report by Sasaki, Bala, Yoshida, and Ito (1995) shows that the increasing PMMA concentration causes the rate of PVdF crystallization to decrease. Kadir et al. (2009) reported that the crystallinity of PEO decreases as chitosan content increases to 60 wt.% in the chitosan-PEO blend. Ramly et al. (2011) reported that starch-PEO blend with a ratio of 7:3 exhibits the least amount of crystallinity and was chosen in the preparation of polymer electrolyte.

Studies on the structure of starch-chitosan blend revealed that starch and chitosan are miscible to each other (Bourtoom & Chinnan, 2008). Liu, Adhikari, Guo, and Adhikari (2013) reported that the addition of chitosan to starch decreases the crystallinity of the starch film. Report by Xu et al. (2005) showed that the crystalline

peaks of chitosan were suppressed when the starch ratio in the blend film was increased. Based on information obtained from the literature, it is important to determine the appropriate amount of starch and chitosan to serve as the polymer host.

4.2 XRD Analysis

The XRD results are shown in Figure 4.1.

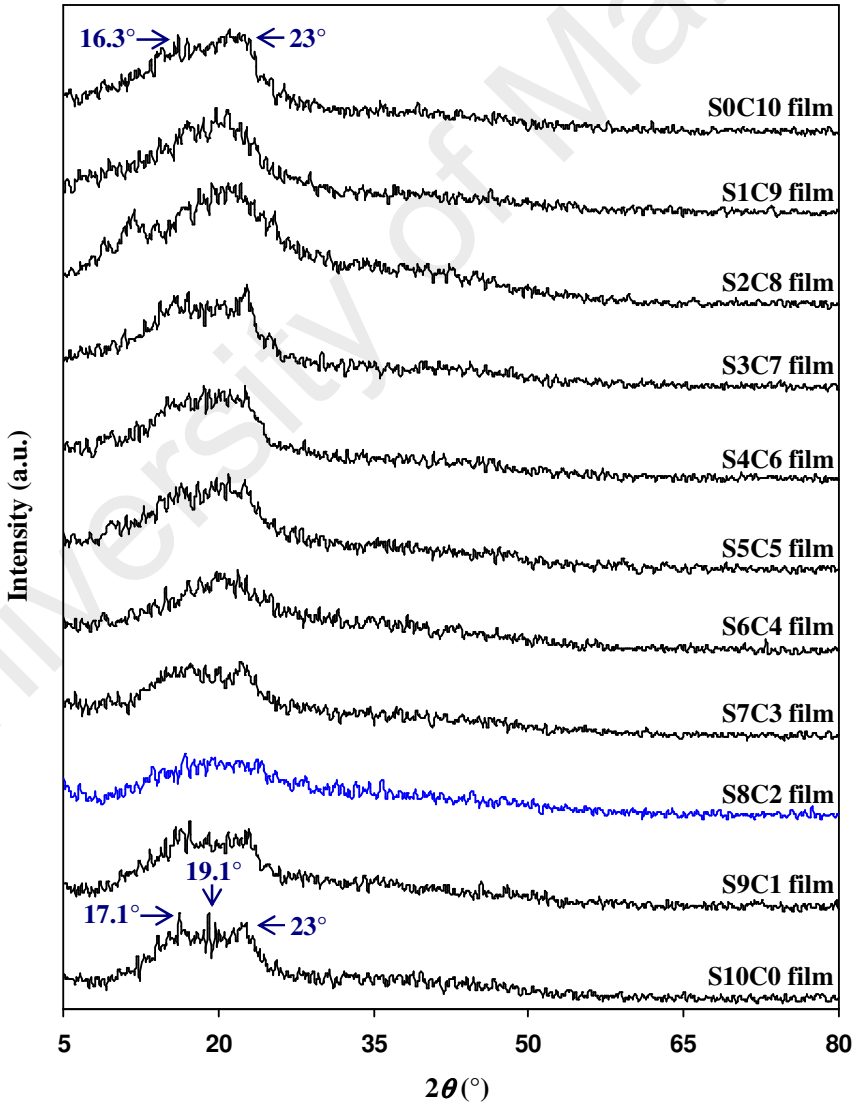

Figure 4.1: XRD patterns of various starch-chitosan blend films.

From the X-ray diffractogram of S10C0 film, three strong diffraction peaks appear at 2θ = 17.1°, 19.1° and 23°, corresponding to crystalline region of starch (Zhai et al., 2004). These crystalline peaks are observed to superimpose on a broad amorphous background. This result demonstrates that the film shows two phase morphology i.e. crystalline and amorphous states, proving that starch is a semi-crystalline material (El-Kader & Ragab, 2013; Liew, Ramesh, Ramesh, & Arof, 2012). In the X-ray diffractogram of S0C10 film, two crystalline peaks appear at 2θ = 16.3° and 23°. In the work reported by Aziz et al. (2012), the crystalline peaks of chitosan are observed at 2θ = 16.5° and 22.5°, which are comparable with the present result. The XRD patterns of S10C0 and S0C10 films were used as references to see any changes in pattern or peaks position in the diffractogram of starch-chitosan blend films. In the diffractogram of S8C2 film, the crystalline peaks seem to be suppressed by a broad amorphous peak centered at 2θ = 20.3°. This result demonstrates the good miscibility and interaction between starch and chitosan. The interaction may occur through hydrogen bonding between hydroxyl groups of starch and hydroxyl and/or amine groups of chitosan. X-ray diffractogram of S6C4 film consists of a diffraction peak centered at 2θ = 20.6°, but with a narrower XRD hump than S8C2 film, indicating that the amorphous phase of S6C4 is lesser than S8C2 film. According to a report by Salleh et al. (2009), chitosan structure is not influenced by the addition of starch when the chitosan content is higher than starch content in the blend. The similar phenomenon can be observed in the present work as XRD pattern of S4C6 film is almost similar to XRD pattern of S0C10 film. New crystalline peaks are observed in the X-ray diffractogram of S2C8 film at 2θ = 9.4°, 11.8° and 25.5°. This phenomenon indicates that the crystallinity of S2C8 film is higher than S0C10 film.

To confirm the amorphousness of the blend films, the degree of crystallinity (χ_c) of each film is investigated by using two approaches. Firstly, Nara-Komiya method (Nara & Komiya, 1983) has been used. Nara-Komiya method is a technique to analyze the X-ray diffractograms by separating the crystalline and amorphous portions using a line. In this work, the investigation of the degree of crystallinity using Nara-Komiya method is focused in the region of $5° \leq 2\theta \leq 50°$ where crystalline and amorphous phases of starch, chitosan and starch-chitosan blends can be observed (Liew et al., 2012; Salleh et al., 2009). A baseline curve was drawn beginning from $2\theta = 5°$ to $2\theta = 50°$ by

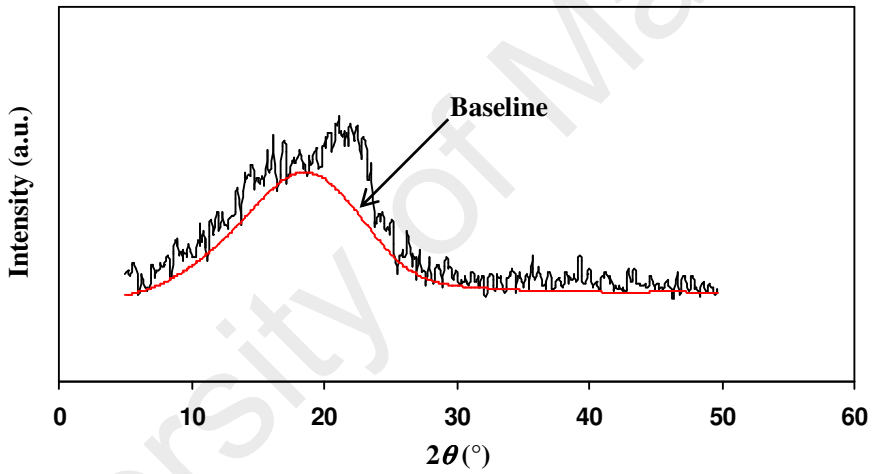

Figure 4.2: XRD pattern of S0C10 film.

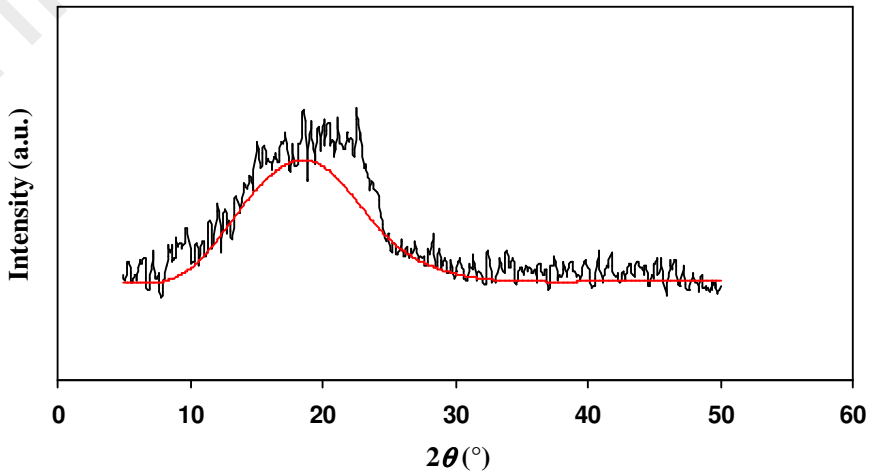

Figure 4.3: XRD pattern of S4C6 film.

joining together the minimum intensities corresponding to the crystalline peaks. The area above the baseline curve is corresponded to crystalline region while area below the baseline curve is corresponded to amorphous region (Nara & Komiya, 1983; Noor et al., 2013). Figures 4.2 to 4.5 show the analysis of selected starch-chitosan blend films using Nara-Komiya method. The degree of crystallinity was then calculated by using the following equation:

$$\chi_c = \frac{A_T - A_a}{A_T} \times 100\% \qquad (4.1)$$

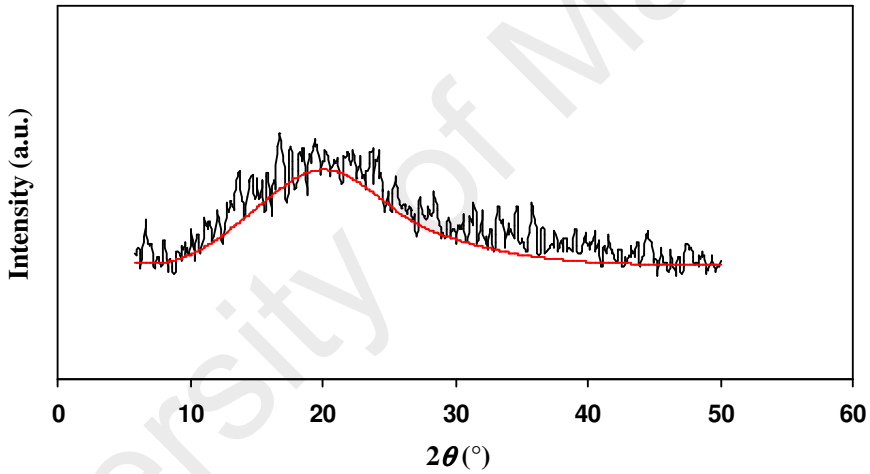

Figure 4.4: XRD pattern of S8C2 film.

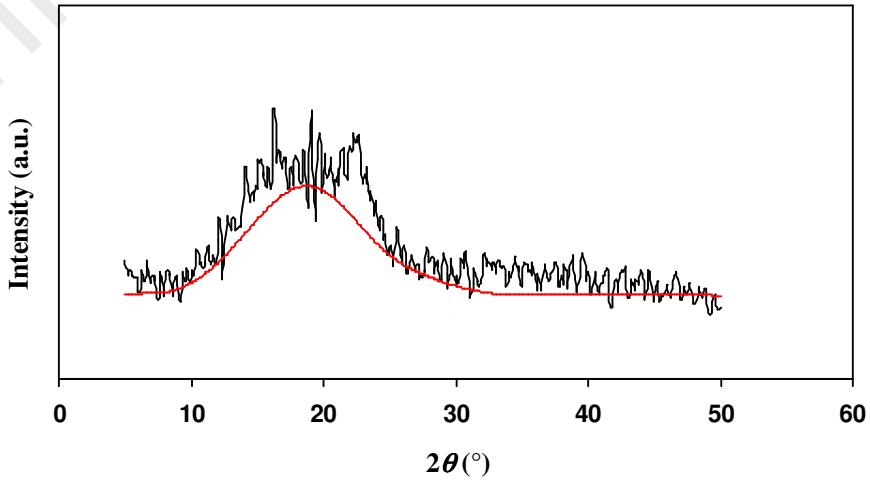

Figure 4.5: XRD pattern of S10C0 film.

Here, A_a and A_T are the areas of amorphous and total humps, respectively. The areas of amorphous and total humps have been calculated using the OriginPro 9.0 software. The degree of crystallinity values estimated by Nara-Komiya method are tabulated in Table 4.1. The degree of crystallinity of S8C2 film is the lowest, confirming this blend as the most amorphous.

Table 4.1: Degree of crystallinity of starch-chitosan blend films using Nara-Komiya method.

Sample	χ_c **(%)**
S10C0	38.93
S9C1	35.07
S8C2	26.31
S7C3	29.81
S6C4	28.67
S5C5	29.30
S4C6	30.00
S3C7	32.94
S2C8	36.82
S1C9	29.44
S0C10	33.72

In an XRD pattern, overlapping of peaks can occur e.g. crystalline peaks superimposed on the amorphous humps. In order to separate the overlapping patterns, the XRD diffractograms were deconvoluted using the OriginPro 9.0 software. One of the advantages of this method is that the diffraction peaks can be separated from the continuous scattering background. Baseline correction was done prior to fitting multi-peaks using Gaussian distribution. The sharp, narrow and small peaks indicate crystalline peaks while broad peaks indicate amorphous regions. The area under the

deconvoluted peaks was used to calculate the degree of crystallinity using Equation (4.1).

Figure 4.6 shows the result of deconvolution on XRD pattern of S0C10 film. Instead of two, there are three crystalline peaks appear in the diffractogram at 2θ = 15.5°, 18.1° and 21.9°. It is revealed that there are two broad amorphous peaks centered at 2θ = 17.7° and 38.1°. The present results are comparable with the reports from literature (Aziz, 2012; Buraidah, 2012; Fadzallah, Majid, Careem, & Arof, 2014; Hassan, Woo, Aziz, Kufian, & Majid , 2013).

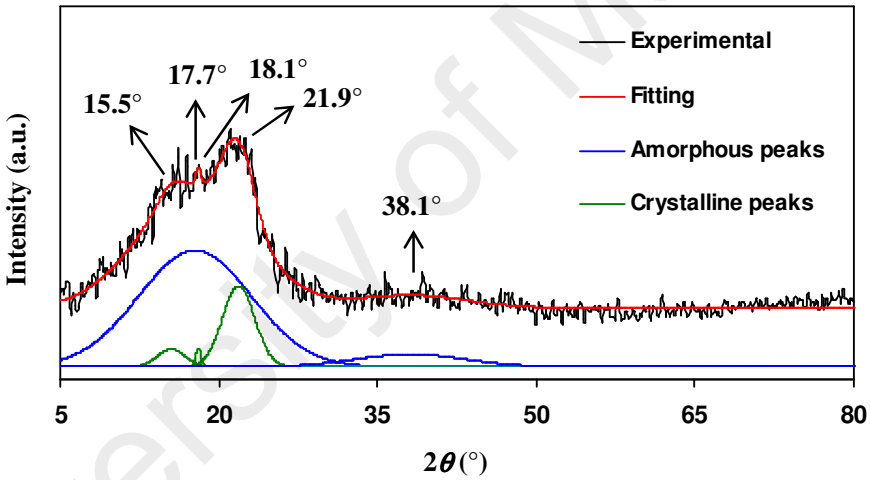

Figure 4.6: Deconvoluted XRD pattern of S0C10 film.

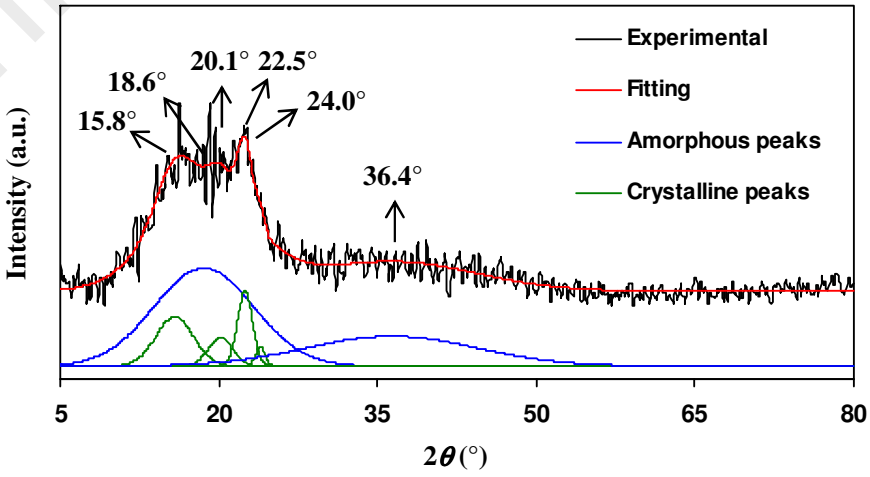

Figure 4.7: Deconvoluted XRD pattern of S10C0 film.

The result of deconvolution on XRD pattern of S10C0 film is represented in Figure 4.7. It can be observed that the diffractogram consists of four crystalline peaks at 2θ = 15.8°, 20.1°, 22.5° and 24.0° and two broad amorphous peaks centered at 2θ = 18.6° and 36.4°.

Figures 4.8 to 4.11 show the results of deconvolution of selected starch-chitosan blend films. It is observed that the crystalline peaks in the XRD pattern of S8C2 film are less sharp and less intense compared to the other blends.

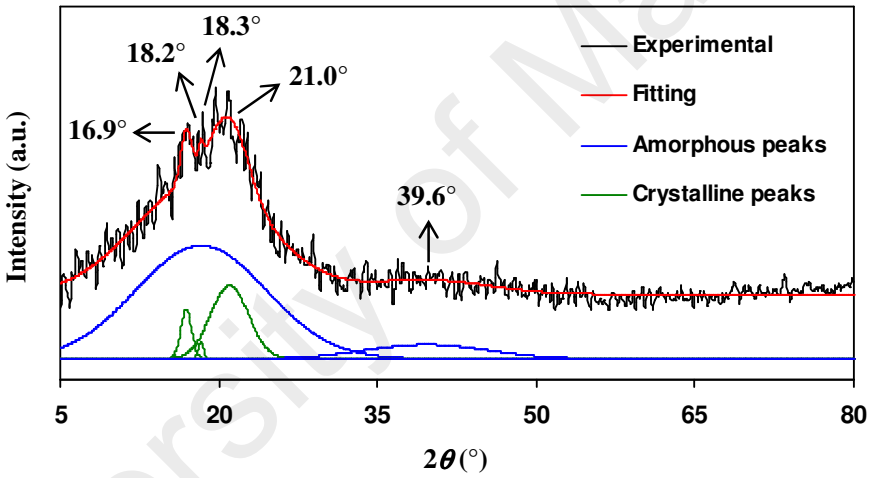

Figure 4.8: Deconvoluted XRD pattern of S1C9 film.

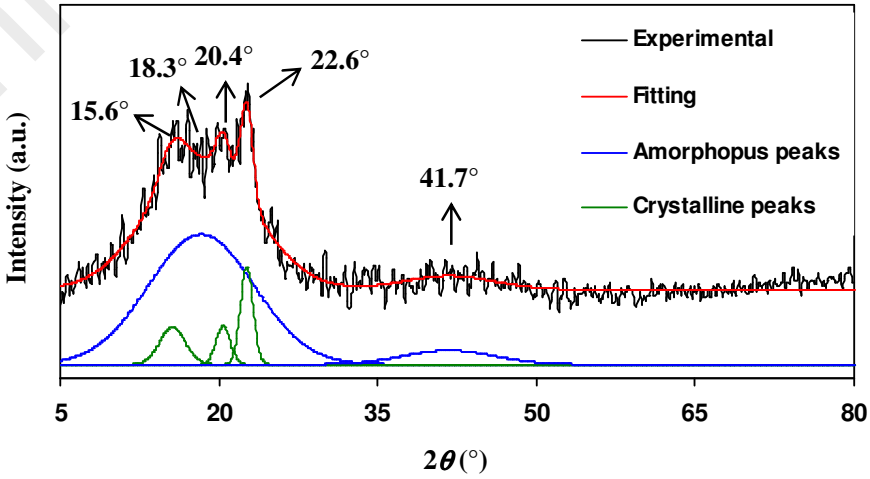

Figure 4.9: Deconvoluted XRD pattern of S3C7 film.

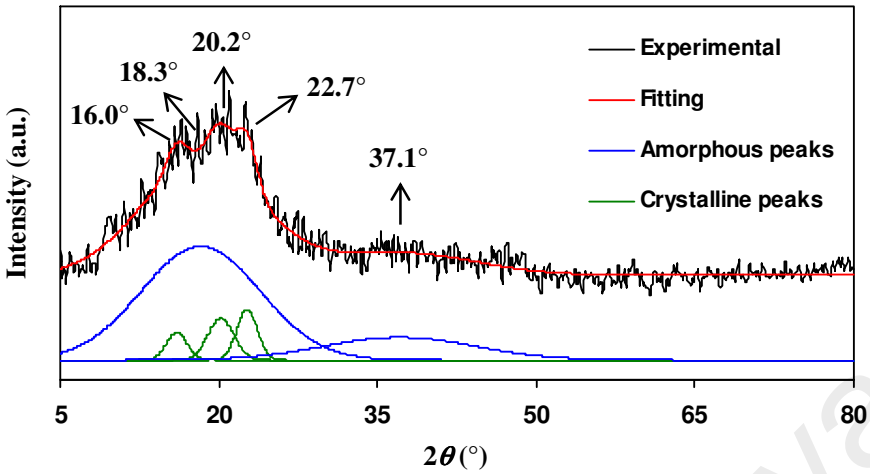

Figure 4.10: Deconvoluted XRD pattern of S5C5 film.

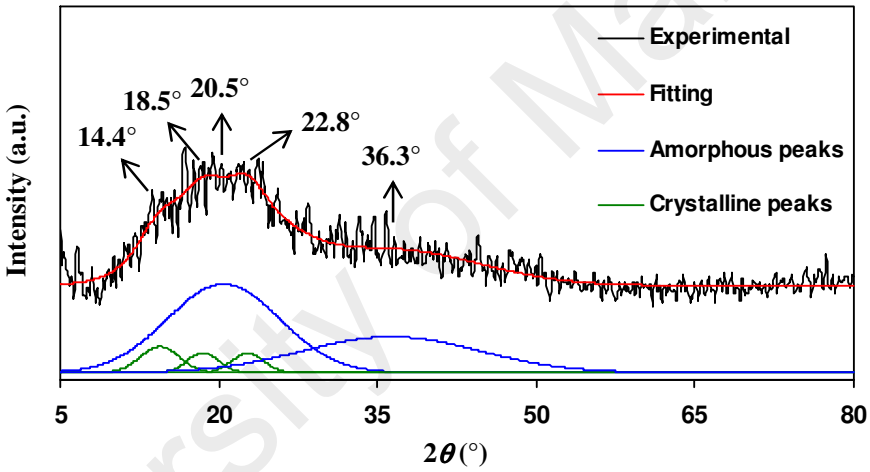

Figure 4.11: Deconvoluted XRD pattern of S8C2 film.

From Figures 4.6 and 4.7, the deconvoluted XRD patterns for S0C10 and S10C0 films reveal the existence of two broad amorphous peaks. These amorphous peaks are observed in the diffractograms of starch-chitosan blend films regardless of starch:chitosan ratio as shown in Figures 4.8 to 4.11. By knowing the area under the deconvoluted peaks, the degree of crystallinity of the films have been calculated and showed in Table 4.2. It is observed that by using the deconvolution method, S8C2 film is still the most amorphous blend with the least degree of crystallinity that strengthen the fact that this sample is the most suitable to be chosen as polymer host.

Table 4.2: Degree of crystallinity of starch-chitosan blend films using deconvolution method.

Sample	χ_c (%)
S10C0	20.53
S9C1	18.66
S8C2	12.05
S7C3	16.04
S6C4	13.13
S5C5	13.66
S4C6	15.35
S3C7	15.42
S2C8	18.68
S1C9	17.12
S0C10	18.09

4.3 Miscibility Studies

4.3.1 SEM Analysis

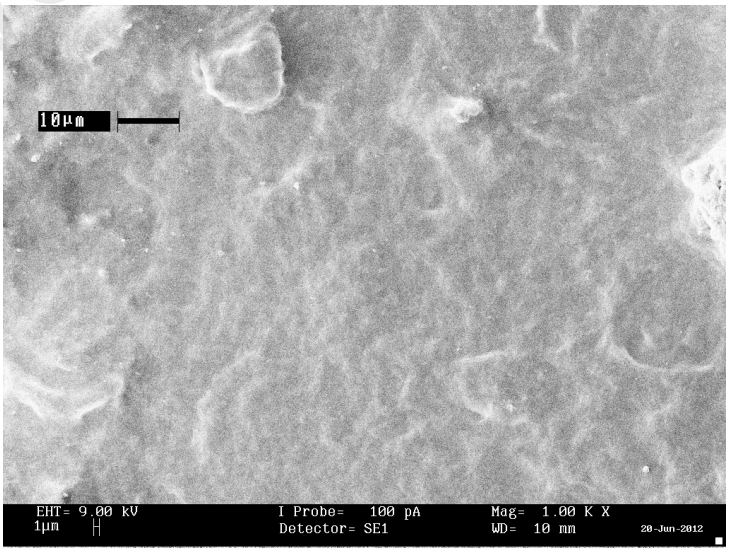

Figure 4.12: Surface micrograph of S10C0 film.

SEM analysis is one of the techniques to study the miscibility between the components in a polymer blend. The miscibility can be implied from the smooth and homogenous surface of the blend film (Kadir, 2010). The surface micrograph of S10C0 film is shown in Figure 4.12. It is observed that the micrograph of S10C0 film exhibits characteristic patterns on the surface. These patterns represent the withered ghost granules of starch (Salleh et al., 2009). These ghosts were formed during the gelatinization process where the external layers of starch granules form granule envelopes which degrade into ghost remnants (Atkin, Abeysekera, & Robards, 1998).

In Figure 4.13, the micrograph of S0C10 film shows a smooth and homogenous surface. The same observation on pure chitosan film has been reported in the literature (Chen et al., 2009).

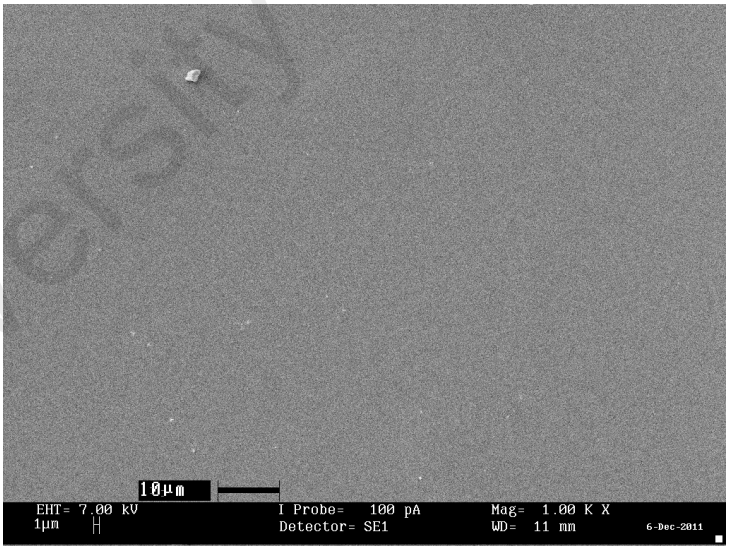

Figure 4.13: Surface micrograph of S0C10 film.

Figure 4.14 depicts the SEM micrograph of S9C1 film. The surface is observed to have a rough structure. This observation indicates partial immiscibility of the

polymers, as reported in other polymer blend systems (Rotta, Minatti, & Barreto, 2011; Yin, Luo, Chen, & Khutoryanskiy, 2006).

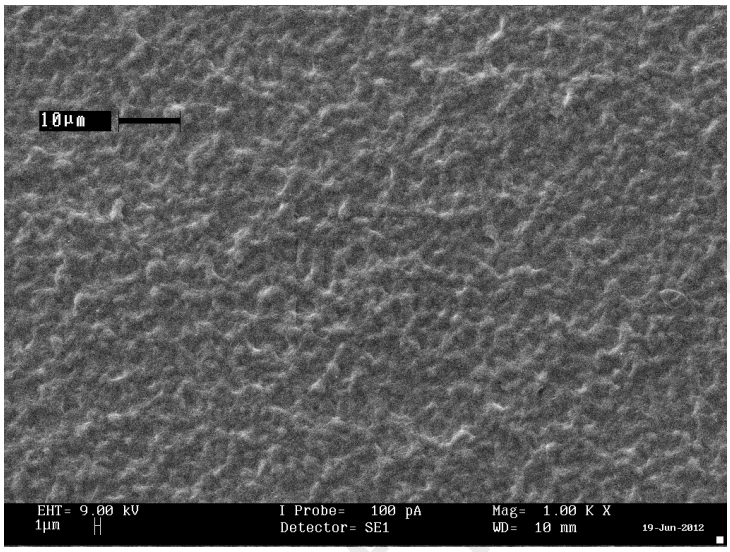

Figure 4.14: Surface micrograph of S9C1 film.

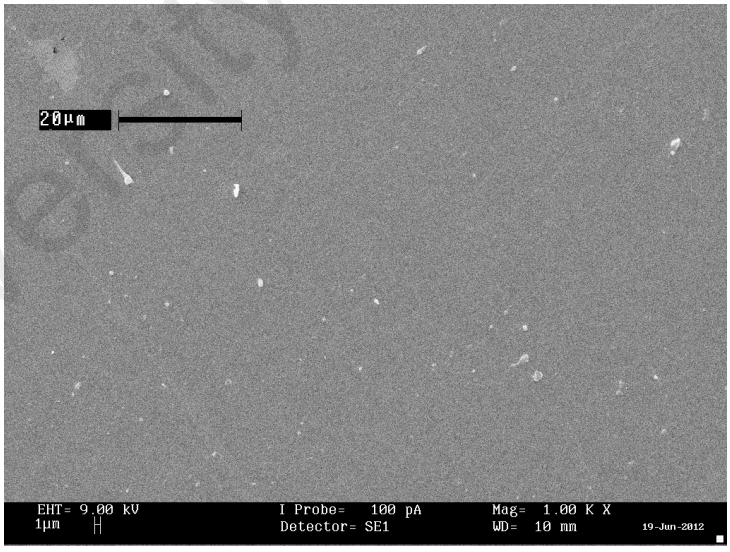

Figure 4.15: Surface micrograph of S8C2 film.

Figure 4.15 depicts the SEM micrograph of S8C2 film. It is observed that the surface is homogeneous without phase separation, suggesting that 80 wt.% starch and

20 wt.% chitosan are miscible to each other. The same type of micrograph can be seen for other blend films as shown in Figures 4.16-4.19. The present observation is quite similar to a report by Jayaprakash, Kumar, Sreenivasa, Mohan, and Shashidar (2013) for potato starch-chitosan blend.

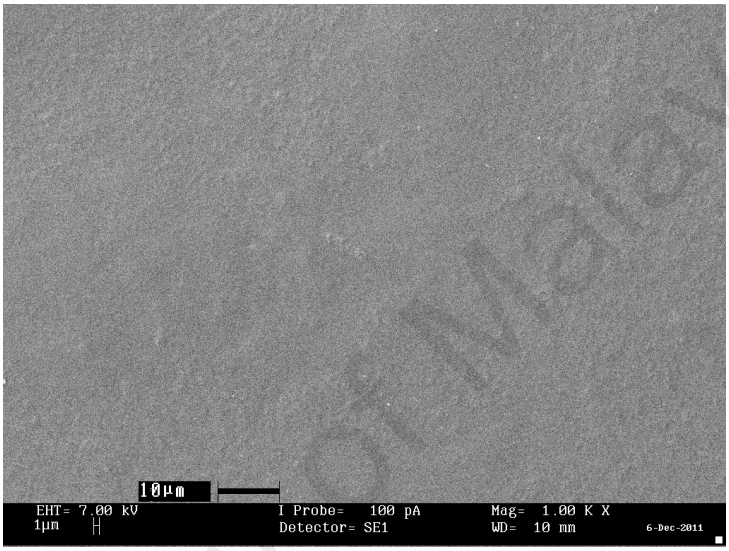

Figure 4.16: Surface micrograph of S5C5 film.

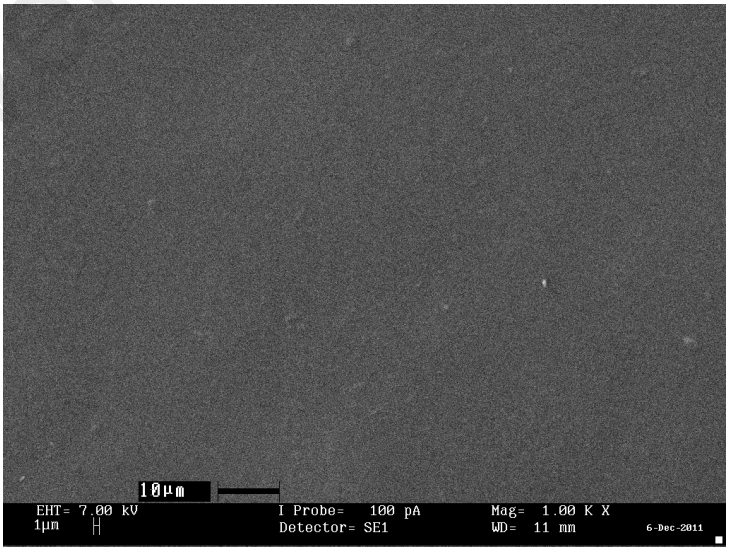

Figure 4.17: Surface micrograph of S4C6 film.

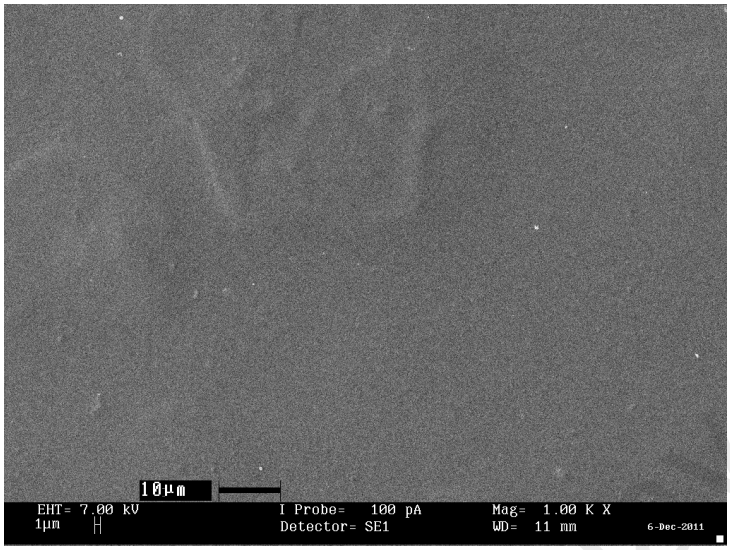

Figure 4.18: Surface micrograph of S3C7 film.

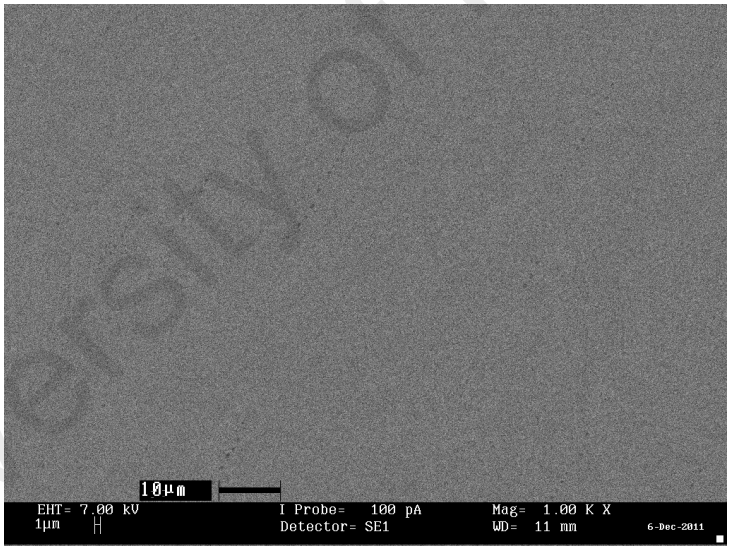

Figure 4.19: Surface micrograph of S2C8 film.

4.3.2 DSC Analysis

Thermal characterization of polymer blends is a well established method for determining the miscibility of polymer blends. Thus, to further confirm the miscibility

between starch and chitosan in S8C2 film, DSC measurements on S10C0, S0C10 and S8C2 films were carried out. In DSC technique, if the blend shows two transitions, it means that there is phase separation and the polymer components are immiscible to each other (Chiou et al., 2014; Kok, Demirelli, & Aydogdu, 2008). If the polymer components are miscible to each other, only one transition will be observed (Chiou et al., 2014).

Figures 4.20 to 4.22 show the DSC curves of S10C0, S0C10 and S8C2 films, respectively. The T_g value for S10C0 and S0C10 films are found to be 67.21 °C and 97.41 °C, respectively. These results are close to the values reported by Liu, Yu, Liu, Chen, and Li (2009) and Cheung, Wan, and Yu (as cited in Correia, Caridade, & Mano, 2014). Only one T_g value is observed for S8C2 film, which is found to fall in between the T_g values of S10C0 and S0C10 films, at 82.33 °C. The DSC results confirm the miscibility between starch and chitosan in S8C2 film.

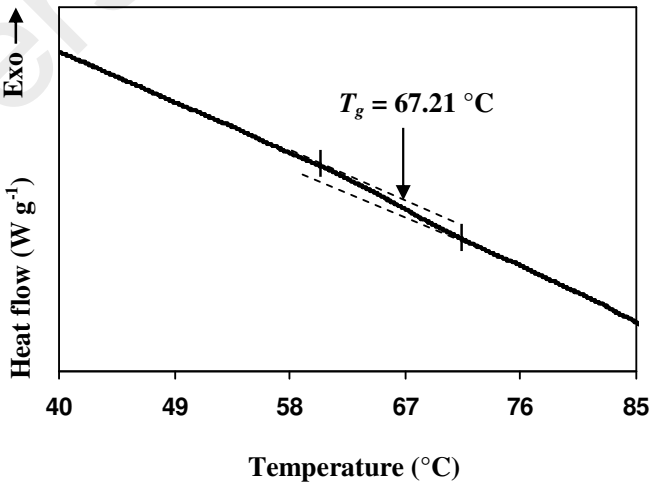

Figure 4.20: DSC thermogram of S10C0 film.

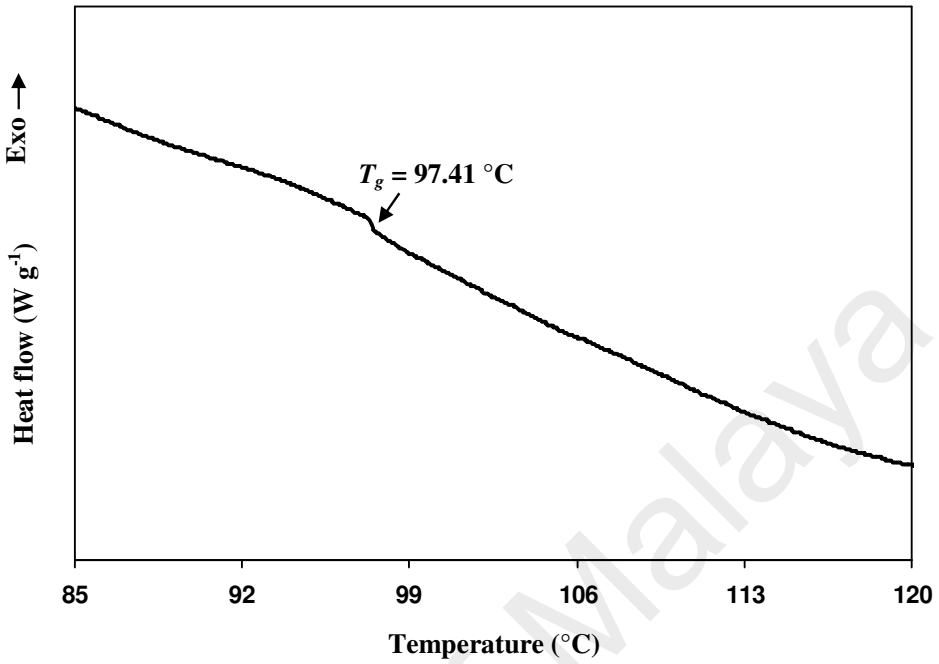

Figure 4.21: DSC thermogram of S0C10 film.

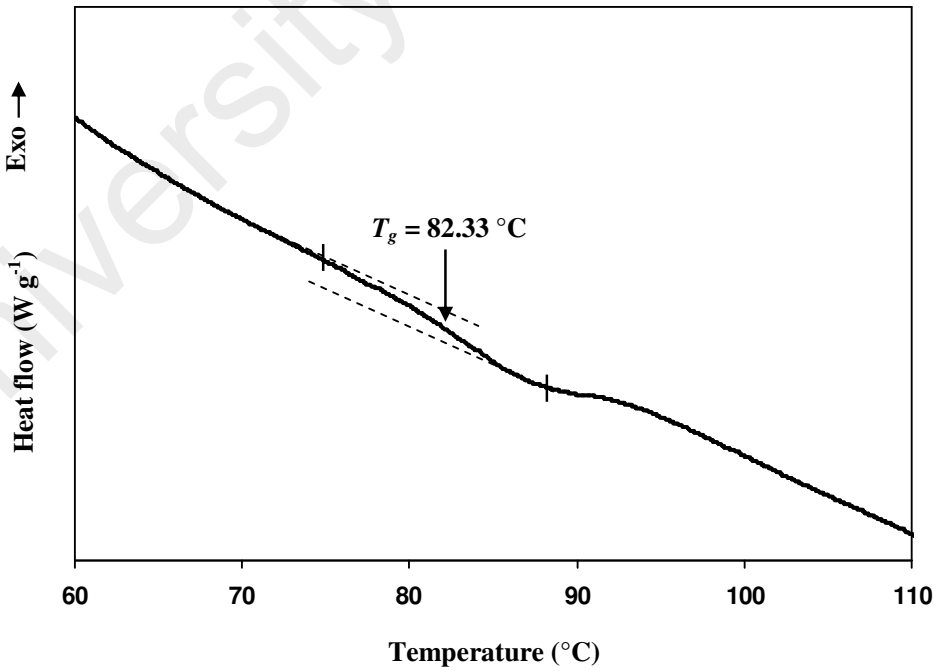

Figure 4.22: DSC thermogram of S8C2 film.

4.4 TGA Analysis

To study the effect of polymer blending on thermal stability, TGA measurements of S10C0, S0C10 and S8C2 films were carried out. Figure 4.23 shows the TGA thermograms of S10C0, S0C10 and S8C2 films.

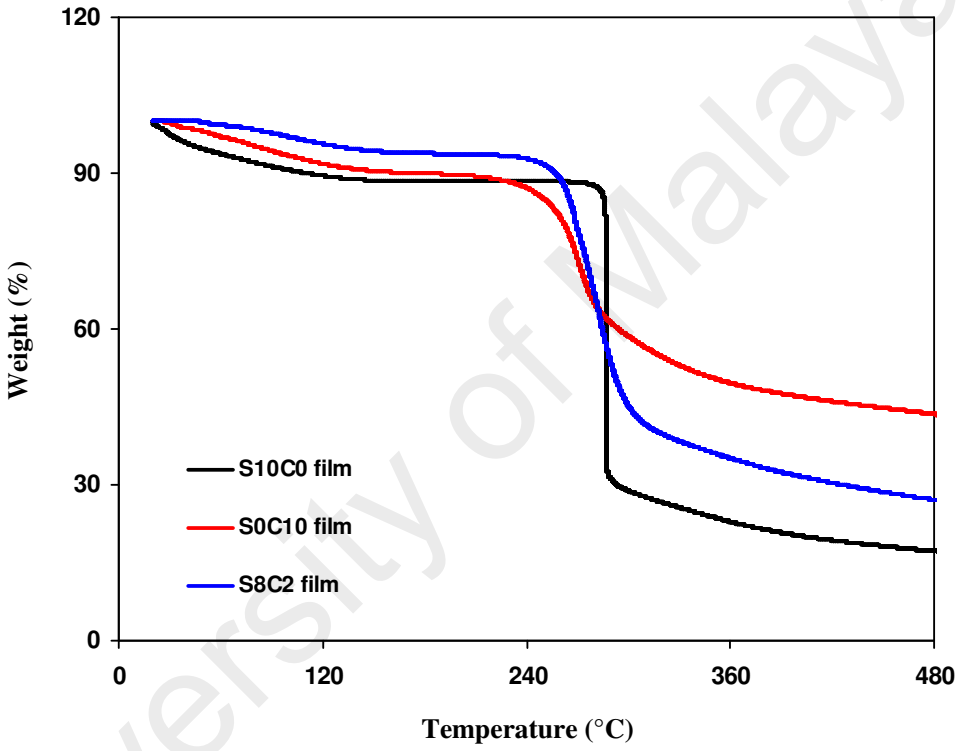

Figure 4.23: TGA thermograms of S10C0, S0C10 and S8C2 films.

From Figure 4.23, both S10C0 and S0C10 films exhibit first weight loss in between room temperature to 160 °C due to loss of water. In this region, S0C10 film exhibits ~ 10% weight loss, while S10C0 film exhibits ~ 12% weight loss. Major decomposition of S0C10 film occurs at 270 °C with a weight loss of ~ 30%. The second weight loss of ~ 58% for S10C0 film starts at 280 °C. Ramesh, Shanti, and Morris (2012) reported that pure corn starch undergoes one-step weight loss process with the

decomposition temperature of 280 °C, which is similar as the present result. The glucose monomers that initially built up the corn starch tend to detach from the long polymer chain and subsequent heating beyond the decomposition temperature results in carbonization and ash formation (Ramesh et al., 2012). Since pure starch has high moisture sensitivity, blending starch with other polymers is one of the methods to overcome the problem (Lu et al., 2009). From the thermogram of S8C2 film, a weight loss of ~ 6% from room temperature to 160 °C is observed. This result shows that the water content of starch is decreased by blending starch with chitosan. The decomposition temperature does not change on blending starch with chitosan, as S8C2 film decomposes at 270 °C.

4.5 Summary

The suitable ratio of starch-chitosan blend to serve as polymer host has been examined using XRD analysis where the blend of 80 wt.% starch and 20 wt.% chitosan is the most amorphous blend. SEM analysis confirmed that starch and chitosan is miscible to one another by forming homogenous films. Further confirmation of starch-chitosan miscibility has been made to the blend of 80 wt.% starch and 20 wt.% chitosan by DSC. Blending 80 wt.% starch with 20 wt.% chitosan has decreased the water content of the film as shown in TGA thermograms. Thus, the blend of 80 wt.% starch and 20 wt.% chitosan has been chosen as the polymer host for further characterization.

CHAPTER 5

FTIR STUDIES

5.1 Introduction

This chapter presents the investigation on interactions between the electrolyte materials using FTIR analysis. The interaction can be revealed by the changes in the position and shape intensity of the bands' peak. The interaction between the electrolyte materials prefers to take place in the amorphous region (Ramamohan & Sharma, 2013). According to Ratner and Shriver (as cited in Ulaganathan, Nithya, Rajendran, & Raghu, 2012), the ionic conduction in the polymer electrolyte occurs mainly in the amorphous region. Thus, the FTIR analysis can provide the evidence of the existence of ion in the complexation sites.

From the literature, the interaction between chitosan and salt occurred between the lone pair electron of oxygen or nitrogen atoms of chitosan and the conducting charge species (Majid & Arof, 2005, 2008; Morni et al., 1997; Yahya & Arof, 2003). Kadir, Aspanut, Majid and Arof (2011) reported that the cations of NH_4NO_3 are attached to the PVA-chitosan blend host due to the carboxamide, amine and hydroxyl bands experiencing a distinctive shift in the spectra. The shift in the hydroxyl band of pure starch film upon addition of salt proves the occurrence of starch-salt interaction (Khanmirzaei & Ramesh, 2013; Ramesh et al., 2011; Shukur, Ibrahim, Majid, Ithnin, & Kadir, 2013).

Apart from proving the interaction between the polymer host and the salt, FTIR analysis can also predict the conductivity trend (Kadir, Aspanut, Majid, & Arof, 2011; Mason, Hu, Glatzhofer, & Frech, 2010; Subban & Arof, 2004). The difference in the number of ions attached to the host functional groups should result in changes in the vibrational modes of the molecules in the polymer host. Besides, the effect of salt recrystallization on the conductivity can also be predicted. The schematic diagrams showing the interaction between the electrolyte components will be proposed.

5.2 FTIR Analysis of Starch Film

Figure 5.1 depicts the spectra of pure starch powder and pure starch film (S10C0) in the region that contains hydroxyl (OH) band.

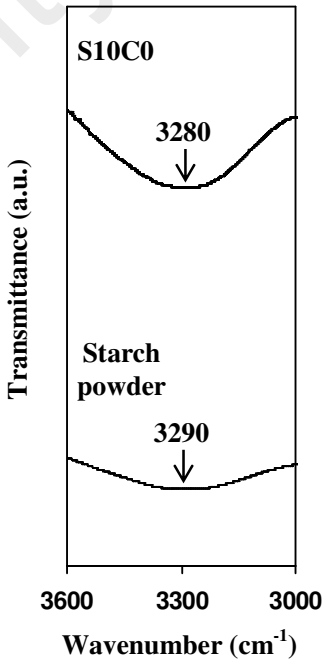

Figure 5.1: FTIR spectra for pure starch powder and S10C0 film in the region of 3000-3600 cm^{-1}.

The hydroxyl band in the spectrum of pure starch powder appears at 3290 cm^{-1} while that of S10C0 film appears at 3280 cm^{-1}. Kadir, Aspanut, Majid, and Arof (2011) reported that the hydroxyl band in the spectrum of pure PVA powder has shifted from 3354 to 3343 cm^{-1} in the spectrum of pure PVA film. The authors claim that the band shift indicates the occurrence of interaction between polymer and the acetic acid solvent, which is relevant to our result. The strong and wide absorption in the hydroxyl band region of pure starch film indicates that there are several hydroxyl groups in starch (Teoh et al., 2012).

Figure 5.2(a) and (b) shows the spectra of pure starch powder and S10C0 film in the 1065-1095 cm^{-1} and 2850-2970 cm^{-1} regions, respectively.

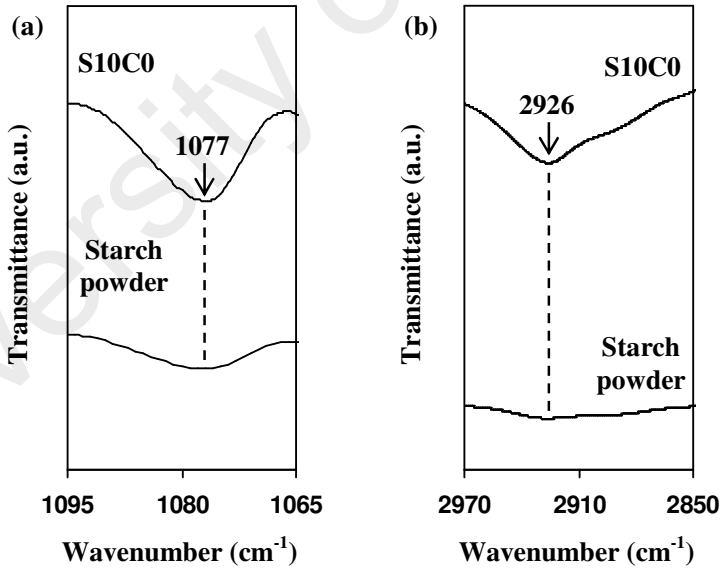

Figure 5.2: FTIR spectra for pure starch powder and S10C0 film in the region of (a) 1065-1095 cm^{-1} and (b) 2850-2970 cm^{-1}.

In Figure 5.2(a), the peak at 1077 cm^{-1} in the spectrum of pure starch powder corresponds to C-O bond stretching of C-O-C group in the anhydroglucose ring in

starch (Ning, Xingxiang, Haihui, & Benqiao, 2009). As shown in the spectrum of S10C0 film, the intensity of this peak increases revealing the interaction between starch and acetic acid solvent in this band. Even though the wavenumber of this peak shows no significant shift, the changes in intensity and sharpness of the shape also provide the evidence of interaction between those materials (Ramesh & Liew, 2013). The same observation can be seen in the region of C-H stretching mode of starch in Figure 5.2(b). Although starch-acetic acid do not interact in this region, its FTIR spectra can also be affected, thus proves the starch-acetic acid interaction (Stygar, Zukowska, & Wieczorek, 2005).

Another evidence of starch-acetic acid interaction can be observed by the shifting of the peak in the region of 900-950 cm^{-1} as shown in Figure 5.3.

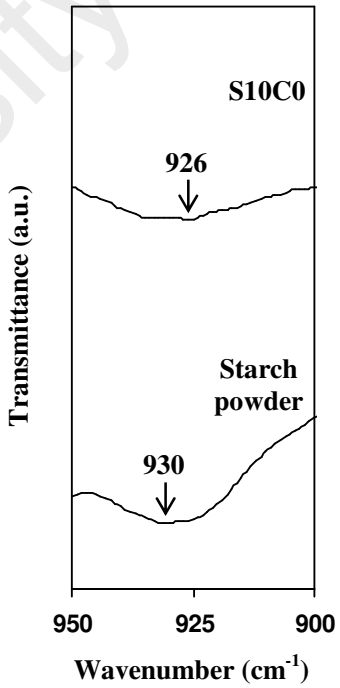

Figure 5.3: FTIR spectra for pure starch powder and S10C0 film in the region of 900-950 cm^{-1}.

The peak observed in Figure 5.3 corresponds to the skeletal mode vibration of glycosidic linkage (C-O-C) (Juneja, Kaur, Odeku, & Singh, 2014; Khanmirzaei & Ramesh, 2013). This peak is located at 930 cm^{-1} in the spectrum of starch powder but shifts to 926 cm^{-1} in the spectrum of S10C0 film. This result indicates that the acetic acid has interacted with oxygen atoms in glycosidic linkages.

Figure 5.4 depicts the proposed schematic diagram of starch having an interaction with acetic acid.

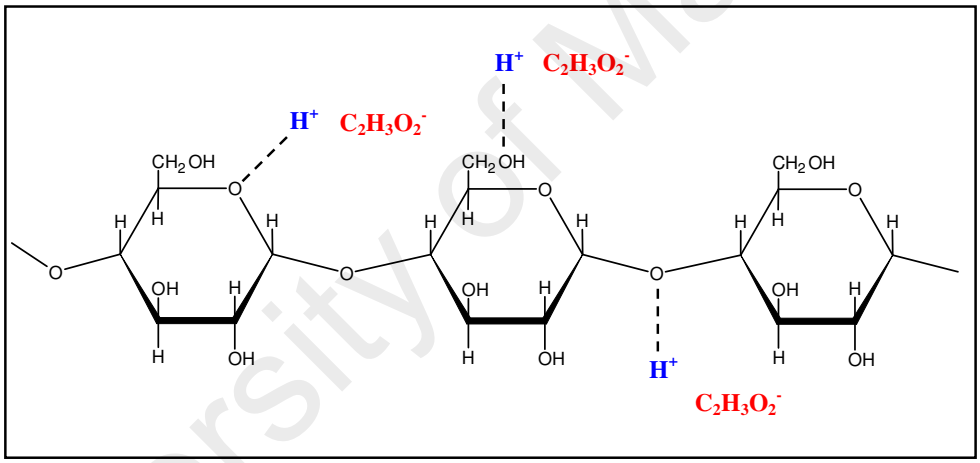

Figure 5.4: Schematic diagram of interaction between starch and acetic acid in S10C0 film. The dotted lines (- - - -) represent dative bonds between cations and the complexation sites.

Based on the FTIR results in Figures 5.1 to 5.3, the H^+ ions from the acetic acid have interacted with the oxygen atoms in hydroxyl, C-O-C in the anhydroglucose ring and glycosidic linkages. This is because the oxygen atoms in those functional groups contain unused electrons which are known as lone pair electrons (Yap, 2012). The lone pair electrons can form a dative bond with the H^+ ion as shown in Figure 5.4.

5.3 FTIR Analysis of Chitosan Film

Figure 5.5(a) depicts the spectra of pure chitosan powder and pure chitosan film (S0C10) in the region of hydroxyl band. There is a change in intensity of the peak at 3354 cm^{-1} revealing the interaction between chitosan and acetic acid solvent in the hydroxyl band. The position of the hydroxyl band for S0C10 film is in good agreement with that reported by Kadir, Aspanut, Majid, and Arof (2011).

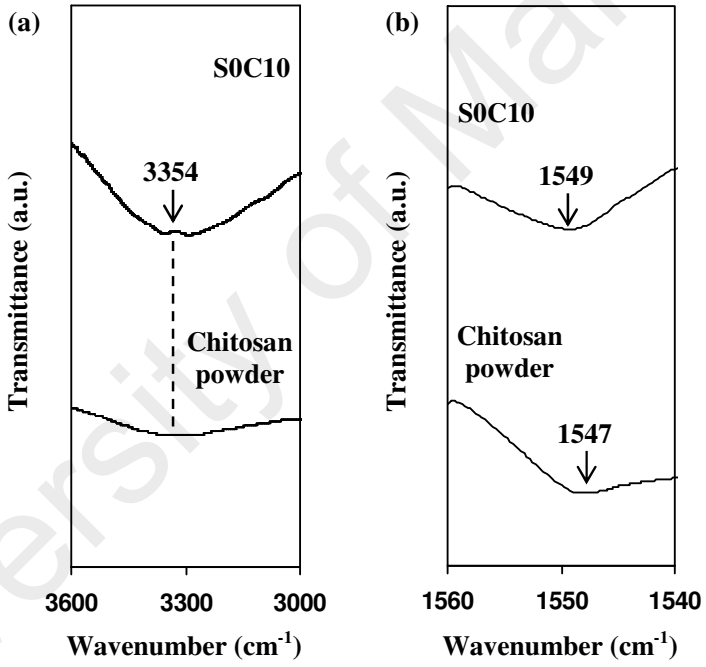

Figure 5.5: FTIR spectra for pure chitosan powder and S0C10 film in the region of (a) 3000-3600 cm^{-1} and (b) 1540-1560 cm^{-1}.

Figure 5.5(b) depicts the spectra of pure chitosan powder and S0C10 film in the region that contains amine (NH_2) band. The amine band is observed at 1547 cm^{-1} in the spectrum of pure chitosan powder. In the spectrum of S0C10 film, this band is located at 1549 cm^{-1} proving the interaction between the acetic acid solvent and the nitrogen

donor of chitosan. Buraidah (2012) and Osman and Arof (2003) also inferred the occurrence of chitosan-acetic acid interaction at the nitrogen atom of amine based on the shifting of amine band's position.

During the deacetylation process of chitin, carboxamide (O=C-NHR) band is removed to release amine band (Badawy & Rabea, 2011; Zakaria, Izzah, Jawaid, & Hassan, 2012). However, due to incomplete deacytelation process, the presence of carboxamide band in chitosan is still there (Buraidah, 2012). Figure 5.6 shows FTIR spectra of pure chitosan powder and S0C10 film in the region that contains the carboxamide band. The carboxamide band in the spectra of pure chitosan powder and S0C10 film is located at 1652 cm^{-1}. However, change in intensity of the peak can be observed thus provides the evidence of the interaction between acetic acid solvent and chitosan in carboxamide band.

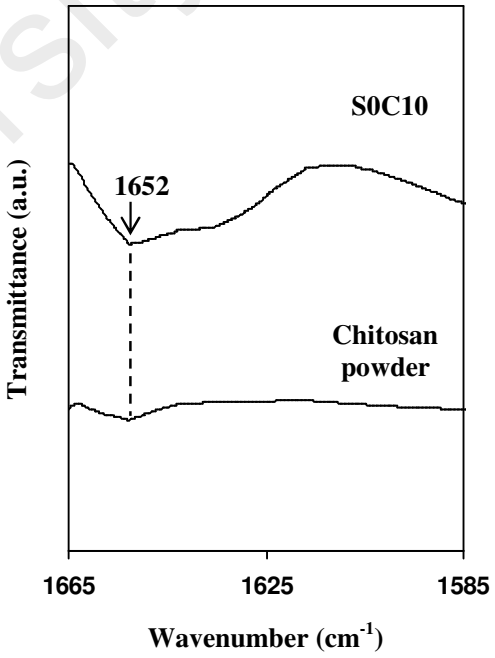

Figure 5.6: FTIR spectra for pure chitosan powder and S0C10 film in the region of 1585-1665 cm^{-1}.

In Figure 5.7(a), two peaks appear at 1074 and 1022 cm^{-1} in the spectrum of chitosan powder. These peaks are assigned to C-O-C stretching vibration (Nivethaa, Narayanan, & Stephen, 2014). In the spectrum of S0C10 film, these two peaks shift to 1062 and 1025 cm^{-1} accompanied by the increase in intensity indicating the involvement of this band in chitosan-acetic acid interaction. In Figure 5.7(b), a peak corresponding to glycosidic bonding (C-O-C) vibration appears at 897 cm^{-1} in the spectrum of chitosan powder but shift to 895 cm^{-1} with an increase in intensity in the spectrum of S0C10 film.

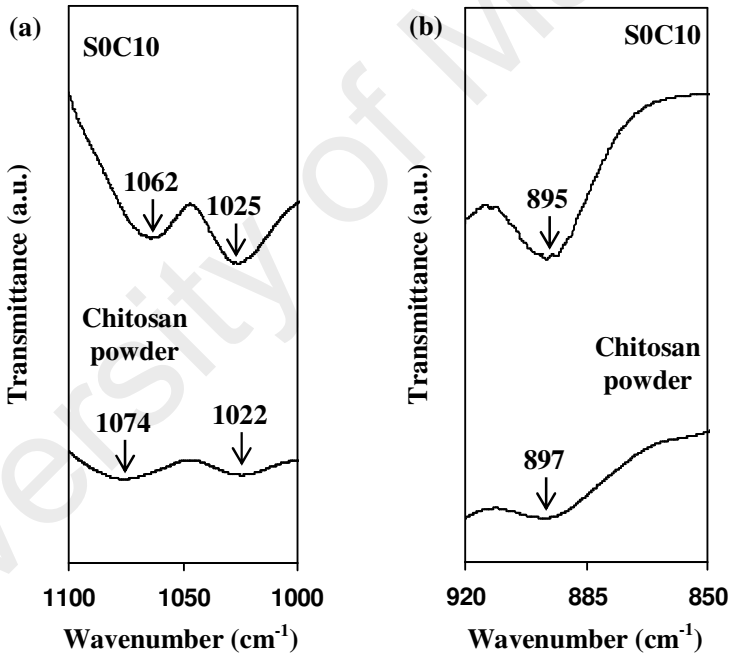

Figure 5.7: FTIR spectra for pure chitosan powder and S0C10 film in the region of (a) 1000-1100 cm^{-1} and (b) 850-920 cm^{-1}.

Based on the results in Figures 5.5 to 5.7, the schematic diagram of proposed interaction between chitosan and acetic acid solvent is shown in Figure 5.8.

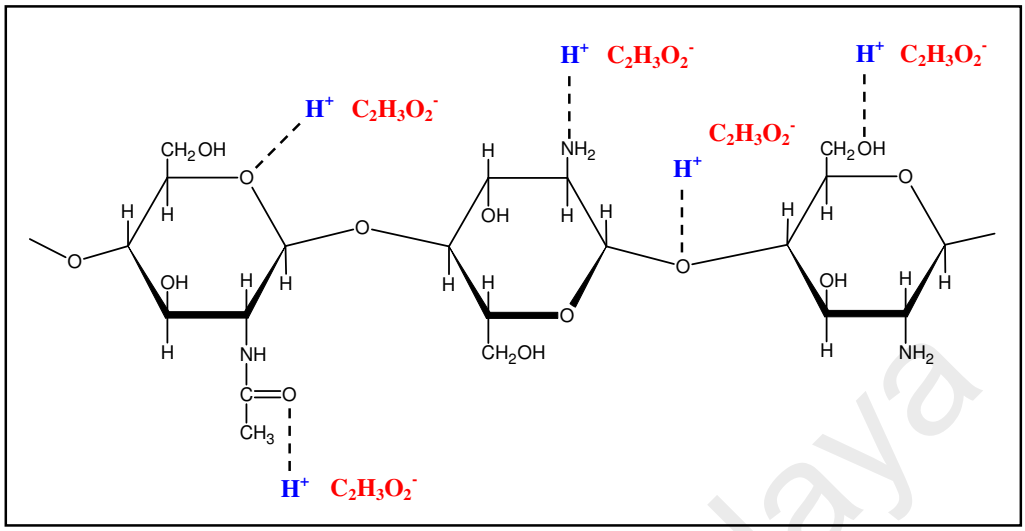

Figure 5.8: Schematic diagram of interaction between chitosan and acetic acid in S0C10 film. The dotted lines (- - - -) represent dative bonds between cations and the complexation sites**.**

5.4 FTIR Analysis of Starch-Chitosan

In a polymer blend, the interaction between the two polymer components occurs through hydrogen bonding (Bouslah & Amrani, 2007; Luo, Hu, Zhao, Goh, & Li, 2003). From a report by Luo et al. (2003), the hydrogen bonding interaction in the blend of poly(4-methyl-5-vinylthiazole) (PMVT) and poly(*p*-vinylphenol) (PVPh) is proven by the shifting of hydroxyl band of pure PVPh upon addition of PMVT.

Figure 5.9 shows the spectra of S0C10, S10C0 and starch-chitosan blend with the ratio of 80:20 (S8C2) in the hydroxyl band and amine band regions. In Figure 5.9(a), the hydroxyl band in the spectrum of S0C10 film appears at 3354 cm^{-1}. In the spectrum of S10C0 film, hydroxyl band appears at 3280 cm^{-1}. The mixture of two or more materials will reflect the physical blends and chemical reactions based on the changes in characteristics spectral peaks (Ashori & Bahrami, 2014). In the spectrum of S8C2 film,

the hydroxyl band has shifted to 3288 cm^{-1}. In Figure 5.9(b), the amine band of S0C10 film is located at 1549 cm^{-1}. In the spectrum of S8C2 film, the amine band has shifted to 1548 cm^{-1}. Bajer and Kaczmarek (2010) reported that the position of the amine band of chitosan shifted from 1561 to 1560 cm^{-1} in starch-chitosan film. Based on Figure 5.9, starch-chitosan interaction may occur between hydroxyl groups of starch and the hydroxyl groups of chitosan as well as between hydroxyl groups of starch and the amine groups of chitosan.

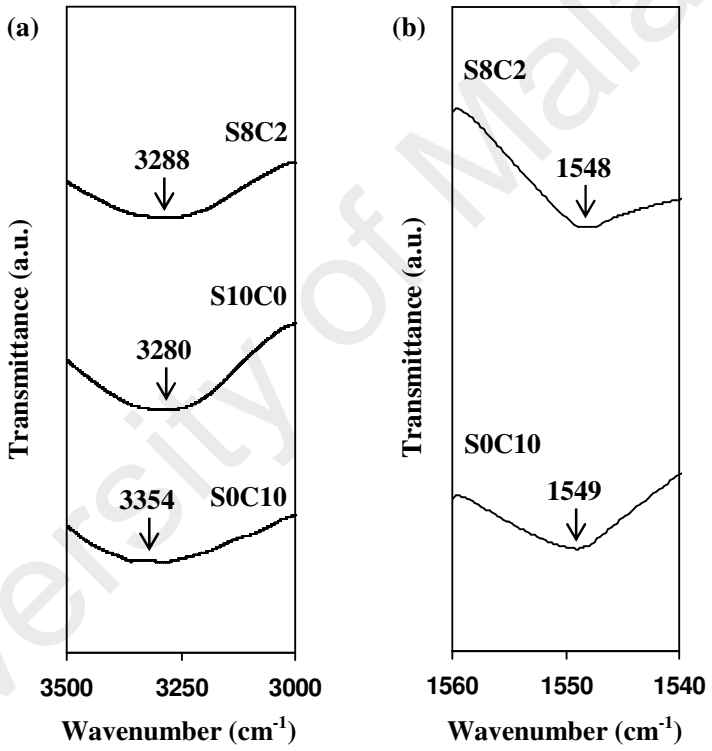

Figure 5.9: FTIR spectra for S0C10, S10C0 and S8C2 films in the region of (a) 3000-3500 cm^{-1} and (b) 1540-1560 cm^{-1}.

Figure 5.10 depicts the FTIR spectra of S0C10 and S8C2 films in the carboxamide band region. No peak shifting is observed. Besides, no significant change in intensity can be seen inferring that no interaction occurs between chitosan and starch at the carboxamide band.

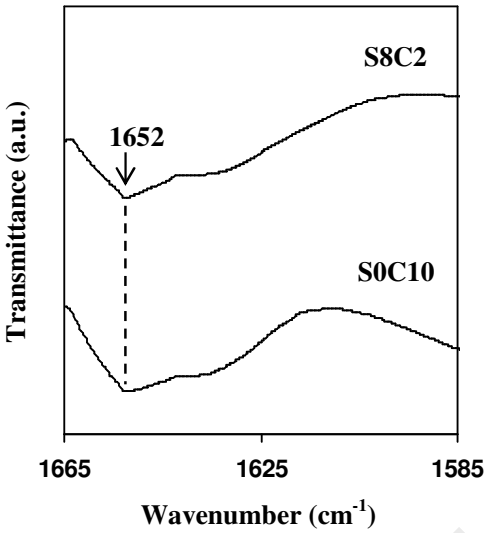

Figure 5.10: FTIR spectra for S0C10 and S8C2 films in the region of 1585-1665 cm^{-1}.

Figure 5.11 represents the spectra of S0C10, S10C0 and S8C2 films in the 1010-1100 cm^{-1} and 880-950 cm^{-1} regions.

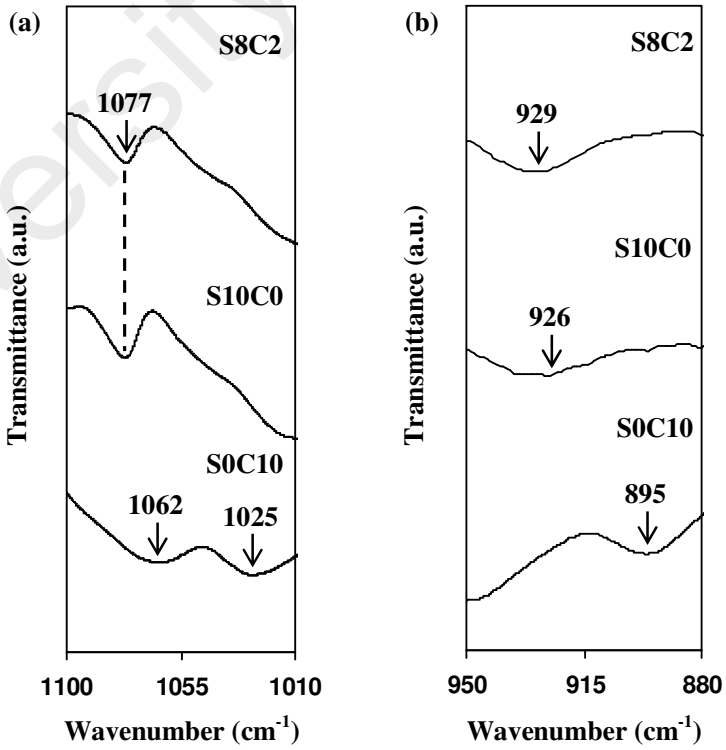

Figure 5.11: FTIR spectra for S0C10, S10C0 and S8C2 films in the region of (a) 1010-1100 cm^{-1} and (b) 880-950 cm^{-1}.

From Figure 5.11(a), the C-O bond stretching peak at 1077 cm^{-1} in the spectrum of S10C0 film is observed unshifted in the spectrum of S8C2 film. Besides, no significant change in intensity can be seen indicating that the oxygen atom in anhydroglucose ring of starch does not involve in hydrogen bonding interaction with chitosan. In Figure 5.11(b), the peak corresponds to glycosidic linkage of starch at 926 cm^{-1} has shifted to 929 cm^{-1} upon blending starch with chitosan, inferring the interaction occurs in this region. It is noticed that the C-O-C stretching vibration peaks and glycosidic bonding (C-O-C) vibration peak in the spectrum of S0C10 film do not appear in the spectrum of S8C2 film. The absence of those peaks suggests good miscibility between starch and chitosan in the blend, mainly due to the hydrogen bond interaction between hydroxyl groups of starch with amino and hydroxyl groups of chitosan (El-Hefian, Nasef, & Yahaya, 2010; El-Hefian, Nasef, Yahaya, & Khan, 2010; Ramya, Sudha, & Mahalakshmi, 2012; Thenmozhi, Gomathi, & Sudha, 2013). According to Viswanathan and Dadmun (2002), the formation of hydrogen bonds between two polymers in a blend enhances the miscibility between the polymers. Thus, the FTIR result further strengthens the DSC and SEM analysis on starch-chitosan miscibility as presented in Chapter 4.

In starch-chitosan blend, the interaction occurs mainly through hydrogen bonding between the amylose of starch and chitosan molecules as it is easier for amylose to mix with chitosan than the branched chain amylopectin (Mathew & Abraham, 2008). This is because the branching structure in amylopectin has greater steric hindrance and thus prevents chemical reactions rather than the linear structure of the amylose (Khiar & Arof, 2010). The schematic diagram of proposed interaction between starch, chitosan and acetic acid in S8C2 film is depicted in Figure 5.12.

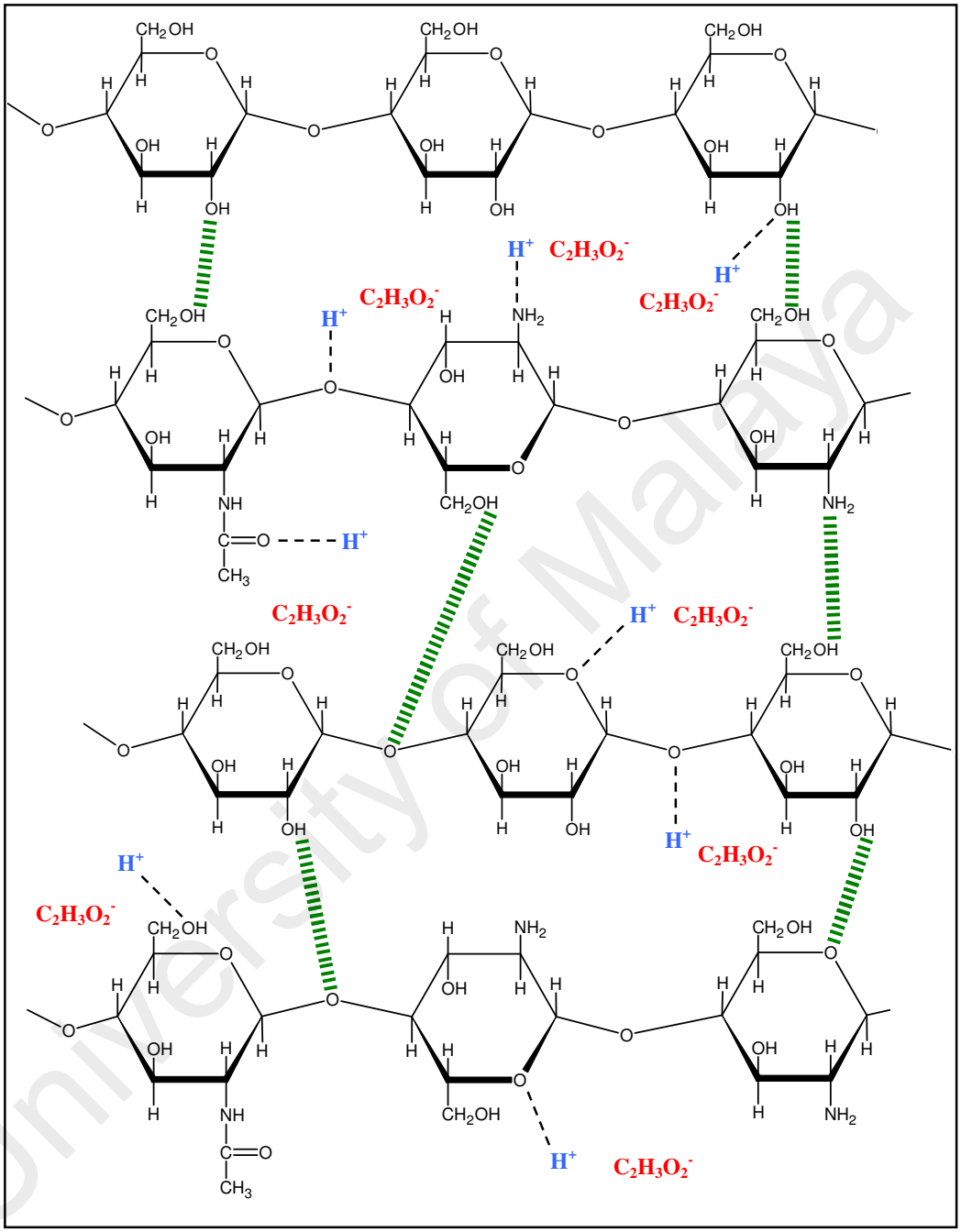

Figure 5.12: Schematic diagram of interaction between starch, chitosan and acetic acid in S8C2 film. The black dotted lines (- - - -) represent dative bonds between cations and the complexation sites. The green lines (||||||||||) represent hydrogen bonds between starch and chitosan.

5.5 FTIR Analysis of Starch-Chitosan-NH_4Cl

Figure 5.13 shows the FTIR spectra for selected electrolytes in starch-chitosan-NH_4Cl (salted) system in the region of hydroxyl band. The hydroxyl band is located at 3288 cm^{-1} in the spectrum of S8C2 film. However, the hydroxyl band has shifted to lower wavenumbers of 3284, 3278 and 3264 cm^{-1} on addition of 5, 10 and 25 wt.% NH_4Cl (S1, S2 and S5 electrolytes, respectively). Kadir, Aspanut, Yahya, and Arof

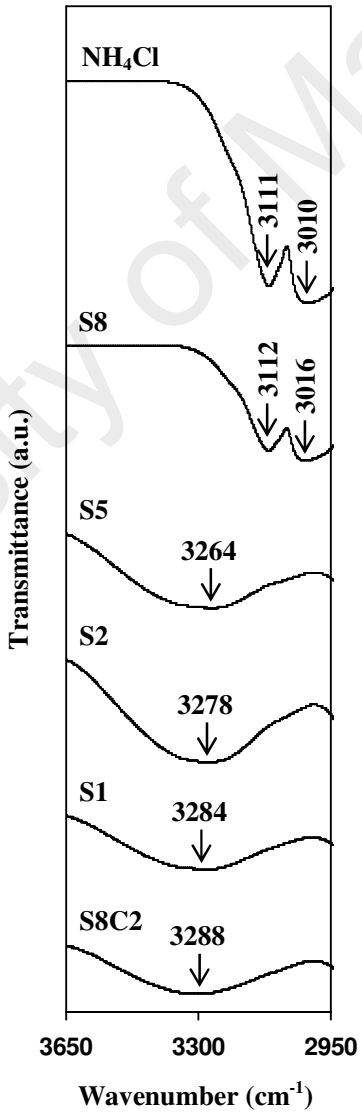

Figure 5.13: FTIR spectra for S8C2, pure NH_4Cl salt and selected electrolytes in the salted system in the region of 2950-3650 cm^{-1}.

(2011) reported that the interaction between chitosan and NH_4NO_3 at hydroxyl band is evidenced by the shifting of the hydroxyl band to lower wavenumbers. Thus it can be concluded that the polymer host in the present work has interacted with NH_4Cl at the hydroxyl band. In the spectrum of S8 electrolyte, two peaks appear at 3112 and 3016 cm^{-1}, corresponding to the asymmetry vibration ($v_{as}(NH_4^+)$) and symmetry vibration ($v_s(NH_4^+)$) modes of NH_4^+, respectively. Those two peaks are located at 3111 and 3010 cm^{-1}, respectively, in the spectrum of pure NH_4Cl salt. The appearance of $v_{as}(NH_4^+)$ and $v_s(NH_4^+)$ modes infers the occurrence of ion reassociation when more than 25 wt.% NH_4Cl is added to the electrolyte. The reassociation of ions has formed ion aggregates. According to Mason et al. (2010), the higher aggregation had resulted in fewer available charge carriers in their polymer electrolyte system resulting in conductivity decrement. In the present work, it can be inferred that the addition of more than 25 wt.% NH_4Cl would decrease the conductivity of electrolyte due the formation of ion aggregates.

Figure 5.14 represents the FTIR spectra for selected electrolytes in salted system in the carboxamide band region. In the spectrum of S8C2 film, the carboxamide band is located at 1652 cm^{-1}. As the NH_4Cl content increases to 25 wt.%, the carboxamide band shifts to lower wavenumbers. The carboxamide band appears at 1629 cm^{-1} in the spectrum of S5 electrolyte. This result again provides the evidence of starch-chitosan-NH_4Cl interaction. In the spectrum of S6 and S7 electrolytes, the carboxamide band shift back to higher wavenumbers of 1632 and 1633 cm^{-1}, respectively. This phenomenon may be attributed to the decrease in number density of ions resulting in the reduction of interaction between the salt and the polymer host at the oxygen atoms of carboxamide band.

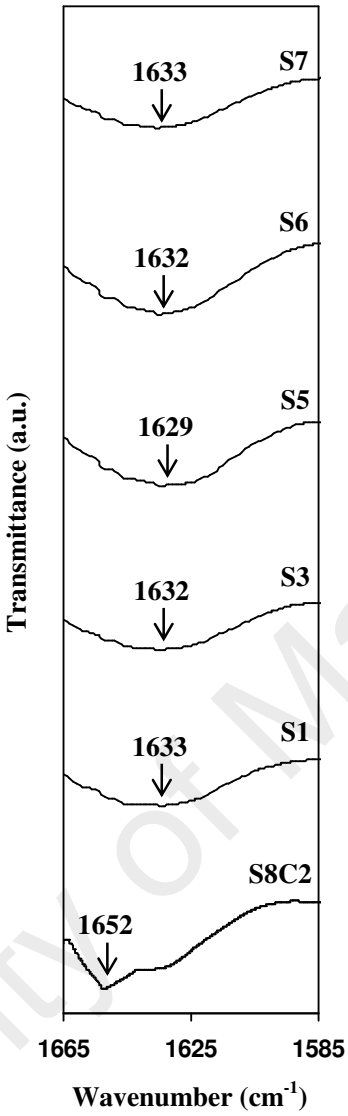

Figure 5.14: FTIR spectra for S8C2 and selected electrolytes in the salted system in the region of 1585-1665 cm^{-1}.

The amine band is located at 1548 cm^{-1} in the spectrum of S8C2 film as shown in Figure 5.15. In the spectrum of S1 electrolyte, the amine band is observed at 1532 cm^{-1} and further shifted to 1526 and 1524 cm^{-1} in the spectra of S5 and S6 electrolytes. This result provides the evidence of starch-chitosan-NH_4Cl interaction at the nitrogen atom of amine group. In the spectrum of S8 electrolyte, the amine band's peak does not appear suggesting that the ions had reassociated back to form neutral ion pairs, which can lead to the conductivity decrement.

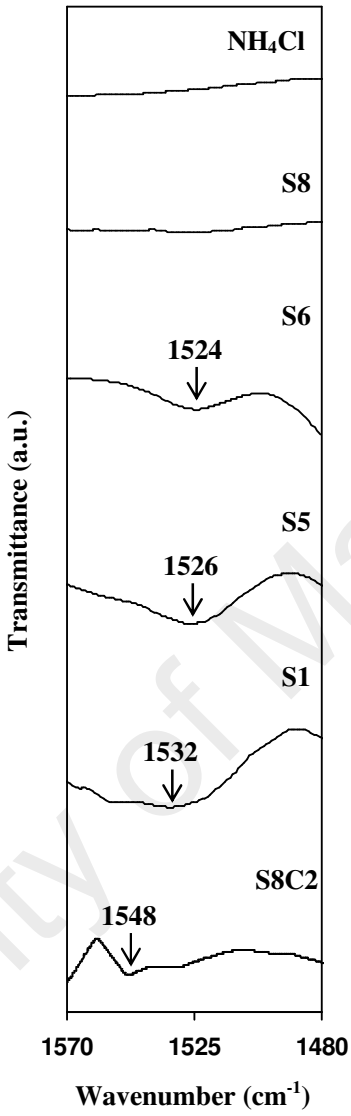

Figure 5.15: FTIR spectra for S8C2, pure NH_4Cl salt and selected electrolytes in the salted system in the region of 1480-1570 cm^{-1}.

In the spectrum of S2, S3 and S5 electrolytes in Figure 5.16, the peak which corresponds to C-O-C group has shifted to lower wavenumbers of 1076, 1075 and 1074 cm^{-1}, respectively. This result indicates that the cations have interacted with oxygen atoms in C-O-C group and further prove the interaction of polymer host with NH_4Cl. In the spectrum of S6 electrolyte, the C-O bond stretching band has shifted to higher

wavenumber of 1075 cm^{-1}. No peak is observed in the spectrum of S8 electrolyte indicating the recrystallization of the salt which can lead to the decrease in conductivity.

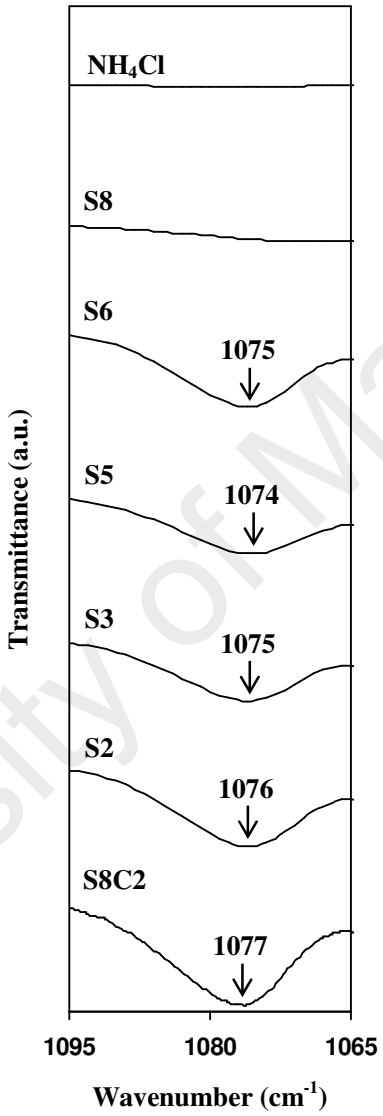

Figure 5.16: FTIR spectra for S8C2, pure NH_4Cl salt and selected electrolytes in the salted system in the region of 1065-1095 cm^{-1}.

From Figure 5.17, the peak which corresponds to glycosidic linkage at 929 cm^{-1} in the spectrum of S8C2 film is observed to shift to 934 cm^{-1} in the spectrum of S2, S3, S5 and S6 electrolytes. The present result proves that the cations from NH_4Cl interact

with oxygen atoms in the glycosidic linkages of polymer host. No peak is observed in the spectrum of S8 electrolyte indicating the recrystallization of the salt which can lead to the decrease in conductivity.

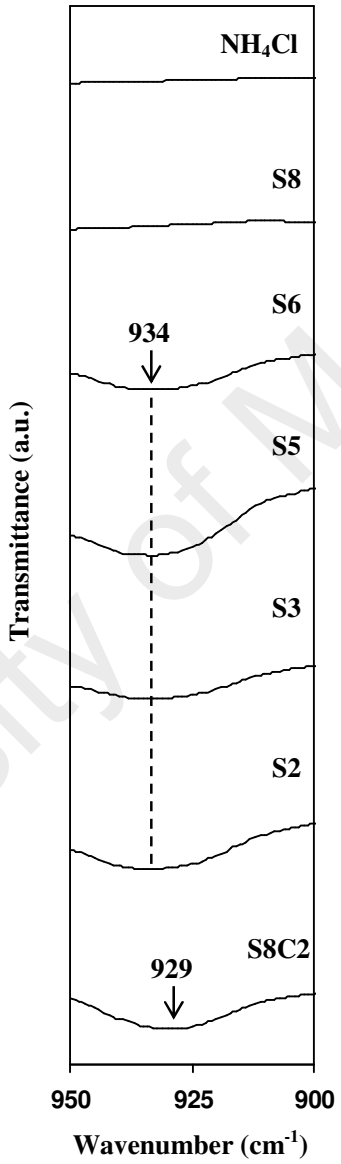

Figure 5.17: FTIR spectra for S8C2 film, pure NH_4Cl salt and selected electrolytes in the salted system in the region of 900-950 cm^{-1}.

The proposed interaction between starch-chitosan blend with NH_4Cl and acetic acid solvent is illustrated in Figure 5.18.

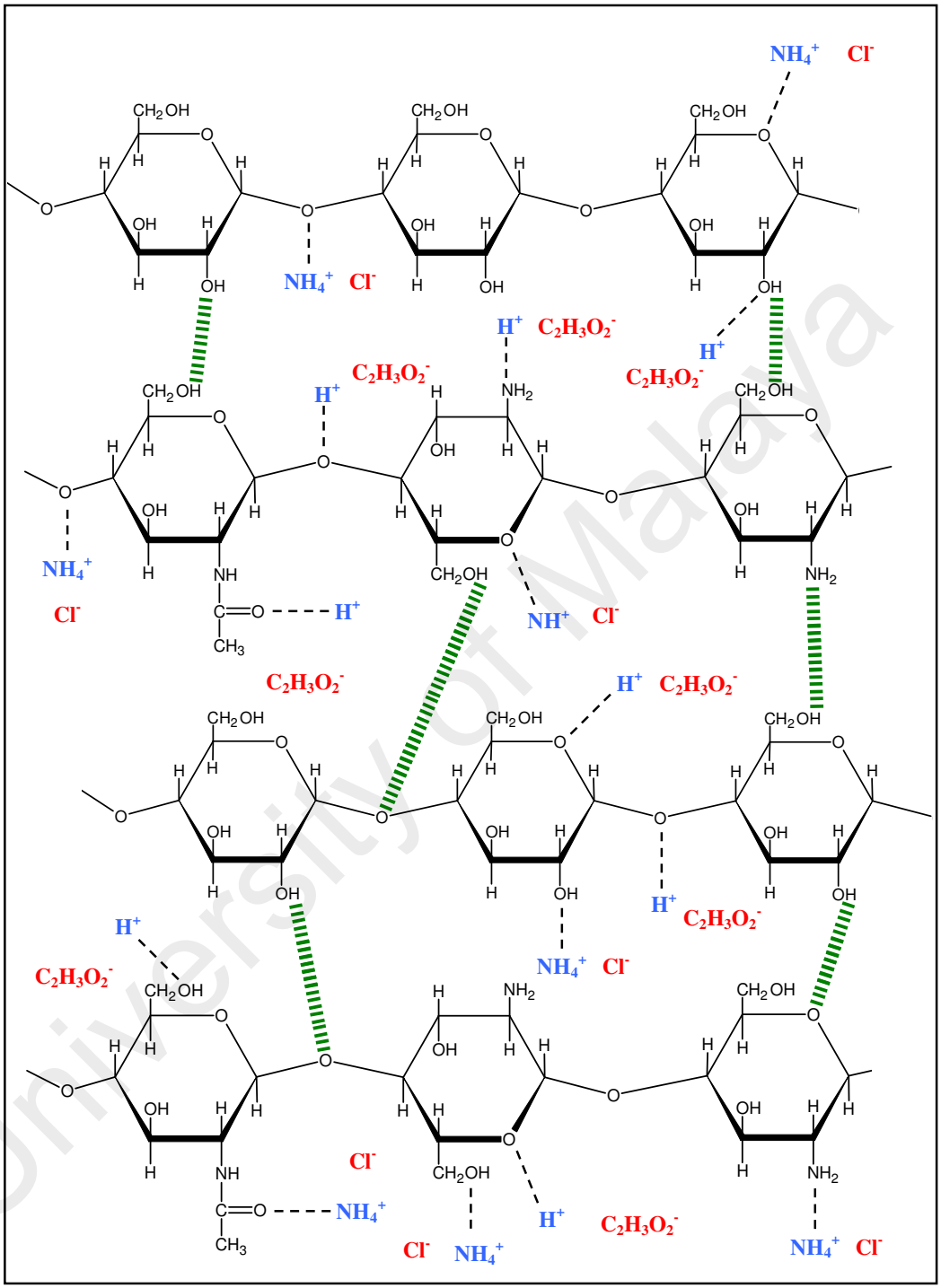

Figure 5.18: Schematic diagram of interaction between starch, chitosan, NH_4Cl and acetic acid. The black dotted lines (- - - -) represent dative bonds between cations and the complexation sites. The green lines (||||||||||) represent hydrogen bonds between starch and chitosan.

5.6 FTIR Analysis of Starch-Chitosan-Glycerol

Figure 5.19(a) depicts the FTIR spectra in the hydroxyl band region for S8C2, pure glycerol and starch-chitosan-glycerol films. The peak which is located at 3288 cm^{-1} in the spectrum of S8C2 film has shifted to 3291 cm^{-1} after the addition of 5 wt.% glycerol. The peak has further shifted to 3294 cm^{-1} on addition of 35 wt.% glycerol. Glycerol has multi-hydroxyl moiety structure and possesses the strong ability to interact with the polysaccharide matrix through hydrogen bonding interactions (Liang, Huang, Liu, & Yam, 2009). Based on Figure 5.19(a), it can be indicated that glycerol and the

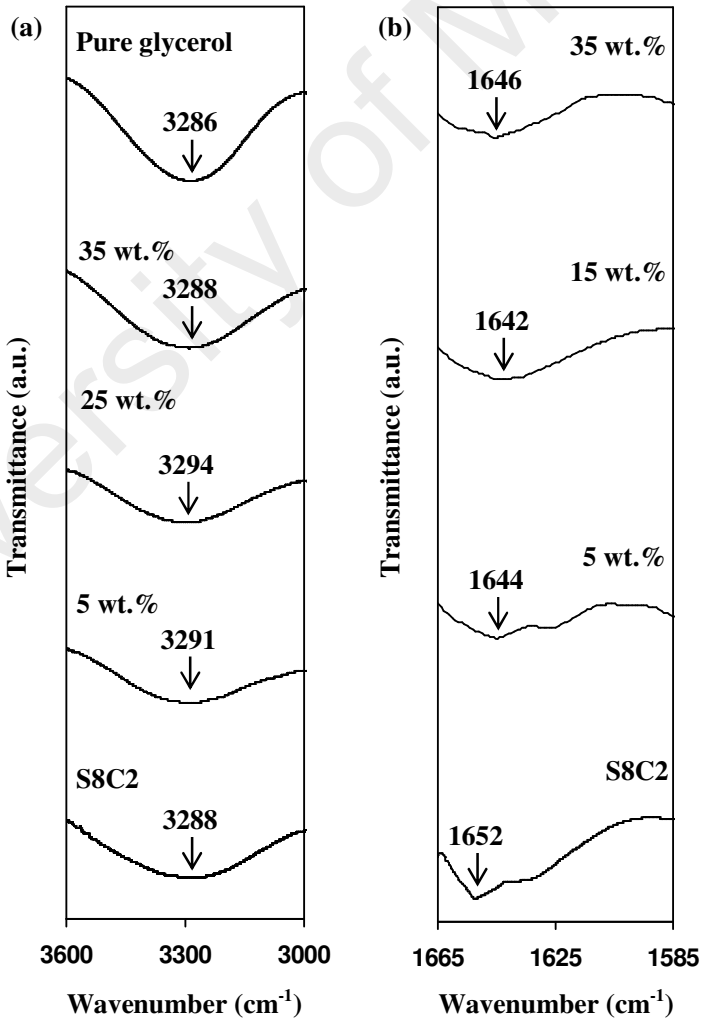

Figure 5.19: FTIR spectra for S8C2 film, pure glycerol and starch-chitosan-glycerol films in the region of (a) 3000-3600 cm^{-1} and (b) 1585-1665 cm^{-1}.

polymer blend have formed hydrogen bonding at the hydroxyl groups of both materials. The interaction between starch-chitosan blend and glycerol is further evidenced by the shifting of carboxamide band towards lower wavenumbers as the glycerol concentration increases to 15 wt.% as shown in Figure 5.19(b). When 35 wt.% glycerol is added to the polymer, the carboxamide band has shifted back to higher wavenumber of 1646 cm^{-1}. At 35 wt.% concentration, the interaction between polymer and glycerol may be decreased since there is competition between the plasticizer molecules to form hydrogen bonding with the polymer molecules. Thus, this phenomenon may leads to the increase in glycerol-glycerol interaction instead of polymer-glycerol interaction. Figure 5.20 shows the FTIR spectra of starch-chitosan-glycerol films in the amine band region.

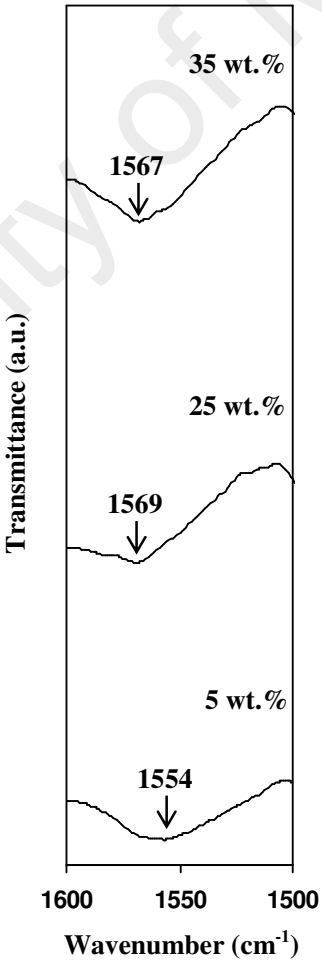

Figure 5.20: FTIR spectra for starch-chitosan-glycerol films in the region of 1500-1600 cm^{-1}.

From Figure 5.20, the amine band peak is observed to locate at 1554, 1569 and 1567 cm^{-1} with the addition of 5, 25 and 35 wt.% glycerol indicating the interaction between polymer and glycerol in this band.

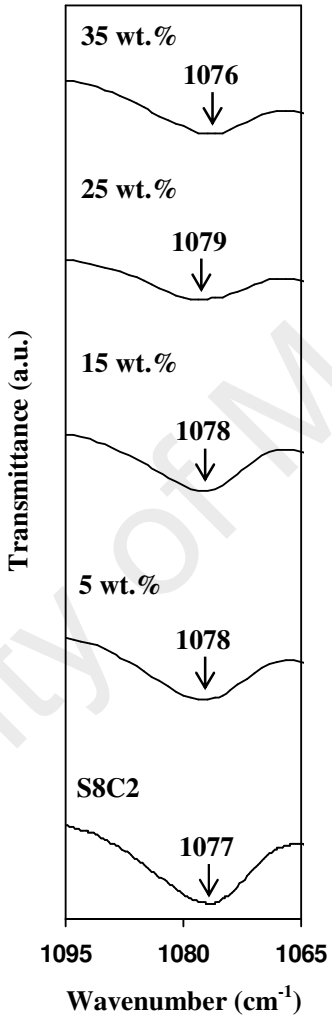

Figure 5.21: FTIR spectra for S8C2 and starch-chitosan-glycerol films in the region of 1065-1095 cm^{-1}.

From Figure 5.21, the peak which corresponds to C-O bond stretching of C-O-C group at 1077 cm^{-1} in the spectrum of S8C2 film is observed to shift to 1079 cm^{-1} as the glycerol content increases to 25 wt.%. Thus, it can be inferred that the hydroxyl groups of glycerol have interacted with oxygen atoms in the C-O-C group.

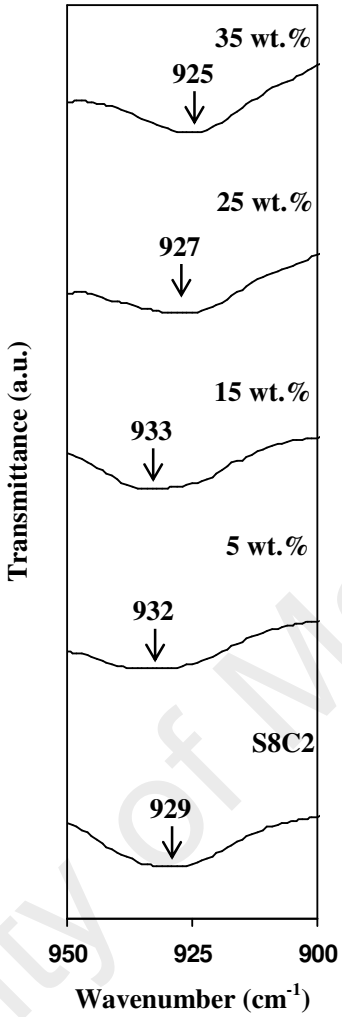

Figure 5.22: FTIR spectra for S8C2 and starch-chitosan-glycerol films in the region of 900-950 cm^{-1}.

From Figure 5.22, the peak at 929 cm^{-1} in the spectrum of S8C2 film has shifted to 932, 933, 927 and 925 cm^{-1} on addition of 5, 15, 25 and 35 wt.% glycerol, respectively. These results indicate the occurrence of interaction between the polymer blend and glycerol at glycosidic linkages.

The proposed interaction between starch-chitosan blend with glycerol and acetic acid solvent is illustrated in Figure 5.23.

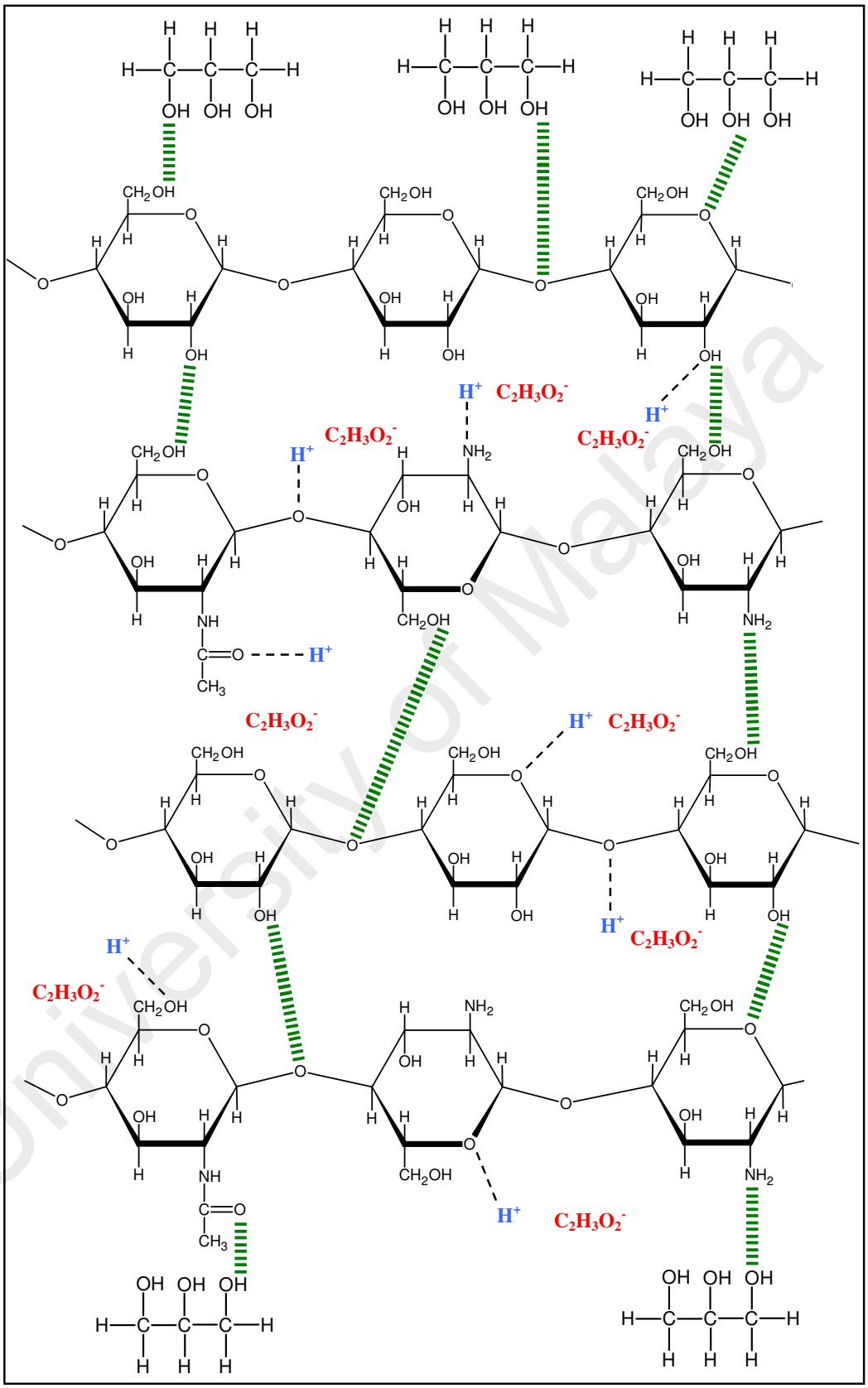

Figure 5.23: Schematic diagram of interaction between starch, chitosan, acetic acid and glycerol. The black dotted lines (- - - -) represent dative bonds between cations and the complexation sites. The green lines (||||||||||) represent hydrogen bonds between starch, chitosan and glycerol.

5.7 FTIR Analysis of Glycerol-NH_4Cl

For a plasticized electrolyte, it is important to determine if there is interaction between the salt and the plasticizer. If the interaction occurs, then interaction should occur between the cation of the salt and the hydroxyl group of glycerol. Figure 5.24 shows the FTIR spectra of pure glycerol and glycerol mixed with different weight percentage of NH_4Cl.

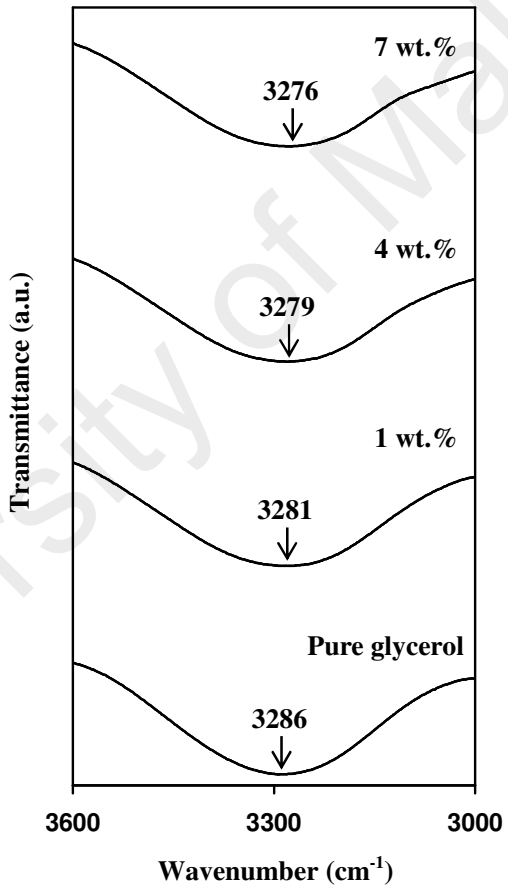

Figure 5.24: FTIR spectra for pure glycerol and glycerol with 1, 4 and 7 wt.% NH_4Cl in the region of 3000-3600 cm^{-1}.

The peak of hydroxyl band has shifted from 3286 cm^{-1} to the lower wavenumbers of 3281, 3279 and 3276 cm^{-1} on addition of 1, 4 and 7 wt.% NH_4Cl,

respectively. The peak shifting proves the interaction between the NH_4^+ ion and the oxygen atom of glycerol molecule. The schematic diagram in Figure 5.25 presents the possible interaction between glycerol and NH_4Cl.

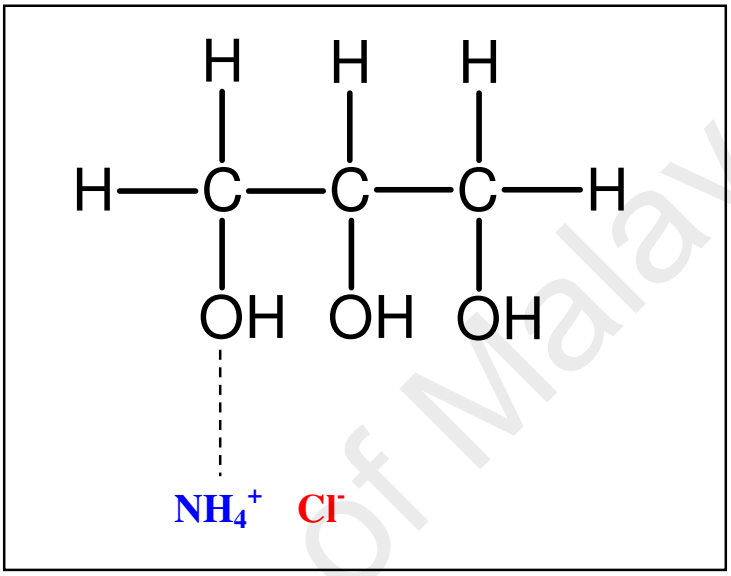

Figure 5.25: Schematic diagram of interaction between glycerol and NH_4Cl. The black dotted line (- - - -) represents dative bond between cation and the complexation site.

5.8 FTIR Analysis of Starch-Chitosan-NH_4Cl-Glycerol

FTIR spectra for the selected electrolytes in plasticized system in the hydroxyl band region are shown in Figure 5.26. The hydroxyl band has shifted to lower wavenumber of 3254 cm^{-1} on addition of 30 wt.% glycerol (P6 electrolyte) and further shifted to 3247 cm^{-1} on addition of 35 wt.% glycerol (P7 electrolyte). Apart from hydrogen bonding formation with the polymer host, the addition of plasticizer also promote ion dissociation, thus more ions have interacted with the polymer host at the hydroxyl band as evidenced by the shifting of FTIR spectra in Figure 5.26. This phenomenon can assist the conductivity enhancement. In the spectrum of P8 electrolyte,

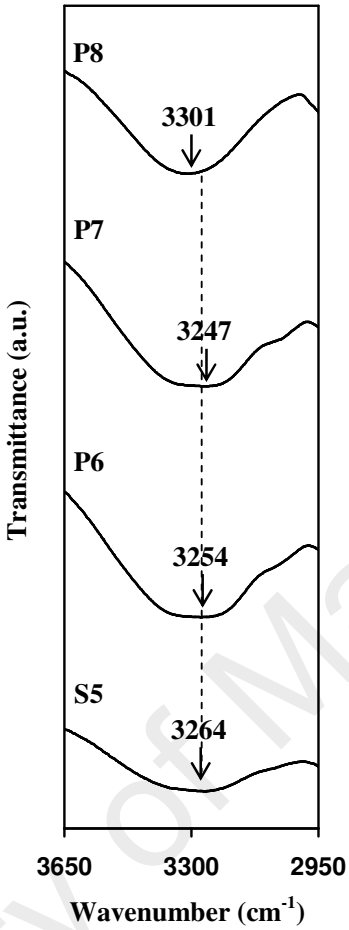

Figure 5.26: FTIR spectra for S5 and selected electrolytes in plasticized system in the region of 2950-3650 cm^{-1}.

the hydroxyl band has shifted to higher wavenumber of 3301 cm^{-1}. Less ions interact with the polymer host at the hydroxyl band, resulting in a shift to higher wavenumber of FTIR spectrum in Figure 5.26.

Figure 5.27 represents the FTIR spectra for selected electrolytes in plasticized system in the carboxamide band region. In the spectrum of S5 film, the carboxamide band is located at 1629 cm^{-1}. As the glycerol content increases to 35 wt.%, the carboxamide band has shifted to higher wavenumbers. The carboxamide band appears

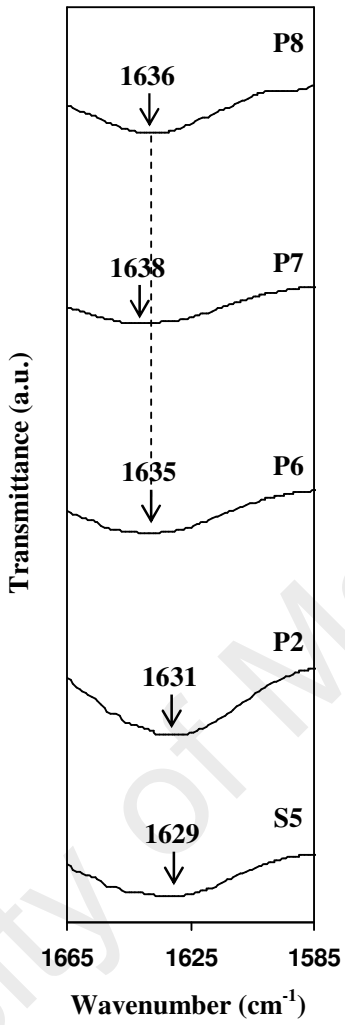

Figure 5.27: FTIR spectra for S5 and selected electrolytes in plasticized system in the region of 1585-1665 cm^{-1}.

at 1638 cm^{-1} in the spectrum of P7 electrolyte. In the spectrum of P8 electrolyte, the carboxamide band has shifted back to lower wavenumber of 1636 cm^{-1}.

FTIR spectra for the selected electrolytes in plasticized system in the amine band region are shown in Figure 5.28. The amine band is located at 1526 cm^{-1} in the spectrum of S5 electrolyte. The amine band has shifted to lower wavenumbers of 1525, 1524 and

1523 cm^{-1} in the spectra of P2, P3 and P5 electrolytes. With the addition of plasticizer, more ions interact with the nitrogen donor of chitosan in starch-chitosan blend host.

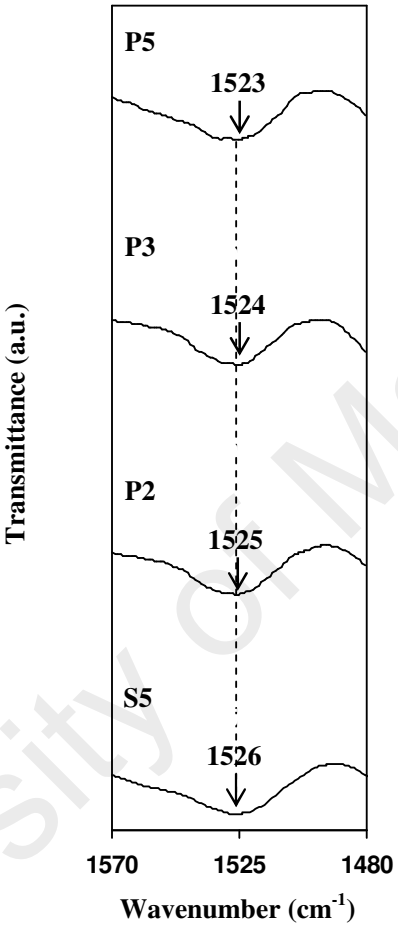

Figure 5.28: FTIR spectra for S5 and selected electrolytes in plasticized system in the region of 1500-1590 cm^{-1}.

In the spectrum of P1 electrolyte in Figure 5.29(a), the peak corresponding to C-O bond stretching of C-O-C group has shifted from 1074 cm^{-1} to 1073 cm^{-1}. As the glycerol content in the electrolyte increases to 10 and 15 wt.%, the peak shifts to lower wavenumbers of 1072 cm^{-1} and 1071 cm^{-1}, respectively. This result indicates that more ions have interacted with oxygen atoms in C-O-C group as glycerol content increases.

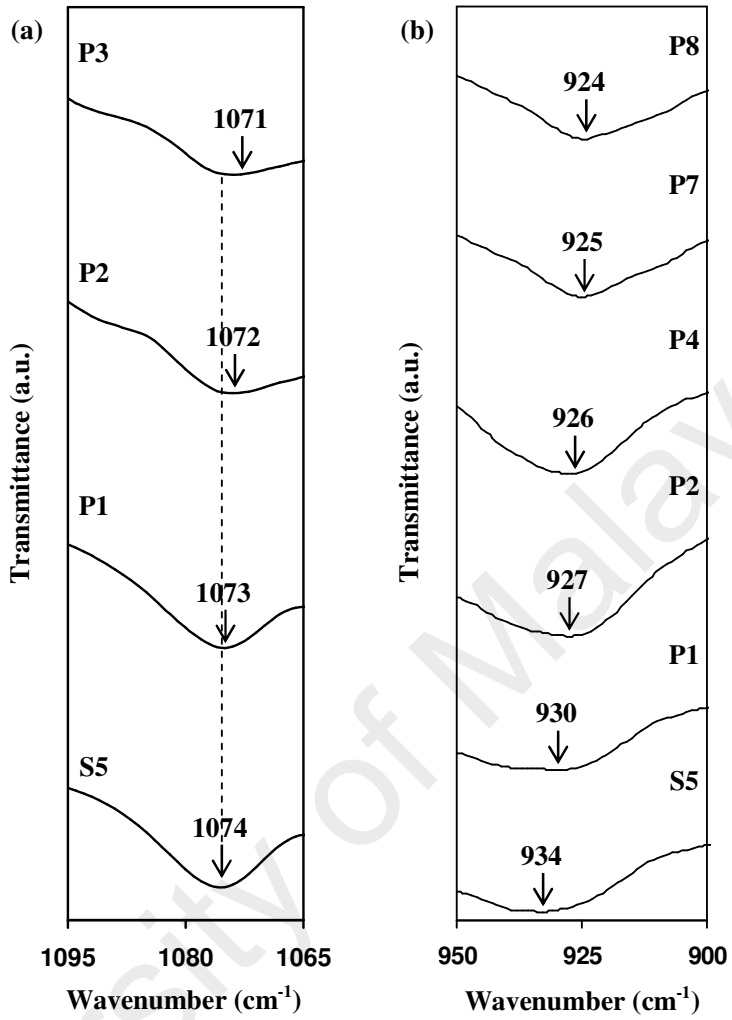

Figure 5.29: FTIR spectra for S5 and selected electrolytes in plasticized system in the region of (a) 1065-1095 cm^{-1} and (b) 900-950 cm^{-1}.

From Figure 5.29(b), the peak corresponding to glycosidic linkage at 934 cm^{-1} in the spectrum of S5 electrolyte is observed to shift to higher wavenumber as glycerol content increases. The present result proves that more NH_4^+ cations from NH_4Cl interact with oxygen atoms in the glycosidic linkages with the addition of glycerol. The proposed interaction between starch-chitosan blend with NH_4Cl, acetic acid solvent and glycerol is illustrated in Figure 5.30.

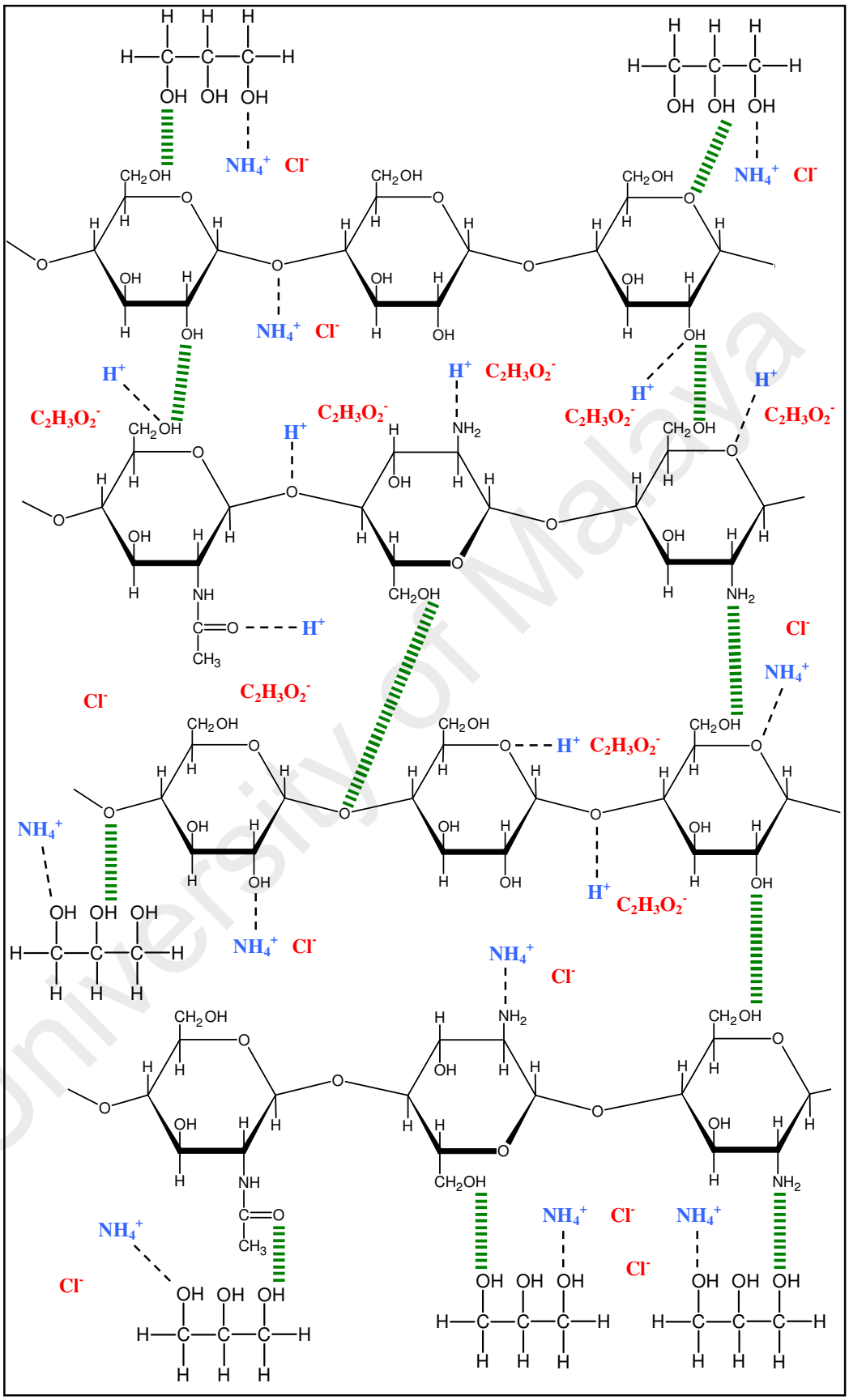

Figure 5.30: Schematic diagram of interaction between starch, chitosan, acetic acid, NH_4Cl and glycerol.

5.9 Summary

From FTIR analysis on starch and chitosan films, starch-acetic acid and chitosan-acetic acid interactions occur at the oxygen atoms of hydroxyl, C-O-C and glycosidic linkages of the polymers. Chitosan-acetic acid interaction also occurs at the carboxamide and amine bands. Upon blending 80 wt.% starch with 20 wt.% chitosan, the shift of the peak at hydroxyl and amine bands as well as the glycosidic linkage of starch proves the involvement of these functional groups in hydrogen bonding formation. When NH_4Cl was added to the starch-chitosan blend, cations are inferred to interact with oxygen atoms of hydroxyl, carboxamide, C-O-C and glycosidic linkage. Nitrogen atom of amine band is also inferred to provide the coordination site for the cations by the shifting of the band to lower wavenumbers on addition of salt. The interaction between glycerol and NH_4Cl is proven by the shifting of the hydroxyl band's peak of glycerol to lower wavenumbers on addition of salt. The shift in peak's position of hydroxyl, carboxamide, amine, C-O-C and glycosidic linkage spectra proves the starch-chitosan-glycerol interaction. From the FTIR analysis on starch-chitosan-NH_4Cl-glycerol, the addition of glycerol has dissociated more salt hence more ions interact with the polymer host. It is also inferred that glycerol is able to provide additional pathways for the ions to conduct.

CHAPTER 6

CONDUCTIVITY AND TRANSPORT ANALYSIS

6.1 Introduction

From chapter 4, the blend of 80 wt.% starch and 20 wt.% chitosan is found to be the most amorphous blend. The blend is chosen to be the polymer host for ionic conduction, where NH_4Cl is used to provide the charge carriers. Thus in this chapter, the conductivity of two polymer electrolyte systems, starch-chitosan-NH_4Cl (salted) and starch-chitosan-NH_4Cl-glycerol (plasticized) will be presented. The variation of room temperature conductivity with NH_4Cl and glycerol concentration will be discussed. The variation of conductivity with temperature will also be presented.

To gain some understanding on the effect of salt and plasticizer content on the conductivity, the Rice and Roth model (as cited in Samsudin et al., 2012) will be employed to determine the transport parameters of the electrolytes, such as number density and mobility of ions. The electrolytes will be further characterized by XRD, SEM and DSC studies. The determination of conducting charge species will be done by ionic transference number measurement. The result of cation transference number will be presented to reveal the contribution of cation to the conductivity.

6.2 Impedance Studies

Figure 6.1(a) and (b) represents the Cole-Cole plots of pure starch-chitosan film (S8C2) and starch-chitosan with 5 wt.% NH_4Cl (S1 electrolyte), respectively, at room temperature. Each Cole-Cole plot shows an incomplete semicircle curve.

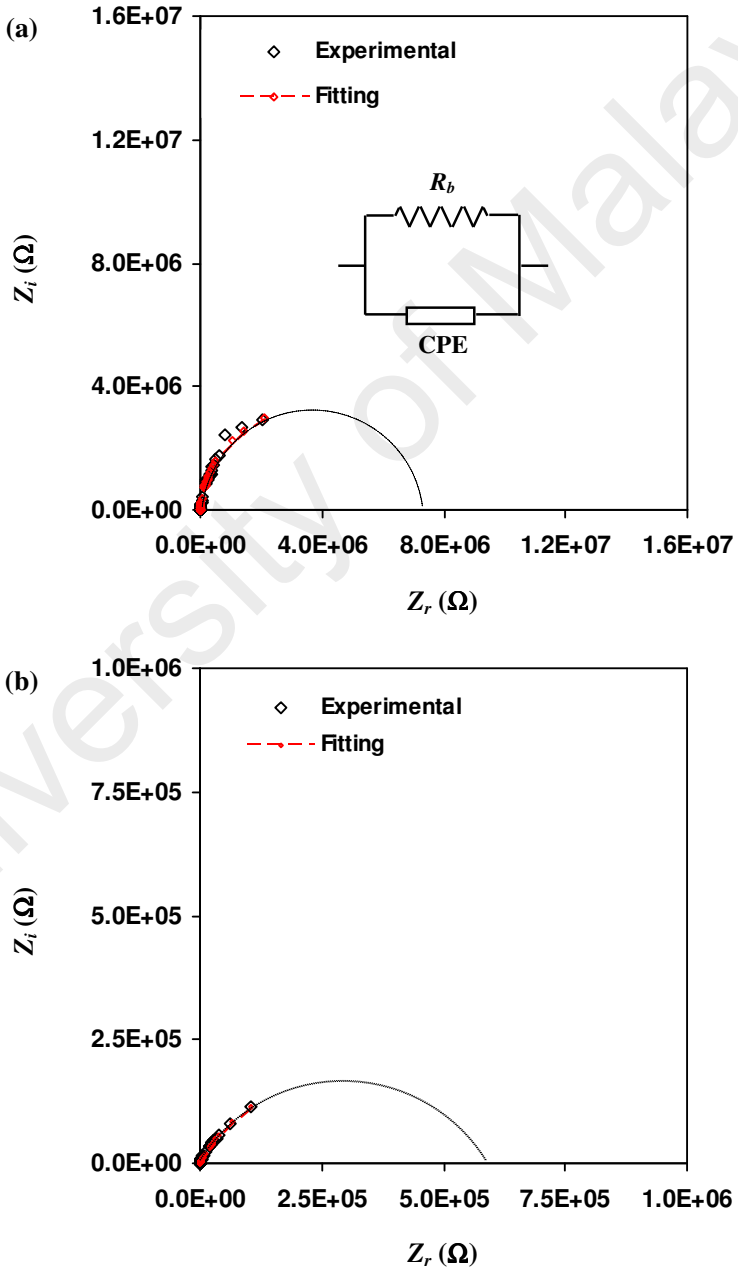

Figure 6.1: Cole-Cole plot of (a) S8C2 film and (b) S1 electrolyte at room temperature. The inset figure shows the corresponding equivalent circuit.

The semicircle part of a Cole-Cole plot is related to ionic conduction in the bulk of the electrolyte (Samsudin et al., 2012). According to Malathi et al. (2010), the bulk conductivity is due to the parallel combination of bulk resistance and bulk capacitance of the polymer electrolytes. In Figure 6.1, the value of bulk resistance (R_b) is determined from the intercept of the semicircle with the real axis.

Figure 6.2 represents the Cole-Cole plot of starch-chitosan with 25 wt.% NH_4Cl (S5 electrolyte) at room temperature. The Cole-Cole plot consists of a semicircular arc at the higher frequency region and a line adjacent to the semicircular arc at the lower frequency region.

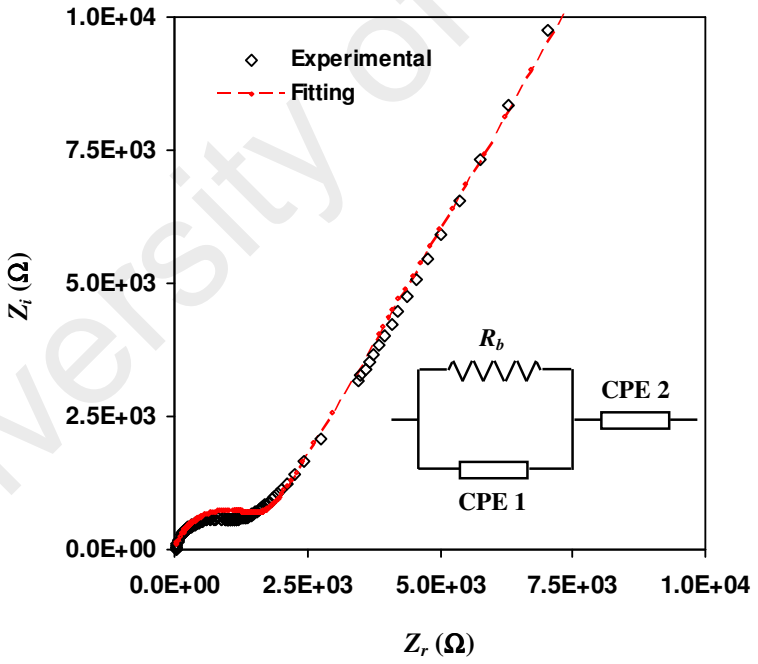

Figure 6.2: Cole-Cole plot of S5 electrolyte at room temperature. The inset figure shows the corresponding equivalent circuit.

In Figure 6.2, the adjacent line to the semicircle is attributed to the effect of electrode polarization which is characteristic of diffusion process (Samsudin et al.,

2012). The adjacent lines to the semicircles inclined at an angle less than 90° with the real axis. This type of impedance plot may be due to roughness of the electrode-electrolyte interface or inhomogeneous distribution of salt in the polymer matrix (Kartha, 2013; Stephan et al., 1999). Since the blocking electrodes have been used in the impedance measurement, the electrode-electrolyte interface could be regarded as a capacitance (Hema et al., 2008). By comparing the Cole-Cole plots in Figures 6.1 and 6.2, it can be observed that the semicircle part is lessening as the salt content increases to 25 wt.%. The value of R_b in Figure 6.2 is determined from the intercept of the semicircle with the adjacent line to the semicircle. The R_b decreases as the salt content increases to 25 wt.% and this may be due to the increase in the number density of mobile charge carriers (Khiar & Arof, 2010; Selvasekarapandian et al., 2005).

Figure 6.3 depicts the Cole-Cole plot of starch-chitosan with 35 wt.% NH_4Cl (S7 electrolyte) at room temperature.

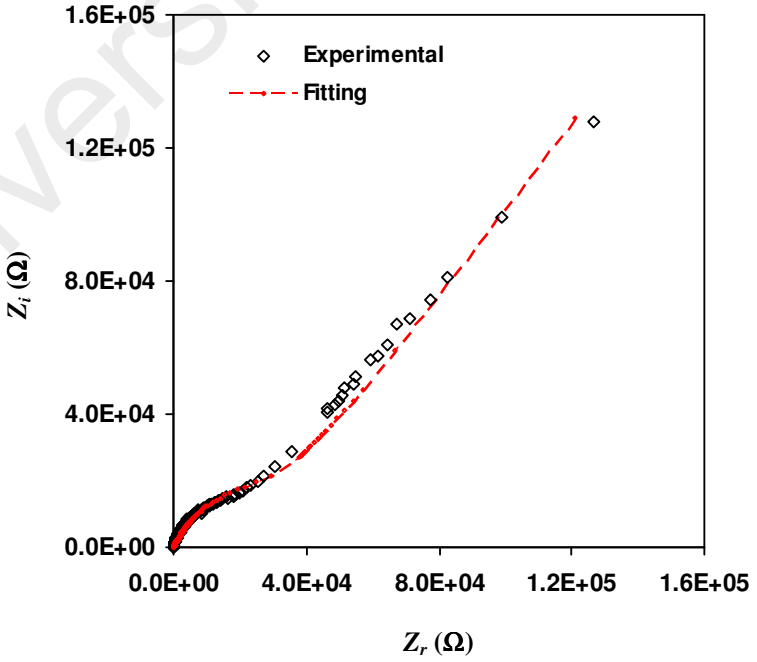

Figure 6.3: Cole-Cole plot of S7 electrolyte at room temperature.

It can be observed that the semicircle part in Figure 6.3 is larger than that in Figure 6.2 inferring that the R_b increases when 35 wt.% NH_4Cl is added to the electrolyte. This phenomenon could be due to the formation of ion aggregates which can impede the ionic conduction thus leading to a decrease in conductivity.

The electrical equivalent circuit representation is commonly used in impedance analysis because it is fast, simple and provides the complete picture of the system (Han & Choi, 1998). The impedance data can be fitted by an idealized equivalent circuit model composed of discrete electrical components by superimposing the best fit of the dispersion data by trial and error (Shuhaimi et al., 2012; Woo, 2013). The fitting of impedance plots can further confirm the values of R_b. In the present work, since the impedance data of S8C2 film and S1 electrolyte consists only the semicircle curve as shown in Figure 6.1, the equivalent circuit (see inset of Figure 6.1(a)) can be represented by a parallel combination of R_b and constant phase element (CPE) (Teo, Buraidah, Nor, & Majid, 2012). In general a CPE is used in a model instead of a capacitor to compensate for inhomogeneity in the system (Qian et al., 2001). The impedance of CPE (Z_{CPE}) can be expressed as (Shuhaimi et al., 2012; Teo et al., 2012):

$$Z_{CPE} = \frac{1}{C\omega^{p}}\left[\cos\left(\frac{\pi p}{2}\right) - i\sin\left(\frac{\pi p}{2}\right)\right] \tag{6.1}$$

where C is the capacitance of CPE, ω is angular frequency and p is related to the deviation of the plot from the axis. The real and imaginary parts of impedance, Z_r and Z_i, respectively, associated to the equivalent circuit can be expressed as:

$$Z_r = \frac{R_b + {R_b}^2 C\omega^p \cos\left(\frac{\pi p}{2}\right)}{1 + 2R_b C\omega^p \cos\left(\frac{\pi p}{2}\right) + {R_b}^2 C^2 \omega^{2p}} \tag{6.2}$$

$$Z_i = \frac{{R_b}^2 C\omega^p \sin\left(\frac{\pi p}{2}\right)}{1 + 2R_b C\omega^p \cos\left(\frac{\pi p}{2}\right) + {R_b}^2 C^2 \omega^{2p}} \tag{6.3}$$

The impedance plot of S5 and S7 electrolytes consists of a semicircle and an inclined adjacent line to the semicircle as shown in Figures 6.2 and 6.3. The equivalent circuit (see inset of Figure 6.2) can be represented by a parallel combination of R_b and CPE with another CPE in series (Teo et al., 2012). The values of Z_r and Z_i associated to the equivalent circuit can be expressed as:

$$Z_r = \frac{R_b + {R_b}^2 C_1 \omega^{p_1} \cos\left(\frac{\pi p_1}{2}\right)}{1 + 2R_b C_1 \omega^{p_1} \cos\left(\frac{\pi p_1}{2}\right) + {R_b}^2 {C_1}^2 \omega^{2p_1}} + \frac{\cos\left(\frac{\pi p_2}{2}\right)}{C_2 \omega^{p_2}} \tag{6.4}$$

$$Z_i = \frac{{R_b}^2 C_1 \omega^{p_1} \sin\left(\frac{\pi p_1}{2}\right)}{1 + 2R_b C_1 \omega^{p_1} \cos\left(\frac{\pi p_1}{2}\right) + {R_b}^2 {C_1}^2 \omega^{2p_1}} + \frac{\sin\left(\frac{\pi p_2}{2}\right)}{C_2 \omega^{p_2}} \tag{6.5}$$

where C_1 is the capacitance at high frequency, C_2 is the capacitance at low frequency, p_1 is the deviation of the radius of the circle from the imaginary axis and p_2 is the deviation of the inclined adjacent line to the semicircle from the real axis. The parameters of the circuit elements for the selected electrolytes in salted system are tabulated in Table 6.1.

Table 6.1: The parameters of the circuit elements for selected electrolytes in salted system at room temperature.

Electrolyte	p_1 (rad)	C_1 (F)	p_2 (rad)	C_2 (F)
S8C2	0.95	3.33×10^{-10}	-	-
S1	0.68	6.67×10^{-8}	-	-
S5	0.86	4.55×10^{-9}	0.67	6.37×10^{-7}
S7	0.82	8.33×10^{-9}	0.58	2.22×10^{-7}

It is observed that the value of capacitance is higher at low frequency than high frequency, which satisfies the following equation:

$$C = \frac{\varepsilon_o \varepsilon_r A_e}{t} \tag{6.6}$$

where ε_o is vacuum permittivity, ε_r is dielectric constant, A_e is electrode-electrolyte contact area and t is thickness of electrolyte. Many reports (Hema et al. 2008; Selvasekarapandian et al., 2005; Teo et al., 2012) have shown that the value of ε_r of a polymer electrolyte decreases with increasing frequency, which in turn decreases the capacitance. The result of ε_r in this work will be discussed in Chapter 7.

Figures 6.4 to 6.7 show the Cole-Cole plots of selected electrolytes in plasticized system at room temperature. Each Cole-Cole plot consists of a tilted line. The disappearance of semicircle at high frequency region in these figures suggests that only the resistive component of the polymer prevails (Hema et al., 2008). In this case, the R_b value is determined by the interception of the line with the real axis. The R_b decreases as

the glycerol content increases to 35 wt.% (P7 electrolyte). The addition of plasticizer promotes the dissociation of salt thus decreases the formation of ion aggregates.

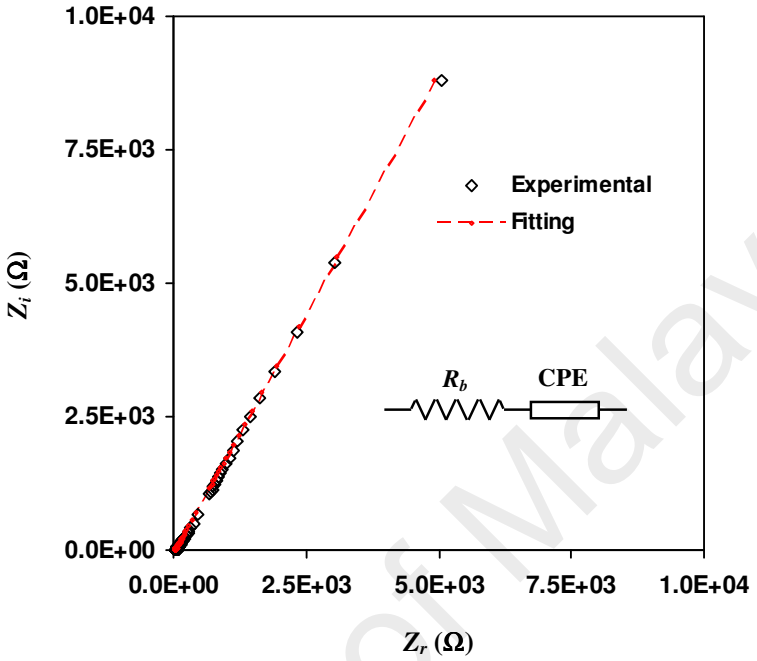

Figure 6.4: Cole-Cole plot of P5 electrolyte at room temperature. The inset figure shows the corresponding equivalent circuit.

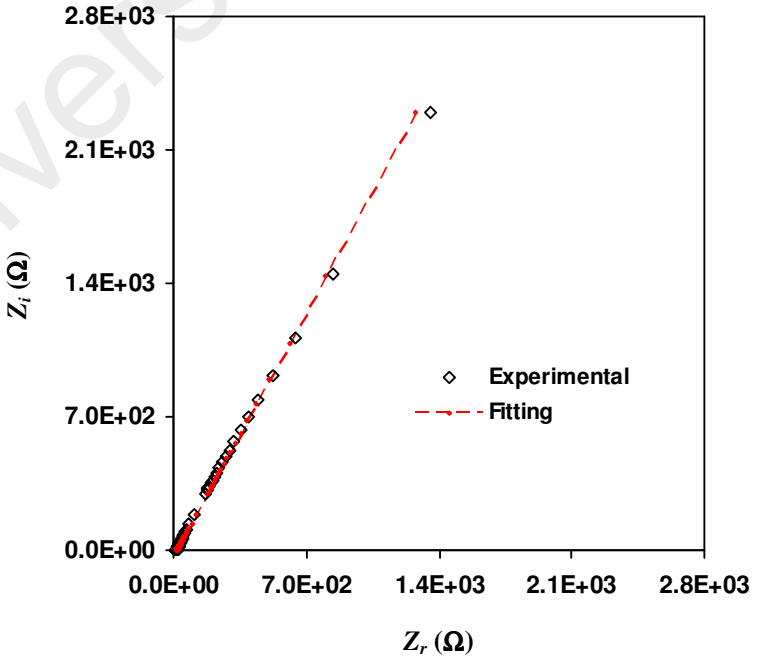

Figure 6.5: Cole-Cole plot of P6 electrolyte at room temperature.

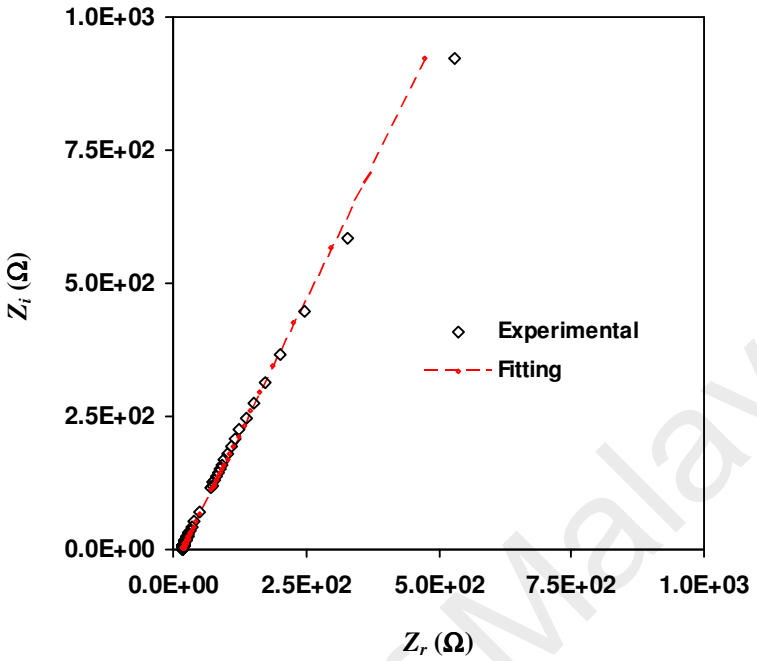

Figure 6.6: Cole-Cole plot of P7 electrolyte at room temperature.

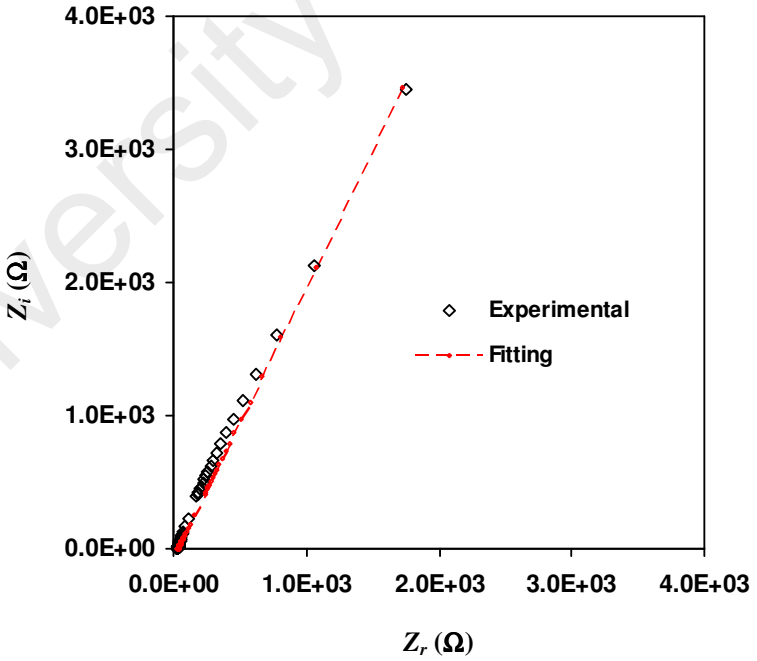

Figure 6.7: Cole-Cole plot of P9 electrolyte at room temperature.

Based on Figures 6.4 to 6.7, the equivalent circuit (see inset of Figure 6.4) for the plasticized electrolytes can be represented by a combination of R_b and CPE in series (Shuhaimi et al., 2012). The values of Z_r and Z_i associated to the equivalent circuit can be expressed as:

$$Z_r = R_b + \frac{\cos\left(\frac{\pi p}{2}\right)}{C\omega^p} \tag{6.7}$$

$$Z_i = \frac{\sin\left(\frac{\pi p}{2}\right)}{C\omega^p} \tag{6.8}$$

The parameters of the circuit elements for the selected electrolytes in plasticized system are tabulated in Table 6.2. It is observed that the value of capacitance for plasticized electrolyte is higher than that of salted electrolyte. Addition of plasticizer increases the number of ion in the electrolyte, which increases the value of ε_r (Shukur, Ithnin, et al., 2013). According to Equation (6.6), increasing ε_r will increase the value of capacitance.

Table 6.2: The parameters of the circuit elements for selected electrolytes in plasticized system at room temperature.

Electrolyte	***p* (rad)**	***C* (F)**
P5	0.68	2.02×10^{-6}
P6	0.68	7.61×10^{-6}
P7	0.71	1.67×10^{-5}
P9	0.71	4.39×10^{-6}

Figures 6.8 to 6.12 depict the Cole-Cole plots at selected temperatures for S5 electrolyte.

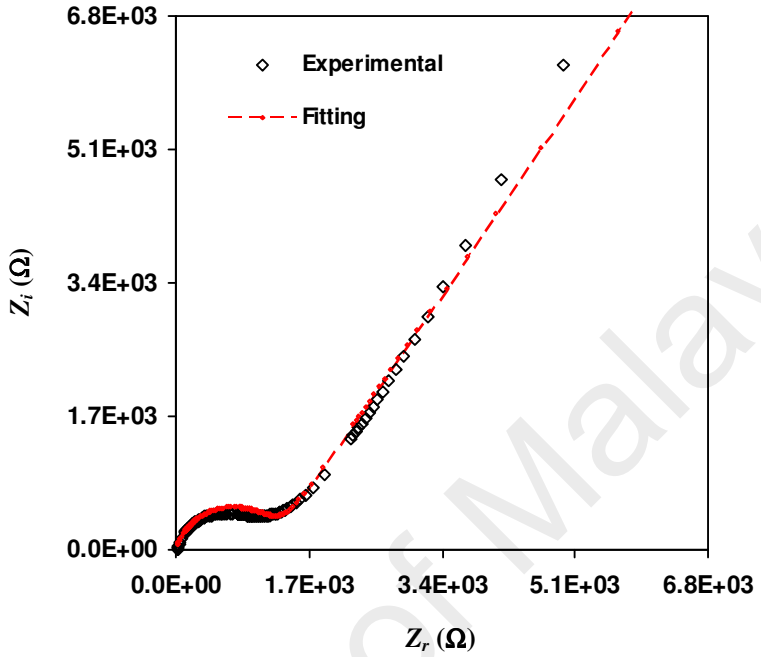

Figure 6.8: Cole-Cole plot of S5 electrolyte at 303 K.

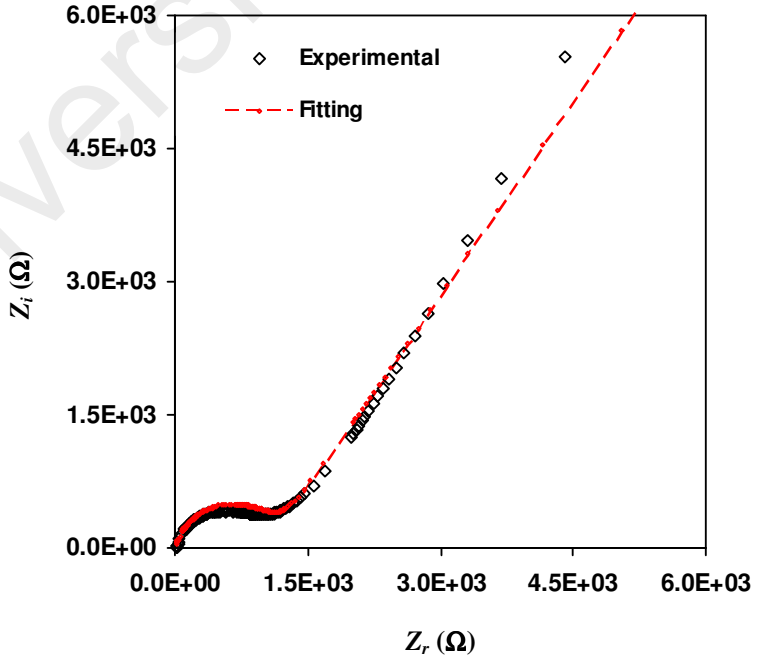

Figure 6.9: Cole-Cole plot of S5 electrolyte at 308 K.

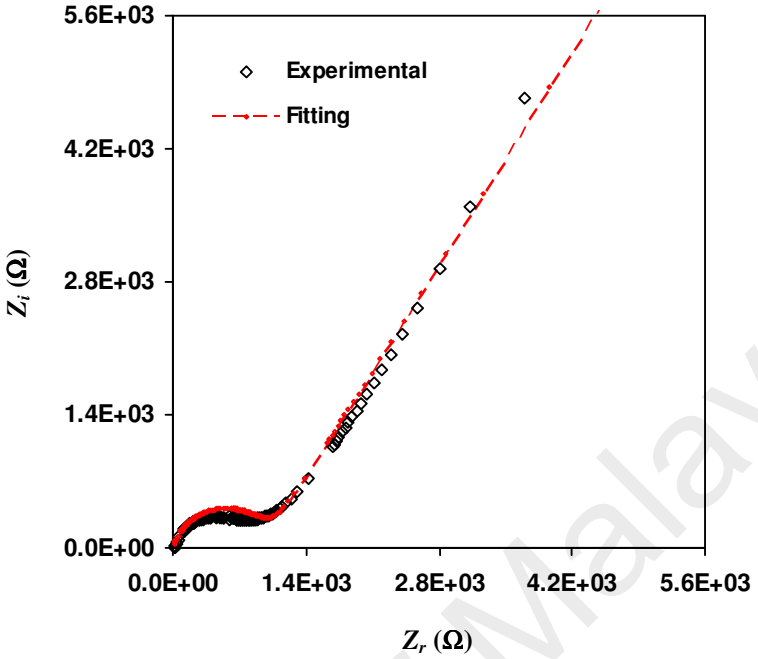

Figure 6.10: Cole-Cole plot of S5 electrolyte at 313 K.

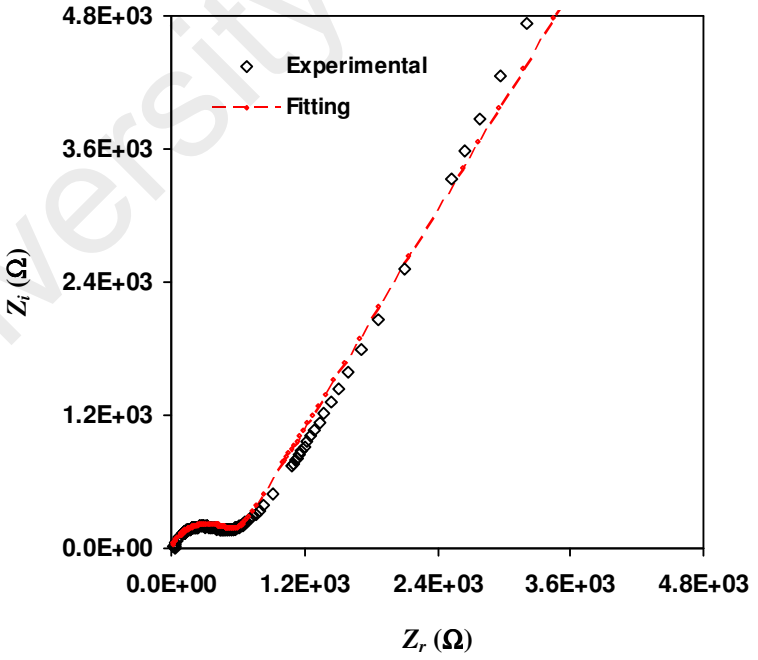

Figure 6.11: Cole-Cole plot of S5 electrolyte at 328 K.

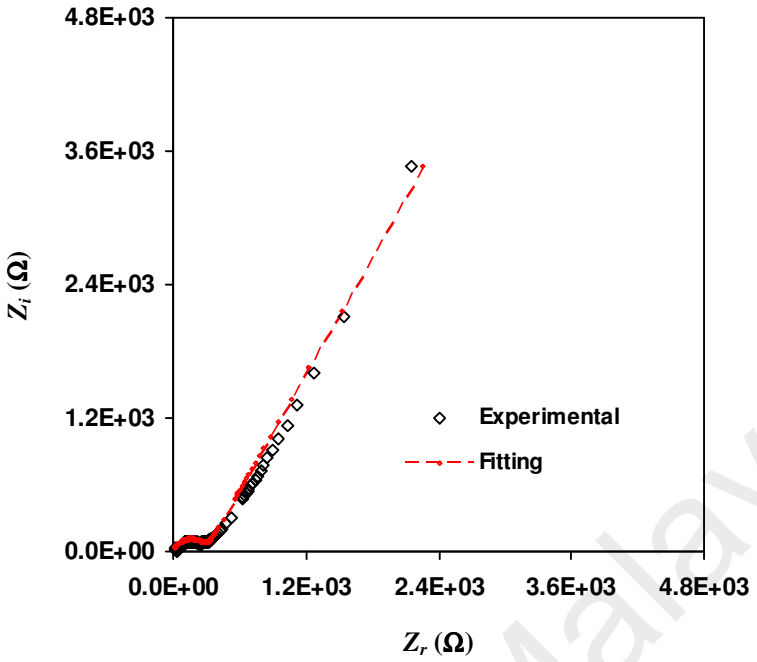

Figure 6.12: Cole-Cole plot of S5 electrolyte at 343 K.

From Figures 6.8 to 6.12, it can be observed that the semicircle part is lessening with increasing temperature. As the temperature increases, the segmental motion of the polymer chain and dissociation of the salt increases resulting in the decrease in R_b value (D.A. Kumar, Selvasekarapandian, Baskaran, Savitha, & Nithya, 2012). The equivalent circuit for S5 electrolyte at different temperatures is represented by a parallel combination of R_b and CPE with another CPE in series. The values of Z_r and Z_i associated to the equivalent circuit at various temperatures were calculated using Equations (6.4) and (6.5). The parameters of the circuit elements for S5 electrolyte at various temperatures are tabulated in Table 6.3.

Table 6.3: The parameters of the circuit elements for S5 electrolyte at various temperatures.

T (K)	p_1 (rad)	C_1 (F)	p_2 (rad)	C_2 (F)
298	0.86	4.55×10^{-9}	0.67	6.37×10^{-7}
303	0.85	7.41×10^{-9}	0.62	2.29×10^{-6}

Table 6.3, continued

308	0.85	7.69×10^{-9}	0.62	2.63×10^{-6}
313	0.84	1.11×10^{-8}	0.65	2.74×10^{-6}
318	0.79	2.50×10^{-8}	0.65	2.99×10^{-6}
323	0.79	2.78×10^{-8}	0.66	3.12×10^{-6}
328	0.79	2.94×10^{-8}	0.67	3.70×10^{-6}
333	0.78	3.13×10^{-8}	0.66	4.01×10^{-6}
338	0.76	3.25×10^{-8}	0.66	4.85×10^{-6}
343	0.78	3.33×10^{-8}	0.67	5.30×10^{-6}

Figures 6.13 to 6.16 depict the Cole-Cole plots at selected temperatures for P7 electrolyte. The R_b decreases with increasing temperature.

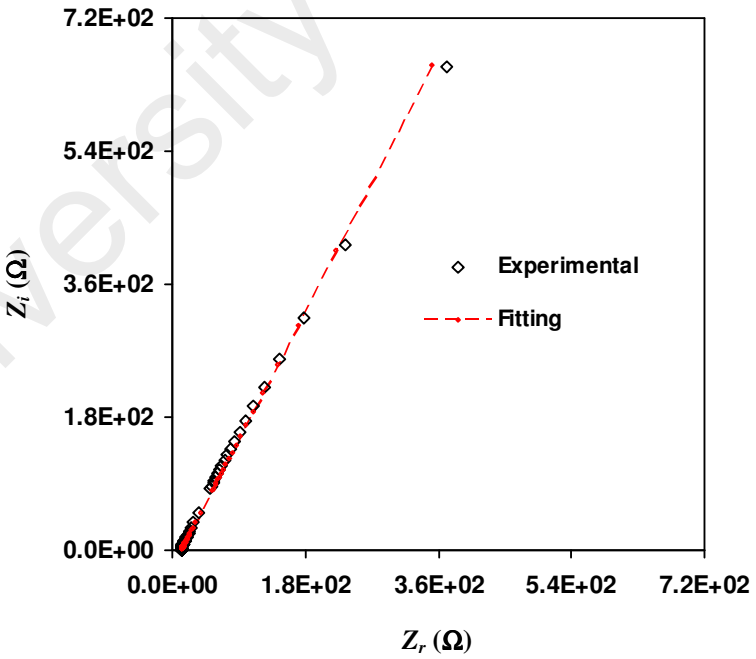

Figure 6.13: Cole-Cole plot of P7 electrolyte at 313 K.

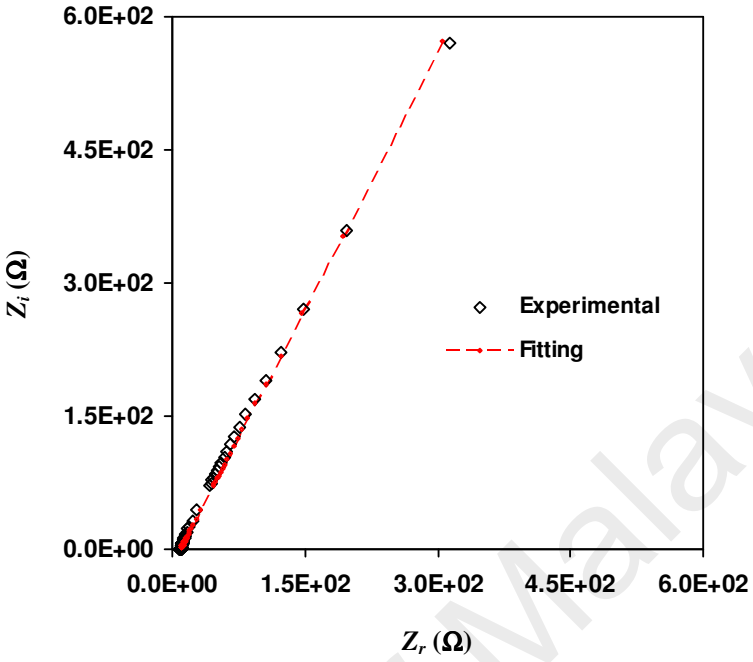

Figure 6.14: Cole-Cole plot of P7 electrolyte at 323 K.

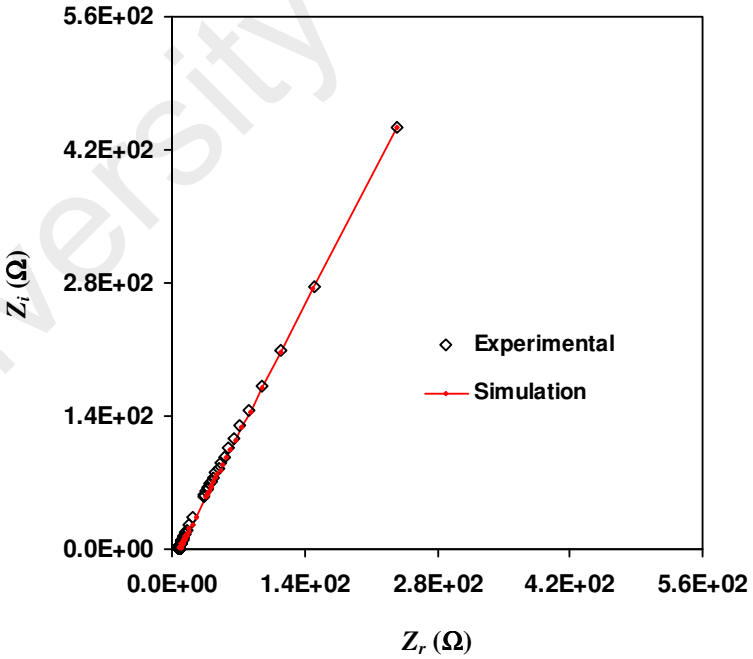

Figure 6.15: Cole-Cole plot of P7 electrolyte at 333 K.

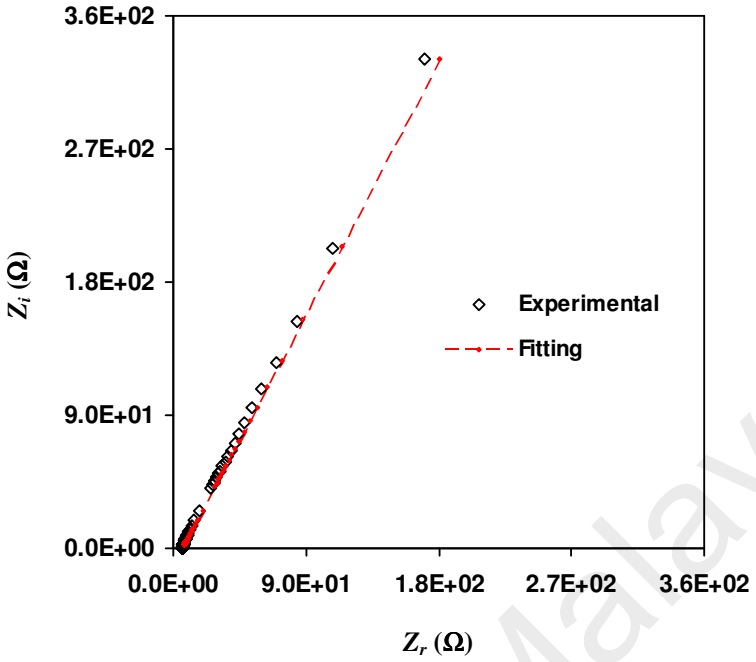

Figure 6.16: Cole-Cole plot of P7 electrolyte at 343 K.

The equivalent circuit for P7 electrolyte at different temperatures is represented by a combination of R_b and CPE in series. The Z_r and Z_i associated to the equivalent circuit were calculated using Equations (6.7) and (6.8). The parameters of the circuit elements for P7 electrolyte at various temperatures are tabulated in Table 6.4. From Tables 6.3 and 6.4, the values of capacitance are observed to increase with increasing temperature. The CPE represents the electrode-electrolyte interfaces as well as the polymer chains. Capacitance indicates the CPE's ability to store charges/ions. As the temperature increases, thermal movement of polymer chain segments and the dissociation of salts have be improved (Khiar & Arof, 2010). These phenomena increase the number density of ions, or in other words, more ions are stored by the CPE thus enhances the capacitance.

Table 6.4: The parameters of the circuit elements for P7 electrolyte at various temperatures.

***T* (K)**	***p* (rad)**	***C* (F)**
298	0.71	1.67×10^{-5}
303	0.69	2.06×10^{-5}
308	0.68	2.44×10^{-5}
313	0.70	2.48×10^{-5}
318	0.69	2.68×10^{-5}
323	0.70	2.83×10^{-5}
328	0.70	3.19×10^{-5}
333	0.70	3.65×10^{-5}
338	0.70	4.21×10^{-5}
343	0.69	5.03×10^{-5}

6.3 Room Temperature Conductivity

The dependence of conductivity on salt content at room temperature is shown in Figure 6.17.

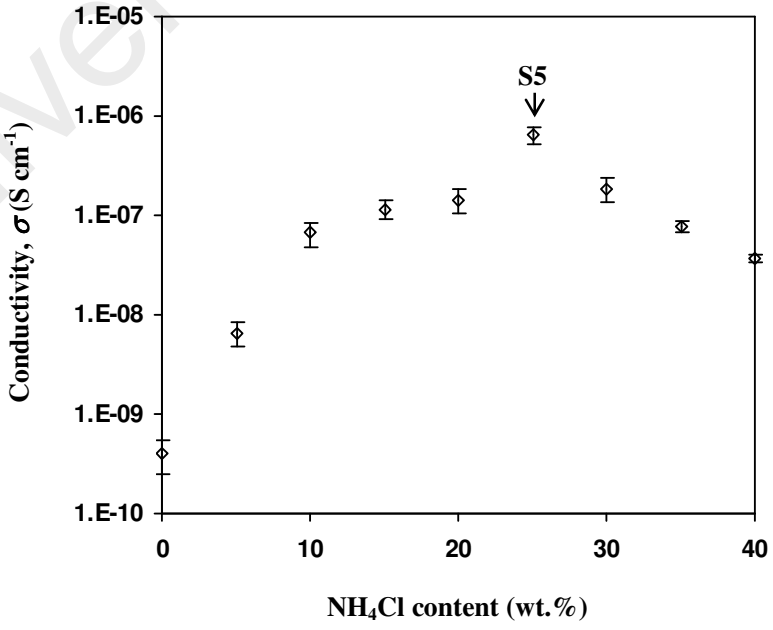

Figure 6.17: Room temperature conductivity as a function of NH_4Cl content.

From Figure 6.17, it is observed that the conductivity of pure starch-chitosan (S8C2) film is $(4.00 \pm 1.53) \times 10^{-10}$ S cm^{-1}. The incorporation of 5 wt.% NH_4Cl increases the conductivity to $(6.51 \pm 1.80) \times 10^{-9}$ S cm^{-1}. As NH_4Cl content increases, the conductivity increases and is optimized at $(6.47 \pm 1.30) \times 10^{-7}$ S cm^{-1} on addition of 25 wt.% NH_4Cl (i.e. S5 electrolyte). The increase in conductivity can be attributed to the increase in the number of mobile ions (Khiar & Arof, 2010). On addition of 30 wt.% NH_4Cl, the conductivity decreases to $(1.85 \pm 0.51) \times 10^{-7}$ S cm^{-1} and further decreases with addition of 35 and 40 wt.% NH_4Cl. At higher NH_4Cl content, the distance between dissociated ions become closer that they are able to recombine and form neutral ion pairs, thus decreases the number density of mobile ions leading to a drop in conductivity (Kadir et al., 2010).

The dependence of conductivity on glycerol content at room temperature is shown in Figure 6.18.

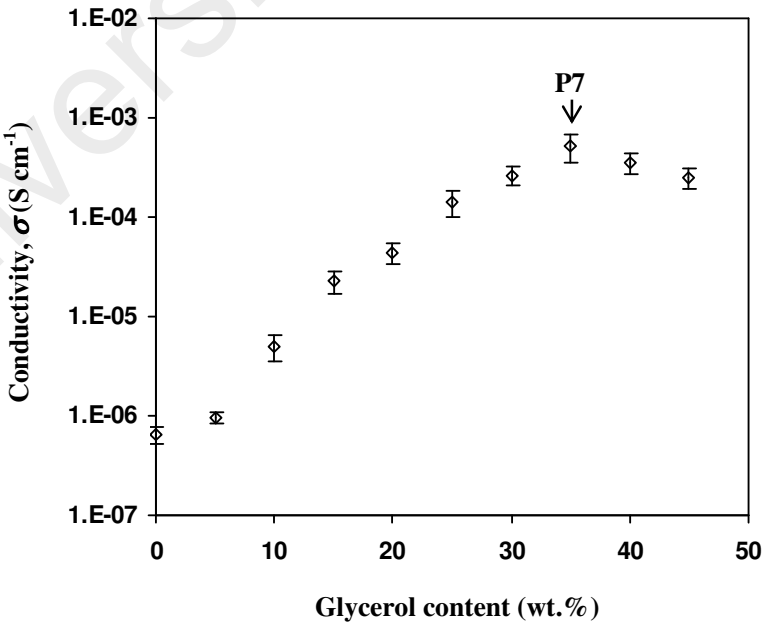

Figure 6.18: Room temperature conductivity as a function of glycerol content.

The addition of a plasticizer promotes the dissociation of excess salt into ions and generates separate conducting pathways for the migration of free ions, which should results an increase in conductivity (Gondaliya, Kanchan, & Sharma, 2013). Besides, plasticizer molecules being relatively small in size compared to polymer molecules penetrate the polymer matrix and establish attractive forces/reduce the cohesive forces between the polymer chains and increase the segmental mobility, which enhances the conductivity of polymer electrolyte (Sekhar, Kumar, & Sharma, 2012b). In the present work, the highest conductivity value of $(5.11 \pm 1.60) \times 10^{-4}$ S cm^{-1} is obtained with addition of 35 wt.% glycerol (i.e. P7 electrolyte) as shown in Figure 6.18. The conductivity decreases on addition of more than 35 wt.% glycerol. The decrease in conductivity may be caused by the displacement of the host polymer by plasticizer molecules within the salt complexes (Ibrahim & Johan, 2012). The formation of linkages between the plasticizer causes the salt to recrystallize, resulting in a conductivity decrement (Johan & Ting, 2011).

6.3.1 XRD Analysis

Figure 6.19 shows the XRD patterns of NH_4Cl salt and selected electrolytes in the salted system. In the XRD pattern of NH_4Cl, crystalline peaks appear at $2\theta = 23.1°$, 32.5°, 40.4°, 47.0°, 52.7°, 58.2°, 68.3°, 73.2° and 77.9°, showing the crystalline nature of the salt. Addition of salt into the starch-chitosan blend host produces a peak superimposed on the broad peak of the XRD patterns of S1, S2 and S5. This phenomenon suggests the coexistence of the amorphous and some crystalline phases (Suryanarayana, 2004). Based on the peak position, it can be indicated that the peak is attributed to the NH_4Cl salt. This result implies the inability of the polymer host to

accommodate all the salt during the film formation (Noor, Careem, Majid, & Arof, 2011).

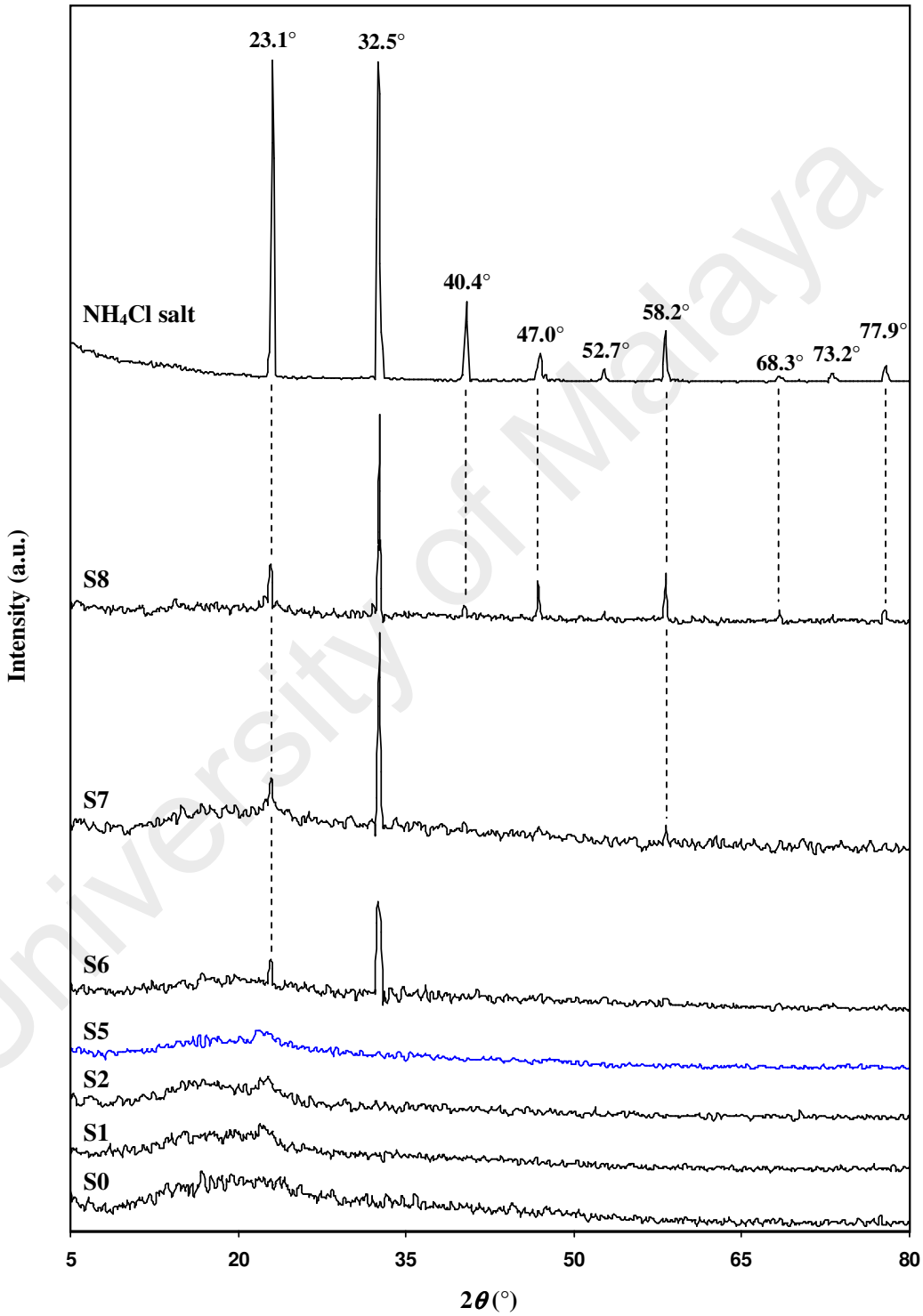

Figure 6.19: XRD patterns of selected electrolytes in salted system.

The incorporation of salt to the polymer host is expected to increase the amorphousness of the electrolyte. In order to determine the degree of crystallinity of the electrolytes, again, two methods have been used to calculate the amorphous and crystalline areas of the XRD patterns. Table 6.5 shows the estimated degree of crystallinity using Nara-Komiya method (as cited in Noor et al., 2013) where S5 electrolyte has the least degree of crystallinity.

Table 6.5: Degree of crystallinity of selected electrolytes in salted system using Nara-Komiya method.

Sample	χ (%)
S8C2	26.31
S1	25.77
S2	23.98
S5	19.30

As shown in Figure 6.17, the room temperature conductivity was optimized with addition of 25 wt.% NH_4Cl, i.e. S5 electrolyte. As ion concentration in the electrolyte increases, both the fraction of amorphous phase and charge carriers increase simultaneously (Aji, Masturi, Bijaksana, Khairurrijal, & Abdullah, 2012). Ions are generally mobile in the amorphous region since their motion is assisted by polymer segmental motion (Gadjourova et al., 2001; Noor et al., 2013; Subbu, Mathew, Kesavan, & Rajendran, 2014). This XRD result has given some answers for the increasing conductivity with increasing NH_4Cl content up to 25 wt.%. The room temperature conductivity decreases with addition of more than 25 wt.% NH_4Cl. In the XRD pattern of S6 electrolyte, the intensity of the crystalline peak at 2θ = 22.9° increases and another crystalline peak appear at 2θ = 32.5°. In the X-ray diffractograms

of S7 and S8 electrolytes, the intensity of these crystalline peaks increases accompanied by the appearance of another crystalline peaks. This result indicates the recrystallization of salt leading to the decrease in number density of ions, hence decreases the conductivity.

Figures 6.20 to 6.22 depict the deconvolution of XRD patterns for selected electrolytes in salted system.

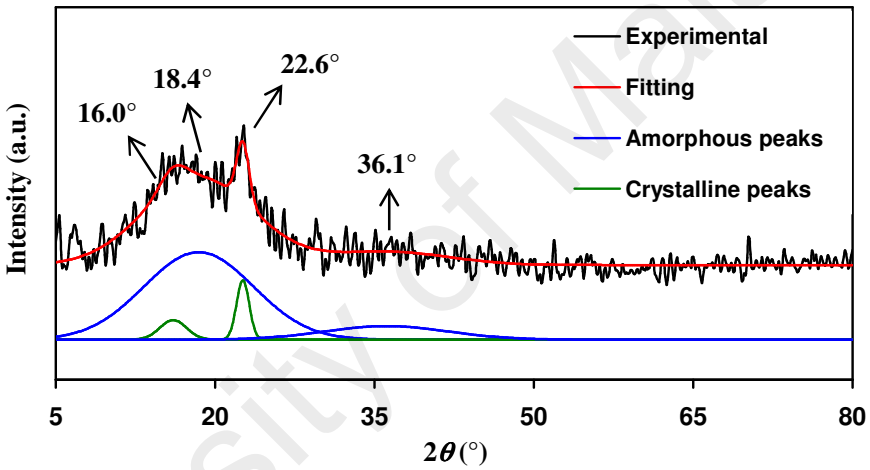

Figure 6.20: Deconvoluted XRD pattern of S2 electrolyte.

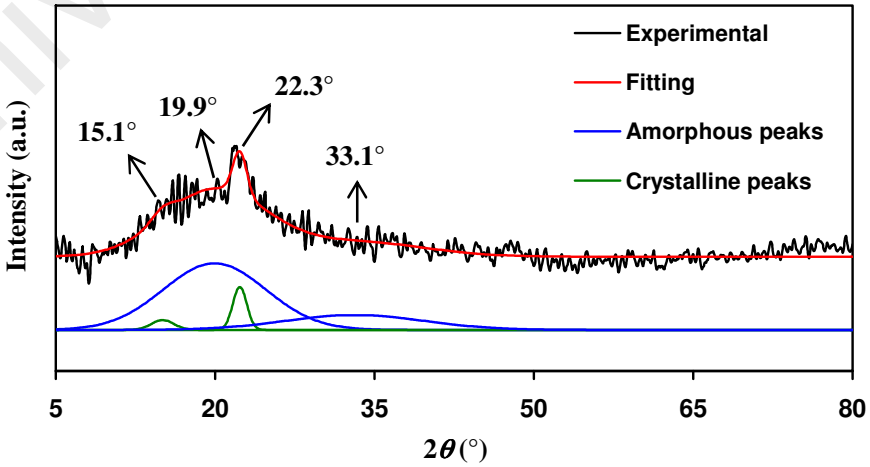

Figure 6.21: Deconvoluted XRD pattern of S5 electrolyte.

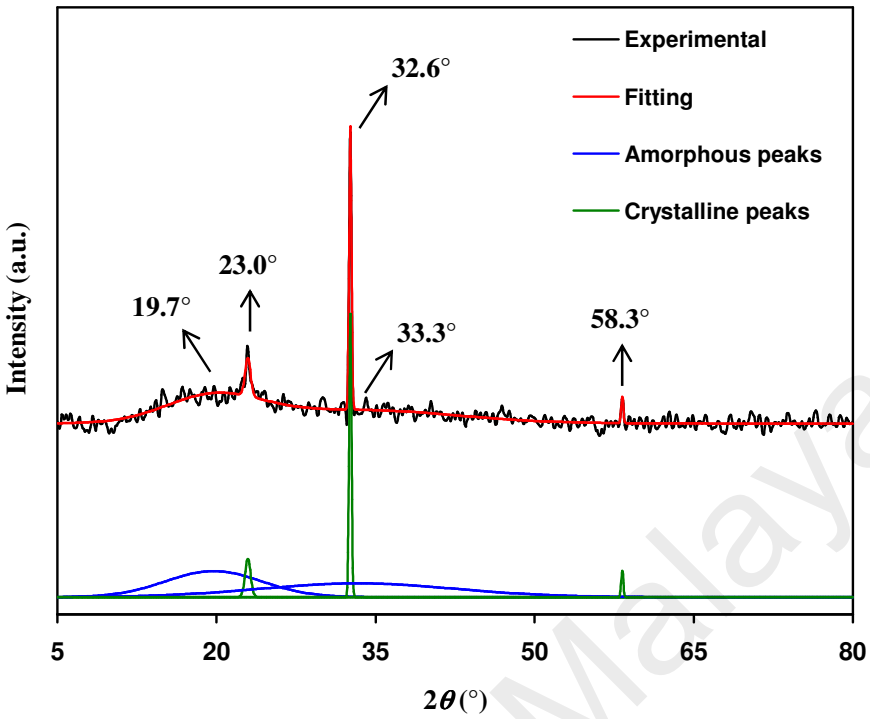

Figure 6.22: Deconvoluted XRD pattern of S7 electrolyte.

From Figure 6.20, the XRD pattern of S2 electrolyte consists of two broad amorphous peaks centered at 2θ = 18.4° and 36.1° and two crystalline peaks at 2θ = 16.0° and 22.6°. These peaks are observed in the XRD pattern of S5 electrolyte in Figure 6.21. However, the degree of crystallinity of S5 electrolyte is lower than that of S2 electrolyte as listed in Table 6.6, which is in good agreement with the conductivity result in Figure 6.17. According to Woo (2013), the decrease in the degree of crystallinity with increasing salt content can be correlated to the formation of complexation between the polymer host and cations. This phenomenon has been discussed in Chapter 5. From Figure 6.22, the crystalline peak which appears at 2θ = 16.0° and 15.1° in the XRD patterns of S2 and S5 electrolytes, respectively, is not appear. However, there are appearance of two crystalline peaks at 32.6 and 58.3, where the former is highly intense. This result leads to the increase in the degree of crystallinity as shown in Table 6.6.

Table 6.6: Degree of crystallinity of selected electrolytes in salted system using deconvolution method.

Sample	χ (%)
S8C2	12.05
S1	11.11
S2	10.19
S5	8.45
S6	14.54
S7	15.43

Figure 6.23 depicts the XRD patterns of selected electrolytes in plasticized system.

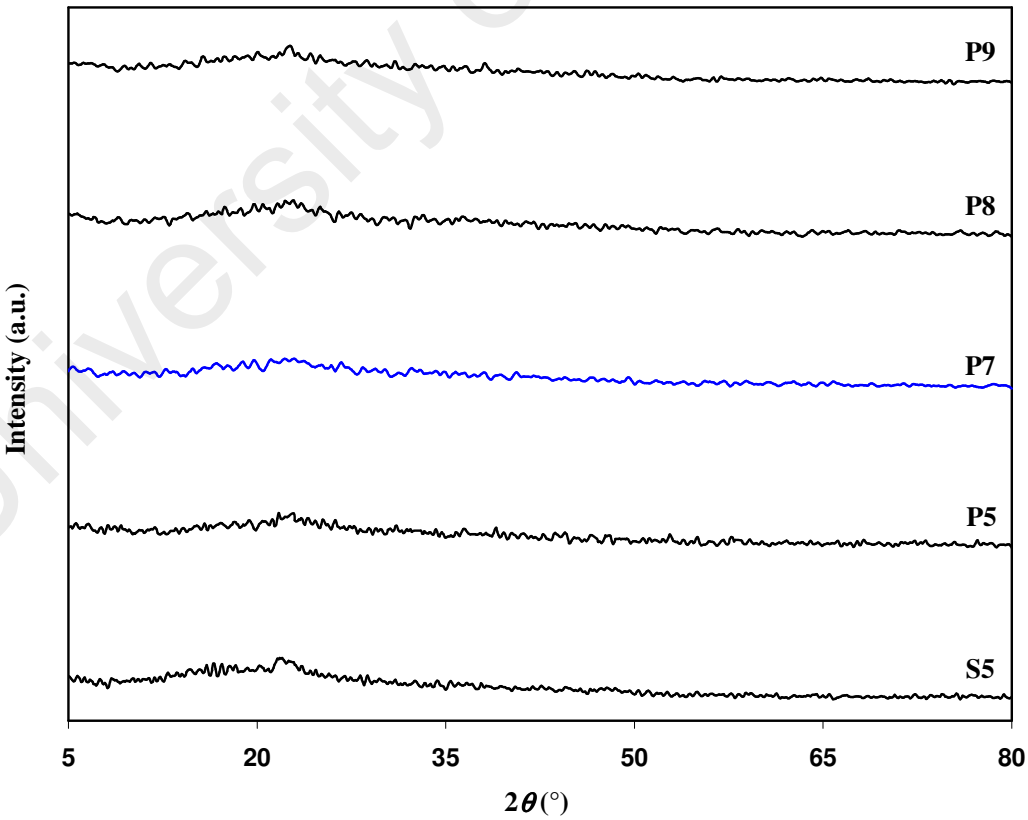

Figure 6.23: XRD patterns of selected electrolytes in plasticized system.

From Figure 6.23, in the XRD pattern of P5 electrolyte, the intensity of the crystalline peak at $2\theta = 22.9°$ decreases and the degree of crystallinity (estimated using Nara-Komiya method) of P6 electrolyte is lower than that of S5 electrolyte as shown in Table 6.7. In the XRD pattern of P7 electrolyte, the peak at $2\theta = 22.9°$ disappears and this electrolyte is more amorphous than P5 electrolyte. This result shows that the presence of glycerol in the electrolyte assists salt dissociation which in turn decreases the occurrence of salt recrystallization. Besides, the plasticizer has created alternative pathways for ion conduction, thus helping the polymer host to accommodate the salt. These phenomena increase the amorphousness of the electrolytes. From Figure 6.18, the conductivity is maximized with addition of 35 wt.% glycerol, i.e. P7 electrolyte. Thus, it can be concluded that the increase in amorphousness leads to the increase in conductivity (Pitawala, Dissanayake, Seneviratne, Mellander, & Albinson, 2008). In the XRD patterns of P8 and P9 electrolytes, the peak at $2\theta = 22.9°$ reappears. The degree of crystallinity values of P8 and P9 electrolytes are found to be higher than that of P7 electrolyte, inferring that P8 and P9 electrolytes are less amorphous than P7 electrolyte which decreases the conductivity.

Table 6.7: Degree of crystallinity of selected electrolytes in plasticized system using Nara-Komiya method.

Sample	χ (%)
P5	17.50
P7	11.52
P8	12.34
P9	14.40

Figures 6.24 to 6.27 depict the deconvolution of XRD patterns for selected electrolytes in plasticized system.

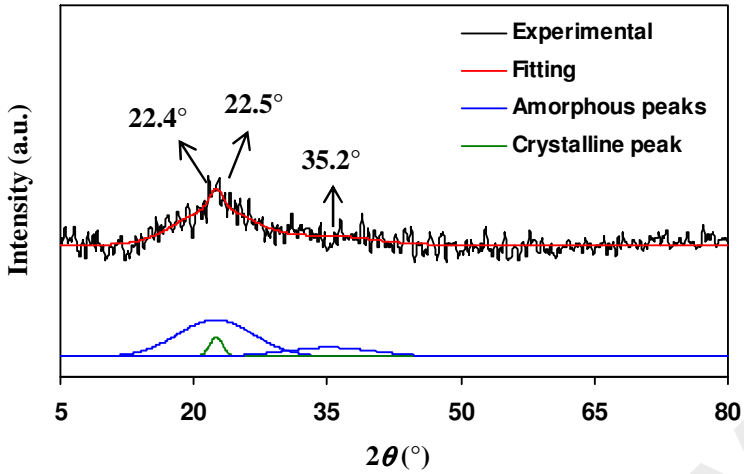

Figure 6.24: Deconvoluted XRD pattern of P5 electrolyte.

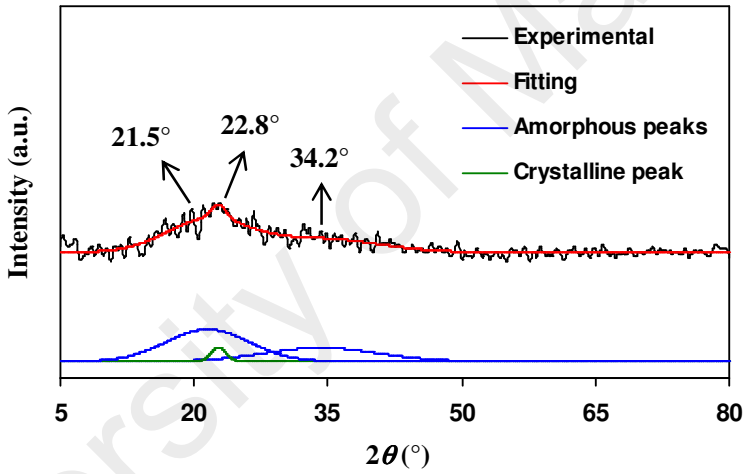

Figure 6.25: Deconvoluted XRD pattern of P7 electrolyte.

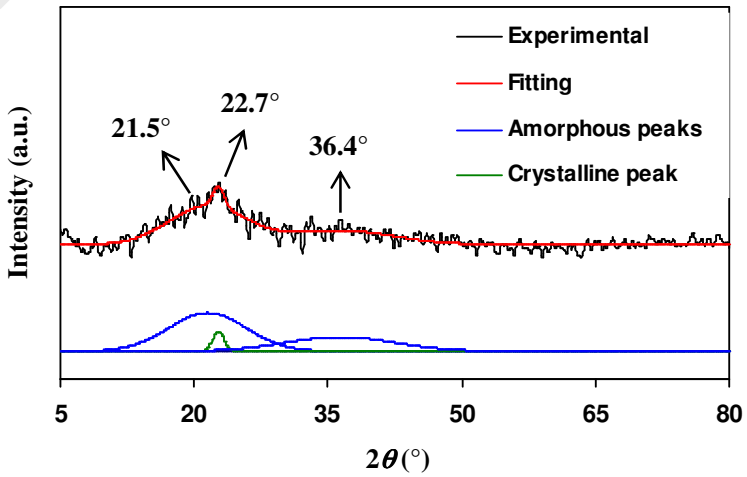

Figure 6.26: Deconvoluted XRD pattern of P8 electrolyte.

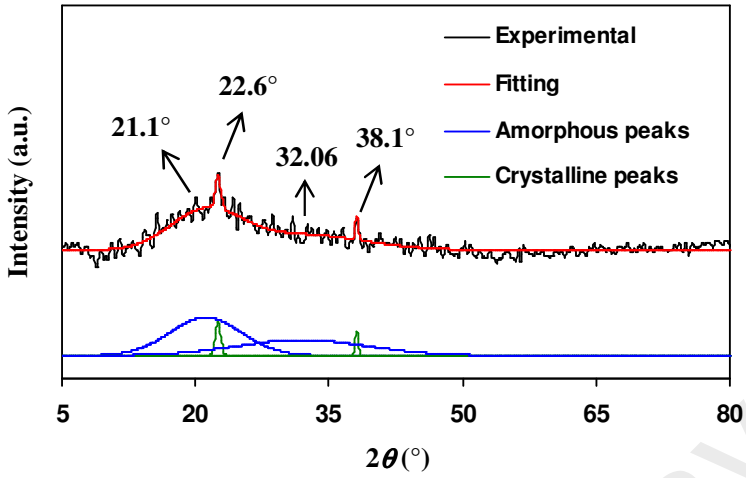

Figure 6.27: Deconvoluted XRD pattern of P9 electrolyte.

From Figure 6.24, a crystalline peak at 2θ = 22.5° superimposed on a broad amorphous peak centered at 2θ = 22.4° in the XRD pattern of P5 electrolyte is detected. This crystalline peak can be observed in the XRD pattern of P7 electrolyte in Figure 6.25. Due to its low intensity, this crystalline peak is hardly observed in the experimental data. The XRD pattern of P9 electrolyte contains two sharp crystalline peaks at 2θ = 22.6° and 38.1°, indicating the recrystallization of salt which leads towards conductivity decrement as shown in Figure 6.18. Table 6.8 lists the estimated degree of crystallinity of selected electrolytes in plasticized system using deconvolution method. The result is in good agreement with conductivity result.

Table 6.8: Degree of crystallinity of selected electrolytes in plasticized system using deconvolution method.

Sample	χ (%)
P5	6.46
P7	4.59
P8	4.69
P9	4.94

6.3.2 SEM Analysis

Figure 6.28 depicts the SEM micrograph of the surface of S8C2 film. The surface of S8C2 film is observed to be smooth and homogenous without any phase separation. This type of surface is the same as shown in Figure 4.15.

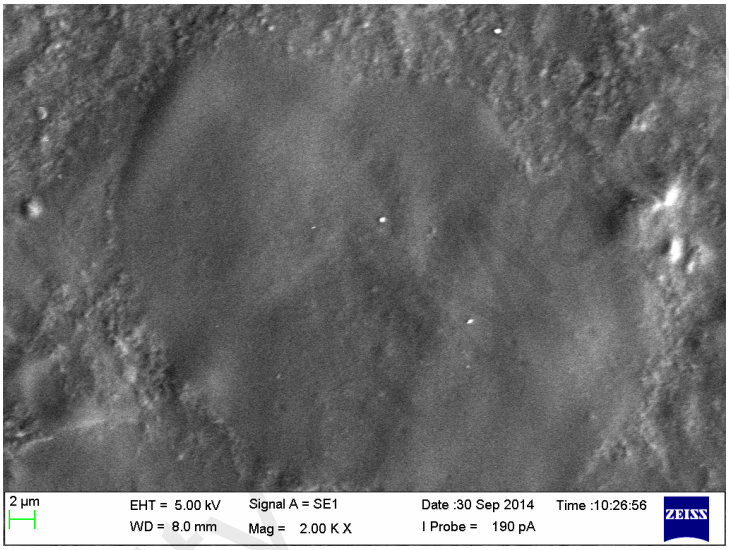

Figure 6.28: Surface micrograph of S8C2 film.

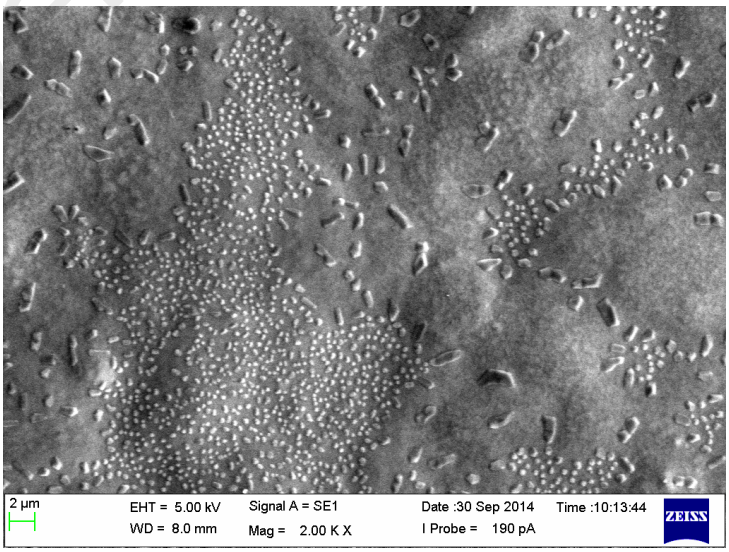

Figure 6.29: Surface micrograph of S4 electrolyte.

When 20 wt.% of NH_4Cl is added to the polymer host, several particles are observed on the electrolyte surface as shown in micrograph of S4 electrolyte in Figure 6.29. These particles act as the channels for ion conduction through the electrolyte (Bhad & Sangawar, 2013). The same observations on other polymer electrolyte systems have been reported in the literature (Ahmad, Rahman, Low, & Su'ait, 2010; Bhad & Sangawar, 2013).

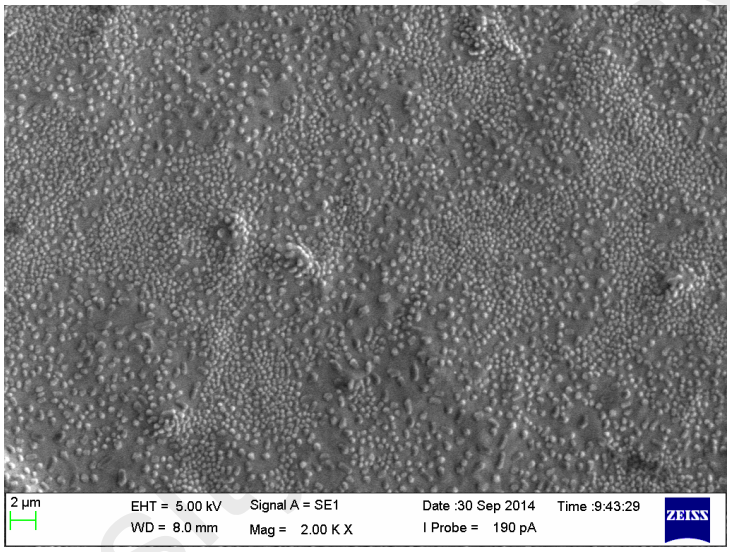

Figure 6.30: Surface micrograph of S5 electrolyte.

Figure 6.30 depicts the SEM micrograph of the surface of S5 electrolyte. More particles are observed on the surface of S5 electrolyte indicating more channels are available for ionic conduction which can lead to the increase in number density of ions. This SEM result further strengthens our conductivity result where S5 electrolyte is the highest conducting electrolyte in the salted system.

In micrograph of S8 electrolyte in Figure 6.31, even more particles are observed but some of the particles agglomerate. The agglomeration of these particles may lead

towards ion pairs formation, which do not contribute to ionic conduction. This phenomenon decreases the conductivity.

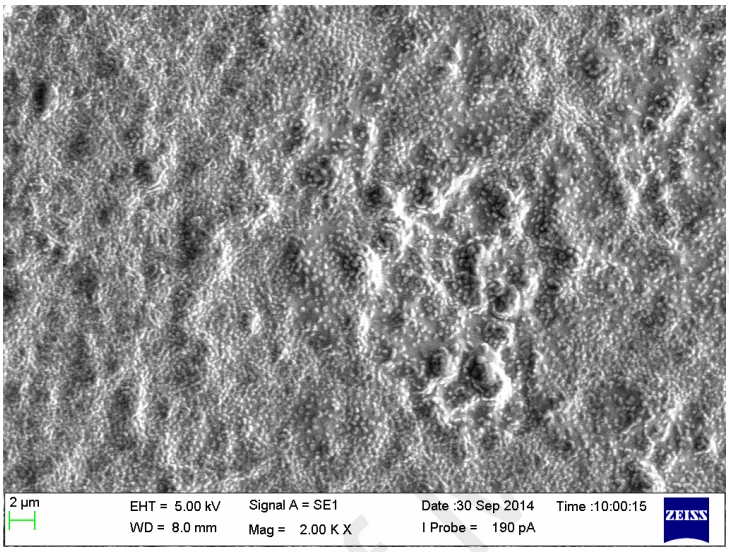

Figure 6.31: Surface micrograph of S8 electrolyte.

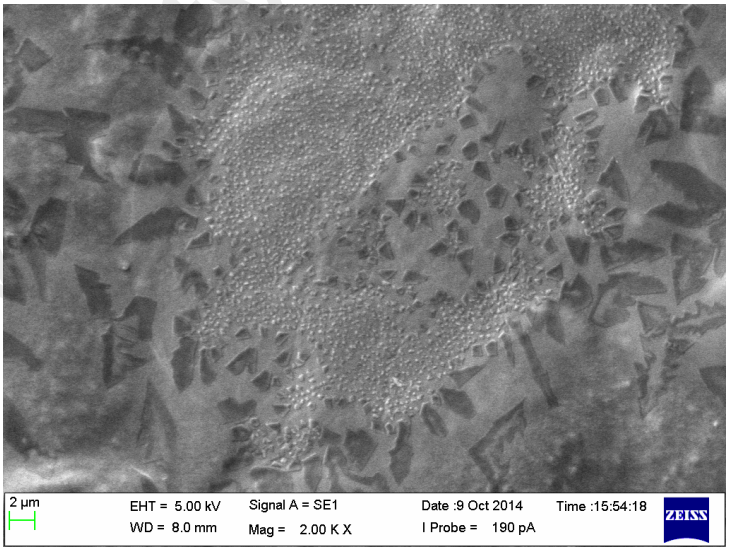

Figure 6.32: Surface micrograph of P2 electrolyte.

From Figure 6.18, the addition of glycerol has enhanced the conductivity. The addition of plasticizer would alter the morphology of the electrolyte. The SEM

micrograph of the surface of P2 electrolyte is depicted in Figure 6.32. It can be seen that the addition of 10 wt.% glycerol reduces the number of particle whereas the dark areas start to appear. Reports elsewhere suggest that the dark region in surface micrograph represents the amorphous phase of the electrolyte (Ahmad et al., 2010; Su'ait, Ahmad, Hamzah, & Rahman, 2011). Thus, it can be inferred that the addition of glycerol increases the amorphous phase of the electrolyte.

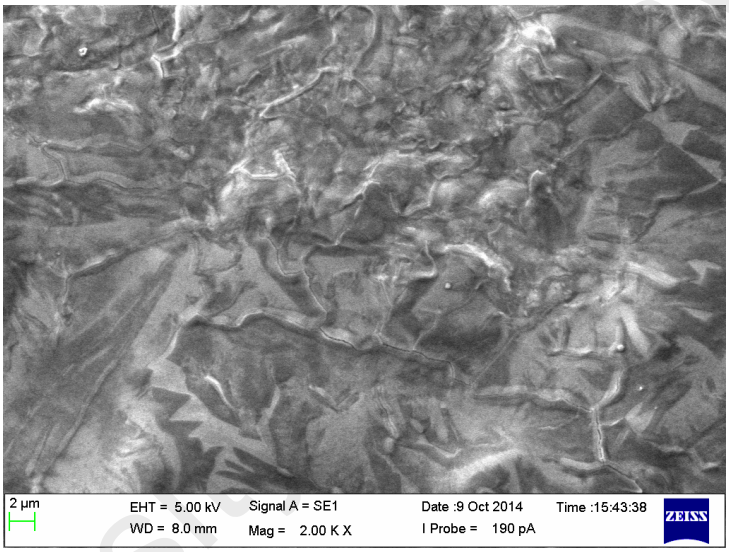

Figure 6.33: Surface micrograph of P4 electrolyte.

Figure 6.33 depicts the SEM micrograph of the surface of P4 electrolyte. The dark region starts to dominate accompanied by the appearance of linkage like structures when 20 wt.% glycerol was added. The plasticizer is believed to act as a spacer between molecules of polymer by forming links with them (Pandey, Asthana, Dwivedi, & Chaturvedi, 2013). Besides, the plasticizer has created alternative pathways for ion conduction which can enhance the conductivity (Imperiyka, Ahmad, Hanifah, & Rahman, 2014; Kadir, 2010; Subramaniam, Chiam-Wen, Yee, & Morris, 2012).

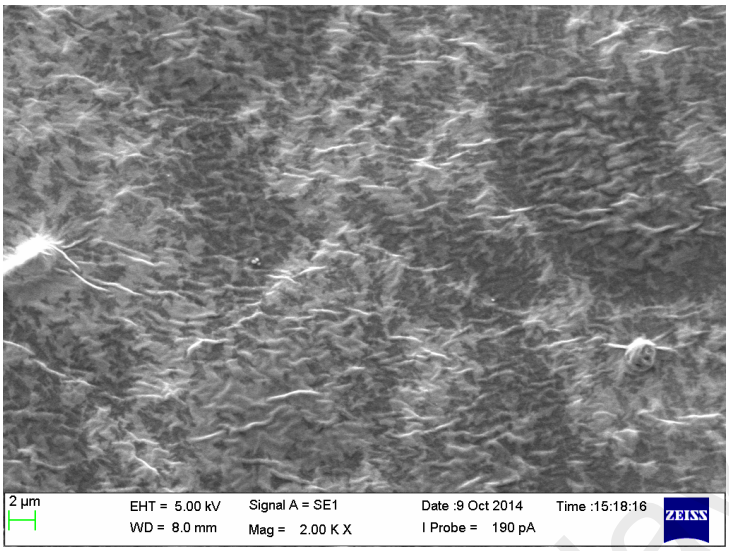

Figure 6.34: Surface micrograph of P7 electrolyte.

The micrograph of P7 electrolyte in Figure 6.34 shows the maximum dominancy of the dark region as well as increasing number of link. This result indicates the high amorphous phase within P7 electrolyte thus obtained the highest conductivity value as shown in Figure 6.18.

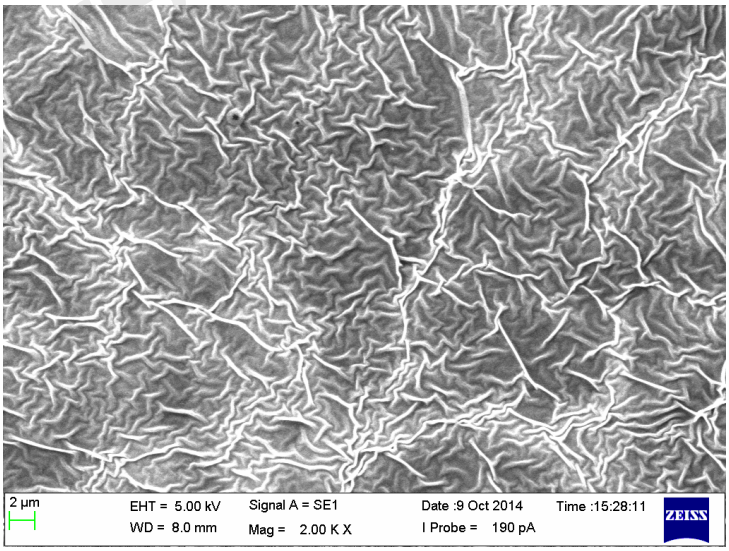

Figure 6.35: Surface micrograph of P8 electrolyte.

The effect of plasticizer overload in the electrolyte can be observed in the micrograph of P8 electrolyte in Figure 6.35. It can be seen that too much links have appeared and the linkages may be formed between the plasticizer itself causing the salt to recrystallize thus decreased the conductivity (Johan & Ting, 2011).

6.3.3 DSC Analysis

Conductivity of the electrolyte is governed by the ionic mobility (Kadir et al., 2010). Ionic mobility depends on the segmental motion of the polymer chains in the amorphous phase, which is characterized by the glass transition temperature (T_g) (Saikia, Pan, & Kao, 2012). From Figure 4.22, the T_g value of S8C2 film is 82.33 °C. The value of T_g for S1 electrolyte is lower at 55.08 °C as shown in Figure 6.36.

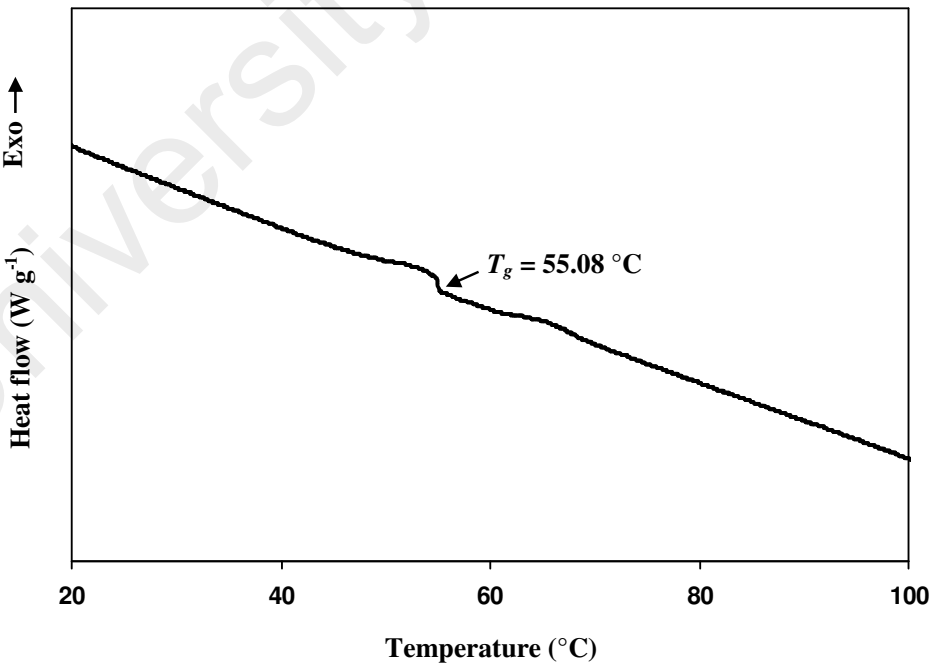

Figure 6.36: DSC thermogram of S1 electrolyte.

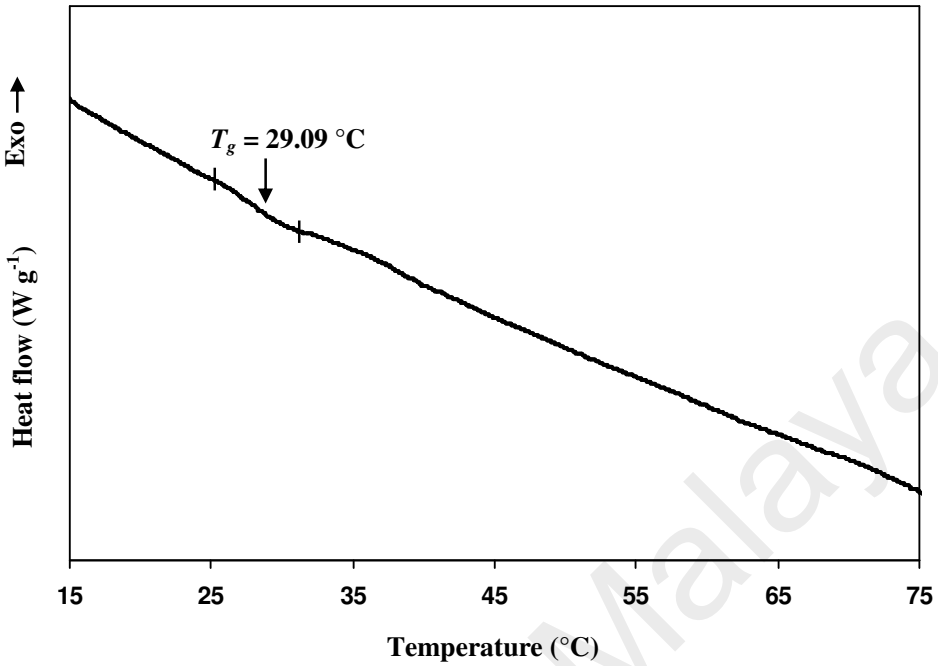

Figure 6.37: DSC thermogram of S5 electrolyte.

Figure 6.37 shows the DSC thermogram of S5 electrolyte. The T_g of S5 electrolyte is observed to be lower than that of S1 electrolyte. The decrease in T_g with increasing salt content is also been observed by Vijaya et al. (2013) on PVP-NH_4Cl electrolytes. This phenomenon can be due to the plasticizing effect contributed by the salt on the polymer host (Noor et al., 2013; Vijaya et al., 2013). The plasticization effect is related to the weakening of the dipole-dipole interactions between the polymer chains due to the presence of salt (Malathi et al., 2010). This phenomenon stimulates the flexibility of polymer backbone thus enables the ions to move easily through the polymer chain network when an electric field is applied (Liew et al., 2014; Malathi et al., 2010). The low T_g leads to faster segmental motion of the polymer electrolyte resulting in an increase in conductivity (Vijaya et al., 2013).

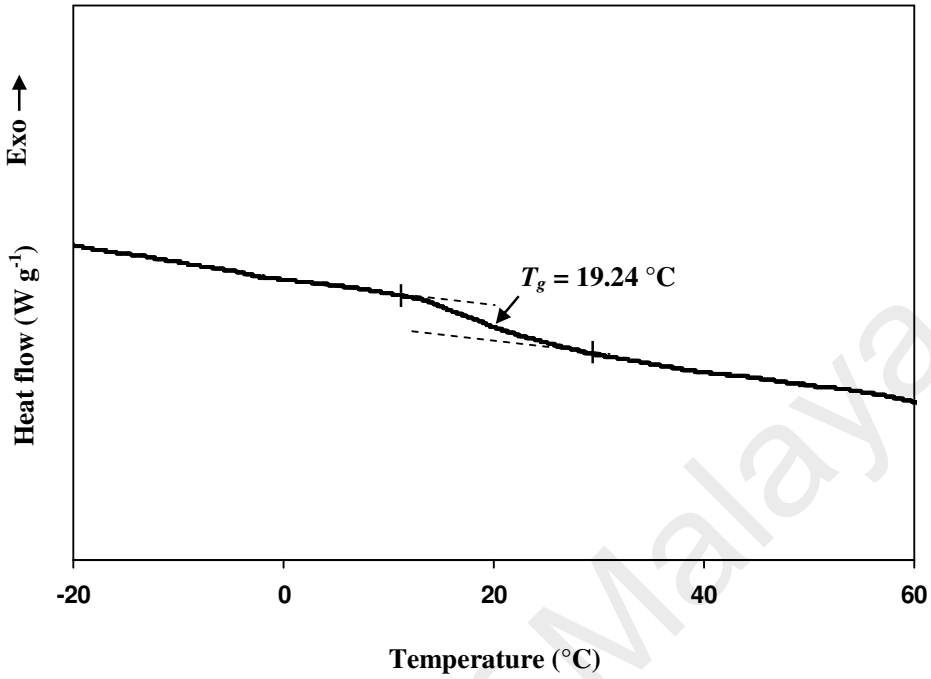

Figure 6.38: DSC thermogram of P3 electrolyte.

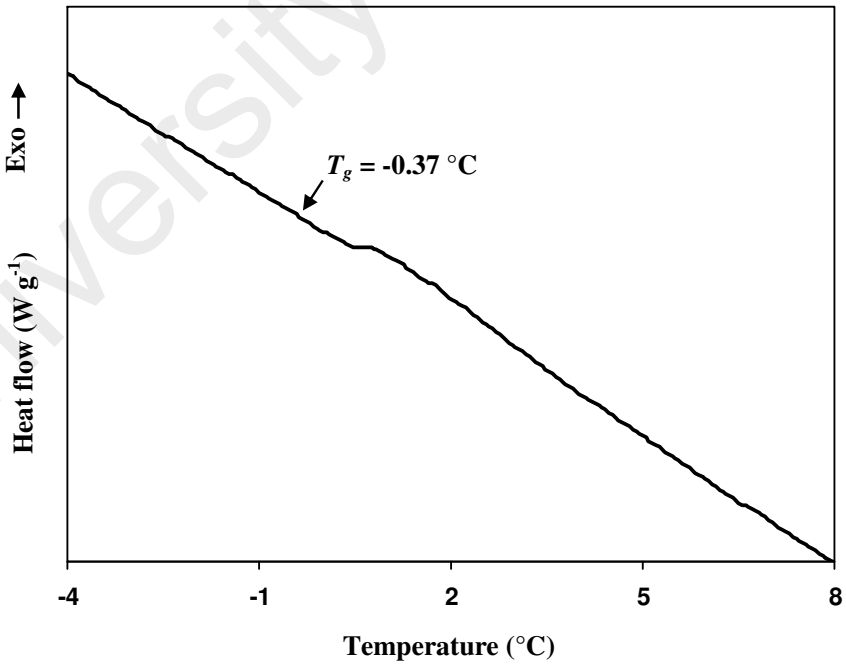

Figure 6.39: DSC thermogram of P7 electrolyte.

The addition of glycerol to the polymer electrolyte increases the chain flexibility which results in a decrease in T_g (Kumar & Sekhon, 2002). This result leads to an increase in conductivity as shown in Figure 6.18. Further decrease of T_g can be observed in the thermogram of P3 and P7 electrolytes as shown in Figures 6.38 and 6.39, respectively. This result satisfies the conductivity result as the conductivity is optimized on addition of 35 wt.% glycerol.

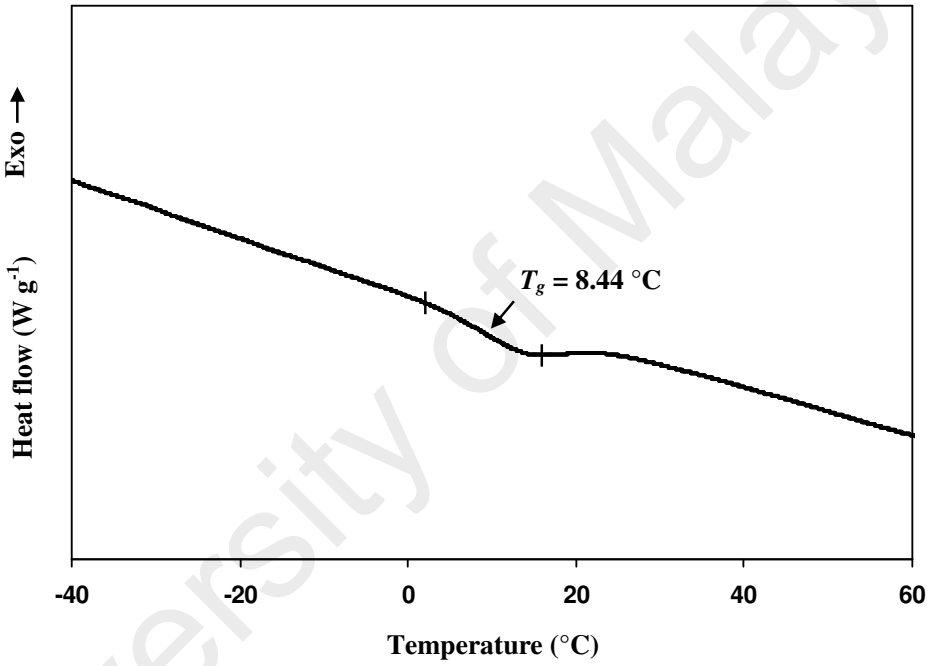

Figure 6.40: DSC thermogram of P9 electrolyte.

The T_g value is observed to increase on addition of 45 wt.% glycerol as observed in thermogram of P9 electrolyte in Figure 6.40. The increase in T_g can be due to the increase in rigidity of the electrolyte (Noor et al., 2013). This phenomenon may have resulted from the recrystallization of salt which impedes the segmental mobility as well as the ionic migration (Liew et al., 2014; Silva, Barros, Smith, & MacCallum, 2004). As a result, a decrease in conductivity is observed as depicted in Figure 6.18.

6.4 Conductivity at Elevated Temperature

Generally, the conductivity-temperature relationship of polymer electrolytes is in accordance with either the Arrhenius or Vogel-Tamman-Fulcher (VTF) rules. If a linear relation is observed, the temperature dependence of conductivity of the polymer electrolyte obeys Arrhenius rule and the conductivity can be expressed as:

$$\sigma = \sigma_o \exp\left[-\frac{E_a}{kT}\right] \tag{6.9}$$

where σ_o is the pre-exponential factor, E_a is activation energy, k is Boltzmann constant and T is absolute temperature. A polynomial relation of conductivity-temperature is best fitted by VTF equation, where the conductivity can be expressed as:

$$\sigma T^{\frac{1}{2}} = A_o \exp\left[-\frac{E_{VTF}}{k(T-T_o)}\right] \tag{6.10}$$

where A_o is the pre-exponential factor proportional to the concentration of carriers, E_{VTF} is pseudo activation energy and T_o is the temperature at which the configuration entropy becomes zero (Kuo et al., 2013).

The variation of conductivity as a function of temperature for all electrolytes in salted and plasticized systems is displayed in Figure 6.41(a) and (b), respectively. The conductivity of all electrolytes is observed to increase with increasing temperature. The linear relations suggest that conductivity-temperature dependence of the present electrolyte systems obeys the Arrhenius rule. The Arrhenian conductivity–temperature

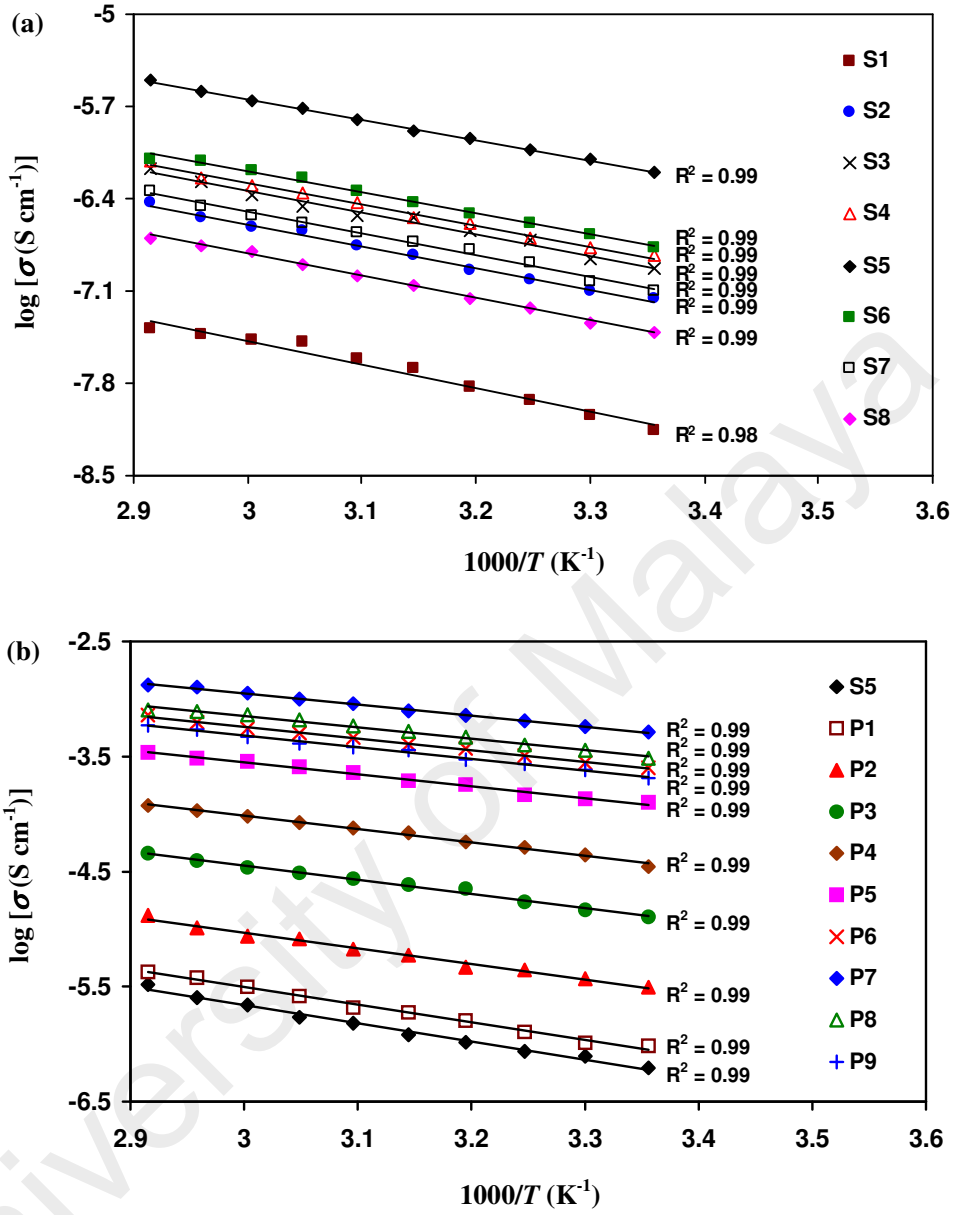

Figure 6.41: Variation of conductivity as a function of temperature for electrolytes in (a) salted and (b) plasticized systems.

relationship has been observed for starch-NH_4NO_3 (Khiar & Arof, 2010), PVA-NH_4Cl (Hema, Selvasekarapandian, Arunkumar, et al., 2009) and chitosan-NH_4I (Buraidah et al., 2009) electrolytes. By using Equation (6.9), the calculated E_a value for each salted and plasticized electrolyte is listed in Tables 6.9 and 6.10, respectively. The value of E_a

is found to be 0.31-0.36 eV for salted electrolytes and 0.19-0.30 eV for plasticized electrolytes. The higher conducting electrolyte has the lower E_a value. This is in agreement with the fact that the density of ions in the electrolyte increases with the increase in NH_4Cl and glycerol content thus the energy barrier for the proton transport decreases leading to a decrease in the E_a value (Selvasekarapandian et al., 2005).

Table 6.9: Activation energy of each electrolyte in salted system.

Sample	E_a (eV)
S1	0.36
S2	0.33
S3	0.32
S4	0.32
S5	0.31
S6	0.32
S7	0.33
S8	0.33

Table 6.10: Activation energy of each electrolyte in plasticized system.

Sample	E_a (eV)
P1	0.30
P2	0.27
P3	0.24
P4	0.23
P5	0.21
P6	0.20
P7	0.19
P8	0.20
P9	0.20

6.4.1 Effect of Water Content on Conductivity

In order to know the water content as well as the thermal stability of the electrolytes, TGA analysis of selected electrolytes has been carried out. Figure 6.42 shows the TGA thermograms of selected electrolytes.

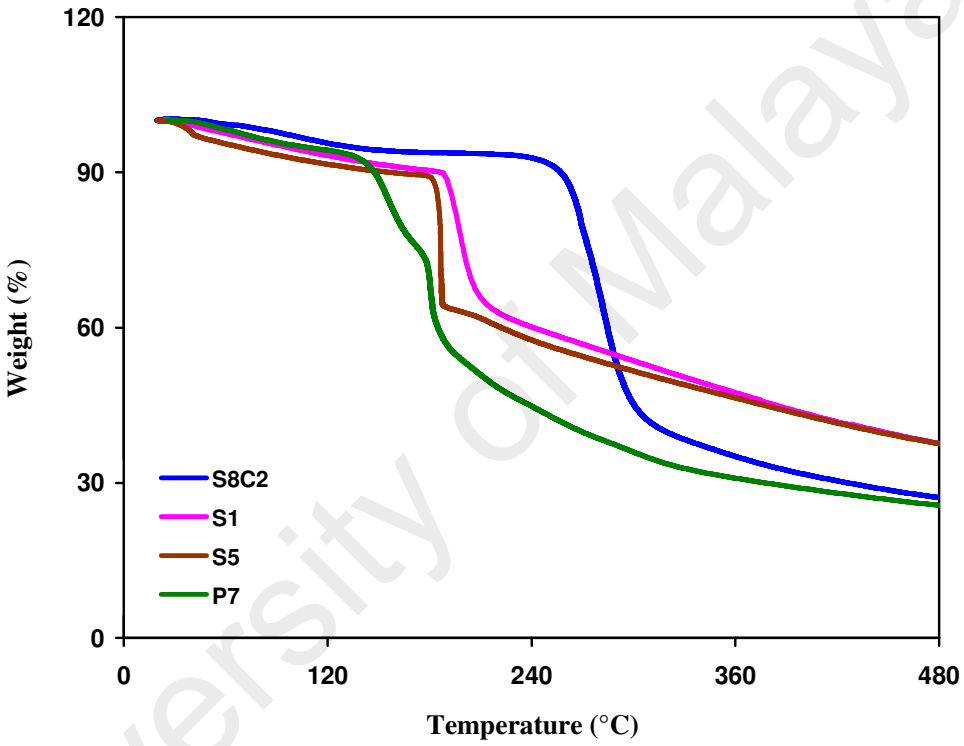

Figure 6.42: TGA thermograms of S8C2, S1, S5 and P7 electrolytes.

From Figure 6.42, it can be observed that the first weight loss of S1, S5 and P7 electrolytes is higher (~ 7-10%) than that of S8C2 film. This result could be due to hydrophilic nature of the salt and glycerol (Halim, Majid, Arof, Kajzar, & Pawlicka, 2012; Noor et al., 2012). This results show higher water content within S1, S5 and P7 electrolytes compare to S8C2 electrolyte. It is observed that the S1 electrolyte decomposes at 198 °C. The decomposition temperature decreases to 185 °C for S5

electrolyte. This observation reveals the decline in the heat-resistivity results from the disruption of strong hydrogen bonding network in the electrolytes (Ramesh et al., 2012). In the thermogram of the P7 electrolyte, the second weight loss of ~ 20% is observed in 136-177 °C. This second transition region is due to the degradation of glycerol in the electrolyte (Ayala, Agudelo, & Vargas, 2012). The major decomposition of P7 electrolyte occurs at 180 °C.

To study the effect of water content on conductivity, variation of conductivity with temperature under one heating-cooling cycle has been carried out. P7 electrolyte was used for this study. The result is shown in figure 6.43.

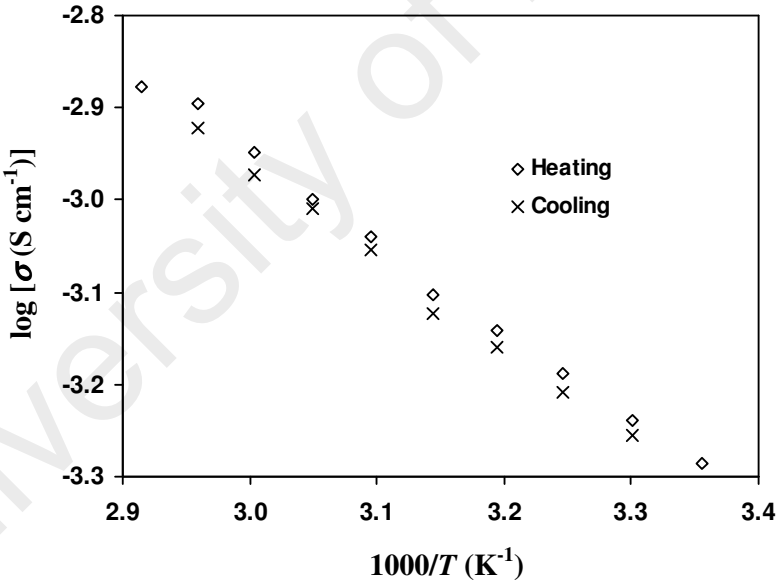

Figure 6.43: Variation of conductivity as a function of temperature under one heating-cooling cycle for P7 electrolyte.

As shown in Figure 6.43, the conductivity is lower during cooling cycle than the conductivity during heating cycle. As an example, the conductivity at 50 °C is 9.12×10^{-4} S cm^{-1} during the heating cycle. However, the conductivity at the same

temperature decreases to 8.83×10^{-4} S cm^{-1} during the cooling cycle. The difference of ~ 3% is attributed to the loss of water from the electrolyte during the heating cycle. From Figure 6.36, the weight loss of P7 electrolyte is ~ 3% as temperature increases to 70 °C, which is due to the loss of water. The conductivity-temperature result in Figure 6.43 verifies the TGA result.

6.5 Transport Analysis

To further verify the conductivity result, the Rice and Roth model was employed to study the dependence of conductivity on number density (n_d) and mobility (μ) of ions. This can be achieved by using Equation (2.2), where conductivity is related to n_d, E_a and travelling time of ion (τ). From Equation (2.3), the value of τ can be determined using the value of l, which is the distance between two complexation sites. Since polymer blend host is used in this work, various values of l are used.

According to Khiar and Arof (2010), the cations of salt would be more easily attached to the amylose compound rather than the amylopectin of starch because the α-1,4-D-glucosidic linkages of amylose are more stable and less steric than the α-1,6-D-glucosidic linkages of amylopectin. In starch, the distance l between two adjacent amylose fibers is 10.4 Å (Khiar & Arof, 2010). Tables 6.11 and 6.12 list the transport parameters of each electrolyte in the salted and plasticized systems, respectively, using l = 10.4 Å.

Table 6.11: Transport parameters of each electrolyte in salted system at room temperature using l = 10.4 Å.

Sample	σ (S cm^{-1})	τ (s)	n_d (cm^{-3})	μ (cm^2 V^{-1} s^{-1})
S1	$(6.51 \pm 1.80) \times 10^{-9}$	1.25×10^{-13}	4.44×10^{16}	9.16×10^{-7}
S2	$(6.70 \pm 1.88) \times 10^{-8}$	1.31×10^{-13}	1.48×10^{17}	2.82×10^{-6}
S3	$(1.16 \pm 0.25) \times 10^{-7}$	1.33×10^{-13}	1.77×10^{17}	4.10×10^{-6}
S4	$(1.43 \pm 0.37) \times 10^{-7}$	1.33×10^{-13}	2.18×10^{17}	4.10×10^{-6}
S5	$(6.47 \pm 1.30) \times 10^{-7}$	1.35×10^{-13}	6.78×10^{17}	5.96×10^{-6}
S6	$(1.85 \pm 0.51) \times 10^{-7}$	1.33×10^{-13}	2.82×10^{17}	4.10×10^{-6}
S7	$(7.86 \pm 1.04) \times 10^{-8}$	1.31×10^{-13}	1.74×10^{17}	2.82×10^{-6}
S8	$(3.70 \pm 0.35) \times 10^{-8}$	1.31×10^{-13}	8.19×10^{16}	2.82×10^{-6}

Table 6.12: Transport parameters of each electrolyte in plasticized system at room temperature using l = 10.4 Å.

Sample	σ (S cm^{-1})	τ (s)	n_d (cm^{-3})	μ (cm^2 V^{-1} s^{-1})
P1	$(9.64 \pm 1.37) \times 10^{-7}$	1.37×10^{-13}	6.96×10^{17}	8.65×10^{-6}
P2	$(5.03 \pm 1.53) \times 10^{-6}$	1.45×10^{-13}	1.19×10^{18}	2.64×10^{-5}
P3	$(2.29 \pm 0.57) \times 10^{-5}$	1.53×10^{-13}	1.79×10^{18}	8.00×10^{-5}
P4	$(4.41 \pm 1.03) \times 10^{-5}$	1.57×10^{-13}	2.38×10^{18}	1.16×10^{-4}
P5	$(1.41 \pm 0.40) \times 10^{-4}$	1.64×10^{-13}	3.66×10^{18}	2.41×10^{-4}
P6	$(2.65 \pm 0.53) \times 10^{-4}$	1.68×10^{-13}	4.77×10^{18}	3.47×10^{-4}
P7	$(5.11 \pm 1.60) \times 10^{-4}$	1.72×10^{-13}	6.39×10^{18}	4.99×10^{-4}
P8	$(3.53 \pm 0.79) \times 10^{-4}$	1.68×10^{-13}	6.35×10^{18}	3.47×10^{-4}
P9	$(2.52 \pm 0.58) \times 10^{-4}$	1.68×10^{-13}	4.54×10^{18}	3.47×10^{-4}

From a report by Filho, Seidl, Correia, and Cerqueira (2000), the authors show that the hydroxyl-hydroxyl distances in starch are in the range of 5.426 Å to 11.044 Å.

Tables 6.13 and 6.14 list the transport parameters of each electrolyte in the salted and plasticized systems, respectively, using l = 5.426 Å.

Table 6.13: Transport parameters of each electrolyte in salted system at room temperature using l = 5.426 Å.

Sample	τ (s)	n_d (cm^{-3})	μ (cm^2 V^{-1} s^{-1})
S1	6.53×10^{-14}	8.50×10^{16}	4.78×10^{-7}
S2	6.82×10^{-14}	2.84×10^{17}	1.47×10^{-6}
S3	6.93×10^{-14}	3.38×10^{17}	2.14×10^{-6}
S4	6.93×10^{-14}	4.17×10^{17}	2.14×10^{-6}
S5	7.04×10^{-14}	1.30×10^{18}	3.11×10^{-6}
S6	6.93×10^{-14}	5.40×10^{17}	2.14×10^{-6}
S7	6.82×10^{-14}	3.33×10^{17}	1.47×10^{-6}
S8	6.82×10^{-14}	1.57×10^{17}	1.47×10^{-6}

Table 6.14: Transport parameters of each electrolyte in plasticized system at room temperature using l = 5.426 Å.

Sample	τ (s)	n_d (cm^{-3})	μ (cm^2 V^{-1} s^{-1})
P1	7.16×10^{-14}	1.33×10^{18}	4.51×10^{-6}
P2	7.54×10^{-14}	2.28×10^{18}	1.38×10^{-5}
P3	8.00×10^{-14}	3.42×10^{18}	4.17×10^{-5}
P4	8.17×10^{-14}	4.56×10^{18}	6.03×10^{-5}
P5	8.56×10^{-14}	7.01×10^{18}	1.26×10^{-4}
P6	8.77×10^{-14}	9.14×10^{18}	1.81×10^{-4}
P7	8.99×10^{-14}	1.23×10^{19}	2.60×10^{-4}
P8	8.77×10^{-14}	1.22×10^{19}	1.81×10^{-4}
P9	8.77×10^{-14}	8.70×10^{18}	1.81×10^{-4}

Tables 6.15 and 6.16 list the transport parameters of each electrolyte in the salted and plasticized systems, respectively, using l = 11.044 Å.

Table 6.15: Transport parameters of each electrolyte in salted system at room temperature using l = 11.044 Å.

Sample	τ (s)	n_d (cm^{-3})	μ (cm^2 V^{-1} s^{-1})
S1	1.33×10^{-13}	4.18×10^{16}	9.73×10^{-7}
S2	1.39×10^{-13}	1.40×10^{17}	3.00×10^{-6}
S3	1.41×10^{-13}	1.66×10^{17}	4.35×10^{-6}
S4	1.41×10^{-13}	2.05×10^{17}	4.35×10^{-6}
S5	1.43×10^{-13}	6.38×10^{17}	6.33×10^{-6}
S6	1.41×10^{-13}	2.65×10^{17}	4.35×10^{-6}
S7	1.39×10^{-13}	1.64×10^{17}	3.00×10^{-6}
S8	1.39×10^{-13}	7.71×10^{16}	3.00×10^{-6}

Table 6.16: Transport parameters of each electrolyte in plasticized system at room temperature using l = 11.044 Å.

Sample	τ (s)	n_d (cm^{-3})	μ (cm^2 V^{-1} s^{-1})
P1	1.46×10^{-13}	6.55×10^{17}	4.51×10^{-6}
P2	1.54×10^{-13}	1.12×10^{18}	1.38×10^{-5}
P3	1.63×10^{-13}	1.68×10^{18}	4.17×10^{-5}
P4	1.66×10^{-13}	2.24×10^{18}	6.03×10^{-5}
P5	1.74×10^{-13}	3.44×10^{18}	1.26×10^{-4}
P6	1.78×10^{-13}	4.49×10^{18}	1.81×10^{-4}
P7	1.83×10^{-13}	6.02×10^{18}	2.60×10^{-4}
P8	1.78×10^{-13}	5.98×10^{18}	1.81×10^{-4}
P9	1.78×10^{-13}	4.27×10^{18}	1.81×10^{-4}

In chitosan, the distance l between two repeating units of amine is 10 Å (Kadir, 2010). Tables 6.17 and 6.18 list the transport parameters of each electrolyte in the salted and plasticized systems, respectively, using l = 10 Å.

Table 6.17: Transport parameters of each electrolyte in salted system at room temperature using l = 10 Å.

Sample	τ (s)	n_d (cm^{-3})	μ (cm^2 V^{-1} s^{-1})
S1	1.20×10^{-13}	4.61×10^{16}	8.81×10^{-7}
S2	1.26×10^{-13}	1.54×10^{17}	2.71×10^{-6}
S3	1.28×10^{-13}	1.84×10^{17}	3.94×10^{-6}
S4	1.28×10^{-13}	2.26×10^{17}	3.94×10^{-6}
S5	1.30×10^{-13}	7.05×10^{17}	5.73×10^{-6}
S6	1.28×10^{-13}	2.93×10^{17}	3.94×10^{-6}
S7	1.26×10^{-13}	1.81×10^{17}	2.71×10^{-6}
S8	1.26×10^{-13}	8.51×10^{16}	2.71×10^{-6}

Table 6.18: Transport parameters of each electrolyte in plasticized system at room temperature using l = 10 Å.

Sample	τ (s)	n_d (cm^{-3})	μ (cm^2 V^{-1} s^{-1})
P1	1.32×10^{-13}	7.23×10^{17}	8.32×10^{-6}
P2	1.39×10^{-13}	1.24×10^{18}	2.54×10^{-5}
P3	1.47×10^{-13}	1.86×10^{18}	7.69×10^{-5}
P4	1.51×10^{-13}	2.48×10^{18}	1.11×10^{-4}
P5	1.58×10^{-13}	3.80×10^{18}	2.31×10^{-4}
P6	1.62×10^{-13}	4.96×10^{18}	3.33×10^{-4}
P7	1.66×10^{-13}	6.65×10^{18}	4.80×10^{-4}
P8	1.62×10^{-13}	6.61×10^{18}	3.33×10^{-4}
P9	1.62×10^{-13}	4.72×10^{18}	3.33×10^{-4}

From Tables 6.11 to 6.18, it is observed that the values of n_d and μ increase with increasing conductivity, where S5 and P7 has the highest n_d and μ values in salted and plasticized systems, respectively. Other reports also show that the increasing conductivity of electrolyte is influenced by the increase in n_d and μ values (Kadir et al., 2010; Khiar & Arof, 2010; Majid & Arof, 2005; Samsudin et al., 2012, Winie & Arof, 2006; Winie, Ramesh, & Arof, 2009).

Tables 6.19 and 6.20 list the average value of each transport parameter for all electrolytes in the salted and plasticized systems, respectively.

Table 6.19: Average value of each transport parameter for all electrolytes in salted system at room temperature.

Sample	τ (s)	n_d (cm^{-3})	μ ($cm^2\ V^{-1}\ s^{-1}$)
S1	$(1.11 \pm 0.31) \times 10^{-13}$	$(5.43 \pm 2.05) \times 10^{16}$	$(8.12 \pm 2.26) \times 10^{-7}$
S2	$(1.16 \pm 0.32) \times 10^{-13}$	$(1.82 \pm 0.69) \times 10^{17}$	$(2.50 \pm 0.70) \times 10^{-6}$
S3	$(1.18 \pm 0.33) \times 10^{-13}$	$(2.16 \pm 0.82) \times 10^{17}$	$(3.63 \pm 1.01) \times 10^{-6}$
S4	$(1.18 \pm 0.33) \times 10^{-13}$	$(2.67 \pm 1.01) \times 10^{17}$	$(3.63 \pm 1.01) \times 10^{-6}$
S5	$(1.20 \pm 0.33) \times 10^{-13}$	$(8.30 \pm 3.14) \times 10^{17}$	$(5.28 \pm 1.47) \times 10^{-6}$
S6	$(1.18 \pm 0.33) \times 10^{-13}$	$(3.45 \pm 1.30) \times 10^{17}$	$(3.63 \pm 1.01) \times 10^{-6}$
S7	$(1.16 \pm 0.32) \times 10^{-13}$	$(2.13 \pm 0.81) \times 10^{17}$	$(2.50 \pm 0.70) \times 10^{-6}$
S8	$(1.16 \pm 0.32) \times 10^{-13}$	$(1.00 \pm 0.38) \times 10^{17}$	$(2.50 \pm 0.70) \times 10^{-6}$

Table 6.20: Average value of each transport parameter for all electrolytes in plasticized system at room temperature.

Sample	τ (s)	n_d (cm^{-3})	μ ($cm^2\ V^{-1}\ s^{-1}$)
P1	$(1.22 \pm 0.34) \times 10^{-13}$	$(8.52 \pm 3.22) \times 10^{17}$	$(7.67 \pm 2.13) \times 10^{-6}$
P2	$(1.28 \pm 0.36) \times 10^{-13}$	$(1.46 \pm 0.55) \times 10^{18}$	$(2.34 \pm 0.65) \times 10^{-5}$
P3	$(1.36 \pm 0.38) \times 10^{-13}$	$(2.19 \pm 0.83) \times 10^{18}$	$(7.09 \pm 1.97) \times 10^{-5}$

Table 6.20, continued

P4	$(1.39 \pm 0.39) \times 10^{-13}$	$(2.92 \pm 1.10) \times 10^{18}$	$(1.02 \pm 0.29) \times 10^{-4}$
P5	$(1.45 \pm 0.40) \times 10^{-13}$	$(4.48 \pm 1.69) \times 10^{18}$	$(2.13 \pm 0.59) \times 10^{-4}$
P6	$(1.49 \pm 0.41) \times 10^{-13}$	$(5.84 \pm 2.21) \times 10^{18}$	$(3.07 \pm 0.86) \times 10^{-4}$
P7	$(1.53 \pm 0.43) \times 10^{-13}$	$(7.83 \pm 2.96) \times 10^{18}$	$(4.42 \pm 1.23) \times 10^{-4}$
P8	$(1.49 \pm 0.41) \times 10^{-13}$	$(7.78 \pm 2.94) \times 10^{18}$	$(3.07 \pm 0.86) \times 10^{-4}$
P9	$(1.49 \pm 0.41) \times 10^{-13}$	$(5.56 \pm 2.10) \times 10^{18}$	$(3.07 \pm 0.86) \times 10^{-4}$

For the transport analysis at various temperatures, the value of l = 10.4 Å is used. From Figures 6.34, the increasing temperature assists the increase in conductivity since the ionic mobility and the degree of salt dissociation are also temperature dependent (Winie et al., 2009). The transport parameters at various temperatures for S5 and P7 electrolytes are shown in Tables 6.21 and 6.22, respectively.

Table 6.21: Transport parameters of S5 electrolyte at various temperatures.

T (K)	σ (S cm^{-1})	n_d (cm^{-3})	μ (cm^2 V^{-1} s^{-1})
303	7.81×10^{-7}	6.82×10^{17}	7.15×10^{-6}
308	9.36×10^{-7}	6.85×10^{17}	8.53×10^{-6}
313	1.12×10^{-6}	6.91×10^{17}	1.01×10^{-5}
318	1.35×10^{-6}	7.07×10^{17}	1.19×10^{-5}
323	1.60×10^{-6}	7.14×10^{17}	1.40×10^{-5}
328	1.90×10^{-6}	7.26×10^{17}	1.63×10^{-5}
333	2.23×10^{-6}	7.34×10^{17}	1.90×10^{-5}
338	2.58×10^{-6}	7.35×10^{17}	2.19×10^{-5}
343	3.05×10^{-6}	7.55×10^{17}	2.52×10^{-5}

Table 6.22: Transport parameters of P7 electrolyte at various temperatures.

T (K)	σ (S cm^{-1})	n_d (cm^{-3})	μ (cm^2 V^{-1} s^{-1})
303	5.77×10^{-4}	6.50×10^{18}	5.54×10^{-4}
308	6.47×10^{-4}	6.58×10^{18}	6.14×10^{-4}
313	7.23×10^{-4}	6.67×10^{18}	6.77×10^{-4}
318	7.97×10^{-4}	6.68×10^{18}	7.44×10^{-4}
323	9.12×10^{-4}	6.98×10^{18}	8.16×10^{-4}
328	1.00×10^{-3}	7.00×10^{18}	8.92×10^{-4}
333	1.13×10^{-3}	7.26×10^{18}	9.71×10^{-4}
338	1.27×10^{-3}	7.51×10^{18}	1.06×10^{-3}
343	1.38×10^{-3}	7.53×10^{18}	1.14×10^{-3}

From Tables 6.21 and 6.22, the value of n_d is observed to have slightly increased with increasing temperature, indicating a weak temperature dependence of n_d. Winie et al. (2009) also reported a weak temperature dependence of n_d for hexanoyl chitosan-$LiCF_3SO_3$-EC-diethyl carbonate (DEC) electrolytes. The authors concluded that the increase in conductivity with increasing temperature is due primarily to the increase in the mobility of free ions. Similar result is obtained in the present work.

6.6 Transference Numbers

6.6.1 Ionic Transference Number

The transference number measurements have been carried out in order to detect the conducting species in the electrolytes. By sandwiching the electrolyte with

conducting species transparent electrodes, a transference number of the conducting species can be known from the ratio of steady state current to the initial current (I_{ss}/I_i). To determine the transference number of electron (t_e), stainless steel foils were used as the electrodes since electrons are transparent to the ion blocking stainless steel electrodes (Kufian et al., 2012). For ionic conductor, the current which flows through the electrode will fall rapidly with time, while for non ionic conductor, the current would not decrease with time (Yap, 2012). The plots of polarization current against time for selected electrolytes are shown in Figures 6.44 to 6.46.

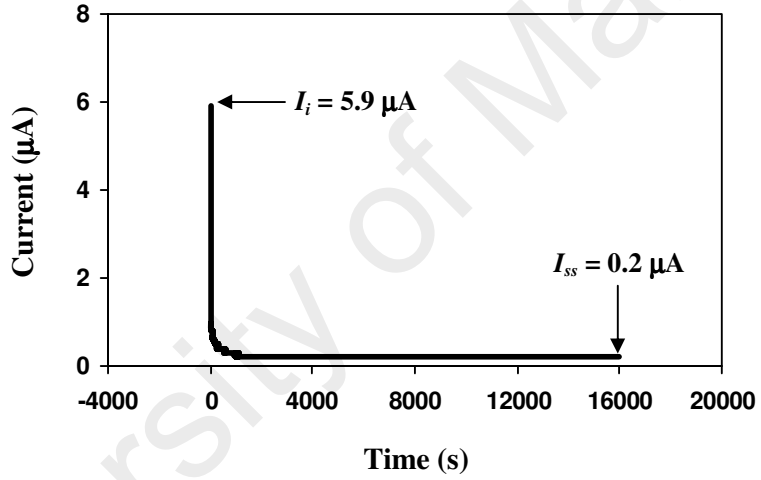

Figure 6.44: Transference number of P5 electrolyte using stainless steel electrodes.

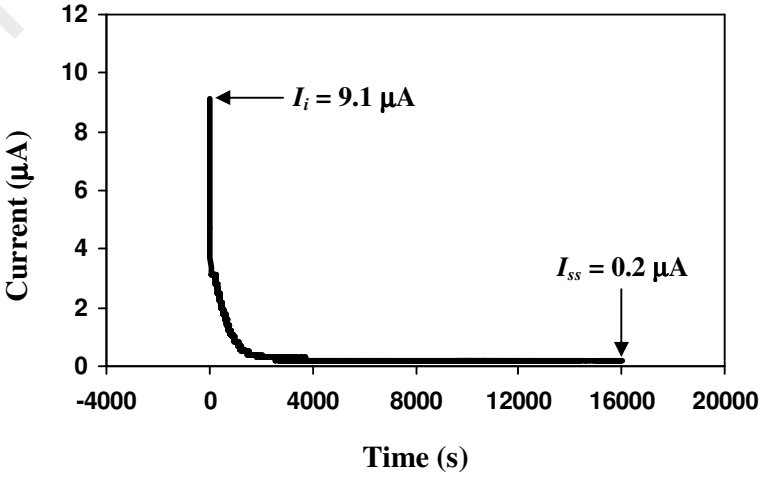

Figure 6.45: Transference number of P7 electrolyte using stainless steel electrodes.

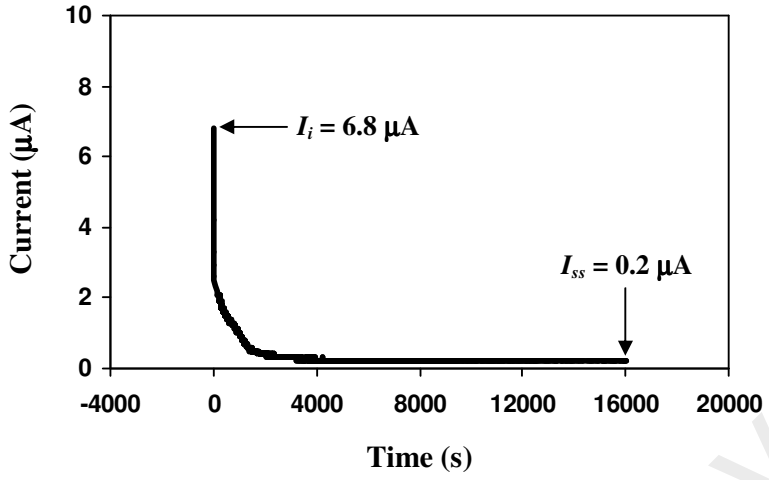

Figure 6.46: Transference number of P9 electrolyte using stainless steel electrodes.

From Figures 6.44 to 6.46, the current is observed to fall rapidly at the initial stage before being saturated at 0.2 μA. The steady state is achieved when the ions movement is balanced by diffusion process. The steady state current is then carried by electronic carriers (Woo et al., 2011b). This phenomenon is an indicator to show that the polymer electrolytes are ionic conductors. By knowing t_e, the transference number of ion (t_{ion}) of the electrolytes was calculated using:

$$t_{ion} = 1 - t_e \tag{6.11}$$

or

$$t_{ion} = \frac{I_i - I_{ss}}{I_i} \tag{6.12}$$

Table 6.23 lists the value of t_{ion} for selected electrolytes in the present work. The values of t_{ion} for the electrolytes are in the range of 0.91-0.98. This result further shows

that the dominant conducting species of the present electrolytes are ion. From Figure 6.18, P7 electrolyte obtained the highest conductivity value. Therefore, it is found that t_{ion} for P7 electrolyte is the highest (0.98). Mohan, Achari, Rao, and Sharma (2011) reported that the highest conducting electrolyte in polyethyl methacrylate (PEMA)-PVC-$NaClO_4$ system obtained the highest t_{ion} value. Vijaya et al. (2013) reported that the t_{ion} values for PVP-NH_4Cl electrolytes are in the range of 0.93-0.97. The present result is comparable with that reported in the literature.

Table 6.23: Ionic and electronic transference numbers of selected electrolytes.

Sample	t_{ion}	t_e
S5	0.91	0.09
P3	0.95	0.05
P4	0.95	0.05
P5	0.97	0.03
P6	0.97	0.03
P7	0.98	0.02
P8	0.97	0.03
P9	0.97	0.03

6.6.2 Cation Transference Number

The value of t_{ion} reveals the contribution of ions, i.e. both anion and cation to the total conductivity (Arof et al., 2012). Different ions have different mobilities thus may carry different portions of the total current (Ghosh et al., 2010). For application in batteries, the electrolyte should have larger cation mobility and negligible anion mobility (Arof, Shuhaimi, et al., 2014). This is because only cations are responsible for

intercalation and deintercalation processes at the cathode during the charge-discharge cycle of a battery. Thus, it is important to reveal the contribution of cations to the total conductivity by measuring the transference number of cation (t_+). To determine the value of t_+ of the electrolytes, suitable anion blocking electrode which is proton transparent should be used. From the literature, MnO_2 has been widely used as cathode active material for intercalation of proton in proton batteries (Kadir et al., 2010; Ng & Mohamad, 2006; Samsudin et al., 2014; Shukur, Ithnin, et al., 2013). Based on this fact, MnO_2 is chosen to be used as the electrodes. Figure 6.47 depicts the plot of polarization current against time for MnO_2/P7/MnO_2 cell.

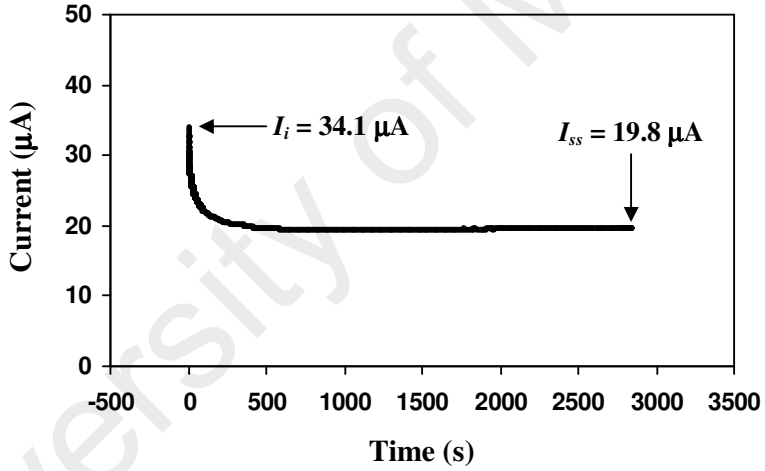

Figure 6.47: Transference number of P7 electrolyte using MnO_2 electrodes.

From a report by Kufian et al. (2012), the lithium ion transference number of PMMA-LiBOB electrolyte is obtained after subtracting I_{ss}/I_i of Li/PMMA-LiBOB/Li cell from the t_e. According to the authors, this is because lithium metal is electron transparent. MnO_2 is also electron transparent (Islam, Islam, & Khan, 2005). In the present work, the value of t_+ is obtained after subtracting I_{ss}/I_i of MnO_2/P7/MnO_2 cell from the t_e. It is found that the value of t_+ of P7 electrolyte is 0.56. As for comparison,

the t_+ measurements for S5 and P3 electrolytes were also determined and the results are shown in Figure 6.48. Table 6.24 lists the t_+ values of the electrolytes.

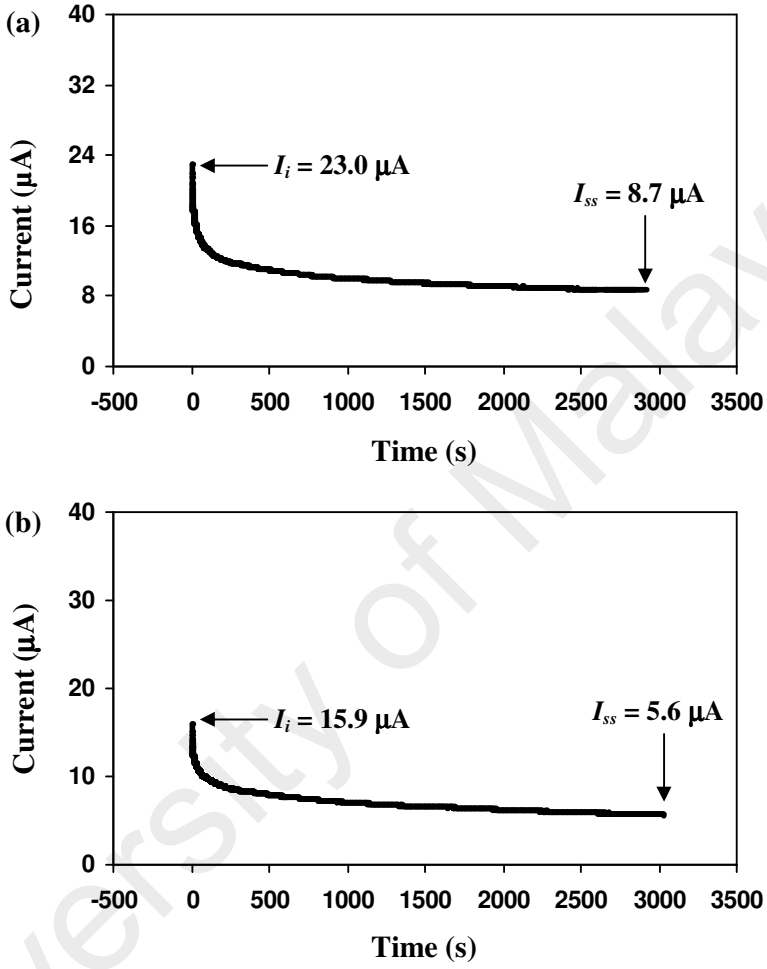

Figure 6.48: Transference numbers of (a) P3 and (b) S5 electrolytes using MnO_2 electrodes.

Table 6.24: Cation transference numbers of selected electrolytes.

Sample	t_+
S5	0.26
P3	0.33
P7	0.56

From Table 6.24, the value of t_+ of P7 electrolyte is higher than that of P3 and S5 electrolytes. According to Angulakshmi et al. (2013), the increase in t_+ value may be attributed to the increase in salt dissociation. In this work, the addition of glycerol up to 35 wt.% enhances the conductivity since it promotes the salt dissociation which increases the number density of ion. Thus, in the present work, the increase in t_+ value with increasing glycerol content up to 35 wt.% can be attributed to the increase in number density of ions.

6.7 Summary

The ionic conductivity of starch-chitosan-NH_4Cl (salted) and starch-chitosan-NH_4Cl-glycerol (plasticized) electrolytes has been presented. The highest room temperature conductivity of the salted electrolyte was obtained to be $(6.47 \pm 1.30) \times 10^{-7}$ S cm^{-1} at 25 wt.% NH_4Cl concentration (S5 electrolyte). In plasticized system, the conductivity was optimized at $(5.11 \pm 1.60) \times 10^{-4}$ S cm^{-1} with addition of 35 wt.% glycerol (P7 electrolyte). XRD results relate the variation in conductivity with the variation in the degree of crystallinity of the electrolytes. From SEM studies, the addition of glycerol has transformed the electrolyte's morphology from particulate surface to linked surface, as well as increases the amorphous phase of the electrolyte. DSC results show that the increase in conductivity can be attributed to the decrease in the T_g of electrolyte.

Conductivity-temperature studies imply that the conductivity is thermally assisted and follow the Arrhenius rule. The highest conducting electrolyte possessed the lowest E_a and vice versa. Transport parameters of all electrolytes have been calculated

using the Rice and Roth model. The conductivity is found to be influenced by the number density and mobility of ions. From the ionic transference number studies, it is known that the charge transport in the electrolytes is dominated by the ions.

CHAPTER 7

DIELECTRIC STUDIES

7.1 Introduction

Studies on the dielectric properties of an electrolyte are important to relate the increase in ionic conductivity with the increase in the number of free mobile ions (Vani et al., 2014). Knowledge on the effect of salt and plasticizer content on the ion transport mechanism can be gained by the comparative analysis of dielectric behaviour (Sengwa, Dhatarwal, & Choudhary, 2015). The main objective of this chapter is to investigate the dielectric behaviour of the electrolytes in salted and plasticized systems. Dielectric properties such as dielectric constant, dielectric loss, ion relaxation and electrical modulus will be presented. The ac conduction mechanism model of the ions for the highest conducting electrolyte in each system will be analyzed using Jonscher's universal power law.

7.2 Dielectric Constant and Dielectric Loss Analysis

The conductivity trend in the present work can be further verified by dielectric studies. Dielectric constant (ε_r) represents charge stored in a material while dielectric loss (ε_i) represents the amount of energy losses to move ions when the polarity of

electric field reverses rapidly (Buraidah et al., 2009; Woo et al., 2012). The values of ε_r and ε_i were calculated from the equations:

$$\varepsilon_r = \frac{Z_i}{\omega C_o (Z_r^{\,2} + Z_i^{\,2})} \tag{7.1}$$

$$\varepsilon_i = \frac{Z_r}{\omega C_o (Z_r^{\,2} + Z_i^{\,2})} \tag{7.2}$$

where Z_r is real part of impedance, Z_i is imaginary part of impedance, ω is angular frequency and C_o is vacuum capacitance, where $C_o = \varepsilon_o A_e t^{-1}$.

The NH_4Cl and glycerol content dependence of ε_r and ε_i at room temperature at selected frequencies are shown in Figures 7.1 to 7.4.

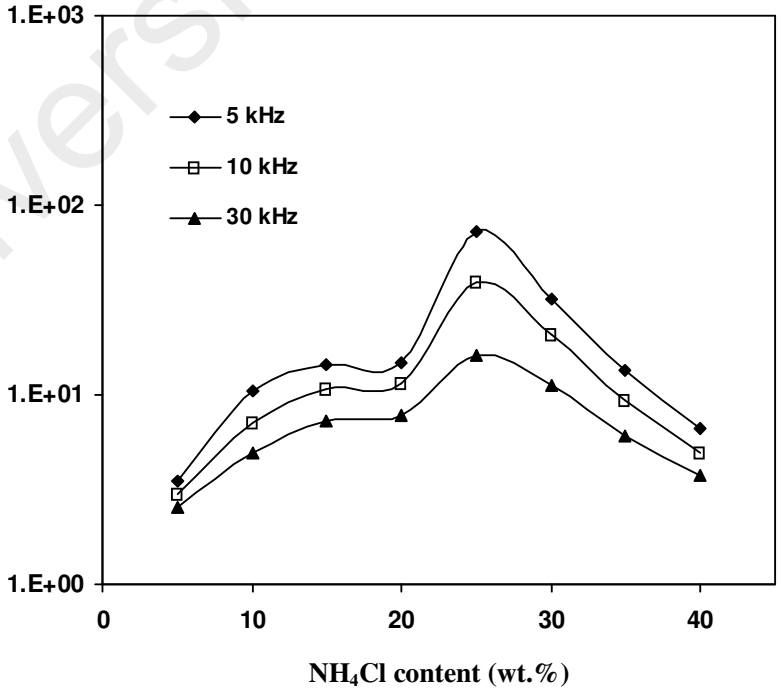

Figure 7.1: The dependence of ε_r on NH_4Cl content at room temperature for selected frequencies.

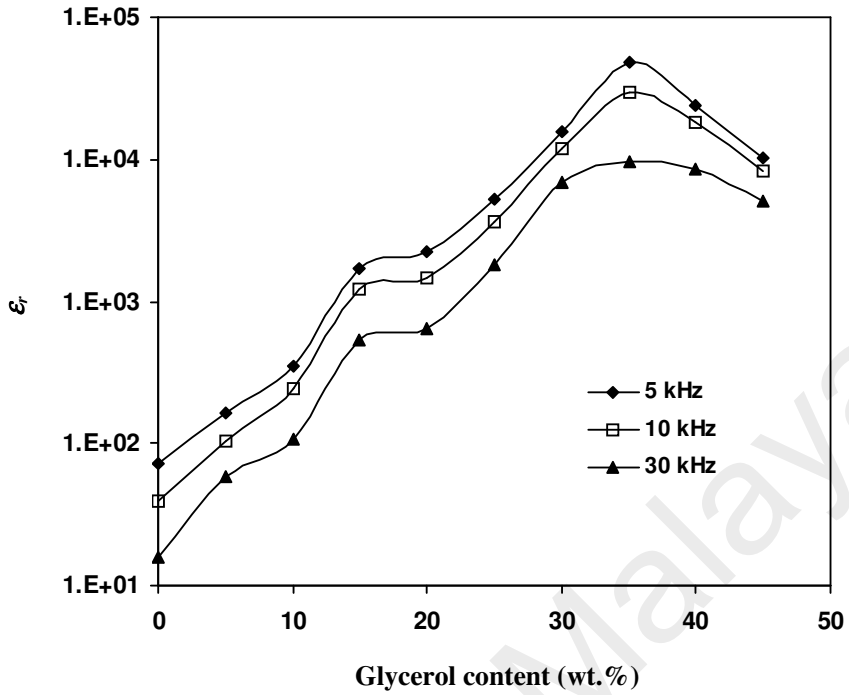

Figure 7.2: The dependence of ε_r on glycerol content at room temperature for selected frequencies.

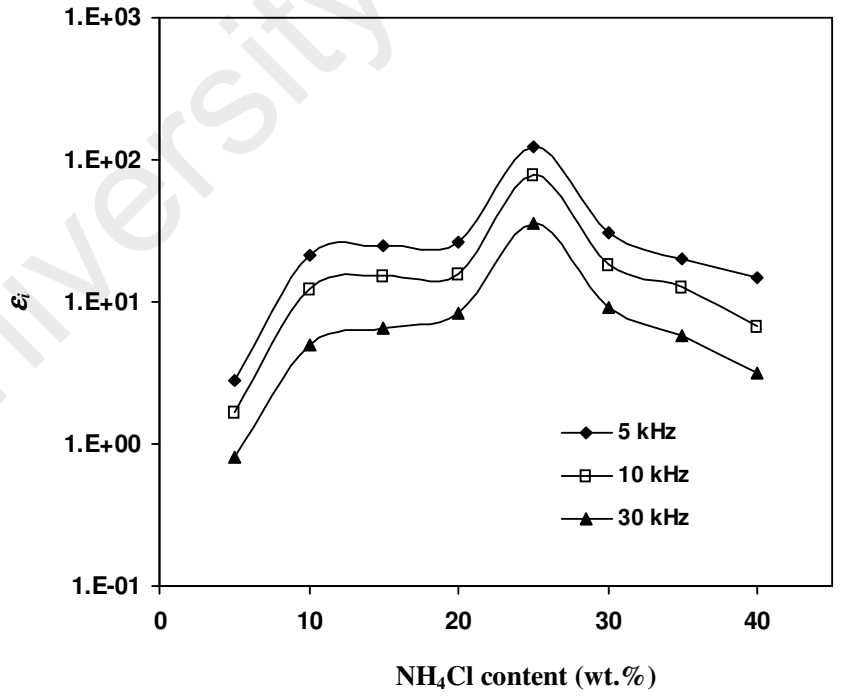

Figure 7.3: The dependence of ε_i on NH_4Cl content at room temperature for selected frequencies.

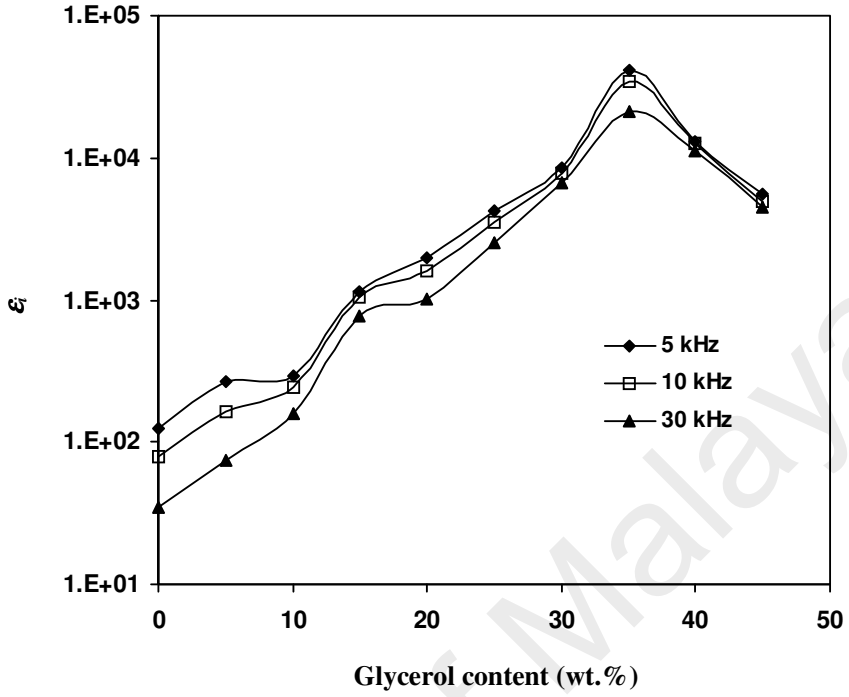

Figure 7.4: The dependence of ε_i on glycerol content at room temperature for selected frequencies.

From Figures 7.1 to 7.4, the values of ε_r and ε_i are observed to increase as NH_4Cl and glycerol content increases to 25 and 35 wt.%, respectively. As NH_4Cl content increases, the charge stored in the electrolyte increases indicating that the number density of mobile ions has increased (Buraidah et al., 2009). This phenomenon increases the conductivity. The decreasing ε_r and ε_i values for electrolytes containing more than 25 wt.% NH_4Cl is attributed to reassociation of ions, leading to a decrease in conductivity (Woo et al., 2011a). Aziz et al. (2012) reported that the dielectric constant result is in good agreement with the conductivity result of phthaloyl chitosan-NH_4SCN electrolyte system, which is comparable with the present work. When glycerol is added to the electrolyte, ion dissociation rate increases which leads toward conductivity enhancement. As reported by Ramesh et al. (2002), the plasticized electrolyte with a

higher conductivity value shows a higher ε_r value than the unplasticized electrolyte. The trend of ε_i in Figures 7.3 and 7.4 is also similar to ε_r. At all NH_4Cl and glycerol concentrations, ε_r and ε_i values are observed to decrease with the increase in frequency. This phenomenon is attributed to the electrode polarization effects (Mishra & Rao, 1998). As frequency increases, the periodic reversal of the electric field occurs so rapidly which disable the charge carriers from orienting themselves in the field direction, resulting in the decrease of ε_r and ε_i (Ali, Harun, Ali, & Yahya, 2011).

The temperature dependence of ε_r and ε_i for S5 and P7 electrolytes at selected frequencies are shown in Figures 7.5 to 7.8.

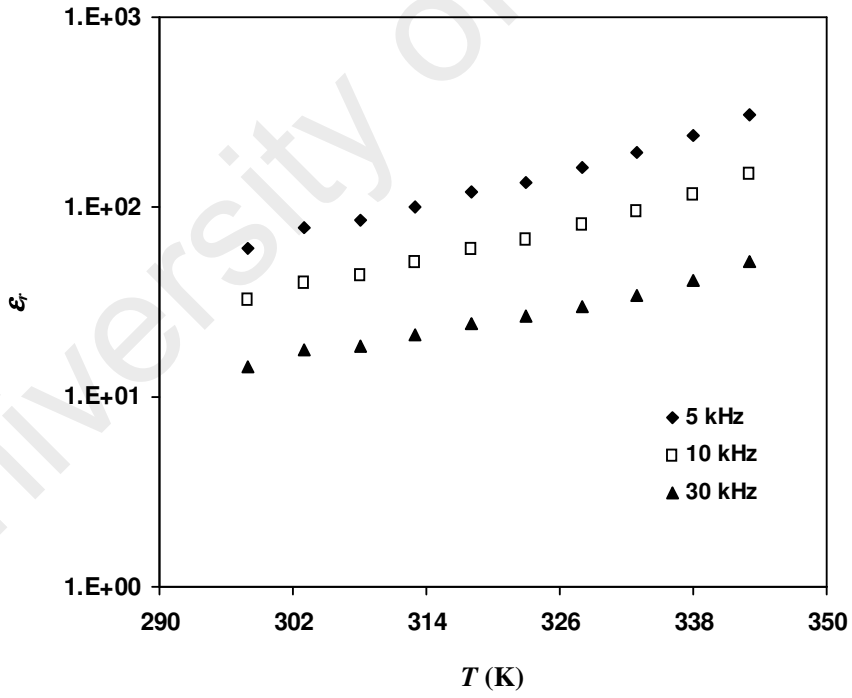

Figure 7.5: The dependence of ε_r on temperature for S5 electrolyte at selected frequencies.

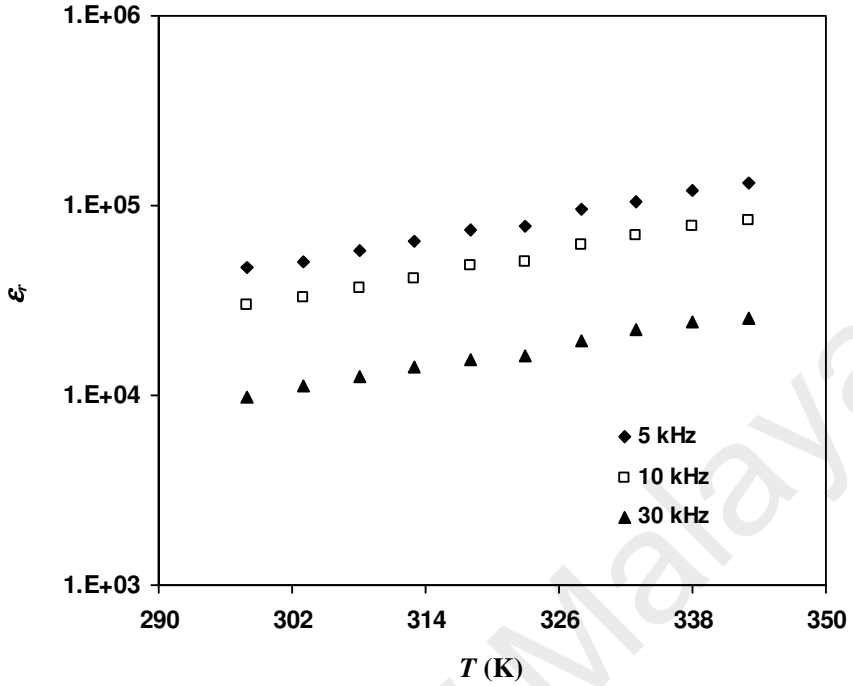

Figure 7.6: The dependence of ε_r on temperature for P7 electrolyte at selected frequencies.

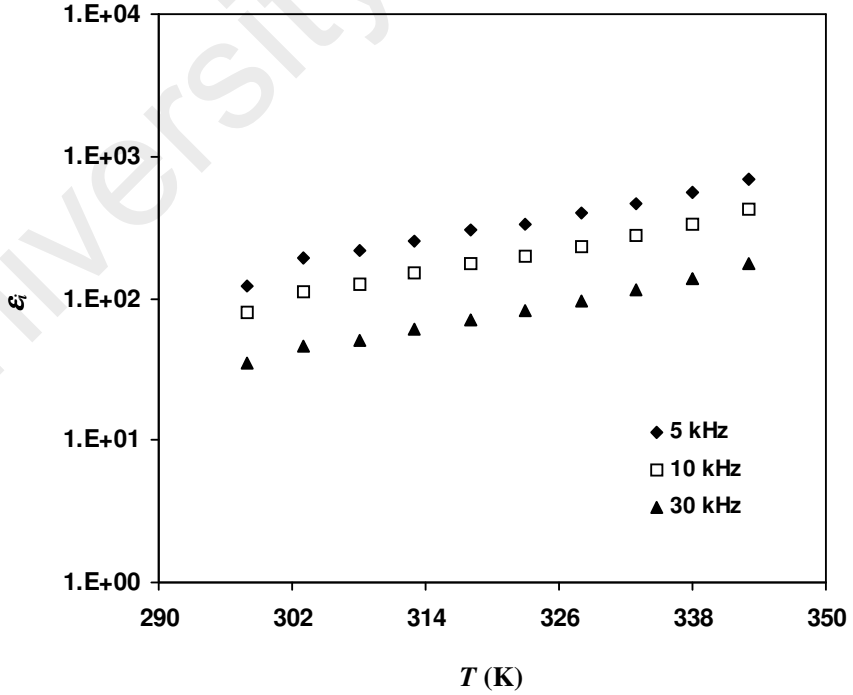

Figure 7.7: The dependence of ε_i on temperature for S5 electrolyte at selected frequencies.

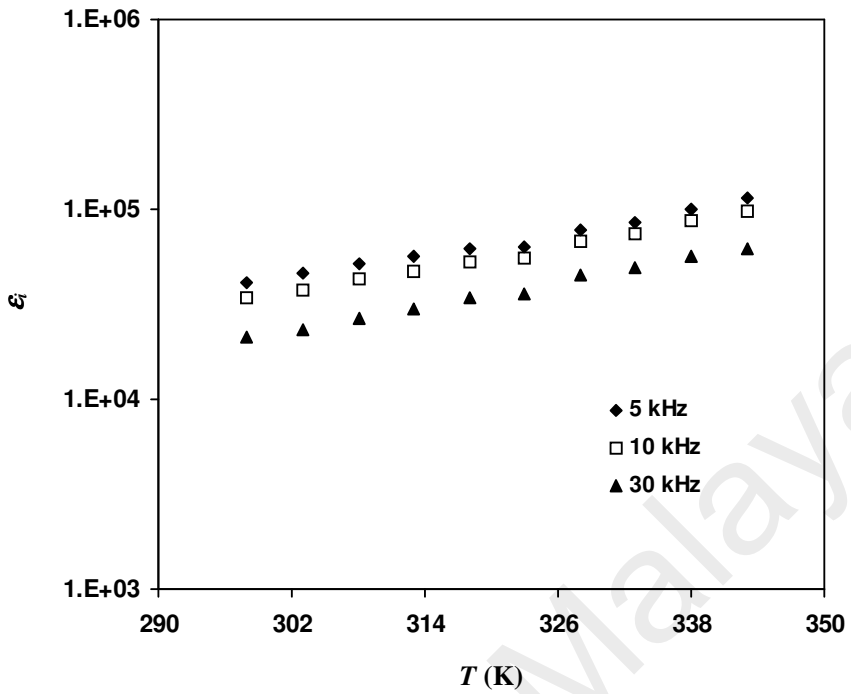

Figure 7.8: The dependence of ε_i on temperature for P7 electrolyte at selected frequencies.

From Figures 7.5 to 7.8, the values of ε_r and ε_i increase with increasing temperature. According to Abdullah et al. (2009), the increasing temperature increases the degree of dissociation and redissociation of ion aggregates hence result in an increase in number of free ions, which assists the conductivity increment. This result is in agreement with the transport parameters shown in Tables 6.21 and 6.22, where the number density of ion increases with the increase in temperature. In Figures 7.5 and 7.7, there is a sudden increase in ε_r and ε_i values of S5 electrolyte at 303 K. Referring to Figure 6.37, the glass transition temperature (T_g) of S5 electrolyte occurs at 29.09 °C (302.09 K). At that temperature, the concentration of ions in the electrolyte is strongly reflected (Kato et al., 2002). This phenomenon reflects to the sudden increase in ε_r and ε_i values as observed at 303 K.

7.3 Electrical Modulus Studies

Further analysis on the dielectric behaviour can be done from the electrical modulus studies, which highlight the bulk dielectric behaviour and suppress the effect of electrode polarization (Khiar, Radzi, & Razak, 2013). The real part and imaginary part of electrical modulus were calculated using:

$$M_r = \frac{\varepsilon_r}{(\varepsilon_r^{\,2} + \varepsilon_i^{\,2})} \tag{7.3}$$

$$M_i = \frac{\varepsilon_i}{(\varepsilon_r^{\,2} + \varepsilon_i^{\,2})} \tag{7.4}$$

where M_r and M_i are real and imaginary parts of electrical modulus, respectively. Figures 7.9 and 7.10 show the variation of M_r with frequency for selected electrolytes in salted and plasticized systems, respectively, at room temperature.

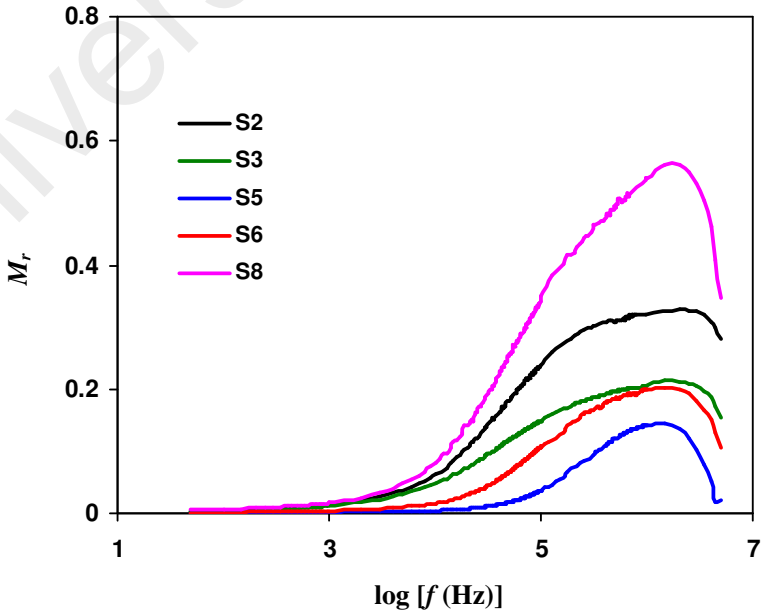

Figure 7.9: The dependence of M_r on frequency for selected electrolytes in salted system at room temperature.

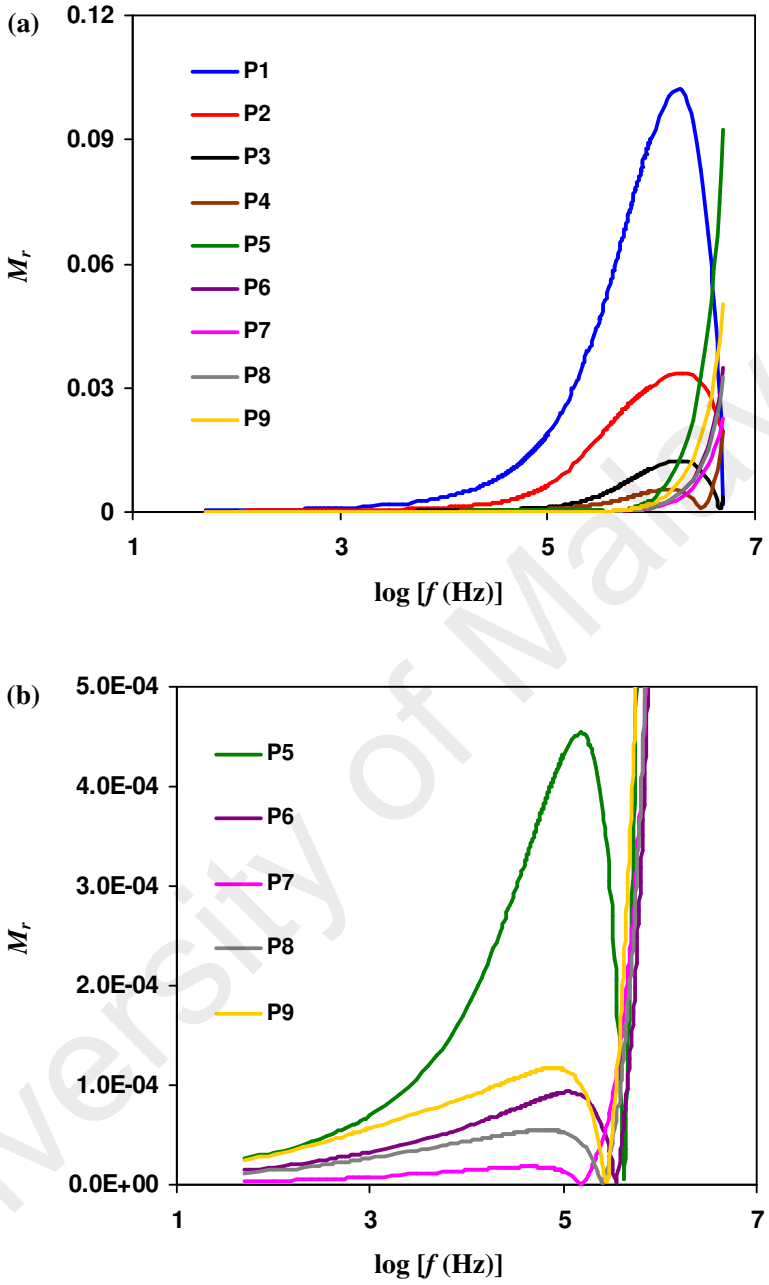

Figure 7.10: (a) The dependence of M_r on frequency for electrolytes in plasticized system at room temperature. (b) Enlarged M_r plots of P5 to P9 electrolytes.

In Figures 7.9 and 7.10, at low frequency region, the value of M_r approaches zero indicating the negligible contribution of the electrode polarization (Ramesh & Arof, 2001). As frequency increases, the value of M_r increases and reaches a maximum

value at high frequency, which is attributed to the distribution of relaxation processes over a range of frequencies (Patro & Hariharan, 2009). The appearance of maximum indicates that the electrolytes are ionic conductor (Ramesh et al., 2011). The lower M_r values for higher conducting electrolyte indicate the increase in charge carriers (Sharma, Kanchan, & Gondaliya, 2012).

Figures 7.11 and 7.12 show the variation of M_r with frequency for S5 and P7 electrolytes, respectively, at various temperatures. It can be observed that the value of M_r decreases with the increase in temperature. According to Aziz et al. (2010b), the decrease in M_r at increasing temperature is a result from the increase in the mobility of charge carriers with the temperature. This fact is proven in Tables 6.21 and 6.22. The positions of the peaks do not change strongly with temperature.

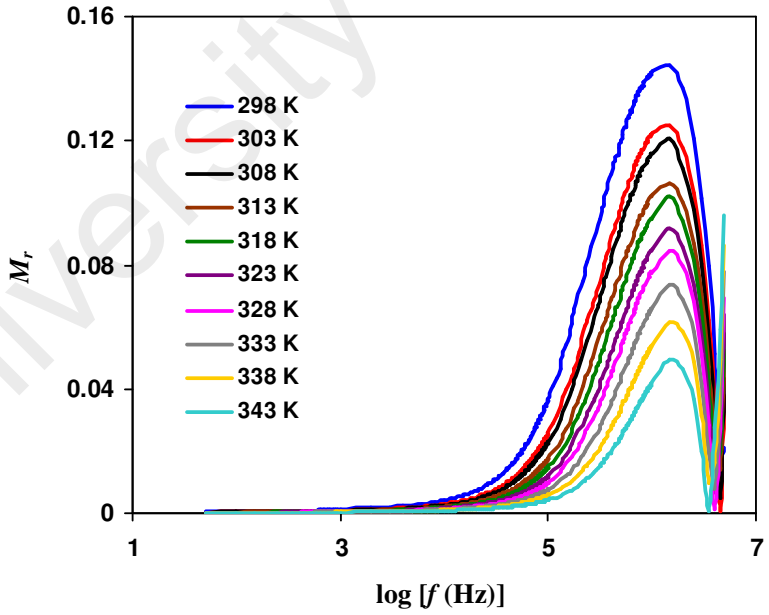

Figure 7.11: The dependence of M_r on frequency for S5 electrolyte at various temperatures.

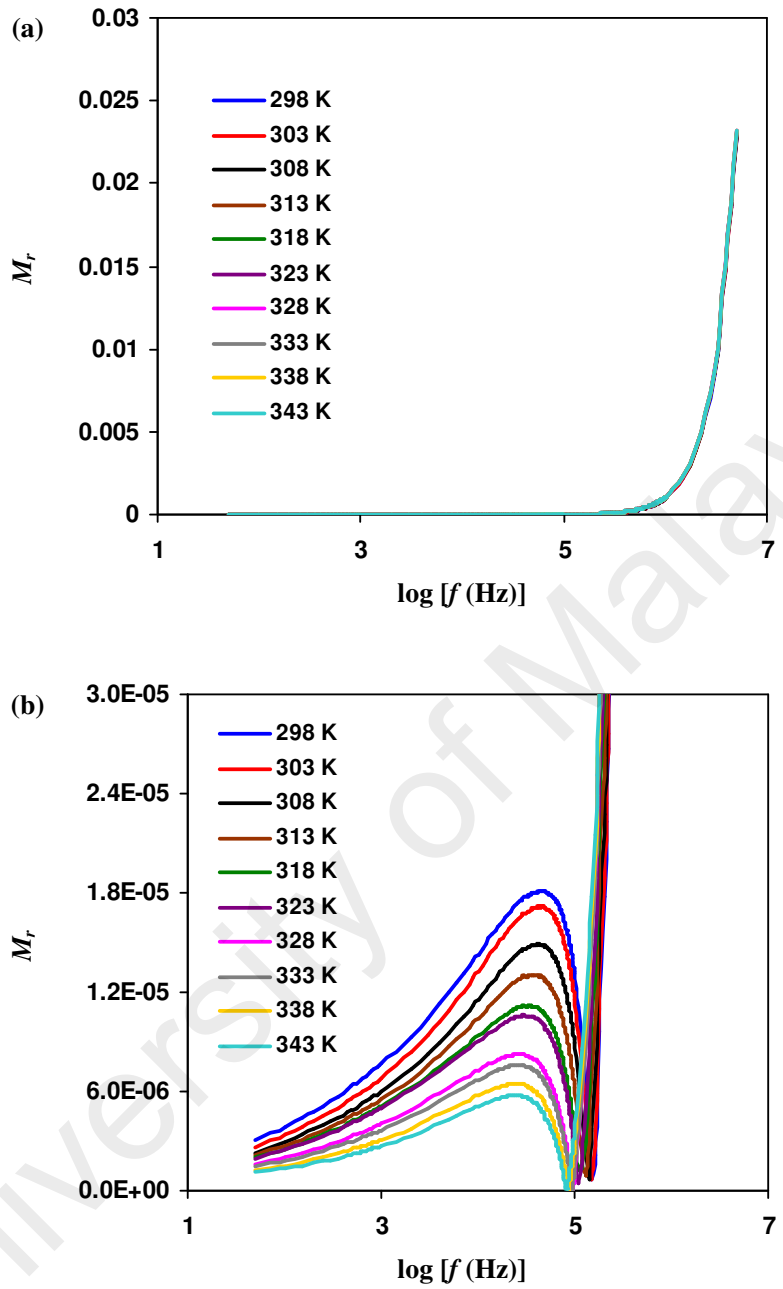

Figure 7.12: (a) The dependence of M_r on frequency for P7 electrolyte at various temperatures. (b) Enlarged of M_r plots of P7 electrolyte at various temperatures.

Figure 7.13(a) and (b) shows the variation of M_i with frequency for selected electrolytes in salted and plasticized systems, respectively, at room temperature.

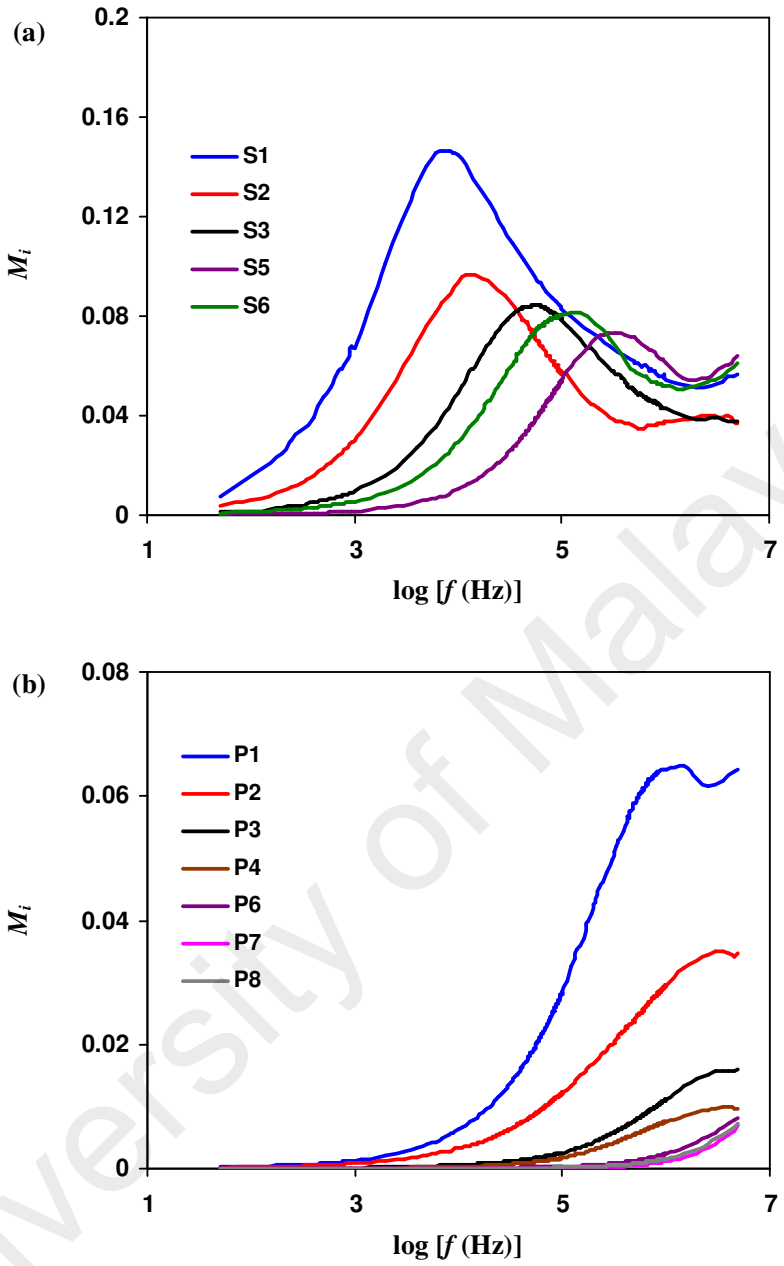

Figure 7.13: The dependence of M_i on frequency for selected electrolytes in (a) salted and (b) plasticized systems at room temperature.

From Figure 7.13(a), the M_i plot shows an asymmetric behaviour with respect to peak maxima. The left regions of the peak indicate the conduction process while the right regions of the peak are associated to the relaxation process (Badapanda, Harichandan, Nayak, Mishra, & Anwar, 2014). The peak in M_i plot can be attributed to

ionic conduction (Costa, Terezo, et al., 2010). In Figure 7.13(b), the peak is observed only in P1 and P2 plots. The characteristic frequency of the peak which corresponds to relaxation frequency is used for the evaluation of relaxation time of M_i (t_{Mi}) using the equation:

$$t_{Mi}\omega_{peak} = 1 \tag{7.5}$$

where ω_{peak} is the angular frequency of the relaxation peak. The peak is observed to shift towards high frequency region for higher conducting electrolyte indicating lower t_{Mi} for higher conducting electrolyte. The occurrence of relaxation time is the result of the efforts carried out by ionic charge carriers to obey the change in the direction of the applied field (Ramly et al., 2011). The values of t_{Mi} for the selected electrolytes in salted and plasticized systems are presented in Tables 7.1 and 7.2, respectively. From Table 7.1, S5 electrolyte possesses the lowest t_{Mi} value of 4.82×10^{-7} s. In plasticized system, t_{Mi} value is observed to decrease to 4.55×10^{-8} s as glycerol content increases to 10 wt.% (P2 electrolyte) as shown in Table 7.2.

Table 7.1: Relaxation time of M_i for selected electrolytes in salted system at room temperature.

Sample	t_{Mi} **(s)**
S1	2.27×10^{-5}
S2	1.33×10^{-5}
S3	2.84×10^{-6}
S5	4.82×10^{-7}
S6	1.06×10^{-6}

Table 7.2: Relaxation time of M_i for selected electrolytes in plasticized system at room temperature.

Sample	t_{Mi} (s)
P1	1.06×10^{-7}
P2	4.55×10^{-8}

Figure 7.14 shows the variation of M_i with frequency for S5 electrolyte at various temperatures.

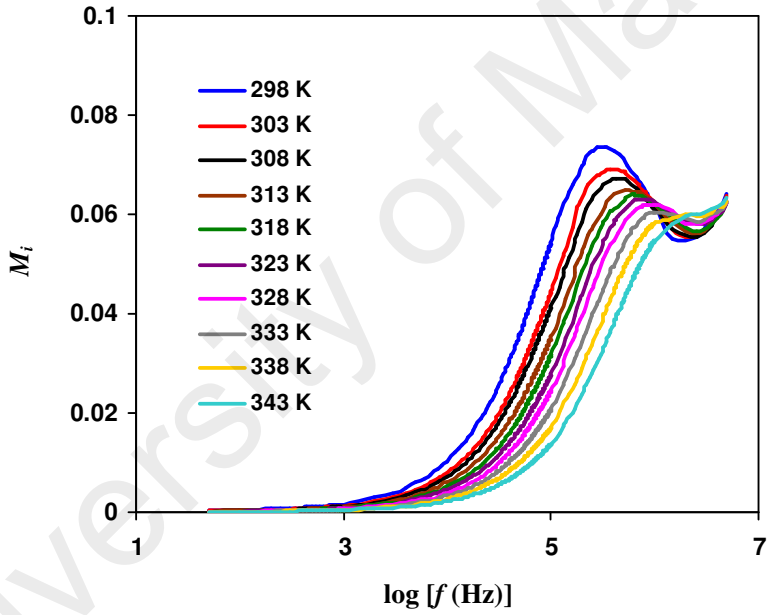

Figure 7.14: The dependence of M_i on frequency for S5 electrolyte at various temperatures.

From Figure 7.14, the long tail of small values at lower frequencies is mainly due to high capacitance values which is associated with the electrode, as a result of accumulation of charge carriers at the electrode-electrolyte interface (Aziz et al., 2010b; Hema, Selvasekarapandian, Nithya, Sakunthala, & Arunkumar, 2009; Khiar & Arof, 2010; Ramesh & Arof, 2001). The same observation can be seen in Figure 7.15 for P7

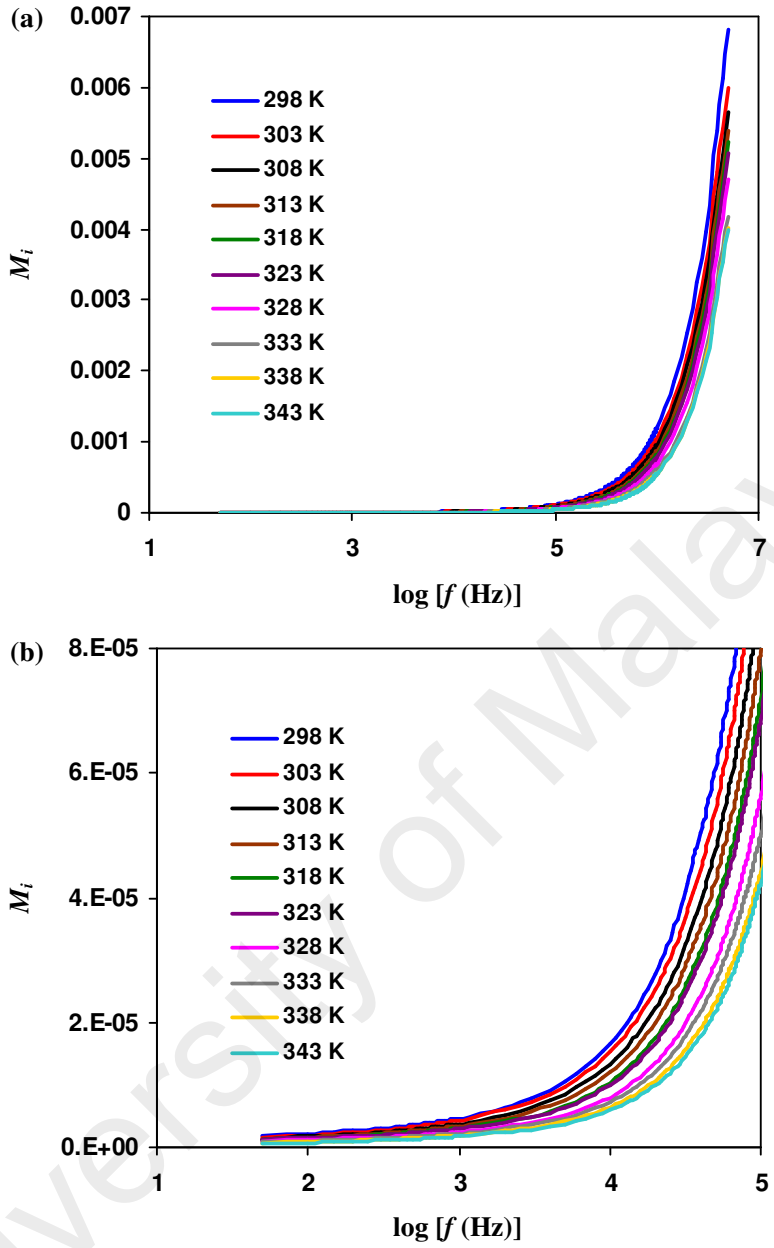

Figure 7.15: (a) The dependence of M_i on frequency for P7 electrolyte at various temperatures. (b) Enlarged of M_i plots of P7 electrolyte at various temperatures.

electrolyte. From Figure 7.14, well define peaks are observed from 298 K to 333 K. The frequency range where the peaks are located is indicative of the transition of ion mobility from a long range to short range mobility as frequency increases (Costa, Junior, & Sombra, 2010). No peak appears at 338 and 343 K due to experimental frequency limitation. The disappearance of maximum in Figure 7.15 is also due to

experimental frequency limitation. Table 7.3 lists the t_{Mi} for S5 electrolyte at various temperatures.

Table 7.3: Relaxation time of M_i for S5 electrolyte at various temperatures.

T (K)	t_{Mi} (s)
298	4.82×10^{-7}
303	4.19×10^{-7}
308	3.79×10^{-7}
313	3.06×10^{-7}
318	2.31×10^{-7}
323	1.96×10^{-7}
328	1.79×10^{-7}
333	1.59×10^{-7}

Figure 7.16 shows the dependence of frequency at M_i peak (f_{peak}) on temperature for S5 electrolyte.

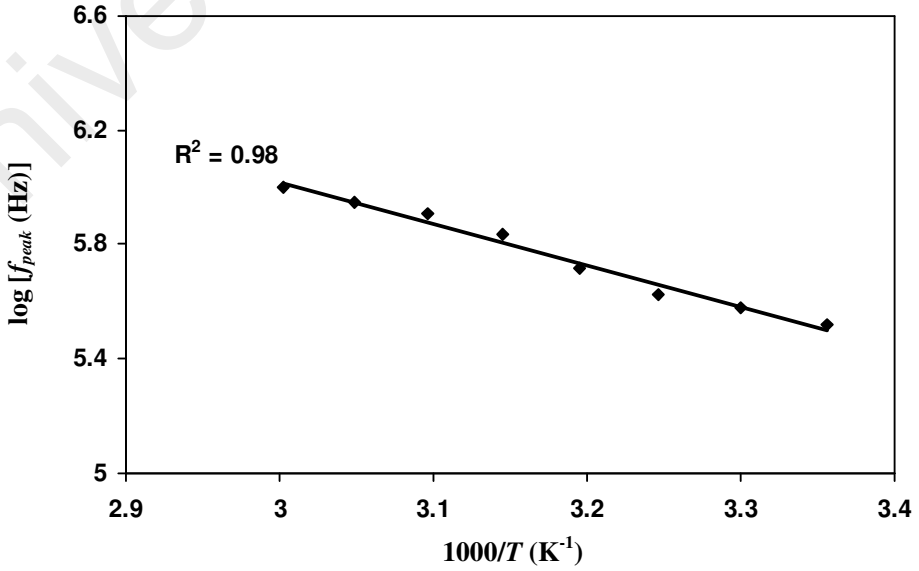

Figure 7.16: The dependence of f_{peak} on temperature for S5 electrolyte.

The plot in Figure 7.16 obeys Arrhenius rule and the relationship between f_{peak} and temperature can be described as:

$$f_{peak} = f_o \exp\left[-\frac{E_{f\ peak}}{kT}\right] \tag{7.6}$$

where f_o is the pre-exponential factor of relaxation frequency and $E_{f\,peak}$ is the activation energy of relaxation of M_i. Using the slope of the plot, $E_{f\,peak}$ for S5 electrolyte is found to be 0.29 eV, which is close to E_a value from the conductivity-temperature plot in Chapter 5.

7.4 Loss Tangent Analysis

The plot of loss tangent (tan δ) as a function of frequency helps to obtain the information of the relaxation phenomena. The value of tan δ was determined from the following equation:

$$\tan \delta = \frac{\varepsilon_i}{\varepsilon_r} \tag{7.7}$$

The frequency dependence of tan δ for electrolytes in salted system at room temperature is shown in Figure 7.17. The maximum of tan δ (tan δ_{max}), which represents the relaxation peak, is located at higher frequency for higher conducting electrolyte. In S5 plot, two peaks appear confirming the plurality of relaxation processes in the electrolyte.

The same observation can be seen in Figures 7.18 for P3 and P4 electrolytes. Due to frequency range limitation, tan δ_{max} for S1 and S8 electrolytes is not observed.

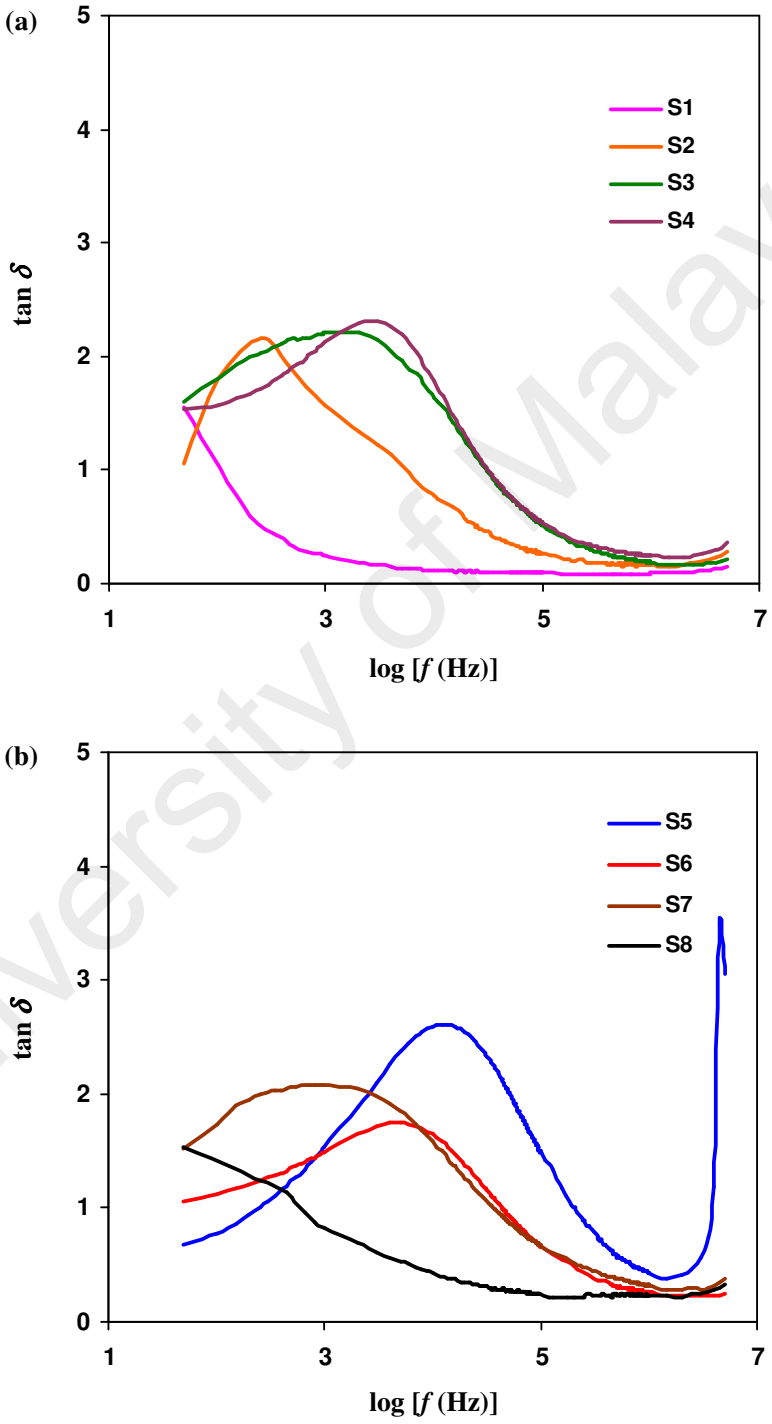

Figure 7.17: The dependence of tan δ on frequency for electrolytes in salted system at room temperature.

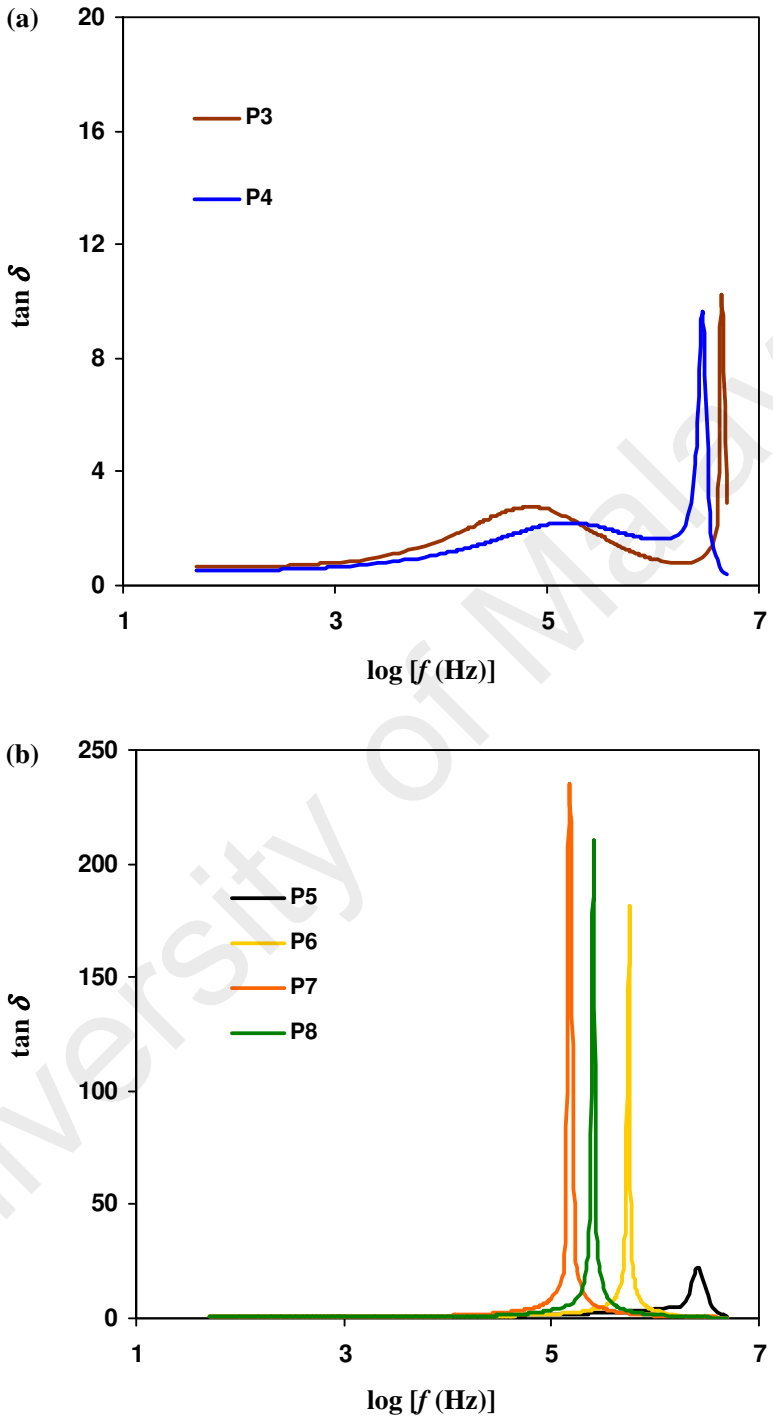

Figure 7.18: (a) The dependence of tan δ on frequency for P3 and P4 electrolytes at room temperature. (b) The dependence of tan δ on frequency for P5, P6, P7 and P8 electrolytes at room temperature.

According to Malathi et al. (2006), the relaxation at lower frequencies is attributed to α relaxation while the relaxation at higher frequencies is attributed to β relaxation. The α and β relaxations are ascribed to the relaxation mechanisms in the crystalline and amorphous phases, respectively (Hess et al., 2013; Suljovrujic, Micic, and Milicevic; 2013). In Figure 7.18, both α and β peaks appear in the tan δ plots of P3 and P4 electrolytes. Comparing the two plots, it is observed that the α peak locates at higher frequency for higher conducting electrolyte while the β peak locates at lower frequency for higher conducting electrolyte. However, only a single peak appears in each plot of P5, P6, P7 and P8 electrolytes. This single peak is known as $\alpha\beta$ absorption (Alvarez, Lorenzo, & Riande, 2005).

With respect to α peak, the relaxation time of tan δ ($t_{\tan\,\delta}$) for each electrolyte was obtained from the relation:

$$t_{\tan\,\delta}\omega_{peak} = 1 \tag{7.8}$$

The occurrence of relaxation time is the result of the efforts carried out by ionic charge carriers to obey the change in the direction of the applied field (Ramly et al., 2011). The values of $t_{tan\ \delta}$ for the electrolytes in salted and plasticized systems are presented in Tables 7.4 and 7.5, respectively. From Table 7.4, S5 electrolyte possesses the lowest $t_{tan\ \delta}$ value of 1.33×10^{-5} s. From Table 7.5, $t_{tan\ \delta}$ value is observed to decrease to 1.06×10^{-6} s as glycerol content increases to 20 wt.% (P4 electrolyte). Other reports also show that the higher conducting electrolytes have the lower values of $t_{tan\ \delta}$ (Hashim & Khiar, 2011; Ramly et al., 2011; Subban & Arof, 2003a).

Table 7.4: Relaxation time of tan δ for selected electrolytes in salted system at room temperature.

Sample	$t_{\tan \delta}$ (s)
S2	6.37×10^{-4}
S3	1.59×10^{-4}
S4	5.30×10^{-5}
S5	1.33×10^{-5}
S6	3.18×10^{-5}
S7	1.77×10^{-4}

Table 7.5: Relaxation time of tan δ for selected electrolytes in plasticized system at room temperature.

Sample	$t_{\tan \delta}$ (s)
P1	1.06×10^{-5}
P2	5.13×10^{-6}
P3	2.18×10^{-6}
P4	1.06×10^{-6}

Figures 7.19 and 7.20 show the frequency dependence of tan δ for S5 and P1 electrolytes, respectively, at various temperatures in the frequency range of 50 Hz to 1 MHz. As temperature increases, the relaxation peak is observed to shift to higher frequencies, meaning that the value of $t_{\tan \delta}$ decreases as shown in Tables 7.6 and 7.7. This phenomenon indicates that the charge carrier is thermally activated (Ramya, Selvasekarapandian, Hirankumar, Savitha, & Angelo, 2008). The height of tan δ_{max} also increases which is attributed to the decrease in resistivity of the electrolytes (Idris, Senin, & Arof, 2007).

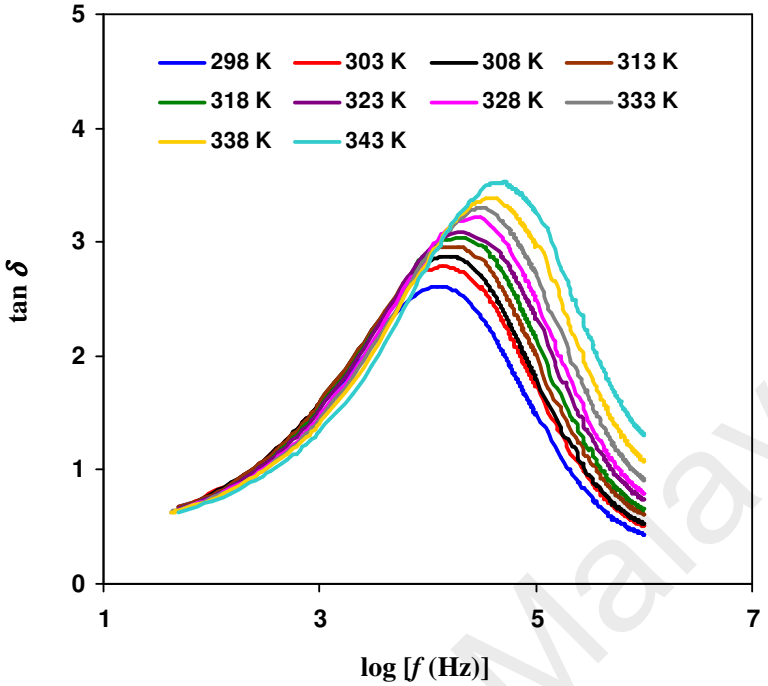

Figure 7.19: The dependence of tan δ on frequency for S5 electrolyte at various temperatures.

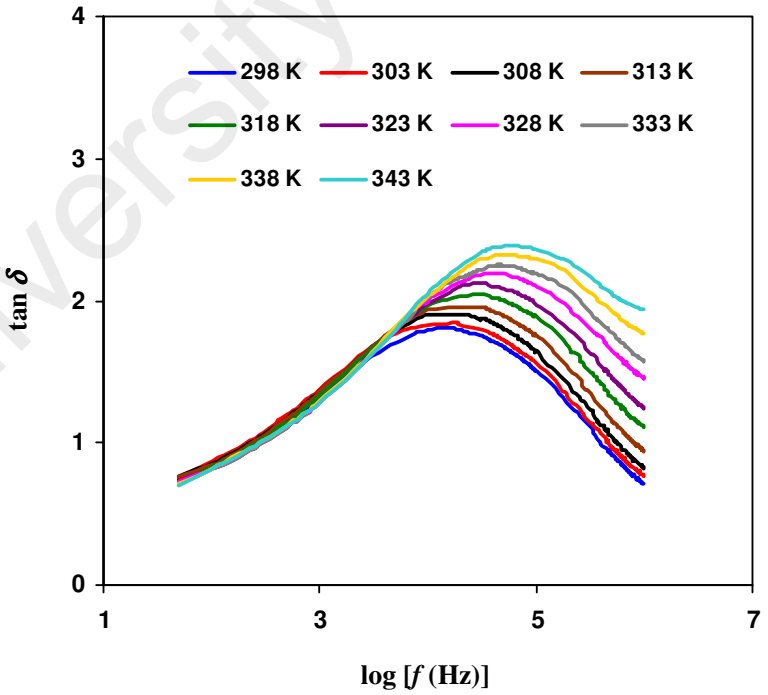

Figure 7.20: The dependence of tan δ on frequency for P1 electrolyte at various temperatures.

Table 7.6: Relaxation time of tan δ for S5 electrolyte at various temperatures.

T (K)	$t_{tan\ \delta}$ (s)
298	1.33×10^{-5}
303	1.14×10^{-5}
308	9.95×10^{-6}
313	8.38×10^{-6}
318	7.23×10^{-6}
323	6.63×10^{-6}
328	5.30×10^{-6}
333	4.68×10^{-6}
338	3.70×10^{-6}
343	3.12×10^{-6}

Table 7.7: Relaxation time of tan δ for P1 electrolyte at various temperatures.

T (K)	$t_{tan\ \delta}$ (s)
298	1.06×10^{-5}
303	8.84×10^{-6}
308	7.23×10^{-6}
313	6.63×10^{-6}
318	5.68×10^{-6}
323	4.68×10^{-6}
328	4.19×10^{-6}
333	3.33×10^{-6}
338	3.00×10^{-6}
343	2.65×10^{-6}

Figure 7.21 shows the dependence of frequency at tan δ_{max} (f_{max}) on temperature for S5 and P1 electrolytes.

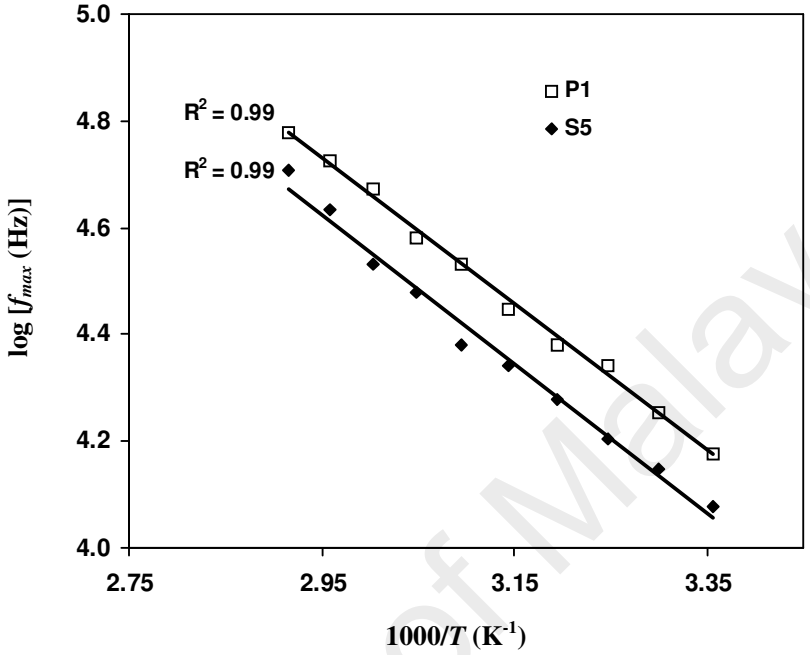

Figure 7.21: The dependence of f_{max} on temperature for S5 and P1 electrolytes.

The plot can be considered as Arrhenian since the regression value (R^2) of the points is 0.99. By employing the Arrhenius equation, the relationship between f_{max} and temperature can be described as:

$$f_{\max} = f_o \exp\left[-\frac{E_{f\max}}{kT}\right] \tag{7.9}$$

where $E_{f\max}$ is the activation energy of relaxation of tan δ. Using the slope of the plot, $E_{f\ \max}$ is obtained and found to be 0.28 and 0.27 eV for S5 and P1 electrolytes, respectively. The values of $E_{f\ \max}$ are close to E_a values from the conductivity-temperature plot for S5 and P1 electrolytes as shown in Tables 6.9 and 6.10,

respectively. Idris et al. (2007) reported that $E_{f\ \max}$ value is close to E_a value for chitosan-PEO-LiTFSI electrolyte. In the present work, since $E_{f\ \max} \approx E_a$, it can be indicated that the ion transport mechanism has the same potential energy barrier upon conducting and relaxing (Ali, Bahron, Subban, Kudin, & Yahya, 2009).

7.4.1 Scaling of tan δ

The distribution of relaxation times can be described by Kohlrausch-Williams-Watts law (Idris et al., 2007):

$$\phi(t) = \exp\left[-\left(\frac{t}{t_{\tan\delta}}\right)^{\beta_{KWW}}\right] \tag{7.10}$$

where $\phi(t)$ describes the time evolution of the electric field within a material and β_{KWW} is the Kohlrausch exponent. In the present work, the values of β_{KWW} for S5 and P1 electrolytes at selected temperatures are determined from the full width at half maximum (FWHM) of the normalized plot of tan δ/(tan δ)$_{\max}$ against f/f_{max} in Figure 7.22 using the following equation:

$$\beta_{KWW} = \frac{1.14}{FWHM} \tag{7.11}$$

For a typical Debye peak, the value of FWHM is 1.14 decades, which gives β_{KWW} = 1 for Debye relaxation (Dutta, Biswas, & De, 2002; Idris et al., 2007). According to Padmasree, Kanchan, and Kulkarni (2006), the value of β_{KWW} for a

practical solid electrolyte is less than 1. It is found that the value of β_{KWW} for S5 electrolyte at 298-343 K is 0.57-0.60. For P1 electrolyte, the value of β_{KWW} is found to be 0.42-0.47 at 298-343 K. The small value of β_{KWW} in the present system shows the deviation of relaxation with respect to Debye relaxation.

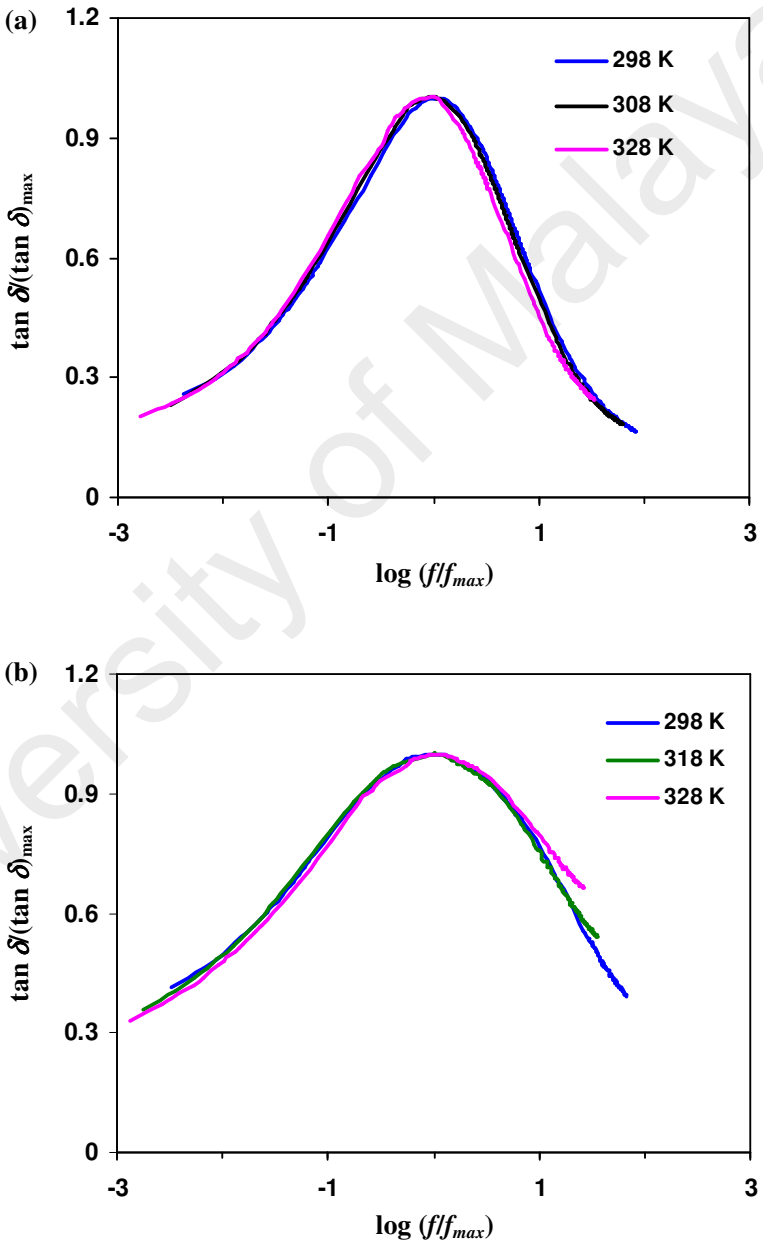

Figure 7.22: Normalized plot of tan $\delta/(\tan \delta)_{max}$ against f/f_{max} for (a) S5 electrolyte and (b) P1 electrolyte at selected temperatures.

7.5 Conduction Mechanism

The ac conduction mechanism of an electrolyte can be determined by employing Jonscher's universal power law (Buraidah et al., 2009; Winie & Arof, 2004):

$$\sigma(\omega) = \sigma_{ac} + \sigma_{dc} \tag{7.9}$$

$$\sigma(\omega) = A\omega^{s} + \sigma_{dc} \tag{7.10}$$

where $\sigma(\omega)$ is the total conductivity, σ_{ac} is the ac conductivity and σ_{dc} is the dc conductivity. The ac conductivity is represented by $A\omega^{s}$, where A is temperature dependent parameter and s is power law exponent. The ac conductivity can also be obtained using the following equation:

$$\sigma_{ac} = \varepsilon_{o}\varepsilon_{i}\omega \tag{7.14}$$

By substituting $\sigma_{ac} = A\omega^{s}$ into Equation (7.14), the value of exponent s was determined by plotting the following relation:

$$\ln \varepsilon_{i} = \ln \frac{A}{\varepsilon_{o}} + (s-1)\ln \omega \tag{7.15}$$

The exponent s was determined from the slope of the plots in Figure 7.23. In this work, the slope is only taken in the frequency region of $81 \leq f \leq 90$ kHz since at high frequency region, no or minimal impact of electrode polarization occurs (Buraidah et al., 2009).

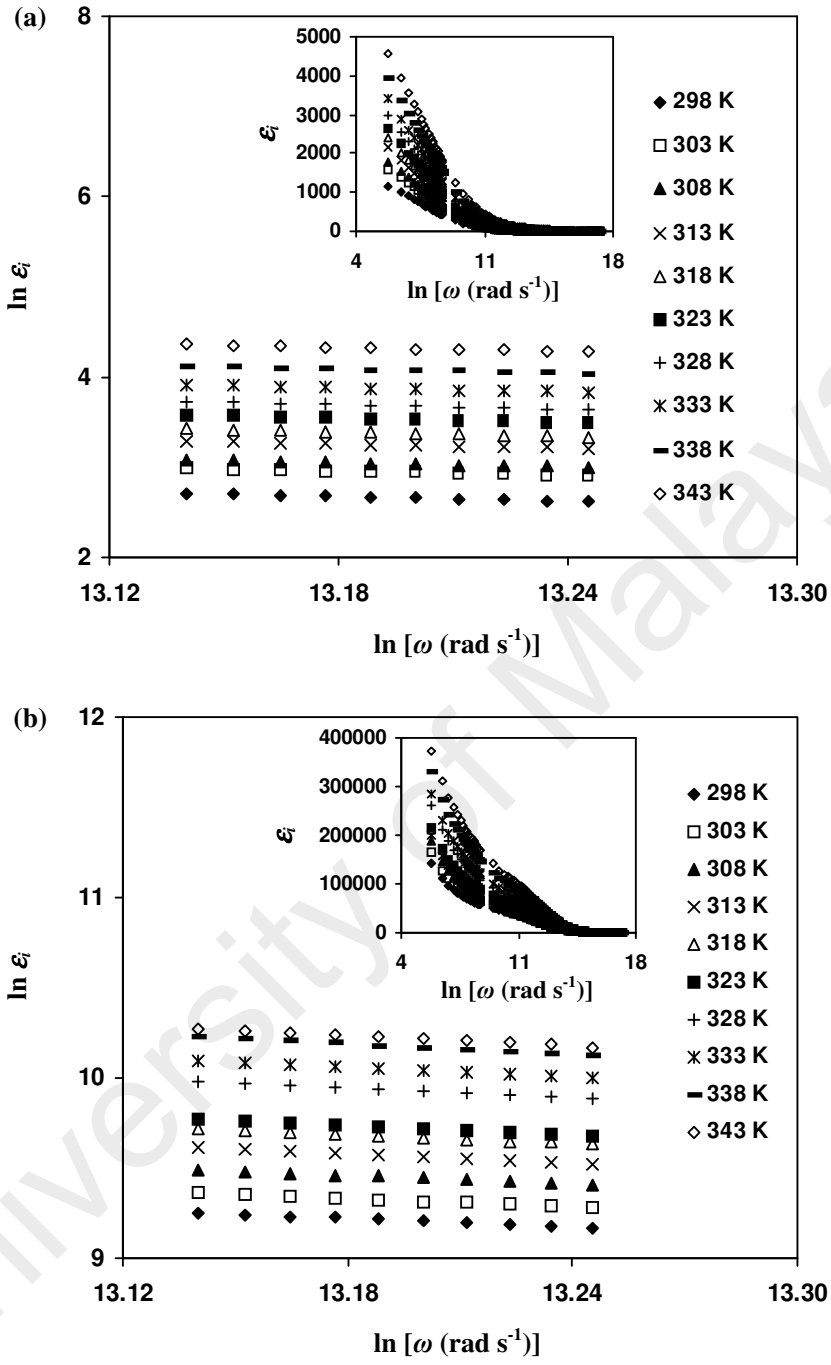

Figure 7.23: Variation of ln ε_i with frequency at different temperatures for (a) S5 electrolyte and (b) P7 electrolyte. The inset figures show the dependence of ε_i on frequency at different temperatures.

The variation of exponent *s* with temperature for S5 and and P7 electrolytes is shown in Figure 7.24.

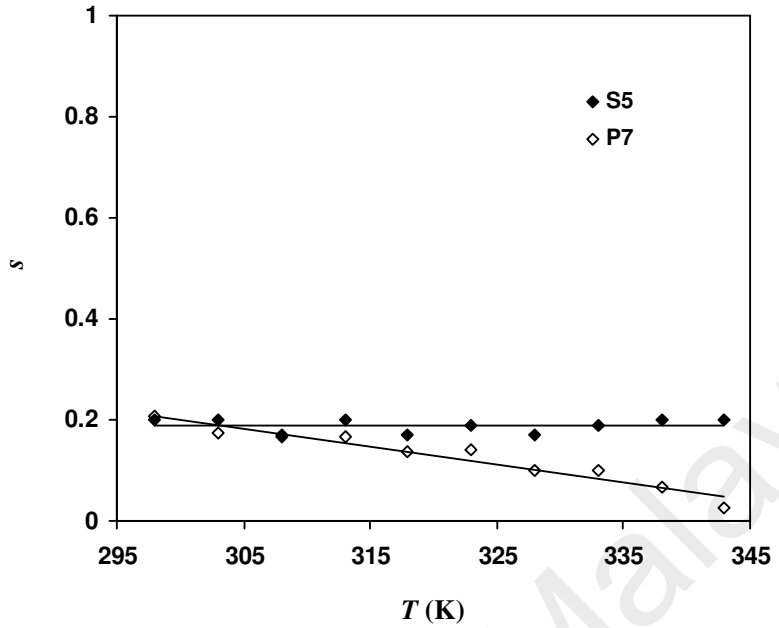

Figure 7.24: Variation of exponent *s* with temperature for S5 and P7 electrolytes.

Various models have been suggested to explain the conduction mechanism based on the variation of exponent *s* with temperature. In the correlated barrier hopping (CBH) model, the exponent *s* is predicted to be temperature dependent with exponent $s \rightarrow 1$ as $T \rightarrow 0$ K (El-Deen, 2000). The quantum mechanical tunneling (QMT) model predicts the exponent *s* is temperature independent (Kadir et al., 2009). In the overlapping large polaron tunneling (OLPT) model, the exponent *s* is predicted to decrease with increasing temperature, exhibit a minimum value and increase again as temperature increases (Kufian, Majid, & Arof, 2007). Small polaron hopping (SPH) model predicts that the exponent *s* increases with increasing temperature (Kadir et al., 2009). From the variation of exponent *s* with temperature for S5 electrolyte in Figure 7.24, it is observed that *s* is almost constant as temperature increases. The plot of *s* against *T* for S5 electrolyte can be fitted to the equation $s = 0.00004T + 0.1773$, where the small value of gradient shows that the *s* value is almost independent of temperature.

Thus, it can be implied that the conduction mechanism for S5 electrolyte follows QMT model. Buraidah and Arof (2011) reported that the conduction mechanism for chitosan-PVA-NH_4I occurred by way of QMT model in which the plot of exponent s against T can be fitted to the equation $s = 0.00004T + 0.1256$. Their result is comparable with the present work. According to this model, the polarons, which resembled by the protons and their stress fields, are able to tunnel through the potential barrier that exists between two complexation sites (Majid & Arof, 2007). The plot of s against T for P7 electrolyte in Figure 7.24 can be fitted to the equation $s = -0.0035T + 1.2653$, where $s \rightarrow 1$ as $T \rightarrow 0$ K. Thus, it can be implied that the conduction mechanism for P7 follows CBH model. The conduction mechanism for chitosan-NH_4I is reported to occur by way of CBH model in which the plot of exponent s against T can be fitted to the equation $s = -0.0023T + 1.0281$ (Buraidah et al., 2009). Their result is comparable with the present work. In this model, the ions reside in a potential well. The ions are assumed to be surrounded by several potentials e.g. the Columbic repulsive potential between the ions and the potential well. After acquiring enough energy, the ions can hop from one site to another whether back to the initial site or continue to move in the forward direction, in which the hops are thermally activated (Buraidah et al., 2009).

7.6 Summary

The dielectric properties of starch-chitosan blend based electrolytes have been presented. The values of ε_r and ε_i increase in accordance with increasing conductivity and temperature. The maximum of tan δ is located at higher frequency for higher conducting electrolyte, indicating lower relaxation time of tan δ for higher conducting electrolyte. Relaxation time of tan δ decreases with increasing temperature. The

activation energy of relaxation of tan δ for S5 and P1 electrolytes are 0.28 eV and 0.27 eV, respectively. Scaling of tan δ shows the deviation of the relaxation from the Debye type relaxation. The conduction mechanism of the ion for S5 and P7 electrolytes is best explained by QMT and CBH models, respectively.

CHAPTER 8

FABRICATION AND CHARACTERIZATION OF ELECTROCHEMICAL DEVICES

8.1 Introduction

Based on Chapter 5 to Chapter 7, it is proven that P7 electrolyte obtained the highest room temperature conductivity of $(5.11 \pm 1.60) \times 10^{-4}$ S cm^{-1}. G.P.Pandey et al. (2011) stated that polymer electrolyte which possesses a conductivity of ~ 10^{-4} S cm^{-1} is acceptable from the electrochemical double layer capacitor (EDLC) application point of view. According to Pratap et al. (2006), electrolyte with conductivity of ~ 10^{-4} S cm^{-1} is suitable enough for application in proton battery.

In this chapter, P7 electrolyte is applied as separator in an EDLC and proton batteries. A variety of techniques for characterizing the devices are presented.

8.2 Electrochemical Stability of Electrolytes

The electrochemical stability of electrolyte is a crucial parameter to be evaluated for their application point of view in electrochemical devices (Pandey, Kumar, & Hashmi, 2010). Linear sweep voltammetry (LSV) measurement was carried out in order to determine the decomposition voltage of the electrolyte, i.e., the maximum operational voltage of an electrochemical device employing the electrolyte (Arof et al., 2010).

Figure 8.1 shows the LSV curve of P7 electrolyte at 5 mV s^{-1} scan rate at room temperature. As for comparison, LSV measurements for other selected electrolytes were also been carried out. The results are shown in the same figure.

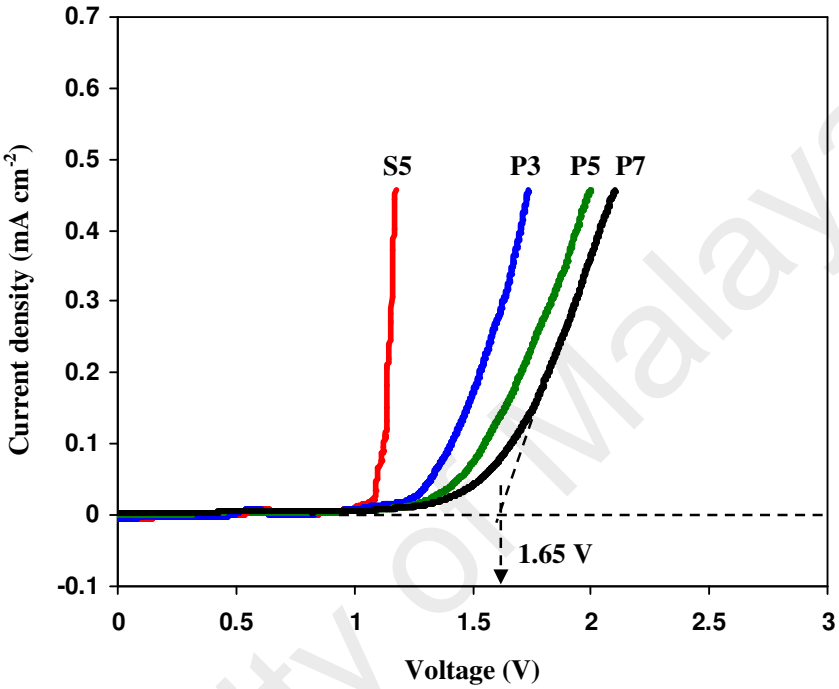

Figure 8.1: LSV curves of selected electrolytes at 5 mV s^{-1}.

From Figure 8.1, it is clearly seen that among the electrolytes, the electrochemical stability of S5 electrolyte is the narrowest while P7 electrolyte shows wider electrochemical stability than other electrolytes. Therefore, it can be concluded that the addition of glycerol has enhanced the electrochemical stability of the electrolyte. According to Asmara et al. (2011), electrochemical stability may be influenced by the dielectric constant of the polymer host and the lattice energy of the salt. The authors added that a high dielectric constant of the polymer would give a higher concentration of charge carriers. In the present work, since the same polymer host and salt are used in the electrolytes, the difference in electrochemical stability

could be due to the concentration of charge carriers, i.e. number density of ions. In Chapter 6, P7 electrolyte obtained the highest number density of ions, followed by P5, P3 and S5 electrolytes, respectively. From this result, it may be inferred that the decomposition voltage is influenced by the conductivity (Shuhaimi, 2011). The current increases drastically when the potential reaches 1.65 V indicating the decomposition of P7 electrolyte. Samsudin et al. (2014) reported that the decomposition voltage of carboxymethyl cellulose-NH_4Br electrolyte is 1.42 V and the electrolyte was used in the fabrication of proton batteries. The decomposition voltage of methyl cellulose-NH_4NO_3 is reported to be ~ 1.5 V and the electrolyte was used in the fabrication of an EDLC (Shuhaimi, Majid, & Arof, 2009). The present result shows that the highest conducting electrolyte in the present work is suitable for fabrication of EDLC and proton batteries.

8.3 EDLC Characterization

The EDLC was fabricated by sandwiching P7 electrolyte with two carbon based electrodes using perspex plates (see Figure 3.11). The EDLC was characterized using galvanostatic charge-discharge measurement and cyclic voltammetry (CV) technique at room temperature.

8.3.1 Galvanostatic Charge-Discharge

The cycle life performance is important for practical applications. Figure 8.2 shows the typical charging and discharging performance of the EDLC at constant current density of 0.063 mA cm^{-2} between 0 to 0.85 V for selected cycles. The discharge

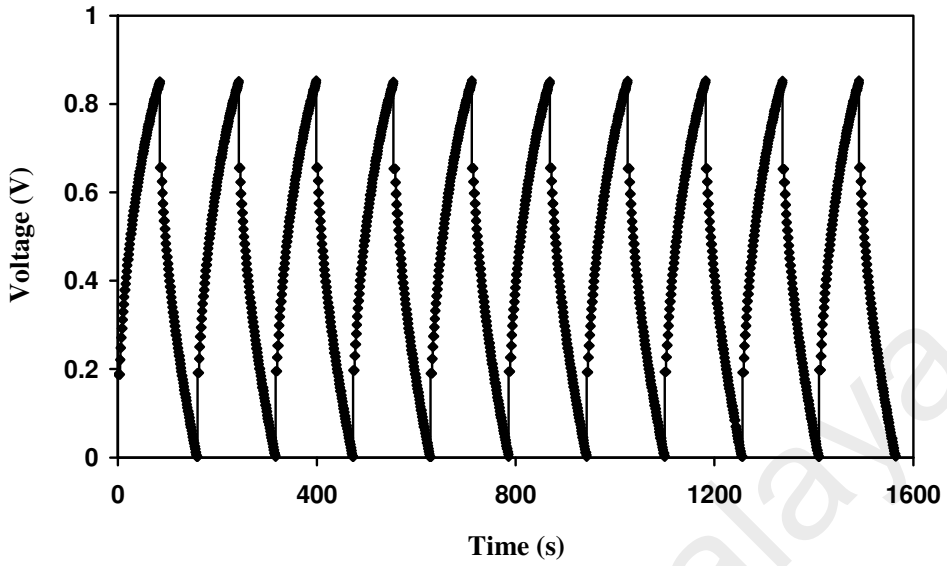

Figure 8.2: Charge-discharge curves of the EDLC at 81st to 90th cycles.

curves are observed to be almost linear, confirming the capacitive behaviour of the fabricated EDLC (Asmara et al., 2011). The instantaneous voltage drop upon discharge is attributed to the internal resistance resulted from resistance due to electrolyte, current collector and the inter-fluid resistance between the current collector and the electrolyte (Arof et al., 2012). This internal resistance is referred as equivalent series resistance (ESR) of the EDLC (G.P. Pandey et al., 2011). ESR was calculated using the equation below:

$$ESR = \frac{V_{drop}}{i} \tag{8.1}$$

where V_{drop} is the voltage drop upon discharge and i is the constant current. For the entire 500 cycles, ESR ranges from 2.0 kΩ to 2.9 kΩ.

The charge-discharge curves in Figure 8.2 are quite comparable to those reported in the literature (Arof et al., 2010; Kumar & Bhat, 2009; Shuhaimi et al., 2009; Sudhakar & Selvakumar, 2012). Using the slope of the discharge curves, the values of specific capacitance (C_s) were calculated using the following equation:

$$C_s = \frac{i}{m}\left(\frac{1}{s_d}\right) \tag{8.2}$$

Here, m is the mass of active material and s_d is the slope of discharge curve. The result is represented in Figure 8.3. Towards the 70th cycle, the value of C_s is observed to decrease to 3915 mF g^{-1}. After the 70th cycle, the value of C remains constant at ~ 3444 mF g^{-1} until it completes 500 cycles.

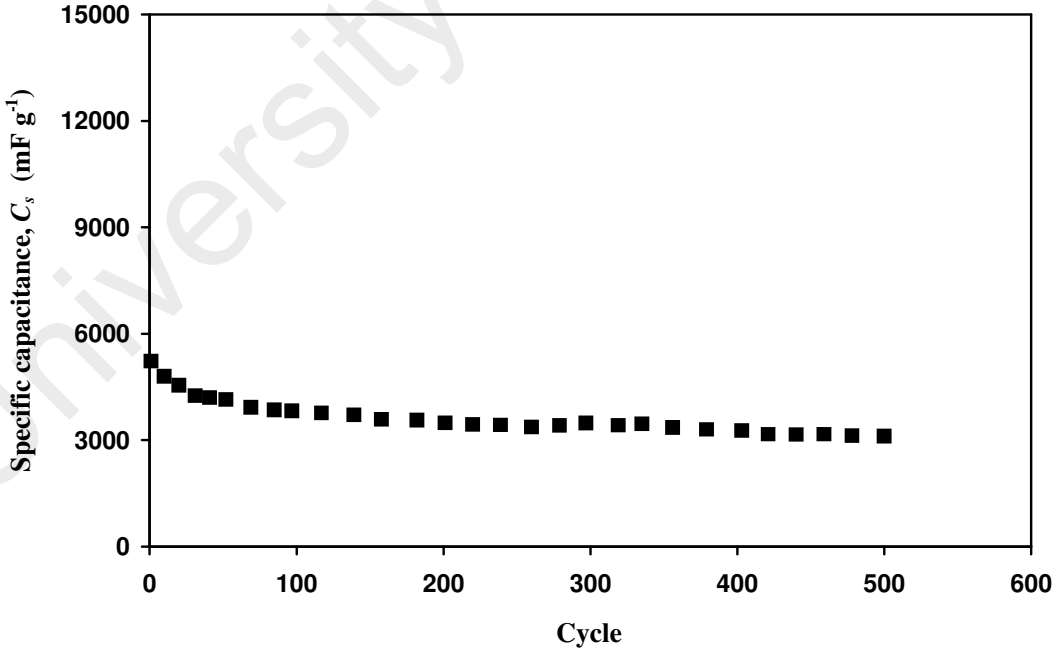

Figure 8.3: Specific capacitance versus cycle number.

It is known that the C_s value of EDLC relies on the conductivity of electrolyte as reported in the literature (Liew et al., 2014; Liew, Ramesh, & Arof, 2015; Lim, Teoh, Liew, & Ramesh, 2014b; Majid, 2007). The highest conducting electrolyte in this work obtains a conductivity of the order ~ 10^{-4} S cm^{-1}. From the literature, the C_s value obtained in this work is comparable with that of EDLCs using activated carbon electrodes and solid polymer electrolyte (SPE) ($\sigma \leq 10^{-4}$ S cm^{-1}) as listed in Table 8.1.

Table 8.1: Comparison of specific capacitance of the present EDLC with other reports using galvanostatic charge-discharge measurement unless stated.

Electrolytes	**σ (S cm^{-1})**	**Charge-discharge cycles**	**C_s (F g^{-1})**	**References**
Methyl cellulose-NH_4NO_3	2.10×10^{-6}	Not stated	1.67 (at 15th cycle)	Shuhaimi et al., 2009
PVA-$NH_4C_2H_3O_2$	$(1.94 \pm 0.01) \times 10^{-5}$	-	0.14 (From CV)	Liew et al., 2015
Chitosan-H_3PO_4-Al_2SiO_5	$(1.12 \pm 0.18) \times 10^{-4}$	100	0.216-0.220	Majid, 2007
Chitosan-H_3PO_4-NH_4NO_3-Al_2SiO_5	$(1.82 \pm 0.10) \times 10^{-4}$	100	$0.22 < C_s < 0.25$	Majid, 2007
Starch-chitosan-NH_4Cl-glycerol	$(5.11 \pm 1.60) \times 10^{-4}$	500	~ 3.44	Present work

Ionic mobility has an influence on the electrolyte's conductivity, which in turn can affect the device's performance. The average ionic mobility for the highest conducting electrolyte in the present work is $(4.42 \pm 1.23) \times 10^{-4}$ cm^2 V^{-1} s^{-1}, obtained using the Rice and Roth model. The C_s value of EDLC using activated carbon electrodes and chitosan-H_3PO_4-NH_4NO_3-Al_2SiO_5 electrolyte with ionic mobility of 3.17×10^{-6} cm^2 V^{-1} s^{-1} (obtained using Rice and Roth model) is found to be

($200 < C_s < 250$) mF g^{-1} (Majid, 2007). Thus, from this comparison, it can be concluded that the higher the ionic mobility, the greater the C_s value.

Coulombic efficiency (η) is an important parameter since it represents the cycling stability of the EDLC (Shukur et al., 2014). The Coulombic efficiency of the EDLC at each cycle was calculated according to the equation:

$$\eta = \frac{t_d}{t_c} \times 100\% \tag{8.3}$$

where t_d is the discharge time and t_c is the charge time. The plot of efficiency against cycle number is shown in Figure 8.4. Towards the 50th cycle, the efficiency increases from 69% to 91%. The efficiency remains constant at ~ 90-95% thereafter. Efficiency of ~ 90% indicates the intimate contact between electrolyte and electrodes (Lim et al., 2014a). This result shows that the present EDLC exhibits good cycling stability for 500 cycles.

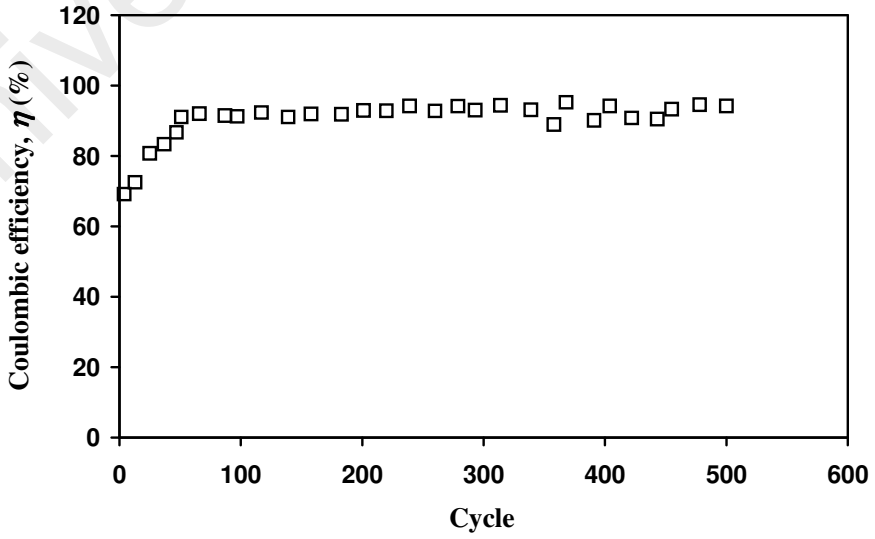

Figure 8.4: Coulombic efficiency versus cycle number.

8.3.2 Cyclic Voltammetry

The performance of the EDLC was studied by CV at different scan rates in the potential range of 0 to 0.85 V at room temperature. From the CV measurement of the EDLC, the nature of charge storage at the electrode-electrolyte interfaces can be gathered (Kumar, Pandey, & Hashmi, 2012). Figure 8.5 depicts the cyclic voltammogram of the EDLC before the charge-discharge process (fresh EDLC) at different scan rates.

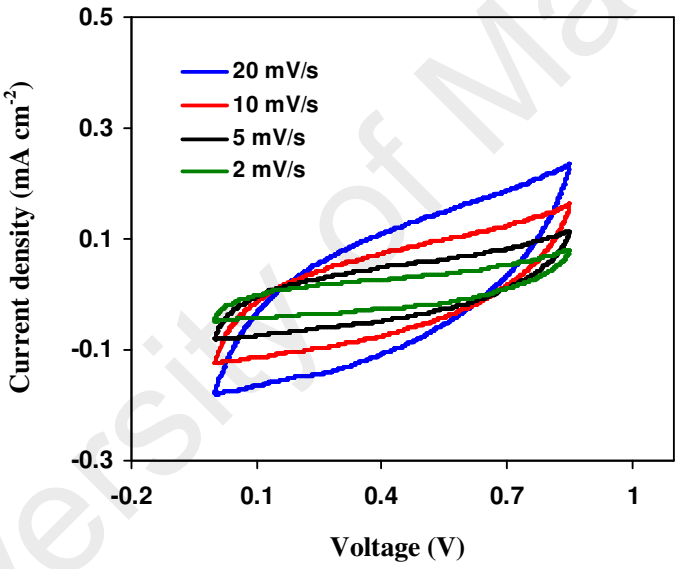

Figure 8.5: Cyclic voltammogram of fresh EDLC at different scan rates.

From Figure 8.5, the cyclic voltammogram of the fresh EDLC turns from leaf like shape to almost rectangular shape as the scan rate decreases from 20 mV s^{-1} to 2 mV s^{-1}. As the scan rate increases, the discrepancy of the cyclic voltammogram from a perfect rectangular shape can be assigned to the internal resistance and the carbon porosity, which produces a current dependence of the potential (Kadir & Arof, 2011). As the scan rate decreases, nearly rectangular behavior without redox peaks was

observed inferring that the capacitance is stored by an accumulation of ions between the electrode-electrolyte interfaces which is known as electric double layer capacitance (Ma et al., 2014). The values of C_s at different scan rates were calculated using the following equation (Chen, Beidaghi, et al., 2010; Chen, Fan, Gu, Bao, & Wang, 2010):

$$C_s = \frac{\int_{V_1}^{V_2} I(V)\,dV}{2m(V_2 - V_1)\left(\frac{dV}{dt}\right)} \tag{8.4}$$

where $I(V)$ is the current at a given potential, V_1 is the initial potential, V_2 is the final potential, $\int_{V_1}^{V_2} I(V)\,dV$ is the area of the plot, (V_2-V_1) is the potential window and $\frac{dV}{dt}$ is the scan rate. Table 8.2 lists the C_s values for fresh EDLC at different scan rates.

Table 8.2: Specific capacitance using CV at different scan rates.

Scan rate (mV s^{-1})	**C_s for fresh EDLC (F g^{-1})**	**C_s for EDLC after 500 charge-discharge cycles (F g^{-1})**
20	1.92	1.14
10	2.72	1.74
5	3.60	2.44
2	5.25	3.64

From Table 8.2, it is observed that the C_s value decreases as the scan rate increases. As the scan rate increases, energy loss increases and the stored charge on the electrode surface decreases leading to a decrease in C_s (Nasibi, Golozar, & Rashed, 2012). At low scan rates, ions can utilize all the vacant sites in the active electrode material, in view of the fact that the ions have enough time to diffuse into vacant sites

leading to the higher value of C_s (Lim et al., 2014b). It can be concluded that the present EDLC shows the characteristic of capacitor cells, since it is scan rate dependent (Hashmi, Kumar, & Tripathi, 2004).

The CV of the EDLC after 500 galvanostatic charge-discharge cycles at various scan rates is shown in Figure 8.6.

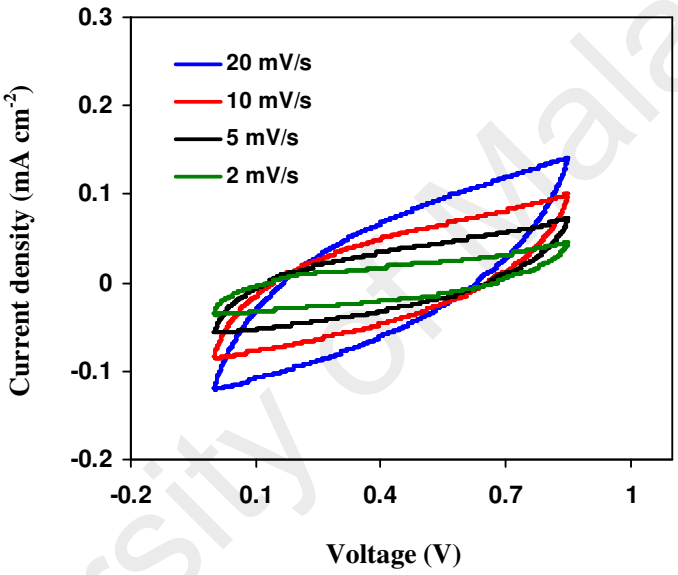

Figure 8.6: Cyclic voltammogram of the EDLC after 500 charge-discharge cycles at different scan rates.

By comparing the CV curves in Figures 8.5 and 8.6, it can be observed that at all scan rates, the enclosed area of the CV curve become smaller after 500 charge-discharge cycles, suggesting that the value of C_s decreases. This phenomenon is resulted from the effect of internal resistance. Internal resistance is reported to increase with increasing charge-discharge cycle (Arof et al., 2010; Liew et al., 2015; Pendashteh, Rahmanifar, Kaner, & Mousavi, 2014). At higher resistance, less charges flow causes less current flow which result a decrease in C_s value as shown in Table 8.2.

8.4 Proton Batteries Characterization

Primary proton batteries were fabricated by sandwiching P7 electrolyte with anode and cathode in coin cells. The properties of the primary proton batteries i.e. open circuit potential (OCP), discharge properties as well as *I-V* and *J-P* characteristics were identified. To test the charging-discharging ability, P7 electrolyte was also employed in secondary proton battery.

8.4.1 Primary Proton Batteries

The OCP of the primary proton batteries for 48 h is presented in Figure 8.7. It can be observed that there is a slight decrease of potential at initial hours. This phenomenon could be due to the oxidation of anode (Samsudin et al., 2014). The

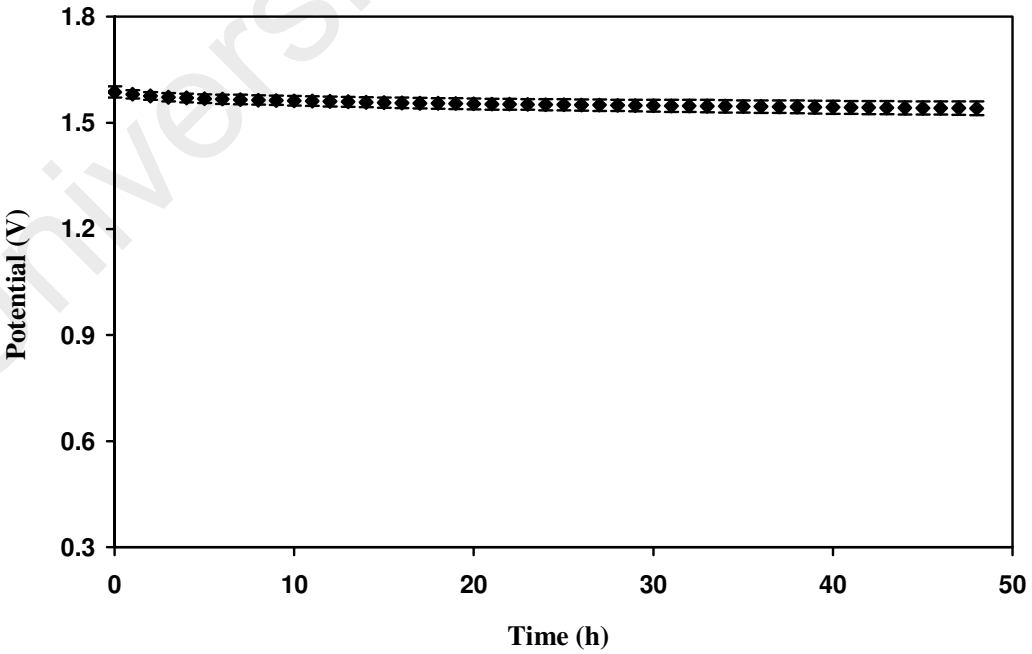

Figure 8.7: OCP of primary proton batteries for 48 h.

potential of the batteries is then stabilized at (1.54 ± 0.02) V until the 48th hour. This result shows that the fabricated proton batteries are practically stable in an open circuit condition (Jamaludin & Mohamad, 2010).

Table 8.3 lists the comparison of OCP value of the present primary proton batteries with other works which use the same anode and cathode active materials.

Table 8.3: Comparison of OCP value of the present primary proton batteries with other reports.

Electrolytes	OCP (V)	Time (h)	References
PVA-Chitosan-NH_4NO_3-EC	1.63	24	Kadir et al., 2010
Chitosan-NH_4NO_3-EC	1.56 ± 0.06	24	Ng & Mohamad, 2006
PEO-$(NH_4)_2SO_4$	0.647	Not stated	Ali et al., 1998
Cellulose acetate-$NH_4CF_3SO_3$-EC	1.4	24	Saaid et al., 2009
Starch-chitosan-NH_4Cl-glycerol	1.54 ± 0.02	48	Present work

In the present work, the possible chemical reactions at the anode and cathode are shown in Table 8.4 (Alias et al., 2014; Vanysek, 2011).

Table 8.4: Possible chemical reactions occur at the electrodes of the proton batteries (Alias et al., 2014; Vanysek, 2011).

Electrode	Possible reaction	*V* (V)
Anode	$Zn \rightarrow Zn^{2+} + 2e^-$	0.76
	$ZnSO_4 \cdot 7H_2O \rightarrow ZnSO_4 + 7H^+ + 7OH^-$	-0.82
Cathode	$MnO_2 + 2e^- + 4H^+ \rightarrow Mn^{2+} + 2H_2O$	1.22
Overall	$Zn + ZnSO_4 \cdot 7H_2O + MnO_2 + \rightarrow Zn^{2+} + 2e^- + ZnSO_4 + 7H^+ + 7OH^- 2e^- + 4H^+ + Mn^{2+} + 2H_2O$	1.28

From Table 8.4, the overall reaction should provide the batteries with potential of 1.28 V. Result of OCP shows that the potential of present batteries is (1.54 ± 0.02) V, which is 20.31% higher than the expected potential. The difference between the theoretical and experimental result of OCP is due to several factors, such as concentration and transport of ions (Botte & Muthuvel, 2012). A similar result has been reported in the literature (Alias et al., 2014; Samsudin et al., 2014).

The discharge profiles of the proton batteries at different constant currents are depicted in Figure 8.8. It is observed that at each constant discharge current, the plateau region of the discharge curve is lasted at ~ 1.0 V before the potential decreases significantly. During the discharge process, the zinc is oxidized and MnO_2 is reduced (McComsey, 2001). This phenomenon forms Mn_2O_3-ZnO, which is a semiconductor

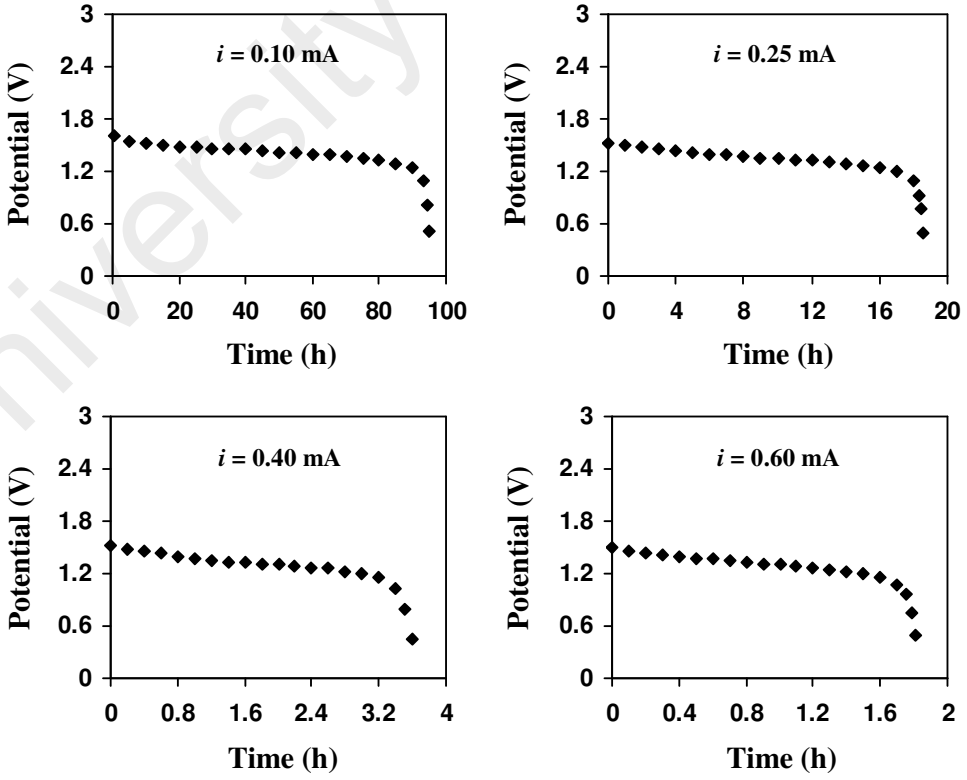

Figure 8.8: Discharge profiles of primary proton batteries at different constant currents.

particle (McComsey, 2001; Rahman et al., 2013). The sudden decrease in potential at ~ 1.0 V is caused by the increase in charge transfer resistance due to the increasing formation of Mn_2O_3-ZnO (Wang et al., 2005). It is observed that at lower constant current, the plateau region become wider. Using the value of the discharge time at the plateau region ($t_{plateau}$), the discharge capacity (Q) was calculated using the following equation:

$$Q = it_{plateau} \tag{8.5}$$

Table 8.5 summarizes the discharge properties of the primary proton batteries at different constant discharge currents. The discharge capacity is found to increase with decreasing discharge current. At high discharge current, the variation of ion concentration along the pores depth of an electrode increases, forcing a non-uniform H^+ insertion process (Roscher, Bohlen, & Vetter, 2011).

Table 8.5: Discharge capacity of the primary proton batteries at different constant discharge currents.

Discharge current (mA)	***Q*** **(mA h)**
0.60	1.04
0.40	1.37
0.25	4.57
0.10	9.36

The *I-V* and *J-P* characteristics of the primary proton batteries are presented in Figure 8.9.

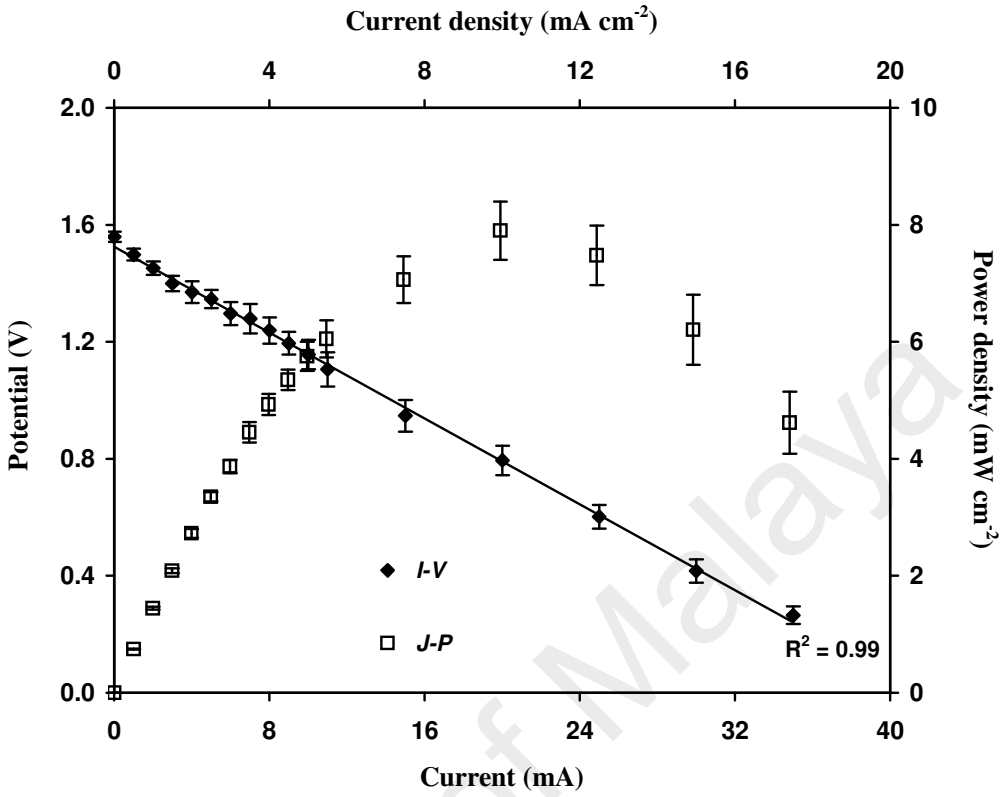

Figure 8.9: Plot of *I-V* and *J-P* of the primary proton batteries.

From Figure 8.9, the *I-V* plot is observed to be linear, indicating that the electrode polarization is dominated by the ohmic contributions (Yap & Mohamad, 2007). The linear *I-V* plot can be represented by the equation:

$$V = V_o - Ir \tag{8.6}$$

where V_o is the OCP and r is internal resistance. The r value is calculated from the slope of the *I-V* plot and found to be 36.74 Ω. The short circuit current of the batteries is 35 mA. From the *J-P* plot, the maximum power density is (7.90 ± 0.50) mW cm^{-2}. The characteristics of the present primary proton batteries are comparable with other reported works (Kadir et al., 2010; Ng & Mohamad, 2006; Shukur, Ithnin, et al., 2013).

8.4.2 Secondary Proton Batteries

The OCP of the secondary proton batteries for 48 h is shown in Figure 8.10.

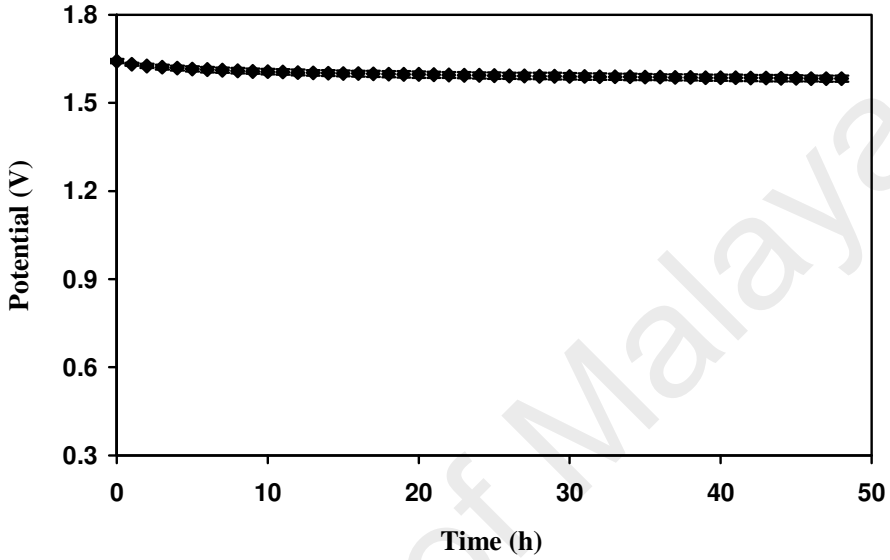

Figure 8.10: OCP of secondary proton batteries for 48 h.

In order to fabricate a rechargeable (secondary) proton battery, the highest conducting electrolyte solution has been added to the cathode. The addition of the electrolyte in liquid phase is predicted to enable the intercalated proton to deintercalate from the cathode active material and enter the anode through the SPE, thus obtain a rechargeable battery (Kadir et al., 2010). As shown in Figure 8.10, the OCP of the secondary battery is lasted at (1.58 ± 0.01) V, slightly higher than the primary one.

Table 8.6 lists the comparison of the OCP value of the present secondary proton batteries with other works using SPE.

Table 8.6: Comparison of OCP value of the present secondary proton batteries with other reports.

Electrolytes	OCP (V)	Time (h)	References
Carboxymethyl cellulose-NH_4Br	1.36	24	Samsudin et al., 2014
PEO-NH_4ClO_4-PC	1.55	24	Pratap et al., 2006
Chitosan-PVA-NH_4NO_3-EC	1.65	24	Kadir et al., 2010
PEO-NH_4SCN-Mg-Zn ferrite	1.57	Not stated	Pandey, Singh, Asthana, Dwivedi, & Agrawal, 2011
Starch-chitosan-NH_4Cl-glycerol	1.58 ± 0.01	48	Present work

Where;
Mg = magnesium **PC = propylene carbonate**
NH_4ClO_4 = ammonium perchlorate

The typical charge-discharge profiles of the secondary proton battery using a constant current of 0.35 mA is displayed in Figure 8.11. At the first cycle, the battery is discharged to 1.00 V before regain its initial potential of 1.58 V after been recharged. This charge-discharge process of the battery cycled for 40 times and lasted for ~ 440 h.

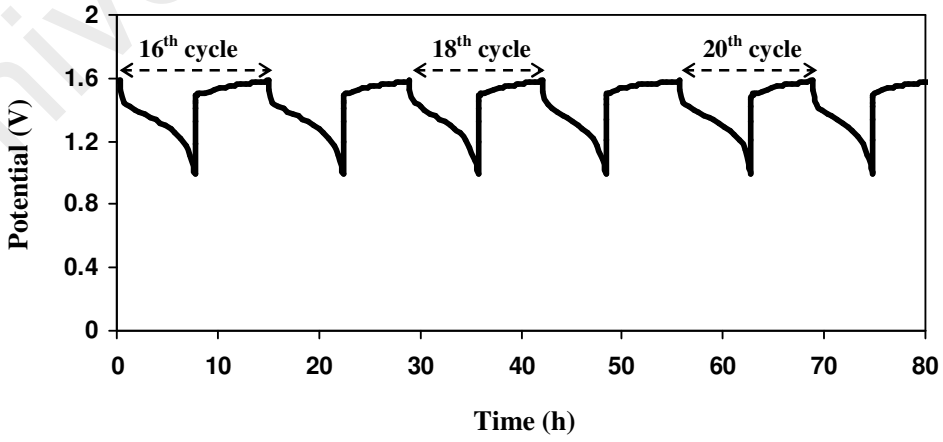

Figure 8.11: Charge-discharge profiles of the secondary proton battery at 16th to 21st cycles.

Figure 8.12 depicts the discharge curves of the secondary batteries at selected cycles.

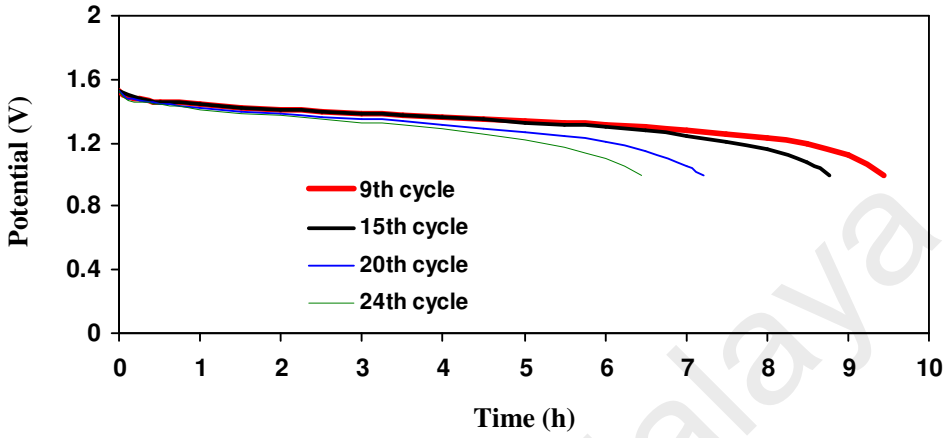

Figure 8.12: Discharge curves of the secondary proton battery at selected cycles.

The calculation of specific discharge capacity (Q_s) has been done with respect to the weight of active cathode material (MnO_2) and is plotted in Figure 8.13. The plot in Figure 8.13 can be divided into three regions. In region 1, the Q_s value decreases from 6.13 mA h g^{-1} to 2.76 mA h g^{-1} after 2nd cycle. However, the Q_s value increases

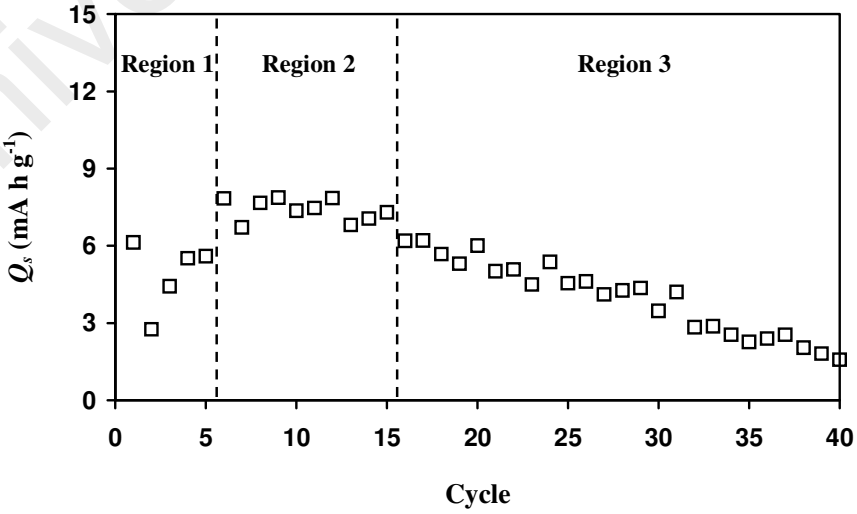

Figure 8.13: Specific discharge capacity versus cycle number.

thereafter and reaches 7.83 mA h g^{-1} after 6th cycle. The decrease in Q_s after the first two cycles can be attributed to the electrode-electrolyte contact, which is not always perfect at the first charge (Guinot, Salmon, Penneau, & Fauvarque, 1998; Mohamad et al., 2003). After the 2nd cycle, an improvement in the electrode-electrolyte contact has generate active materials at the surface of the electrodes to oscillate in $ZnSO_4 \cdot 7H_2O$ discharge state, leading to an increase in Q_s value (Mohamad et al., 2003; Samsudin et al., 2014). In Region 2, the Q_s value is observed to be almost stable from 6th cycle to 15th cycle. At this period, since the electrode-electrolyte contact has been stabilized, the intercalation of proton at the cathode occurs at a nearly constant rate. The longest discharge time occurs during the 9th cycle thus obtain the optimal Q_s value of 7.87 mA h g^{-1}. In Region 3, the Q_s value is observed to decrease until the 40th cycle. This phenomenon may be caused by the poor interfacial stability of the electrode thus develop the large interfacial resistance between the electrode and the electrolyte as reported for other proton batteries (Mishra, Hashmi, & Rai, 2014; Samsudin et al., 2014; Selvasekarapandian, Hema, Kawamura, Kamishima, & Baskaran, 2010).

8.5 Summary

An EDLC has been successfully fabricated employing P7 electrolyte. The EDLC performed at 0.063 mA cm^{-2} current density for 500 cycles. The specific capacitance of the EDLC was obtained at ~ 3444 mF g^{-1}. Primary and secondary proton batteries have been successfully fabricated using P7 electrolyte. The OCP of the primary proton batteries after 48 h is (1.54 ± 0.02) V, while that of secondary proton batteries is (1.58 ± 0.01) V. The discharge capacity of the primary proton batteries is enhanced by lowering the discharge current. The internal resistance and short circuit current of the

primary proton batteries are 36.74 Ω and 35 mA, respectively. The rechargeability of the secondary proton battery is able to perform up to 40 cycles for ~ 440 h.

CHAPTER 9

DISCUSSION

Research on solid polymer electrolytes (SPEs) have been actively carried out in view of their application in electrochemical devices such as EDLC, electrochromic display devices, fuel cells, solid-state batteries and sensors. Problems associated with liquid electrolytes such as solvent vaporization, leakage and corrosion can be avoided while the mechanical stability and flexibility of packaging design can be improved (Dias, Plomp, & Veldhuis, 2000; Fujishima & Zhang, 2005). The development of SPEs has seen the emergence of natural biopolymers such as starch (Khiar & Arof, 2010), methyl cellulose (Shuhami et al., 2012) and chitosan (Buraidah et al., 2009; Majid & Arof, 2005, 2007, 2008) as the polymer host.

In the present work, corn starch is of interest. Starch is composed of amylose and amylopectin where amylose resides mainly in amorphous region of starch (Sajilata et al., 2006; Ochubiojo & Rodrigues, 2012). Since starch is sourced from various foods, the choice of corn starch is based on its higher amylose content than other types of starch as shown in Table 2.3. Corn starch has been used as polymer host in SPE as reported by Khiar and Arof (2010), Liew et al. (2012) and Teoh et al. (2012). Using acetic acid as the solvent is an approach to improve the mechanical properties and hydrophobicity of starch (Gonzalez & Perez, 2002; Song & Cheng, 2014; Xu & Hanna, 2005). In Chapter 5, the shift of the peak at hydroxyl and glycosidic linkage bands as well as changes in intensity of the peak at C-O bond stretching and C-H stretching mode

bands proved the interaction between starch and acetic acid. The interaction has occurred since the oxygen atoms in the functional groups of starch contain lone pair electrons which can form dative bond with H^+ ions from the acetic acid.

The problems possessed by starch based products such as brittle, hydrophilic and low mechanical strength has led towards idea to blend starch with other polymers (Mathew et al., 2006; Miyamoto et al., 2009; Wu & Zhang, 2001; Xu et al., 2005). The reasons to blend starch with chitosan are:

- Good miscibility between both polymers through interactions between amino groups of chitosan and hydroxyl groups of starch (Salleh et al., 2009). Good miscibility indicates strong interaction between the polymers and tends to suppress the crystalline phase, which in turn enhances the amorphous phase.
- Improved the formation condition and ductility of starch-based films (Zhai et al., 2004).
- Able to provide transparent and mechanically strong films (Salleh et al., 2009).
- Both polymers are at low cost (Jiang, Quan, Liao, & Wang, 2006; Lu et al., 2009).

Commonly, the interaction between the polymer components of a polymer blend occurs through hydrogen bonding (Guo, Sato, Hashimoto, & Ozaki, 2010; He, Zhu, & Inoue, 2004). The hydrogen bond is an attractive interaction involving a hydrogen atom bound to a highly electronegative atom and other highly electronegative atom (Arunan et al., 2011). From the FTIR analysis on starch-chitosan blend in Chapter 5, the interaction between the polymers has occurred through hydrogen bonding formation between the functional groups of both polymers as listed below:

- Hydroxyl groups of starch and hydroxyl groups of chitosan,

- hydroxyl groups of starch and amine groups of chitosan,
- hydroxyl groups of starch and glycosidic linkages of chitosan,
- hydroxyl groups of starch and C-O-C groups in chitosan, and
- hydroxyl groups of chitosan and glycosidic linkages of starch.

The results of various characterizations for determination of best ratio of starch-chitosan blend to serve as the polymer host were presented in Chapter 4. From the XRD results, crystalline peaks of starch and chitosan have been suppressed by a broad amorphous hump in the diffractogram of 80 wt.% starch-20 wt.% chitosan blend (S8C2). This result demonstrates the good miscibility and interaction between starch and chitosan in the blend. The calculation of the degree of crystallinity (χ_c) has been done by using two different methods i.e. Nara-Komiya method and deconvolution method. From the deconvolution method, the crystalline and amorphous peaks have been separated via Gaussian fitting. It is noticed that there are three crystalline peaks at 2θ = 14.4°, 18.5° and 22.8° superimposed on the broad amorphous hump centered at 2θ = 20.5° in the XRD diffractogram of S8C2 film, proving that this blend film is not fully amorphous. Although different values of degree of crystallinity have been obtained from the two methods, it is confirmed that the amorphous content in S8C2 film is higher than other blend ratio. According to Kadir (2010), the miscibility between two polymers in a blend can be implied from the smooth and homogenous surface of the blend film. The scanning electron micrograph of S8C2 film shows a homogenous surface without phase separation suggesting the good miscibility between starch and chitosan in the blend. Similar result has been reported by Jayaprakash et al. (2013) on potato starch-chitosan blend.

DSC analysis on pure starch film (S10C0) and pure chitosan film (S0C10) has revealed that the glass transition temperature (T_g) of the films are 67.21 °C and 97.41 °C, respectively. As discussed by He, Xue, Yang, Liu and Song (2009), the T_g of chitosan is still a subject of controversy since no consistent results were reported in the literature. The same thing goes to starch (Liew et al., 2012; Liu et al., 2009). This phenomenon could be due to the fact that natural polymers are originated from different sources or method of extraction which can reflect to the variation in their properties including the T_g value (He et al., 2009). However, the T_g values obtained in this work are comparable to the values reported by Liu et al. (2009) and Cheung et al. (as cited in Correia et al., 2014). DSC thermogram of S8C2 film consists only single T_g at 82.33 °C which is in between the T_g values of S10C0 and S0C10 films. This result has confirmed the miscibility between starch and chitosan in S8C2 film. From TGA analysis, the water content of S8C2 film is lower than that of S0C10 and S10C0 films indicating that the water content of a starch based film can be reduced by blending it with chitosan. According to Xu et al. (2005), the interaction between chitosan and starch molecules has prevented water molecules from diffusing through the film. This phenomenon decreases the water content of starch based film. The decomposition temperature does not change on blending starch with chitosan, as S8C2 film decomposes at 270 °C.

Proton conducting electrolytes have long been recognized as an initiative to lithium ion conductors in electrochemical device applications (Nasef et al., 2007; Panero et al., 2003). Ammonium salts are usually used as proton donor for polymer electrolyte as inorganic acids are problematic choices (Hema et al., 2008). The choice of ammonium chloride (NH_4Cl) as the doping salt is due to its lower lattice energy of 663.0 kJ mol^{-1} compared to other ammonium salts like ammonium acetate, $NH_4C_2H_3O_2$ (703.1 kJ mol^{-1}), ammonium sulfate, $(NH_4)_2SO_4$ (1754.7 kJ mol^{-1}) and ammonium

phosphate, $(NH_4)_3PO_4$ (3443.0 kJ mol^{-1}) (Buraidah & Arof, 2011; Kadir, 2010). Lattice energy of an ammonium salt depends on the size of anion. The radius of Cl^- is ~ 1.68 Å (Roobottom, Jenkins, Passmore, & Glasser, 1999). Larger anion of salt indicates lower lattice energy. Low lattice energy of a salt indicates that less energy is required to break the bond between anion and cation which is favourable for coordination of ions at the functional groups of polymer host (Buraidah, 2012).

From the FTIR results in Chapter 5, the addition of NH_4Cl up to 25 wt.% has shifted the hydroxyl band to lower wavenumbers of 3264 cm^{-1}. Hence it has been proven that interaction has occurred involving the oxygen atom of hydroxyl groups and the cations of salt. The occurrence of salt recrystallization has been detected in S8 electrolyte with the appearance of $v_{as}(NH_4^+)$ and $v_s(NH_4^+)$ modes in its FTIR spectrum. The interaction also occurred at the carboxamide, amine, C-O-C groups and glycosidic linkages as the bands' peak has shifted with the addition of NH_4Cl. Based on these FTIR results, the interaction between the cations and the oxygen and nitrogen atoms of the polymer blend host has been illustrated in Figure 5.18. As mentioned earlier, the oxygen and nitrogen atoms of the functional groups contain lone pair electrons, which provide the coordination site for cations, thus are able to form dative bond with the cations.

In the salted system, the highest conductivity value of $(6.47 \pm 1.30) \times 10^{-7}$ S cm^{-1} has been achieved on addition of 25 wt.% NH_4Cl (S5 electrolyte). The increase in conductivity can be attributed to the increase in the number density (n_d) and mobility (μ) of ions which have been calculated using the Rice and Roth model (as cited in Kadir et al., 2010; Samsudin et al., 2012). This model relates the conductivity with n_d, activation energy (E_a) and time travelling of ion (τ). The E_a values were determined

from the Arrhenius plots while τ values were determined using the value of *l*, which is the distance between two complexation sites. As shown in Tables 6.11, 6.13, 6.15 and 6.17, the n_d and μ values increase as the NH_4Cl concentration increases from 5 to 25 wt.%. This phenomenon perfectly follows the following relation:

$$\sigma = n_d e \mu \tag{9.1}$$

Here, the increase in n_d and μ values will obviously increases the conductivity. A decrease in conductivity was resulted when more than 25 wt.% NH_4Cl was added to the electrolyte. According to Kadir et al. (2010), high salt concentration in an electrolyte causes the distance between dissociated ions become closer that they are able to recombine and form neutral ion pairs. This phenomenon reduces the number density of ions and eventually decreases the conductivity of electrolyte.

Further investigation on conductivity trend in the salted system has been carried out by XRD, SEM and DSC. The addition of salt up to 25 wt.% to the polymer host has decreased the degree of crystallinity as shown in Tables 6.5 and 6.6. From Tables 6.11, 6.13, 6.15 and 6.17, the addition of salt up to 25 wt.% increases the number density of ions. According to Aji et al. (2012), the increase in ion concentration increases both the fraction of amorphous phase and charge carriers simultaneously. The increase in amorphousness of electrolyte assists the mobility of ions, thus provide answer for the increasing conductivity with increasing NH_4Cl content up to 25 wt.%. When more than 25 wt.% NH_4Cl was added to the polymer, a number of crystalline peaks appear in the XRD patterns in Figure 6.19. These crystalline peaks can be attributed to the crystalline nature of the salt. This result indicates the occurrence of recrystallization of salt within

the electrolytes with more than 25 wt.% NH_4Cl. This phenomenon leads to an increase in the degree of crystallinity as shown in Table 6.6, hence decreases the conductivity.

Comparing the SEM micrographs of S8C2 and S4 electrolytes, several particles can be observed on the electrolyte's surface when 20 wt.% of NH_4Cl was added to the polymer host. This type of particles has also been observed in other polymer electrolyte systems by Ahmad et al. (2010) and Bhad & Sangawar (2013). The latter authors inferred that these particles act as the channels for ion conduction through the electrolyte. More particles can be observed in the micrograph of S5 electrolyte, indicating more ions are available for conduction thus further strengthens the conductivity result. Too many particles can be observed in the micrograph of S8 electrolyte, where some of these particles agglomerate. From Figure 6.19, it is inferred that the recystallization of salt has become dominant in S8 electrolyte as crystalline peaks appear in the X-ray diffractogram of S8 electrolyte. From the micrograph of S8 electrolyte, the agglomeration of the particles may lead towards ion pairs formation.

Plasticization technique is one of the most practical ways to optimize the conductivity of electrolyte. Plasticizer possesses a high value of dielectric constant which can ease the dissociation of salt by weakening the Coulombic force between cation and anion. From a report by Ping, Wang, Sun, Feng, and Chen (2011), although ethylene carbonate (EC) has a high value of dielectric constant of 89.6, its high melting point of 39 °C may lead to poor low temperature performance of devices. In this work, glycerol has been chosen as the plasticizer. As stated in Chapter 2, the choice of glycerol is based on the following facts:

- Dielectric constant of 42.5, which is higher than other plasticizers such as dimethylacetamide, DMA (ε_{DMA} = 37.8) (Kumar & Sekhon, 2002),

γ-Butyrolactone, GBL (ε_{GBL} = 39.1) (Ping et al., 2011) and ethylene sulfite, ES (ε_{ES} = 39.6) (Azli, Manan, & Kadir, 2015).

- Melting and boiling points of 18 °C and 290 °C, respectively (Speight, 2002). These values of melting and boiling points ensure that glycerol will not solidify or boil in the present temperature range study.
- Most compatible plasticizer for starch based film (Curvelo, de Carvalho, & Agneli, 2001; Marcondes et al., 2010).

According to Liang et al. (2009), glycerol possesses the strong ability to interact with the polysaccharide matrix through hydrogen bonding interactions. From the FTIR analysis on starch-chitosan-glycerol in Chapter 5, the increase in glycerol content shifts the peak at hydroxyl, C-O-C, glycosidic linkage, carboxamide and amine bands indicating that there are formation of hydrogen bonding between the polymers and glycerol. As shown in Figure 2.4, the glycerol molecule has three hydroxyl groups that can provide the coordination sites for cations of salt. This is proven by the shifting of the hydroxyl band peak of pure glycerol to lower wavenumbers on addition of NH_4Cl up to 7 wt.% as shown in Figure 5.24. This result hypothesizes that apart from assists the salt dissociation, the presence of glycerol in the SPE may provide the additional sites and conducting pathways for ion conduction (Gondaliya et al., 2013). From Figure 5.26, the hydroxyl band peak of S5 electrolyte has shifted to lower wavenumbers of 3254 cm^{-1} in the spectrum of electrolyte with 30 wt.% glycerol (P6 electrolyte) and further shifted to 3247 cm^{-1} in the spectrum of electrolyte with 35 wt.% glycerol (P7 electrolyte). Another peak shifting was observed at carboxamide, amine, glycosidic linkage and C-O-C bands which further proves the interaction between glycerol and other electrolyte's components.

In the plasticized system, the conductivity has been increased with the addition of glycerol up to 35 wt. % concentration with the value of $(5.11 \pm 1.60) \times 10^{-4}$ S cm^{-1}. From Tables 6.12, 6.14, 6.16 and 6.18, the increase in conductivity can be attributed to the increase in the number density and mobility of ions. In the plasticized system, P7 electrolyte has the highest n_d and μ values, confirming its highest conductivity value. However, when more than 35 wt.% glycerol was added to the electrolyte, the conductivity decreases as well as the number density and mobility of ions. To get into a bigger picture about this matter, SEM and XRD analysis were carried out.

From the SEM analysis, the addition of plasticizer has altered the morphology of the electrolyte. On addition of 10 wt.% glycerol (P2 electrolyte), the number of particle observed on the electrolyte's surface has been reduced whereas the dark areas start to appear. On addition of 20 wt.% glycerol (P4 electrolyte), the dark region starts to dominate accompanied by the appearance of linkage like structures. The maximum dominancy of the dark region as well as increasing number of link can be seen in the micrograph of P7 electrolyte. From the literature, the dark region in surface micrograph represents the amorphous phase of the electrolyte (Ahmad et al., 2010; Su'ait et al., 2011). Thus, it can be inferred that the addition of glycerol increases the amorphous phase of the electrolyte. From the XRD analysis, the degree of crystallinity of P7 electrolyte is found to be lower than S5 electrolyte as shown in Tables 6.7 and 6.8. The presence of plasticizer in the electrolyte assists salt dissociation which in turn decreases the occurrence of salt recrystallization. Alternative pathways provided by the plasticizer for ion conduction helps the polymer host to accommodate the salt, as evidenced by the appearance of linkage like structure on plasticizer electrolyte's surface. The plasticizer is believed to act as a spacer between molecules of polymer by forming links with them (Pandey et al., 2013). From the FTIR studies, glycerol has formed hydrogen bond with

the polymer. These phenomena enhance the amorphousness of the electrolytes which in turn increases the number density and mobility of ions. The degree of crystallinity of P8 electrolyte is higher than P7 electrolyte, inferring that P8 is less amorphous than P7 electrolyte. As shown in the SEM micrograph of P8 electrolyte, too much links appear on the electrolyte's surface when 40 wt.% glycerol was added. The linkages may be formed between the plasticizer itself causing the salt to recrystallize thus decreases the conductivity (Johan & Ting, 2011).

In the amorphous region, ionic migration is associated with the polymer segmental motion (Money et al., 2012). The polymer segmental mobility can be enhanced by lowering the T_g (Woo et al., 2013). Since the conductivity is attributable to the increase in segmental motion (Aravindan & Vickraman, 2007), determination of T_g can further enhance the understanding in conductivity trend. On addition of 5 wt.% NH_4Cl, the T_g decreases from 82.33 °C to 55.08 °C. Further decrease in T_g is observed when 25 wt.% NH_4Cl was added to the electrolyte. The decrease in T_g with increasing salt content is also been observed by Vijaya et al. (2013) on PVP-NH_4Cl electrolytes. The presence of salt has weakened the dipole-dipole interactions between the polymer chains thus provides the plasticizing effect on the polymer (Malathi et al., 2010). This phenomenon stimulates the flexibility of polymer backbone thus enables the ions to move easily through the polymer chain network when an electric field is applied (Liew et al., 2014; Malathi et al., 2010). It can be concluded that by lowering the T_g, the conductivity can be increased. The addition of glycerol up to 35 wt.% decreases the T_g, thus satisfies the conductivity result. The addition of glycerol to the electrolyte increases the chain flexibility which results in a decrease in T_g (Kumar & Sekhon, 2002). On addition of 45 wt.% glycerol, the T_g is observed to increase. From the transport analysis, the number density of ion is decreased with the addition of more than 35 wt.% glycerol

due to the recrystallization of salt. This phenomenon increases the rigidity of electrolyte thus impedes the segmental mobility as well as the ionic migration (Liew et al., 2014; Noor et al., 2013; Silva et al., 2004).

TGA analysis of selected electrolytes has been carried out to check the stability of the electrolytes within the temperature range of the present studies. S1 and S5 electrolytes decompose at 198 °C and 185 °C, respectively. According to Ramesh et al. (2012), the decrease in thermal stability with the addition of salt reveals the decline in capability of the polymer chain to sustain its original form upon subject to heating. On addition of 35 wt.% glycerol, there is an additional stage of weight loss at 136-177 °C due to the degradation of glycerol in the electrolyte (Ayala et al., 2012). The major decomposition of P7 electrolyte occurs at 180 °C. The first weight loss of S1, S5 and P7 electrolytes is higher (~ 7-10%) than that of S8C2 film due to the hydrophilic nature of NH_4Cl salt and glycerol (Halim et al., 2012; Noor et al., 2012). These results show higher water content within S1, S5 and P7 electrolytes compare to S8C2 electrolyte. To study the effect of water on conductivity, variation of conductivity of P7 electrolyte with temperature under one heating-cooling cycle has been carried out. The conductivity is found to be lower on cooling cycle than the heating cycle by ~ 3%. This is attributed to the loss of water from the electrolyte during the heating cycle.

Ionic and electronic transference numbers of an electrolyte are crucial in explaining the conductivity of the electrolyte (Sekhar et al., 2012a). For an ionic conductor, ionic transference number (t_{ion}) should be higher than the electronic transference number (t_e) (Aziz et al., 2012; Shukur & Kadir, 2015; Woo et al., 2011b). From Figures 6.44 to 6.46, the current is observed to decrease rapidly at the initial before being saturated at 0.2 μA. Before reaching the saturation level, the current is

carried by both ions and electrons. However, the ions cannot pass through the ion blocking stainless steel electrodes leaving only electrons to carry the current through the electrodes (Woo et al., 2011b). This phenomenon results in saturation of current at 0.2 μA. Generally, ions are mobile in the amorphous phase while crystalline phase favours electron transport (Gadjourova et al., 2001). From the XRD analysis in Chapter 6, the degree of crystallinity of P7 electrolyte is the lowest, followed by P5 and S5. Due to its higher amorphous content than the other two electrolytes, P7 electrolyte has the highest t_{ion} value of 0.98 and the lowest t_e of 0.02.

The contribution of cation to the total conductivity is important to be known due to its major role during the charge-discharge process of a battery. Manganese (IV) oxide (MnO_2) was used as the electrodes for cation transference number (t_+) measurements since it is proton transparent. It is found that the value of t_+ of P7 electrolyte is 0.56. As for comparison, the values of t_+ for other P3 and S5 electrolytes were also determined and found to be 0.33 and 0.26, respectively. According to Suthanthiraraj and Vadivel (2012), the increase in t_+ value with increasing amount of plasticizer in polymer electrolyte could be due to favourable cation migration within the electrolyte. As shown in Chapter 5, the addition of glycerol has provided the alternative pathways for the cations for migration, thus leading to the increase in t_+.

The dielectric constant (ε_r) and dielectric loss (ε_i) as a function of NH_4Cl and glycerol concentration at selected frequencies were presented in Chapter 7. The objective of the presentation of ε_r and ε_i is to correlate the conductivity with those parameters. As NH_4Cl content increases to 25 wt.%, the charge stored in the electrolyte increases indicating an increase in the number density of mobile ions hence increases the conductivity (Buraidah et al., 2009). The decreasing ε_r and ε_i values for electrolytes

containing more than 25 wt.% NH_4Cl can be attributed to ion reassociation, leading to a decrease in conductivity (Woo et al., 2011a). A higher glycerol content up to 35 wt.% increases the value of ε_r and ε_i. As glycerol was added, more undissociated salt become ions, hence the stored charge in the electrolyte increases. The ε_r and ε_i values are observed to decrease with the increase in frequency. As frequency increases, the periodic reversal of the electric field occurs so rapidly which disable the charge carriers from orienting themselves in the field direction, resulting in the decrease of ε_r and ε_i (Ali et al., 2011; Mishra & Rao, 1998).

The ε_r and ε_i values are observed to be affected by temperature as depicted in Figures 7.5 to 7.8. Temperature assists the dissociation of ions by increasing the vibration of the anions and cations which leads towards the break up of the salt and increase the number of ions (Kadir, 2010). This result is in agreement with the transport parameters as shown in Tables 6.21 and 6.22, where the number density of ion increases with the increase in temperature.

The frequency dependent of loss tangent (tan δ) for the electrolytes indicates that the loss peaks (tan δ_{max}) are shifted to high frequency side with increasing conductivity. The shift of tan δ_{max} to high frequencies indicates the decrease in relaxation time ($t_{tan\ \delta}$) (Hashim & Khiar, 2011; Ramly et al., 2011; Subban & Arof, 2003a). The tan δ_{max} are also observed to shift to high frequencies with increasing temperature, meaning that the value of $t_{tan\ \delta}$ decreases as shown in Tables 7.6 and 7.7. The height of tan δ_{max} also increases which attributed to the decrease in resistivity of the electrolytes (Idris et al., 2007). The activation energy of the frequency at tan δ_{max} (f_{max}) is very close to those obtained from the plots of Log σ vs 1000/T in Chapter 6. Thus it can be indicated that

the ion transport mechanism has the same potential energy barrier upon conducting and relaxing (Ali et al., 2009).

Debye relaxation denotes a system with a single relaxation time (Macdonald, 1999). In polymer electrolytes, under an alternating external electric field, different polarization mechanism such as electronic, dipolar and ionic polarization occur. Thus a distribution of relaxation times will occur in polymer electrolytes, which deviates from Debye type relaxation (Aziz, 2012). To prove this matter, scaling of tan δ has been done by plotting the normalized of tan δ/(tan δ)$_{max}$ against f/f_{max} for selected electrolytes. For a typical Debye peak, the value of full width at half maximum (FWHM) of the plot is 1.14 decades, which gives the Kohlrausch exponent (β_{KWW}) = 1 (Dutta et al., 2002; Idris et al., 2007). The value of β_{KWW} for S5 electrolyte at 298-343 K is 0.57-0.60. For P1 electrolyte, the value of β_{KWW} is found to be 0.42-0.47 at 298-343 K. The small value of β_{KWW} in the present system shows the deviation of relaxation from Debye relaxation.

Jonscher's universal power law (Buraidah et al., 2009; Winie & Arof, 2004) has been used to predict the ac conduction mechanism of the highest conducting electrolyte in salted and plasticized systems. The conduction mechanism was predicted from the variation of power law exponent *s* with temperature. For S5 electrolyte, the exponent *s* is almost temperature independent which follows quantum mechanical tunneling (QMT) model (Kadir et al., 2009). In QMT model, the polarons are able to tunnel through the potential barrier that exists between two complexation sites (Majid & Arof, 2007). In S5 electrolyte, the polarons are resembled by the H^+ ions and their stress fields. For P7 electrolyte, the exponent *s* decreases with the increase in temperature, thus follows correlated barrier hopping (CBH) model. In CBH model, the ions are surrounded by several potentials. The ions can only hop from one site to another after acquiring

enough energy (Buraidah, et al, 2009). The difference in conduction mechanism of S5 and P7 electrolytes can be attributed to the difference in E_a value. Due to the higher E_a (0.31 eV), the ions in S5 electrolyte are able to tunnel through the potential barrier. The E_a of P7 electrolyte is lower (0.19 eV). The addition of plasticizer decreases T_g and increases the segmental motion. Hence, the ions can easily hop across the potential barrier (Kufian et al., 2007).

The electrochemical stability of the highest conducting electrolyte (P7) was carried out using LSV measurement with stainless steel foils as working, counter and reference electrodes. As for comparison, LSV measurements for other selected electrolytes were also been carried out using the same type of electrodes. P7 electrolyte was found to be electrochemically more stable than S5, P3 and P5 electrolytes due to its higher conductivity value than the other electrolytes. The current onset of P7 electrolyte was detected at 1.65 V which is suitable for EDLC and proton batteries application.

In an EDLC, the charge storage mechanism is based on the formation of Helmholtz double-layers (Lim et al., 2014a). Since electrodes of the same type (i.e symmetry) were used, the EDLC needed to be charged first to provide the potential difference between the electrodes. During the charging process, electrons from the positive electrodes move towards the negative electrode through the outer circuit. This movement of electrons provides holes at the positive electrode. At the same time, the cations in the electrolyte migrate to the negative electrode while the anions move to the positive electrode. The accumulation of cations and anions at the surface of electrodes to compensate the opposite electronic charges at the electrode surfaces provide the potential difference between the two electrodes. No chemical reactions are involved in this energy storage mechanism. The energy storage mechanism of the EDLC is based on

the physical movement of electrons and ions. During the discharge, these electrons move back from the negative electrode to the positive electrode, and ions are released from the electrode surface into the electrolyte, so the cathode and anode come back to the same potential (Chen, 2011; Ho, Khiew, Isa, & Tan, 2014).

In the present work, the EDLC was fabricated by sandwiching P7 electrolyte with two carbon based electrodes using perspex plates. The EDLC was charged and discharged at a constant current density of 0.063 mA cm^{-2} between 0 to 0.85 V for 500 cycles. The specific capacitance (C_s) is observed to decrease to 3915 mF g^{-1} during the first 70 cycles before remains constant at ~ 3444 mF g^{-1} until 500th cycle. The strong relation between conductivity and mobility of charge carriers means that the EDLC's performance affected by the mobility of charge carriers. The ionic mobility of P7 electrolyte is $(4.42 \pm 1.23) \times 10^{-4}$ cm^2 V^{-1} s^{-1}. Comparing the present result with reports from literature (Arof, Amirudin, et al., 2014; Arof, Shuhaimi, et al., 2014; Majid, 2007), it can be concluded that the higher the ionic mobility, the greater the C_s value. The Coulombic efficiency (η) of the EDLC increases from 69% to 91% towards the 50th cycle before remains constant at ~ 90-95%. Efficiency of ~ 90% indicates the intimate electrode-electrolyte contact (Lim et al., 2014a). This result shows that the present EDLC exhibits good cycling stability for 500 cycles.

The value of C_s is also obtained using the result from cyclic voltammetry (CV) measurements before and after galvanostatic charge-discharge measurement. The C_s value decreases as the scan rate increases. According to Nasibi et al. (2012), when the scan rate was increased, energy loss increases and the stored charge on the electrode surface decreases leading to a decrease in C_s. At low scan rates, ions can utilize all the vacant sites in the active electrode material since they have enough time to diffuse into

the vacant sites leading to the higher C_s value (Lim et al., 2014b). The enclosed area of the CV curve becomes smaller after 500 charge-discharge measurement, indicating smaller C_s value. This phenomenon is due to the effect of internal resistance. From the literature (Arof et al., 2010; Liew et al., 2015; Pendashteh et al., 2014), internal resistance increases with increasing charge-discharge cycle. At higher resistance, less charges flow causes less current flow which result a decrease in C_s value (see Table 8.2).

In a primary battery, the energy storage mechanism is based on the chemical reactions occur at the electrodes. During the discharge of proton battery, zinc at the anode is oxidized and releases Zn^{2+} and electrons. The reaction involving the $ZnSO_4 \cdot 7H_2O$ releases H^+ ions. Electrons from the anode will then move to the cathode through the outer circuit, while the H^+ ions (from the anode and the electrolyte) move to the cathode through the electrolyte. At the cathode, the reaction between MnO_2, electrons and H^+ ions causes MnO_2 to undergo reduction. All these reactions will provide the battery with the potential as shown in Table 8.4. However, as stated in Chapter 8, the difference between the theoretical and experimental result of potential of battery could be due to the concentration and transport of ions (Botte & Muthuvel, 2012).

Primary proton batteries were fabricated by sandwiching P7 electrolyte with zinc based anode and MnO_2 based cathode in coin cells. Result of 48 h open circuit potential (OCP) shows that the potential of the batteries is (1.54 ± 0.02) V, which is 20.31% higher than the expected potential (see Table 8.4). Botte and Muthuvel (2012) stated that the difference between the theoretical and experimental values of OCP is due to several factors e.g. concentration and transport of ions. Similar result has been reported

in the literature (Alias et al., 2014; Samsudin et al., 2014). The batteries were then discharged at different constant currents (0.10, 0.25, 0.40 and 0.60 mA) at room temperature. During the discharge process, the zinc was oxidized while MnO_2 wass reduced thus forming Mn_2O_3-ZnO (McComsey, 2001; Rahman et al., 2013). As the discharge time increases, more Mn_2O_3-ZnO particles are formed causing the increase in charge transfer resistance. This phenomenon has resulted to the abrupt decrease in potential after ~ 1.0 V. The discharge capacity (Q) was found to be higher at lower discharge current (Q = 9.36 mA h at 0.10 mA). According to Roscher et al. (2011), at high discharge current, the variation of ion concentration along the pores depth of an electrode increases, forcing a non-uniform proton insertion process. From the current-potential (I-V) and current density-power density (J-P) characteristics measurement, the internal resistance (r) of the batteries is found to be 36.74 Ω. The maximum power density is (7.90 ± 0.50) mW cm^{-2} while the short circuit current of the batteries is 35 mA. The characteristics of the present primary proton batteries are comparable with other reported works (Kadir et al., 2010; Ng & Mohamad, 2006; Shukur, Ithnin, et al., 2013).

In a secondary proton battery, the battery is able to charge to its initial potential. During the charging process, the process of discharge is reversed where the electrons move back to the anode through the outer circuit while the H^+ ions move to the electrolyte towards the anode. In the present work, P7 electrolyte was also been used in the fabrication of secondary proton battery. Before the fabrication, the highest conducting electrolyte solution has been added to the cathode to enable the deintercalation of proton from the cathode active material and enter the anode through the electrolyte for rechargeable process (Kadir et al., 2010). The OCP of the secondary proton battery for 48 h is lasted at (1.58 ± 0.01) V. The secondary proton battery was

subjected to discharge and charge at a constant current of 0.35 mA. This charge-discharge process was performed for 40 times and lasted for ~ 440 h. At the first cycle, the battery is discharged to 1.00 V before being recharged to 1.58 V. A decrease in specific discharge capacity (Q_s) at 2nd cycle can be attributed to the electrode-electrolyte contact, which is not always perfect at the first charge (Guinot et al., 1998; Mohamad et al., 2003). The Q_s value increases thereafter and reaches 7.83 mA h g^{-1} after 6th cycle. The Q_s value is almost stable until 15th cycle before decreases until the 40th cycle. This phenomenon may be caused by the poor interfacial stability of the electrode thus develop the large interfacial resistance between the electrode and the electrolyte as reported for other proton batteries (Mishra et al., 2014; Samsudin et al., 2014; Selvasekarapandian et al., 2010).

CHAPTER 10

CONCLUSIONS AND SUGGESTIONS FOR FUTURE WORK

10.1 Conclusions

Solid polymer electrolyte systems of starch-chitosan, starch-chitosan-NH_4Cl (salted system) and starch-chitosan-NH_4Cl-glycerol (plasticized system) were successfully prepared via solution cast technique. From XRD analysis, the blend of 80 wt.% starch and 20 wt.% chitosan (S8C2) was found to be the most amorphous blend and was chosen to serve as the polymer host. SEM studies have revealed the miscibility between starch and chitosan. Starch-chitosan miscibility in S8C2 film was further confirmed by the appearance of only one T_g value in the DSC thermogram, which is found to fall in between the T_g values of pure starch (S10C0) and pure chitosan (S0C10) films. TGA analysis shows that the water content of the film has been decreased upon blending starch with chitosan.

From FTIR analysis, the shifting of bands' peak as well as changes in intensity has proved the occurrence of interaction among the materials. Hydrogen bonding interaction between starch and chitosan has been proposed. Interaction between NH_4Cl and the polymer blend host was observed by the shifting of the peak at hydroxyl, carboxamide and amine bands as well as glycosidic linkage and C-O-C group bands. The addition of glycerol has further shift those peaks indicating more ions have interacted with the polymer host.

In the salted system, the addition of 25 wt.% NH_4Cl has optimized the conductivity to $(6.47 \pm 1.30) \times 10^{-7}$ S cm^{-1}. The increase in conductivity was due to the following reasons:

- Increase in the number density of ions with the increase in NH_4Cl concentration up to 25 wt.%.
- Amorphousness of the electrolyte.
- Increase in the mobility of ions since ions are more mobile in the highly amorphous electrolyte.
- Low value of T_g increases the segmental motion of the polymer chains, thus assists the ion mobility.

In the plasticized system, the addition of 35 wt.% glycerol enhanced the conductivity to $(5.11 \pm 1.60) \times 10^{-4}$ S cm^{-1}. The plasticizer has assisted the conductivity enhancement by the ways stated below:

- Its high dielectric constant value helps to weaken the Coulombic force between cation and anion, thus ease the salt disscociation.
- Provides the alternative pathways for ionic conduction.
- Reduces the crystallinity as well as the T_g of electrolytes.

The conductivity-temperature relationship in the temperature range of 298-343 K for all electrolytes was found to follow Arrhenius rule. The increase in conductivity with increasing temperature was contributed by the increase in mobility of ions. Higher conducting electrolyte obtained lower activation energy implying that lower energy is required for ionic conduction in higher conducting electrolyte. From transference number measurements, ion has been found as the dominant conducting species. Transference number of cation for P7 electrolyte was 0.56. The relaxation time

of the electrolytes was found to decrease with increasing conductivity and temperature. Scaling of tan δ confirmed that electrolyte systems in this study obey non-Debye behaviour. The ac conduction mechanism for S5 and P7 electrolytes was best explained by QMT and CBH models, respectively.

LSV results revealed that P7 electrolyte decomposed at 1.65 V, confirming the suitability of P7 electrolyte for EDLC and proton batteries application. The EDLC was charged and discharged for 500 cycles, where the specific capacitance was lasted at ~ 3444 mF g^{-1}. The EDLC's performance has been related to ionic mobility, with comparison to other works. From CV, the specific capacitance was scan rate dependent, and decreases after 500 charge-discharge cycles due to the increasing internal resistance. The OCP of the primary and secondary proton batteries after 48 h was (1.54 ± 0.02) V and (1.58 ± 0.01) V, respectively. The discharge capacity of the primary batteries was enhanced by lowering the discharge current. The internal resistance and short circuit current of the primary proton batteries were 36.74 Ω and 35 mA, respectively. Charge-discharge of the secondary battery was able to perform up to 40 cycles for ~ 440 h.

10.2 Suggestions for Future Work

Since the maximum conductivity of the electrolyte in the present work is in the order of 10^{-4} S cm^{-1}, the conductivity of the electrolyte should be further enhanced by using the following methods:

- Modify the structure of polymer host by inserting an additional functional group using processes such as carboxymethylation (Mobarak, Ramli, Ahmad, &

Rahman, 2012), phthaloylation (Aziz et al., 2012), hydroxyalkylation (Lawal, 2009) and acylation (Zong, Kimura, Takahashi, & Yamane, 2000). This method provides additional complexation site for the ions, thus more salt can be solvated which can increase the conductivity.

- Addition of inorganic filler like aluminum oxide (Al_2O_3) (Aziz, Majid, Yahya, & Arof, 2011), silicon dioxide (SiO_2) (Subban & Arof, 2003b) and titanium dioxide (TiO_2) (Rosli, Chan, Subban, & Winie, 2012) into the electrolyte. The presence of filler can create favourable pathways for ionic conduction, increase the amorphousness and immobilize the anions (Hassan et al., 2013).
- Double salt system (Ramesh & Arof, 2000; Yap, 2012). Mixed salts in an electrolyte can encourage more ion dissociation by anion-anion dipole interactions (Yap, 2012).
- Gamma irradiation treatment on the electrolytes. Irradiation with gamma rays of the electrolytes can cause more ions to dissociate (Rahaman et al., 2014).

The performance of EDLC and proton batteries could be further studies by the following ways:

- The performance of the devices at different temperatures.
- Alteration of the electrodes by addition of suitable additives.
- Increases the surface area of activated carbon.
- Synthesizes the carbon material from natural materials such as fruit shells (Arof et al., 2012) and woods (Abdullah et al., 2001).

REFERENCES

Abdullah, A.H., Kassim, A., Zainal, Z., Hussien, M.Z., Kuang, D., Ahmaf, F., & Wooi, O.S. (2001). Preparation and characterization of activated carbon from gelam wood bark (*Melaleuca cajuputi*). *Malaysian Journal of Analytical Sciences, 7*, 65-68.

Abdullah, A., Abdullah, S.Z., Ali, A.M.M., Winie, T., Yahya, M.Z.A., & Subban, R.H.Y. (2009). Electrical properties of PEO-$LiCF_3SO_3$-SiO_2 nanocomposite polymer electrolytes. *Materials Research Innovations, 13*, 255-258.

Ahmad, A., Rahman, M.Y.A., Low, S.P., & Su'ait, M.S. (2010). Solid polymeric electrolyte of poly(methyl methacrylate)-49% poly(methyl methacrylate) grafted natural rubber-propylene carbonate-lithium tetrafluoroborate. *Current Topics in Electrochemistry, 15*, 17-24.

Agrawal, R.C. (1999). dc polarisation: An experimental tool in the study of ionic conductors. *Indian Journal of Pure and Applied Physics, 37*, 294-301.

Agrawal, R.C., Hashmi, S.A., & Pandey, G.P. (2007). Electrochemical cell performance studies on all-solid-state battery using nano-composite polymer electrolyte membrane. *Ionics, 13*, 295-298.

Agrawal, R.C., Sahu, D.K., Mahipal, Y.K., & Ashrafi, R. (2013). Ion transport property of hot-press cast Mg^{2+}-ion conducting nano-composite polymer electrolyte membranes: Study of effect of active/passive filler particle dispersal on conductivity. *Indian Journal of Pure and Applied Physics, 51*, 320-323.

Agudelo, A., Varela, P., Sanz, T., & Fiszman, S.M. (2014). Native tapioca starch as a potential thickener for fruit fillings. Evaluation of mixed models containing low-methoxyl pectin. *Food Hydrocolloids, 35*, 297-304.

Aji, M.P., Masturi, Bijaksana, S., Khairurrijal, & Abdullah, M. (2012). A general formula for ion concentration-dependent electrical conductivities in polymer electrolytes. *American Journal of Applied Sciences, 9*, 946-954.

Ali, A.M.M., Bahron, H., Subban, R.H.Y., Kudin, T.I.T., & Yahya, M.Z.A. (2009). Frequency dependent conductivity studies on PMMA-$LiCF_3SO_3$ polymer electrolytes. *Materials Research Innovations, 13*, 285-287.

Ali, A.M.M., Mohamed, N.S., & Arof, A.K. (1998). Polyethylene oxide (PEO)-ammonium sulfate ($(NH_4)_2SO4$) complexes and electrochemical cell performance. *Journal of Power Sources, 74*, 135-141.

Ali, A.M.M., Subban, R.H.Y., Bahron, R., Yahya, M.Z.A., & Kamisan, A.S. (2013). Investigation on modified natural rubber gel polymer electrolytes for lithium polymer battery. *Journal of Power Sources, 244*, 636-640.

Ali, A.M.M., Yahya, M.Z.A., Mustaffa, M., Ahmad, A.H., Subban, R.H.Y., Harun, M.K., & Mohamad, A.A. (2005). Electrical properties of plasticized chitosan-lithium imide with oleic acid-based polymer electrolytes for lithium rechargeable batteries. *Ionics, 11*, 460-463.

Ali, R.M., Harun, N.I., Ali, A.M.M., & Yahya, M.Z.A. (2011). Conductivity studies on plasticised cellulose acetate-ammonium iodide based polymer electrolytes. *Materials Research Innovations, 1*5, S39-S42.

Alias, S.S., Chee, S.M., & Mohamad, A.A. (2014). Chitosan-ammonium acetate-ethylene carbonate membrane for proton batteries. *Arabian Journal of Chemistry.* http://dx.doi.org/10.1016/j.arabjc.2014.05.001

Alp, B., Mutlu, S., & Mutlu, M. (2000). Glow-discharge-treated cellulose acetate (CA) membrane for a high linearity single-layer glucose electrode in the food industry. *Food Research International, 33*, 107-112.

Alvarez, C., Lorenzo, V., & Riande, E. (2005). Relaxation response of polymers containing highly flexible side groups monitored by broadband dielectric spectroscopy. *The Journal of Chemical Physics, 122*, 195905.

Angulakshmi, N., Nahm, K.S., Nair, J.R., Gerbaldi, C., Bongiovanni, R., Penazzi, N., & Stephan, A.M. (2013). Cycling profile of $MgAl_2O_4$-incorporated composite electrolytes composed of PEO and $LiPF_6$ for lithium polymer batteries. *Electrochimica Acta, 90*, 179-185.

Antognini, A., Nez, F., Schuhmann, K., Amaro, F.D., Biraben, F., Cardoso, J.M.R., … Pohl, R. (2013). Proton structure from the measurement of 2S-2P transition frequencies of muonic hydrogen. *Science, 339*, 417-420.

Araujo, M.A., Cunha, A.M., & Mota, M. (2004). Enzymatic degradation of starch-based thermoplastic compounds used in protheses: Identification of the degradation products in solution. *Biomaterials, 25*, 2687-2693.

Aravamudhan, A., Ramos, D.M., Nada, A.A., & Kumbar, S.G. (2014). Natural polymers: Polysaccharides and their derivatives for biomedical applications. In S.G. Kumbar, C.T. Laurencin, & M. Deng (Eds.), *Natural and synthetic biomedical polymers* (pp. 67-89). Oxford: Elsevier.

Aravindan, V., & Vickraman, P. (2007). Polyvinylidenefluoride-hexafluoropropylene based nanocomposite polymer electrolytes (NCPE) complexed with $LiPF_3(CF_3CF_2)_3$. *European Polymer Journal, 43*, 5121-5127.

Arof, A.K., & Majid, S.R. (2008). Electrical studies on chitosan based proton conductors and application in capacitors. *Molecular Crystals and Liquid Crystals, 484*, 107-116.

Arof, A.K., Amirudin, S., Yusof, S.Z., & Noor, I.M. (2014). A method based on impedance spectroscopy to determine transport properties of polymer electrolytes. *Physical Chemistry Chemical Physics, 16*, 1856-1867.

Arof, A.K., Aziz, M.F., Noor, M.M., Careem, M.A., Bandara, L.R.A.K., Thotawatthage, C.A., … Dissanayake, M.A.K.L. (2014). Efficiency enhancement by mixed cation effect in dye-sensitized solar cells with a PVdF based gel polymer electrolyte. *International Journal of Hydrogen Energy, 39*, 2929-2935.

Arof, A.K., Kufian, M.Z., Syukur, M.F., Aziz, M.F., Abdelrahman, A.E., & Majid, S.R. (2012). Electrical double layer capacitor using poly(methyl methacrylate)-C_4BO_8Li gel polymer electrolyte and carbonaceous material from shells of *mata kucing* (*Dimocarpus longan*) fruit. *Electrochimica Acta, 74*, 39-45.

Arof, A.K., Morni, N.M., & Yarmo, M.A. (1998). Evidence of lithium-nitrogen interaction in chitosan-based films from X-ray photoelectron spectroscopy. *Materials Science and Engineering B, 55*, 130-133.

Arof, A.K., Shuhaimi, N.E.A., Alias, N.A., Kufian, M.Z., & Majid, S.R. (2010). Application of chitosan/iota-carrageenan polymer electrolytes in electrical double layer capacitor (EDLC). *Journal of Solid State Electrochemistry, 14*, 2145-2152.

Arof, A.K., Shuhaimi, N.E.A., Amirudin, S., Kufian, M.Z., Woo, H.J., & Careem, M.A. (2014). Polyacrylonitrile-lithium bis(oxalate) borate polymer electrolyte for electrical double layer capacitors. *Polymers for Advanced Technologies, 25*, 265-272.

Arunan, E., Desiraju, E.R., Klein, R.A., Sadlej, J., Scheiner, S., Alkorta, I., ... Nesbitt, D.J. (2011). Definition of the hydrogen bond (IUPAC Recommendations 2011). *Pure and Applied Chemistry, 83*, 1637-1641.

Ashori, A., & Bahrami, R. (2014). Modification of physico-mechanical properties of chitosan-tapioca starch blend films using nano graphene. *Polymer-Plastics Technology and Engineering, 53*, 312-318.

Asmara, S.N., Kufian, M.Z., Majid, S.R., & Arof, A.K. (2011). Preparation and characterization of magnesium ion gel polymer electrolytes for application in electrical double layer capacitors. *Electrochimica Acta, 57*, 91-97.

Atkin, N.J., Abeysekera, R.M., & Robards, A.W. (1998). The events leading to the formation of ghost remnants from the starch granule surface and the contribution of the granule surface to the gelatinization endotherm. *Carbohydrate Polymers, 36*, 193-204.

Averous, L., & Pollet, E. (2012). Biodegradable polymers. In L. Averous & E. Pollet (Eds.), *Environmental silicate nano-biocomposites* (pp. 13-39). London, England: Springer.

Ayala, G., Agudelo, A., & Vargas, R. (2012). Effect of glycerol on the electrical properties and phase behavior of cassava starch biopolymers. *DYNA, 79*, 138-147.

Azahari, N.A., Othman, N., & Ismail, H. (2011). Biodegradation studies of polyvinyl alcohol/corn starch blend films in solid and solution media. *Journal of Physical Science, 22*, 15-31.

Aziz, N.A., Majid, S.R., & Arof, A.K. (2012). Synthesis and characterizations of phthaloyl chitosan-based polymer electrolytes. *Journal of Non-Crystalline Solids, 358*, 1581-1590.

Aziz, N.A., Majid, S.R., Yahya, R., & Arof, A.K. (2011). Conductivity, structure, and thermal properties of chitosan-based polymer electrolytes with nanofillers. *Polymers for Advanced Technologies, 22*, 1345-1348.

Aziz, N.A.N., Idris, N.K., & Isa, M.I.N. (2010). Proton conducting polymer electrolytes of methylcellulose doped ammonium fluoride: Conductivity and ionic transport studies. *International Journal of Physical Sciences, 5*, 748-752.

Aziz, S.B. (2012). *Electrical and dielectric properties of solid and nanocomposite polymer electrolytes based on chitosan* (Doctoral thesis, Univeristy of Malaya, Kuala Lumpur, Malaysia). Retrieved from http://studentsrepo.um.edu.my/3811

Aziz, S.B., Abidin, Z.H.Z., & Arof, A.K. (2010a). Effect of silver nanoparticles on the DC conductivity in chitosan-silver triflate polymer electrolyte. *Physica B, 405*, 4429-4433.

Aziz, S.B., Abidin, Z.H.Z., & Arof, A.K. (2010b). Influence of silver ion reduction on electrical modulus parameters of solid polymer electrolyte based on chitosan-silver triflate electrolyte membrane. *Express Polymer Letters, 5*, 300-310.

Azli, A.A., Manan, N.S.A., & Kadir, M.F.Z. (2015). Conductivity and dielectric studies of lithium trifluoromethanesulfonate doped polyethylene oxide-graphene oxide blend based electrolytes. *Advances in Materials Science and Engineering,* 145735

Badapanda, T., Harichandan, R.K., Nayak, S.S., Mishra, A., & Anwar, S. (2014). Frequency and temperature dependence behaviour of impedance, modulus and conductivity of $BaBi_4Ti_4O_{15}$ Aurivillius ceramic. *Processing and Application of Ceramics, 8*, 145-153.

Badawy, M.E.I., & Rabea, E.I. (2011). A biopolymer chitosan and its derivatives as promising antimicrobial agents against plant pathogens and their applications in crop protection. *International Journal of Carbohydrate Chemistry, 2011*, 460381.

Bajer, D., & Kaczmarek, H. (2010). Study of the influence OV UV radiation on biodegradable blends based on chitosan and starch. In M.M. Jaworska, R. Brzezinski, S. Minami, H. Pospieszny, G.A.F. Roberts, S. Senel, & V. Varlamov (Eds.), *Progress on chemistry and application of chitin and its derivatives* (Vol. 15) (pp. 17-24). Lodz, Poland: Polish Chitin Society.

Bansod, S.M., Bhoga, S.S., Singh, K., & Tiwari , R.U. (2007). The role of electrolyte in governing the performance of protonic solid state battery. *Ionics, 13*, 329-332.

Baran, E.T., Mano, J.F., & Reis, R.L. (2004). Starch-chitosan hydrogels prepared by reductive alkylation cross-linking. *Journal of Materials Science: Materials in Medicine, 15*, 759-765.

Barbosa, P.C., Rodrigues, L.C., Silva, M.M., & Smith, M.J. (2011). Characterization of $pTMC_nLiPF_6$ solid polymer electrolytes. *Solid State Ionics, 193*, 39-42.

Bhad, S.N., & Sangawar, V.S. (2013). Optical study of PVA based gel electrolyte. *International Journal of Scientific & Engineering Research, 4*, 1719-1722.

Bhad, S.N., Sangawar, V.S., Maldhure, A.K., Tayade, D.P., & Yerawar, G.R. (2012). Study of proton conducting PVA based gel electrolyte. *International Journal of Innovative Research in Science, Engineering and Technology, 2*, 6009-6013.

Biswas, A., Willet, J.L., Gordon, S.H., Finkenstadt, V.L., & Cheng, H.N. (2006). Complexation and blending of starch, poly(acrylic acid), and poly(*N*-vinyl pyrrolidone). *Carbohydrate Polymers, 65*, 397-403.

Botte, G.G., & Muthuvel, M. (2012). Electrochemical energy storage: Applications, processes, and trends. In J.A. Kent (Ed.), *Handbook of industrial chemistry and biotechnology* (pp 1497-1539). Florida: Springer.

Bourtoom, T., & Chinnan, M.S. (2008). Preparation and properties of rice starch-chitosan blend biodegradable film. *LWT – Food Science and Technology, 41*, 1633-1641.

Bouslah, N., & Amrani, F. (2007). Miscibility and specific interactions in blends of poly[(styrene)-co-(cinnamic acid)] with poly(methyl methacrylate) and modified poly(methyl methacrylate). *Express Polymer Letters, 1*, 44-50.

Breslin, F., & Stephenson, G.P. (1985). Determination of glycerol in pharmaceutical preparations by reversed-phase high-performance liquid chromatography using a refractive index detector. *Journal of Chromatography A, 329*, 434-437.

Buraidah, M.H. (2012). *Ionic conductivity and related studies on chitosan-based electrolytes with application in solar cells* (Doctoral thesis, University of Malaya, Kuala Lumpur, Malaysia). Retrieved from http://studentsrepo.um.edu.my/3878

Buraidah, M.H., & Arof, A.K. (2011). Characterization of chitosan/PVA blended electrolyte doped with NH_4I. *Journal of Non-Crystalline Solids, 357*, 3261-3266.

Buraidah, M.H., Teo, L.P., Majid, S.R., & Arof, A.K. (2009). Ionic conductivity by correlated barrier hopping in NH_4I doped chitosan solid electrolyte. *Physica B, 404*, 1373-1379.

Buraidah, M.H., Teo, L.P., Majid, S.R., & Arof, A.K. (2010). Characteristics of TiO_2/solid electrolyte junction solar cells with I^-/I_3^- redox couple. *Optical Materials, 32*, 723-728.

Chen, L., Tang, C.-Y., Ning, N.-Y., Wang, C.-Y., Fu, Q., & Zhang, Q. (2009). Preparation and properties of chitosan/lignin composite films. *Chinese Journal of Polymer Science, 27*, 739-746.

Chen, P.-Y., Lee, C.-P., Vittal, R., & Ho, K.-C. (2010). A quasi solid-state dye-sensitized solar cell containing binary ionic liquid and polyaniline-loaded carbon black. *Journal of Power Sources, 195*, 3933-3938.

Chen, W., Beidaghi, M., Penmatsa, V., Bechtold, K., Kumari, L., Li, W.Z., & Wang, C. (2010). Integration of carbon nanotubes to C-MEMS for on-chip supercapacitors. IEEE *Transactions on Nanotechnology, 9*, 734-740.

Chen, W., Fan, Z., Gu, L., Bao, X., & Wang, C. (2010). Enhanced capacitance of manganese oxide *via* confinement inside carbon nanotubes. *Chemical Communications, 46*, 3905-3907.

Chen, X. (2011). *Development of electrolytes for Li-ion capacitors* (Master's thesis, The Florida State University). Retrieved from http://diginole.lib.fsu.edu/etd/4766

Chiou, C.-W., Lin, Y.-C., Wang, L., Hirano, C., Suzuki, Y., Hayakawa, T., & Kuo, S.-W. (2014). Strong screening effect of polyhedral oligomeric silsesquioxanes (POSS) nanoparticles on hydrogen bonded polymer blends. *Polymers, 6* , 926-948.

Corn Refiners Association. (2006). *Corn Starch* (11th ed.). Washington, D.C.: Author. Retrieved from http://www.corn.org/wp-content/uploads/2009/12/Starch2006.pdf

Correia, C.O., Caridade, S.G., & Mano, J.F. (2014). Chitosan membranes exhibiting shape memory capability by the action of controlled hydration. *Polymers, 6*, 1178-1186.

Costa, M.M., Junior, G.F.M.P., & Sombra, A.S.B. (2010). Dielectric and impedance properties' studies of the of lead doped (PbO)-Co_2Y type hexaferrite ($Ba_2Co_2Fe_{12}O_{22}$ (Co_2Y)). *Materials Chemistry and Physics, 123*, 35-39.

Costa, M.M., Terezo, A.J., Matos, A.L., Moura, W.A., Giacometti, J.A., & Sombra, A.S.B. (2010). Impedance spectroscopy study of dehydrated chitosan and chitosan containing $LiClO_4$. *Physica B, 405*, 4439-4444.

Curvelo, A.A.S., de Carvalho, A.J.F., & Agnelli, J.A.M. (2001). Thermoplastic starch-cellulosic fibers composites: preliminary results. *Carbohydrate Polymers, 45*, 183-188.

da Silva, G.P., Mack, M., & Contiero, J. (2009). Glycerol: A promising and abundant carbon source for industrial microbiology. *Biotechnology Advances, 27*, 30-39.

Deepa, M., Sharma, N., Agnihotry, S.A., Singh, S., Lal, T., & Chandra, R. (2002). Conductivity and viscosity of liquid and gel electrolytes based on $LiClO_4$, $LiN(CF_3SO_2)_2$ and PMMA. *Solid State Ionics, 152-153*, 253-258.

Deraman, S.K., Mohamed, N.S. & Subban, R.H.Y. (2013). Conductivity and electrochemical studies on polymer electrolytes based on poly vinyl (chloride)-ammonium triflate-ionic liquid for proton battery. *International Journal of Electrochemical Science, 8*, 1459-1468.

Dias, F.B., Plomp, L., & Veldhuis, J.B.J. (2000). Trends in polymer electrolytes for secondary lithium batteries. *Journal of Power Sources, 88*, 169-191.

Dragunski, D.C., & Pawlicka, A. (2002). Starch based solid polymer electrolytes. *Molecular Crystals and Liquid Crystals, 374*, 561-568.

Dutta, P., Biswas, S., & De, S.K. (2002). Dielectric relaxation in polyaniline-polyvinyl alcohol composites. *Materials Research Bulletin, 37*, 193-200.

El-Deen, L.M.S. (2000). The ac conductivity studies for Cu_2O–Bi_2O_3 glassy system. *Materials Chemistry and Physics, 65*, 275-281.

El-Hefian, E.A., Nasef, M.M., & Yahaya, A.H. (2010). The preparation and characterization of chitosan / poly (vinyl alcohol) blended films. *E-Journal of Chemistry, 7*, 1212-1219.

El-Hefian, E.A., Nasef, M.M., Yahaya, A.H., & Khan, R.A. (2010). Preparation and characterization of chitosan/agar blends: Rheological and thermal studies. *Journal of the Chilean Chemical Society, 55*, 130-136.

El-Kader, M.F.H.A., & Ragab, H.S. (2013). DC conductivity and dielectric properties of maize starch/methylcellulose blend films. *Ionics, 19*, 361-369.

Fadzallah, I.A., Majid, S.R., Careem, M.A., & Arof, A.K. (2014). A study on ionic interactions in chitosan-oxalic acid polymer electrolyte membranes. *Journal of Membrane Science, 463*, 65-72.

Filho, L.S.L., Seidl, P.R., Correia, J.C.G., & Cerqueira, L.C.K. (2000). Molecular modelling of reagents for flotation processes. *Minerals Engineering, 13*, 1495-1503.

Fujishima, A., & Zhang, X.-T. (2005). Solid-state dye-sensitized solar cells. *Proceedings of the Japan Academy Series B: Physical and Biological Sciences, 81*, 33-42.

Gadjourova, Z., Andreev, Y.G., Tunstall, D.P., & Bruce, P.G. (2001). Ionic conductivity in crystalline polymer electrolytes. *Nature, 412*, 520-523.

Ghosh, A., Wang, C., & Kofinas, P. (2010). Block copolymer solid battery electrolyte with high Li-ion transference number. *Journal of the Electrochemical Society, 157*, A846-A849.

Ghoshal, S. (2012). *Study of polymer film formation and their characterization using NMR, XRD and DSC* (Doctoral thesis, Ilmenau University of Technology, Ilmenau, Germany). Retrieved from http://d-nb.info/1022376179/34

Gondaliya, N., Kanchan, D.K., & Sharma, P. (2013). Effect of a plasticizer on a solid polymer electrolyte. *Society of Plastics Engineers*. Retrieved from http://4spepro.org/pdf/004646/

Gonzalez, Z., & Perez, E. (2002). Effect of acetylation on some properties of rice starch. *Starch, 54*, 148-154.

Gopalasamy, T., Gopalswamy, M., Gopichand, M., & Raj, J. (2014). Poly meta-aminophenol: Chemical synthesis, characterization and ac impedance study. *Journal of Polymers, 2014*, 827043.

Guinot, S., Salmon, E., Penneau, J.F., & Fauvarque, J.F. (1998). A new class of PEO-based SPEs: Structure, conductivity and application to alkaline secondary batteries. *Electrochimica Acta, 43*, 1163-1170.

Guo, L., Sato, H., Hashimoto, T., & Ozaki, Y. (2010). FTIR study on hydrogen-bonding interactions in biodegradable polymer blends of poly(3-hydroxybutyrate) and poly(4-vinylphenol). *Macromolecules, 43*, 3897-3902.

Guohua, Z., Ya, L., Cuilan, F., Min, Z., Caiqiong, Z., & Zongdao, C. (2006). Water resistance, mechanical properties and biodegradability of methylated-cornstarch/poly(vinyl alcohol) blend film. *Polymer Degradation and Stability, 91*, 703-711.

Halim, N.F.A., Majid, S.R., Arof, A.K., Kajzar, F., & Pawlicka, A. (2012). Gellan gum-LiI gel polymer electrolytes. *Molecular Crystals and Liquid Crystals, 554*, 232-238.

Hamdan, K.Z., & Khiar, A.S.A. (2014). Conductivity and dielectric studies of methylcellulose/chitosan-$NH_4CF_3SO_3$ polymer electrolyte. *Key Engineering Materials, 594-595*, 818-822.

Hamdy, A.S., El-Shenawy, E., & El-Bitar, T. (2006). Electrochemical impedance spectroscopy study of the corrosion behavior of some niobium bearing stainless steels in 3.5% NaCl. *International Journal of Electrochemical Science, 1*, 171-180.

Han, D.G., & Choi, G.M. (1998) Computer simulation of the electrical conductivity of composites: The effect of geometrical arrangement. *Solid State Ionics, 106*, 71-87.

Hashim, M.A., & Khiar, A.S.A. (2011). Supercapacitor based on activated carbon and hybrid solid polymer electrolyte. *Materials Research Innovations, 15*, S63-66.

Hashim, M.A., Majid, S.R., Ibrahim, Z.A., & Arof, A.K. (2005). Electrochemical double layer capacitor based on cellulose-PVA hybrid electrolyte. *Ionics, 11*, 464-467.

Hashmi, S.A., Kumar, A., & Tripathi, S.K. (2004). Experimental studies on solid state electrical double layer capacitors using activated charcoal powder electrodes and PVdF-HFP based gel electrolytes. *Ionics, 10*, 213-220.

Hashmi, S.A., Latham, R.J., Linford, R.G., & Schlindwein, W.S. (1997). Studies on all solid state electric double layer capacitors using proton and lithium ion conducting polymer electrolytes. *Journal of the Chemical Society - Faraday Transactions, 93*, 4177-4182.

Hassan, F., Woo, H.J., Aziz, N.A., Kufian, M.Z., & Majid , S.R. (2013). Synthesis of Al_2TiO_5 and its effect on the properties of chitosan-NH_4SCN polymer electrolytes. *Ionics, 19*, 483-489.

He, L.-H., Xue, R., Yang, D.-B., Liu, Y., & Song, R. (2009). Effects of blending chitosan with PEG on surface morphology, crystallization and thermal properties. *Chinese Journal of Polymer Science, 27*, 501-510.

He, Y., Zhu, B., & Inoue, Y. (2004). Hydrogen bonds in polymer blends. *Progress in Polymer Science, 29*, 1021-1051.

Hegenbart, S. (1996, January 1). *Understanding starch functionality*. Retrieved from http://www.foodproductdesign.com/articles/1996/01/understanding-starch-functionality.aspx

Hejazi, R., & Amiji, M. (2003). Chitosan-based gastrointestinal delivery systems. *Journal of Controlled Release, 89*, 151-165.

Hejri, Z., Seifkordi, A.A., Ahmadpour, A., Zebarjad, S.M., & Maskooki, A. (2013). Biodegradable starch/poly (vinyl alcohol) film reinforced with titanium dioxide nanoparticles. *International Journal of Minerals, Metallurgy, and Materials, 20*, 1001-1011.

Hema, M., Selvasekarapandian, S., Arunkumar, D., Sakunthala, A., & Nithya, H. (2009). FTIR, XRD and ac impedance spectroscopic study on PVA based polymer electrolyte doped with NH_4X (X = Cl, Br, I). *Journal of Non-Crystalline Solids, 355*, 84-90.

Hema, M., Selvasekarapandian, S., Nithya, H., Sakunthala, A., & Arunkumar, D. (2009). Structural and ionic conductivity studies on proton conducting polymer electrolyte based on polyvinyl alcohol. *Ionics, 15*, 487-491.

Hema, M., Selvasekarapandian, S., Sakunthala, A., Arunkumar, D., & Nithya, H. (2008). Structural, vibrational and electrical characterization of PVA-NH_4Br polymer electrolyte system. *Physica B: Condensed Matter, 403*, 2740-2747.

Hess, M., Allegra, G., He, J., Horie, K., Kim, J.-S., Meille, S.V., ... Vohlidah, J. (2013). Glossary of terms relating to thermal and thermo mechanical properties of polymers (IUPAC recommendations 2013). *Pure and Applied Chemistry, 85*, 1017-1046.

Ho, M.Y., Khiew, P.S., Isa, D., & Tan, T.K. (2014). A review of metal oxide composite electrode materials for electrochemical capacitors. *Nano, 9*, 1430002.

Hofmann, A., Schulz, M., & Hanemann, T. (2013). Gel electrolytes based on ionic liquids for advanced lithium polymer batteries. *Electrochimica Acta, 89*, 823-831.

Ibrahim, S., & Johan, M.R. (2012). Thermolysis and conductivity studies of poly(ethylene oxide) (PEO) based polymer electrolytes doped with carbon nanotube. *International Journal of Electrochemical Science, 7*, 2596-2615.

Ibrahim, S., Yasin, S.M.M., Nee, N.M., Ahmad, R., & Johan, M.R. (2012). Conductivity, thermal and infrared studies on plasticized polymer electrolytes with carbon nanotubes as filler. *Journal of Non-Crystalline Solids, 358*, 210-216.

Idris, N.H., Majid, S.R., Khiar, A.S.A., Hassan, M.F., & Arof, A.K. (2005). Conductivity studies on chitosan/PEO blends with LiTFSI salt. *Ionics, 11*, 375-377.

Idris, N.H., Senin, H.B., & Arof, A.K. (2007). Dielectric spectra of LiTFSI-doped chitosan/PEO blends. *Ionics, 13*, 213-217.

Imperiyka, M., Ahmad, A., Hanifah, S.A., & Rahman, M.Y.A. (2014). Preparation and characterization of polymer electrolyte of glycidyl methacrylate-methyl methacrylate-$LiClO_4$ plasticized with ethylene carbonate. *International Journal of Polymer Science, 2014*, 638279.

Isa, K.B.M. (2010). *Electrical and structural studies of Polyacrylonitrile (PAN) complexed with inorganic salts* (Master's thesis, University of Malaya, Kuala Lumpur, Malaysia). Retrieved from http://studentsrepo.um.edu.my/4295

Islam, A.K.M.F.U., Islam, R., & Khan, K.A. (2005). Effects of deposition variables on spray-deposited MnO_2 thin films prepared from $Mn(C_2H_3O_2)_2{\cdot}4H_2O$. *Renewable Energy, 30*, 2289-2302.

Jamaludin, A., & Mohamad, A.A. (2010). Application of liquid gel polymer electrolyte based on chitosan-NH_4NO_3 for proton batteries. *Journal of Applied Polymer Science, 118*, 1240-1243.

Jane, J., Xu, A., Radosavljevic, M., & Seib, P.A. (1992). Location of amylose in normal starch granules. I. Susceptibility of amylose and amylopectin to cross-linking reagents. *Cereal Chemistry*, 69, 405-409.

Jayaprakash, M.S., Kumar, K.S., Sreenivasa, S., Mohan N.R., & Shashidar (2013). Solid state studies of chitosan and starch blend films. *Journal of Modern Chemistry & Chemical Technology, 4*, 11-18.

Jiang, G.B., Quan, D., Liao, K., & Wang, H. (2006). Novel polymer micelles prepared from chitosan grafted hydrophobic palmitoyl groups for drug delivery. *Molecular Pharmaceutics, 3*, 152-160.

Johan, M.R., & Ting, L.M. (2011). Structural, thermal and electrical properties of nano-manganese-composite polymer electrolytes. *International Journal of Electrochemical Science, 6*, 4737-4738.

Johansson, P. (1998). *Conformations and Vibrations in Polymer Electrolytes* (Doctoral thesis, Uppsala University, Uppsala, Sweden). Retrieved from http://fy.chalmers.se/~jpatrik/thesis.htm

Jones, J.B. (2010). *Physical characteristics and metal binding applications of chitosan films* (Master's thesis, University of Tennessee). Retrieved from http://trace.tennessee.edu/utk_gradthes/722

Jun, H.K., Buraidah, M.H., Noor, M.M., Kufian, M.Z., Majid, S.R., Sahraoui, B., & Arof, A.K. (2013). Application of LiBOB-based liquid electrolyte in co-sensitized solar cell. *Optical Materials, 36*, 151-158.

Juneja, P., Kaur, B., Odeku, O.A., & Singh, I. (2014). Development of corn starch-neusilin UFL2 conjugate as tablet superdisintegrant: Formulation and evaluation of fast disintegrating tablets. *Journal of Drug Delivery, 2014*, 827035.

Ka, B.H., & Oh, S.M. (2008). Electrochemical activation of expanded graphite electrode for electrochemical capacitor. *Journal of the Electrochemical Society, 155*, A685-A692.

Kadir, M.F.Z.A. (2010). *Characteristics of proton conducting PVA-chitosan polymer blend electrolytes* (Doctoral thesis, University of Malaya, Kuala Lumpur, Malaysia). Retrieved from http://studentsrepo.um.edu.my/2744

Kadir, M.F.Z., & Arof, A.K. (2011). Application of PVA-chitosan blend polymer electrolyte membrane in electrical double layer capacitor. *Materials Research Innovations, 15*, S217-S220.

Kadir, M.F.Z., Aspanut, Z., Majid, S.R., & Arof, A.K. (2011). FTIR studies of plasticized poly(vinyl alcohol)-chitosan blend doped with NH_4NO_3 polymer electrolyte membrane. *Spectrochimica Acta Part A, 78*, 1068-1074.

Kadir, M.F.Z., Aspanut, Z., Yahya, R., & Arof, A.K. (2011). Chitosan-PEO proton conducting polymer electrolyte membrane doped with NH_4NO_3. *Materials Research Innovations, 15*, S164-S167.

Kadir, M.F.Z., Majid, S.R. & Arof, A.K. (2010). Plasticized chitosan-PVA blend polymer electrolyte based proton battery. *Electrochimica Acta, 55*, 1475-1482.

Kadir, M.F.Z.A., Teo, L.P., Majid, S.R., & Arof, A.K. (2009). Conductivity studies on plasticised PEO/chitosan proton conducting polymer electrolyte. *Materials research Innovations, 13*, 259-262.

Kampeerapappun, P., Aht-ong, D., Pentrakoon, D., & Srikulkit, K. (2007). Preparation of cassava starch/montmorillonite composite film. *Carbohydrate Polymers, 67*, 155-163.

Kartha, S.A. (2013). *A Preparation of B_2O_3-Li_2O-MO (M=Pb, Zn) glass thin films and study of thin properties* (Doctoral thesis, Mahatma Gandhi University, Kerala, India). Retrieved from http://shodhganga.inflibnet.ac.in:8080/jspui/handle/10603/6510

Kato, Y., Hasumi, K., Yokoyama, S., Yabe, T., Ikuta, H., Uchimoto, Y., & Wakihara, M. (2002). Influence of PEG-borate ester on thermal property and ionic conductivity of the polymer electrolyte. *Journal of Thermal Analysis and Calorimetry, 69*, 889-896.

Khaled, K.F., & Al-Mhyawi, R. (2013). Electrochemical and density function theory investigations of L-arginine as corrosion inhibitor for steel in 3.5% NaCl. *International Journal of Electrochemical Science, 8*, 4055-4072.

Khan, F.A. (2014). *Biotechnology in medical sciences*. Boca Raton: CRC Press.

Khanmirzaei, M.H., & Ramesh, S. (2013). Ionic transport and ftir properties of lithium iodide doped biodegradable rice starch based polymer electrolytes. *International Journal of Electrochemical Science, 8*, 9977-9991.

Khiar, A.S.A., & Arof, A.K. (2010). Conductivity studies of starch-based polymer electrolytes. *Ionics, 16*, 123-129.

Khiar, A.S.A., & Arof, A.K. (2011). Electrical properties of starch/chitosan-Nh_4no_3 polymer electrolyte. *World Academy of Science, Engineering and Technology, 5*, 15-19.

Khiar, A.S.A., Puteh, R., & Arof, A.K. (2006). Conductivity studies of a chitosan-based polymer electrolyte. *Physica B: Condensed Matter, 373*, 23-27.

Khiar, A.S.A., Radzi, S.M., & Razak, N.A. (2013). Conductivity and dielectric behaviour studies of $LiCF_3SO_3$ dissociation in L-chitosan/PMMA-based polymer electrolytes. *Malaysian Journal of Fundamental and Applied Sciences, 9*, 46-50.

Kim, D.-W., Park, J.-K., & Rhee, H.-W. (1996). Conductivity and thermal studies of solid polymer electrolytes prepared by blending poly(ethylene oxide), poly(oligo[oxyethylene]oxysebacoyl) and lithium perchlorate. *Solid State Ionics, 83*, 49-56.

Kim, Y.-T., & Mitani, T. (2006). Competitive effect of carbon nanotubes oxidation on aqueous EDLC performance: Balancing hydrophilicity and conductivity. *Journal of Power Sources, 158*, 1517-1522.

Knorr, D., Heinz, V., & Buckow, R. (2006). High pressure application for food biopolymers. *Biochimica et Biophysica Acta, 1764*, 619-631.

Kok, M., Demirelli, K., & Aydogdu, Y. (2008). Thermophysical properties of blend of poly (vinyl chloride) with poly (isobornyl acrylate). *International Journal of Science and Technology, 3*, 37-42.

Kreuer, K.-D. (1996). Proton conductivity: Materials and applications. *Chemistry of Materials, 8*, 610-641.

Kucinska-Lipka, J., Gubanska, I., & Janik, H. (2014). Polyurethanes modified with natural polymers for medical application. Part II. Polyurethane/gelatin, polyurethane/starch, polyurethane/cellulose. *Polimery/Polymers, 59*, 197-200.

Kufian, M.Z., & Majid, S.R. (2010). Performance of lithium-ion cells using 1 M $LiPF_6$ in EC/DEC (*v*/*v* = 1/2) electrolyte with ethyl propionate additive. *Ionics, 16*, 409-416.

Kufian, M.Z., Aziz, M.F., Shukur, M.F., Rahim, A.S., Ariffin, N.E., Shuhaimi, N.E.A., … Arof, A.K. (2012). PMMA-LiBOB gel electrolyte for application in lithium ion batteries. *Solid State Ionics, 208*, 36-42.

Kufian, M.F., Majid, S.R., & Arof, A.K. (2007). Dielectric and conduction mechanism studies of PVA-orthophosphoric acid polymer electrolyte. *Ionics, 13*, 231-234.

Kulkarni, V.S., Butte, K.D., & Rathod, S.S. (2012). Natural polymers - A comprehensive review. *International Journal of Research in Pharmaceutical and Biomedical Sciences, 3*, 1597-1613.

Kumar, D.A., Selvasekarapandian, S., Baskaran, R., Savitha, T., & Nithya, H. (2012). Thermal, vibrational and ac impedance studies on proton conducting polymer electrolytes based on poly(vinyl acetate). *Journal of Non-Crystalline Solids, 358*, 531-536.

Kumar, M., & Sekhon, S.S. (2002). Role of plasticizer's dielectric constant on conductivity modification of PEO-NH_4F polymer electrolytes. *European Polymer Journal, 38*, 1297-1304.

Kumar, M., Tiwari, T., & Srivastava, N. (2012). Electrical transport behaviour of bio-polymer electrolyte system: Potato starch + ammonium iodide. *Carbohydrate Polymers, 88*, 54-60.

Kumar, M.S., & Bhat, D.K. (2009). Polyvinyl alcohol-polystyrene sulphonic acid blend electrolyte for supercapacitor application. *Physica B, 404*, 1143-1147.

Kumar, Y., Pandey, G.P., & Hashmi, S.A. (2012). Gel polymer electrolyte based electrical double layer capacitors: Comparative study with multiwalled carbon nanotubes and activated carbon electrodes. *Journal of Physical Chemistry C, 116*, 26118-26127.

Kuo, C.-W., Li, W.-B., Chen, P.-R., Liao, J.-W., Tseng, C.-G., & Wu, T.-Y. (2013). Effect of plasticizer and lithium salt concentration in PMMA-based composite polymer electrolytes. *International Journal of Electrochemical Science, 8*, 5007-5021.

Lawal, O.S. (2009). Starch hydroxyalkylation: Physicochemical properties and enzymatic digestibility of native and hydroxypropylated finger millet (*Eleusine coracana*) starch. *Food Hydrocolloids, 23*, 415-425.

Lee, C.-P., Chen, P.-Y., Vittal, R., & Ho, K.-C. (2010). Iodine-free high efficient quasi solid-state dye-sensitized solar cell containing ionic liquid and polyaniline-loaded carbon black. *Journal of Materials Chemistry, 20*, 2356-2361.

Lee, C.-P., Han, T.-H., Hwang, T., Oh, J.-S., Kim, S.-J., Kim, B.-W., ... Nam, J.D. (2012). Electrochemical double layer capacitor performance of electrospun polymer fiber-electrolyte membrane fabricated by solvent-assisted and thermally induced compression molding processes. *Journal of Membrane Science, 409-410*, 365-370.

Lee, C.-P., Lin, L.-Y., Chen, P.-Y., Vittal, R., & Ho, K.-C. (2010). All-solid-state dye-sensitized solar cells incorporating SWCNTs and crystal growth inhibitor. *Journal of Materials Chemistry, 20*, 3619-3625.

Lee, Y.S., Lee, W.-K., Cho, S.-G., Kim, I., & Ha, C.-S. (2007). Quantitative analysis of unknown compositions in ternary polymer blends: A model study on NR/SBR/BR system. *Journal of Analytical and Applied Pyrolysis, 78*, 85-94.

Lei, C., Markoulidis, F., Ashitaka, Z., & Lekakou, C. (2013). Reduction of porous carbon/Al contact resistance for an electric double-layer capacitor (EDLC). *Electrochimica Acta, 92*, 183-187.

Lei, C., Wilson, P., & Lekakou, C. (2011). Effect of poly(3,4-ethylenedioxythiophene) (PEDOT) in carbon-based composite electrodes for electrochemical supercapacitors. *Journal of Power Sources, 196*, 7823-7827.

Li, S.-L., Lin, J., & Chen, X.M. (2014). Effect of chitosan molecular weight on the functional properties of chitosan-maltose Maillard reaction products and their application to fresh-cut *Typha latifolia* L.. *Carbohydrate Polymers, 102*, 682-690.

Liang, S., Huang, Q., Liu, L., & Yam, K.L. (2009). Microstructure and molecular interaction in glycerol plasticized chitosan/poly(vinyl alcohol) blending films. *Macromolecular Chemistry and Physics, 210*, 832-839.

Liew, C.-W., Ramesh, S., & Arof, A.K. (2014). Good prospect of ionic liquid based-poly(vinylalcohol) polymer electrolytes for supercapacitors with excellent electrical, electrochemical and thermal properties. *International Journal of Hydrogen Energy, 39*, 2953-2963.

Liew, C.-W., Ramesh, S., & Arof, A.K. (2015). Characterization of ionic liquid added poly(vinyl alcohol)-based proton conducting polymer electrolytes and electrochemical studies on the supercapacitors. *International Journal of Hydrogen Energy, 40*, 852-862.

Liew, C.-W., Ramesh, S., Ramesh, K., & Arof, A.K. (2012). Preparation and characterization of lithium ion conducting ionic liquid-based biodegradable corn starch polymer electrolytes. *Journal of Solid State Electrochemistry, 16*, 1869-1875.

Lim, C.-S., Teoh, K.H., Liew, C.-W., & Ramesh, S. (2014a). Capacitive behavior studies on electrical double layer capacitor using poly (vinyl alcohol)-lithium perchlorate based polymer electrolyte incorporated with TiO_2. *Materials Chemistry and Physics, 143*, 661-667.

Lim, C.-S., Teoh, K.H., Liew, C.-W., & Ramesh, S. (2014b). Electric double layer capacitor based on activated carbon electrode and biodegradable composite polymer electrolyte. *Ionics, 20*, 251-258.

Ling, L., & Qing-Han, M. (2005). Electrochemical properties of mesoporous carbon aerogel electrodes for electric double layer capacitors. *Journal of Materials Science, 40*, 4105-4107.

Liu, H., Adhikari, R., Guo, Q., & Adhikari, B. (2013). Preparation and characterization of glycerol plasticized (high-amylose) starch-chitosan films. *Journal of Food Engineering, 116*, 588-597.

Liu, P., Yu, L., Liu, H., Chen, L., & Li, L. (2009). Glass transition temperature of starch studied by a high-speed DSC. *Carbohydrate Polymers, 77*, 250-253.

Lu, D.R., Xiao, C.M., & Xu, S.J. (2009). Starch-based completely biodegradable polymer materials. *Express Polymer Letters, 3*, 366-375.

Lu, X., & Weiss, R.A. (1991). Development of miscible blends of polyamide-6 and manganese sulfonated polystyrene using specific interactions. *Macromolecules, 24*, 4381-4385.

Luk, E., Sandoval, A.J., Cova, A., & Muller, A.J. (2013). Anti-plasticization of cassava starch by complexing fatty acids. *Carbohydrate Polymers, 98*, 659-664.

Luo, X.F., Hu, X., Zhao, X.Y., Goh, S.H., & Li, X.D. (2003). Miscibility and interactions in blends and complexes of poly(4-methyl-5-vinylthiazole) with proton-donating polymers. *Polymer, 44*, 5285-5291.

Ma, G., Feng, E., Sun, K., Peng, H., Li, J., & Lei, Z. (2014). A novel and high-effective redox-mediated gel polymer electrolyte for supercapacitor. *Electrochimica Acta, 135*, 461-466.

Ma, X., Yu, J., He, K., & Wang, N. (2007). The effects of different plasticizers on the properties of thermoplastic starch as solid polymer electrolytes. *Macromolecular Materials and Engineering, 292*, 503-510.

Macdonald, J.R. (1999). Dispersed electrical-relaxation response: Discrimination between conductive and dielectric relaxation processes. *Brazilian Journal of Physics, 29*, 332-346.

Mahoney, C., Mccullough, M.B., Sankar, J., & Bhattarai, N. (2012). Nanofibrous structure of chitosan for biomedical applications. *Journal of Nanomedicine & Biotherapeutic Discovery, 2*, 1000102.

Majid, S.R. (2007). *High molecular weight chitosan as polymer electrolyte for electrochemical devices* (Doctoral thesis, University of Malaya, Kuala Lumpur, Malaysia).

Majid, S.R., & Arof, A.K. (2005). Proton-conducting polymer electrolyte films based on chitosan acetate complexed with NH_4NO_3 salt. *Physica B: Condensed Matter, 355*, 78-82.

Majid, S.R., & Arof, A.K. (2007). Electrical behavior of proton conducting chitosan-phosphoric acid-based electrolytes. *Physica B: Condensed Matter, 390*, 209-215.

Majid, S.R., & Arof, A.K. (2008). FTIR studies of chitosan-orthophosphoric acid-ammonium nitrate-aluminosilicate polymer electrolyte. *Molecular Crystals and Liquid Crystals, 484*, 117-126.

Malathi, J., Brahmanandhan, G.M., Hema, M., Hirankumar, G., Khanna, D., Kumar, D.A., & Selvasekarapandian, S. (2006). Dielectric and conductivity studies of PVA-KSCN based solid polymer electrolytes. In B.V.R. Chowdari, M.A. Careem, M.A.K.L. Dissanayake, R.M.G. Rajapakse, & V.A. Seneviratne (Eds.), *Proceedings of the 10th Asian Conference on Solid State Ionics: Advanced Materials for Emerging Technologies* (pp. 696-703). Kandy, Sri Lanka: World Scientific.

Malathi, J., Kumaravadivel, M., Brahmanandhan, G.M., Hema, M., Baskaran, R., & Selvasekarapandian, S. (2010). Structural, thermal and electrical properties of PVA-$LiCF_3SO_3$ polymer electrolyte. *Journal of Non-Crystalline Solids, 356*, 2277-2281.

Maningat, C.C., Seib, P.A., Bassi, S.D., Woo, K.S., & Lasater, G.D. (2009). Wheat starch: Production, properties, modification and uses. In J. BeMiller & R. Whistler (Eds.), *Starch: Chemistry and technology* (pp. 441-510). Oxford, UK: Elsevier.

Marcondes, R.F.M.S., D'Agostini, P.S., Ferreira, J., Girotto, E.M., Pawlicka, A., & Dragunski, D.C. (2010). Amylopectin-rich starch plasticized with glycerol for polymer electrolyte application. *Solid State Ionics, 181*, 586-591.

Marsano, E., Corsini, P., Canetti, M., & Freddi, G. (2008). Regenerated cellulose-silk fibroin blends fibers. *International Journal of Biological Macromolecules, 43*, 106-114.

Mason, R.N., Hu, L., Glatzhofer, D.T., & Frech, R. (2010). Infrared spectroscopic and conductivity studies of poly(N-methylpropylenimine)/lithium triflate electrolytes. *Solid State Ionics, 180*, 1626-1632.

Mathew, S., & Abraham, T.E. (2008). Characterisation of ferulic acid incorporated starch-chitosan blend films. *Food Hydrocolloids, 22*, 826-835.

Mathew, S., Brahmakumar, M., & Abraham, T.E. (2006). Microstructural imaging and characterization of the mechanical, chemical, thermal, and swelling properties of starch-chitosan blend films. *Biopolymers, 82*, 176-187.

Maurya, K.K., Hashmi, S.A., & Chandra, S. (1992). Proton conducting polymer electrolytes: polyethylene oxide + $(NH_4)_2SO_4$ system. *Journal of the Physical Society of Japan, 61*, 1709-1716.

McBreen, J., Lee, H.S., Yang, X.Q., & Sun, X. (2000). New approaches to the design of polymer and liquid electrolytes for lithium batteries. *Journal of Power Sources, 89*, 163-167.

McComsey, D.W. (2001). Zinc-carbon batteries (Leclanche and zinc chloride cell systems). In D. Linden & T.B. Reddy (Eds.), *Handbook of batteries, Third edition* (pp 8.1-8.45). New York: McGraw-Hill Professional.

Mishra, K. (2013). *Preparation, characterization and battery applications of proton conducting polymer electrolytes* (Doctoral thesis, Jaypee Institute of Information

Technology, Uttar Pradesh, India). Retrieved from http://shodhganga.inflibnet.ac.in:8080/jspui/handle/10603/9618

Mishra, K., Hashmi, S.A., & Rai, D.K. (2014). Studies on a proton battery using gel polymer electrolyte. *High Performance Polymers, 26*, 672-676.

Mishra, R., & Rao, K.J. (1998). Electrical conductivity studies of poly(ethyleneoxide)-poly(vinylalcohol) blends. *Solid State Ionics, 106*, 113-127.

Mitani, S., Lee, S.-I., Saito, K., Korai, Y., & Mochida, I. (2006). Contrast structure and EDLC performances of activated spherical carbons with medium and large surface areas. *Electrochimica Acta, 51*, 5487-5493.

Miyamoto, H., Yamane, C., Seguchi, M. & Okajima, K. (2009). Structure and properties of cellulose-starch blend films regenerated from aqueous sodium hydroxide solution. *Food Science and Technology Research, 15*, 403-412.

Mobarak, N.N., Ramli, N., Ahmad, A., & Rahman, M.Y.A. (2012). Chemical interaction and conductivity of carboxymethyl κ-carrageenan based green polymer electrolyte. *Solid State Ionics, 224*, 51-57.

Mohamad, A.A., Mohamed, N.S., Yahya, M.Z.A., Othman, R., Ramesh, S., Alias, Y., & Arof, A.K. (2003). Ionic conductivity studies of poly(vinyl alcohol) alkaline solid polymer electrolyte and its use in nickel-zinc cells. *Solid State Ionics, 156*, 171-177.

Mohamed, N.S., Subban, R.H.Y., & Arof A.K. (1995). Polymer batteries fabricated from lithium complexed acetylated chitosan. *Journal of Power Sources, 56*, 153-156.

Mohan, K.R., Achari, V.B.S., Rao, V.V.R.N, & Sharma, A.K. (2011). Electrical and optical properties of (PEMA/PVC) polymer blend electrolyte doped with $NaClO_4$. *Polymer Testing, 30*, 881-886.

Money, B.K., Hariharan, K., & Swenson, J. (2012). Glass transition and relaxation processes of nanocomposite polymer electrolytes. *Journal of Physical Chemistry B, 116*, 7762-7770.

Morni, N.M., Mohamed, N.S., & Arof, A.K. (1997). Silver nitrate doped chitosan acetate films and electrochemical cell performance. *Materials Science and Engineering B, 45*, 140-146.

Moutzouri, A.G., & Athanassiou, G.M. (2014). Insights into the alteration of osteoblast mechanical properties upon adhesion on chitosan. *BioMed Research International, 2014*, 740726.

Muzzarelli, R.A.A. (1996). Chitosan-based dietary foods. *Carbohydrate Polymers, 29*, 309-316.

Nakamatsu, J., Torres, F.G., Troncoso, O.P., Min-Lin, Y., & Boccaccini, A.R. (2006). Processing and characterization of porous structures from chitosan and starch for tissue engineering scaffolds. *Biomacromolecules, 7*, 3345-3355.

Nara, H., Momma, T., & Osaka, T. (2013). Impedance analysis of the effect of flooding in the cathode catalyst layer of the polymer electrolyte fuel cell. *Electrochimica Acta, 113*, 720-729.

Nara, S., & Komiya, T. (1983). Studies on the relationship between water-satured state and crystallinity by the diffraction method for moistened potato starch. *Starch-Starke, 35*, 407-410.

Nasef, M.M., Saidi, H., & Dahlan, K.Z.M. (2007). Preparation of composite polymer electrolytes by electron beam-induced grafting: Proton- and lithium ion-conducting membranes. *Nuclear Instruments and Methods in Physics Research B, 265*, 168-172.

Nasibi, M., Golozar, M.A., & Rashed, G. (2012). Nano zirconium oxide/carbon black as a new electrode material for electrochemical double layer capacitors. *Journal of Power Sources, 206*, 108-110.

Neelam, K., Vijay, S., & Lalit, S., Various techniques for the modification of starch and the applications of its derivatives. *International Research Journal of Pharmacy, 3*, 25-31.

Ng, L.S., & Mohamad, A.A. (2006). Protonic battery based on a plasticized chitosan-NH_4NO_3 solid polymer electrolyte. *Journal of Power Sources, 163*, 382-385.

Ng, L.S., & Mohamad, A.A. (2008). Effect of temperature on the performance of proton batteries based on chitosan-NH_4NO_3-EC membrane. *Journal of Membrane Science, 325*, 653-657.

Ning, W., Xingxiang, Z., Haihui, L., & Benqiao, H. (2009). 1-Allyl-3-methylimidazolium chloride plasticized-corn starch as solid biopolymer electrolytes. *Carbohydrate Polymers, 76*, 482-484.

Ning, W., Xingxiang, Z., Haihui, L., & Jianping, W. (2009). *N*, *N*-dimethylacetamide/lithium chloride plasticized starch as solid biopolymer electrolytes. *Carbohydrate Polymers, 77*, 607-611.

Nivethaa, E.A.K., Narayanan, V., & Stephen, A. (2014). Chitosan - silver nanocomposite for biosensor application. *International Journal of Chemtech Research, 6*, 2054-2056.

Noor, I.S., Majid, S.R., & Arof, A.K. (2013). Poly(vinyl alcohol)-LiBOB complexes for lithium-air cells. *Electrochimica Acta, 102*, 149-160.

Noor, I.S.M., Majid, S.R., Arof, A.K., Djurado, D., Neto, S.C., & Pawlicka, A. (2012). Characteristics of gellan gum-$LiCF_3SO_3$ polymer electrolytes. *Solid State Ionics, 225*, 649-653.

Noor, M.M., Careem, M.A., Majid, S.R., & Arof, A.K. (2011). Characterisation of plasticised PVDF-HFP polymer electrolytes. *Materials Research Innovations, 15*, S157-S160.

Noor, S.A.M., Ahmad, A., Rahman, M.Y.A., & Talib, I.A. (2010). Solid polymeric electrolyte of poly(ethylene)oxide-50% epoxidized natural rubber-lithium triflate (PEO-ENR50-$LiCF_3SO_3$). *Natural Science, 2*, 190-196.

Ochubiojo, E.M., & Rodrigues, A. (2012). Starch: From food to medicine. In B. Valdez (Ed.), *Scientific, health and social aspects of the food industry* (pp. 355-380). Rijeka, Croatia: InTech.

Ogaji, I.J., Nep, E.I., & Audu-Peter, J.D. (2011). Advances in natural polymers as pharmaceutical excipients. *Pharmaceutica Analytica Acta, 3*, 1000146.

Osman, Z., & Arof, A.K. (2003). FTIR studies of chitosan acetate based polymer electrolytes. *Electrochimica Acta, 48*, 993-999.

Osman, Z., Ghazali, M.I.M., Othman, L., & Isa, K.B.M. (2012). AC ionic conductivity and DC polarization method of lithium ion transport in PMMA-$LiBF_4$ gel polymer electrolytes. *Results in Physics, 2*, 1-4.

Osman, Z., Ibrahim, Z.A., & Arof, A.K. (2001). Conductivity enhancement due to ion dissociation in plasticized chitosan based polymer electrolytes. *Carbohydrate Polymers, 44*, 167-173.

Padmasree, K.P., Kanchan, D.K., & Kulkarni, A.R. (2006) Impedance and modulus studies of the solid electrolyte system $20CdI_2$-$80[xAg_2O$-$y(0.7V_2O_5$-$0.3B_2O_3)]$, where $1 \leq x/y \leq 3$. *Solid State Ionics, 177*, 475-482.

Pandey, G.P., Kumar, Y., & Hashmi, S.A. (2010). Ionic liquid incorporated polymer electrolytes for supercapacitor application. *Indian Journal of Chemistry, 49*, 743-751.

Pandey, G.P., Kumar, Y., & Hashmi, S.A. (2011). Ionic liquid incorporated PEO based polymer electrolyte for electrical double layer capacitors: A comparative study with lithium and magnesium systems. *Solid State Ionics, 190*, 93-98.

Pandey, K., Asthana, N., Dwivedi, M.M., & Chaturvedi, S.K. (2013). Effect of plasticizers on structural and dielectric behaviour of [PEO + $(NH_4)_2C_4H_8(COO)_2$] polymer electrolyte. *Journal of Polymers, 2013*, 752596.

Pandey, K., Singh, M., Asthana, N., Dwivedi, M.M., & Agrawal, S.L. (2011). Development of magnisio ferrite doped polymer electrolyte system for battery application. *International Journal of Material Science, 1*, 9-17.

Panero, S., Ciuffa, F., D'Epifano, A., & Scrosati, B. (2003). New concepts for the development of lithium and proton conducting membranes. *Electrochimica Acta, 48*, 2009-2014.

Park, M., Zhang, X., Chung, M., Less, G.B., & Sastry, A.M. (2010). A review of conduction phenomena in Li-ion batteries. *Journal of Power Sources, 195*, 7904-7929.

Park, S.Y., Marsh, K.S., & Rhim, J.W. (2002). Characteristics of different molecular weight chitosan films affected by the type of organic solvents. *Journal of Food Science, 67*, 194-197.

Patro, L.N., & Hariharan, K. (2009). AC conductivity and scaling studies of polycrystalline SnF_2. *Materials Chemistry and Physics, 116*, 81-87.

Pawlicka, A., Danczuk, M., Wieczorek, W., & Zygadlo-Monikowska, E. (2008). Influence of plasticizer type on the properties of polymer electrolytes based on chitosan. *Journal of Physical Chemistry A, 112*, 8888-8895.

Pendashteh, A., Rahmanifar, M.S., Kaner, R.B., & Mousavi, M.F. (2014). Facile synthesis of nanostructured $CuCo_2O_4$ as a novel electrode material for high-rate supercapacitors. *Chemical Communications, 50*, 1972-1975.

Pereira, A.G.B., Paulino, A.T., Rubira, A.F., & Muniz, E.C. (2010). Polymer-polymer miscibility in PEO/cationic starch and PEO/hydrophobic starch blends. *Express Polymer Letters, 4*, 488-499.

Perera, K., & Dissanayake, M.A.K.L. (2006). Conductivity variation of the liquid electrolyte, EC : PC : $LiCF_3SO_3$ with salt concentration. *Sri Lankan Journal of Physics, 7*, 1-5.

Periasamy, P., Tatsumi, K., Kalaiselvi, N., Shikano, M., Fiyieda, T., Saito, Y., ... Deki, S. (2002). Performance evaluation of PVdF gel polymer electrolytes. *Ionics, 8*, 453-460.

Ping, P., Wang, Q., Sun, J., Feng, X., & Chen, C. (2011). Effect of sulfites on the performance of LiBOB/γ-butyrolactone electrolytes. *Journal of Power Sources, 196*, 776-783.

Pitawala, H.M.J.C., Dissanayake, M.A.K.L., Seneviratne, V.A., Mellander, B.-E., & Albinson, I. (2008). Effect of plasticizers (EC or PC) on the ionic conductivity and thermal properties of the $(PEO)_9LiTf$: Al_2O_3 nanocomposite polymer electrolyte system. *Journal of Solid State Electrochemistry, 12*, 783-789.

Polaskova, J., Pavlackova, J., Vltavska, P., Janirkoca, G., Kasparkova, V., & Janis, R. (2012). The moisturize influence of the commercial cosmetics on the foot skin. In D. Pavelkova, J. Strouhal, & M. Pasekova (Eds.), *Advances in Environment, Biotechnology and Biomedicine* (pp. 272-277). Zlin, Czech Republic: WSEAS Press.

Polu, A.R., & Kumar, R. (2011). Impedance spectroscopy and FTIR studies of PEG - based polymer electrolytes. *E-Journal of Chemistry, 8*, 347-353.

Pradan, D.K., Choudhary, R.N.P., Samantaray, B.K., Karan, N.K., & Katiyar, R.S. (2007). Effect of plasticizer on structural and electrical properties of polymer nanocompsoite electrolytes. *International Journal of Electrochemical Science, 2*, 861-871.

Prajapati, G.K., Roshan, R., & Gupta, P.N. (2010). Effect of plasticizer on ionic transport and dielectric properties of PVA-H_3PO_4 proton conducting polymeric electrolytes. *Journal of Physics and Chemistry of Solids, 71*, 1717-1723.

Pratap, R., Singh, B., & Chandra, S. (2006). Polymeric rechargeable solid-state proton battery. *Journal of Power Sources, 161*, 702-706.

Qian, X., Gu, N., Cheng, Z., Yang, X., Wang, E., & Dong, S. (2001). Impedance study of $(PEO)_{10}LiClO_4$-Al_2O_3 composite polymer electrolyte with blocking electrodes. *Electrochimica Acta, 46*, 1829-1836.

Rahaman, M.H.A., Khandaker, M.U., Khan, Z.R., Kufian, M.Z., Noor, I.S.M., & Arof, A.K. (2014). Effect of gamma irradiation on poly(vinyledene difluoride)-lithium bis(oxalato)borate electrolyte. *Physical Chemistry Chemical Physics, 16*, 11527-11537.

Rahman, M.M., Gruner, G., Al-Ghamdi, M.S., Daous, M.A., Khan, S.B., & Asiri, A.M. (2013). Chemo-sensors development based on low-dimensional codoped Mn_2O_3-ZnO nanoparticles using flat-silver electrodes. *Chemistry Central Journal, 7*, 60.

Raj, C.J., & Varma, K.B.R. (2010). Synthesis and electrical properties of the $(PVA)_{0.7}(KI)_{0.3}{\cdot}xH_2SO_4$ ($0 \leq x \leq 5$) polymer electrolytes and their performance in a primary Zn/MnO_2 battery. *Electrochimica Acta,* 56, 649-656.

Rajendran, S., & Mahendran, O. (2001). Experimental investigations on plasticized PMMA/PVA polymer blend electrolytes. *Ionics, 7*, 463-468.

Rajendran, S., Sivakumar, M., & Subadevi, R. (2004). Investigations on the effect of various plasticizers in PVA-PMMA solid polymer blend electrolytes. *Materials Letters, 58*, 641-649.

Rajeswari, N., Selvasekarapandian, S., Karthikeyan, S., Sanjeeviraja, C., Iwai, Y., & Kawamura, J. (2013). Structural, vibrational, thermal, and electrical properties of PVA/PVP biodegradable polymer blend electrolyte with CH_3COONH_4. *Ionics, 19*, 1105-1113.

Ramamohan, K., & Sharma, A.K. (2013). Effect of plasticizer on (PVC+PEMA+$NaIO_4$) solid polymer blend electrolyte system for battery characterization studies. *Advances in Polymer Science and Technology: An International Journal, 3*, 49-53.

Ramesh, S., & Arof, A.K. (2000). Electrical conductivity studies of polyvinyl chloride-based electrolytes with double salt system. *Solid State Ionics, 136-137*, 1197-1200.

Ramesh, S., & Arof, A.K. (2001). Ionic conductivity studies of plasticized poly(vinyl chloride) polymer electrolytes. *Materials Science and Engineering B, 85*, 11-15.

Ramesh, S., & Liew, C.-W. (2013). Dielectric and FTIR studies on blending of [*x*PMMA-(1 - *x*)PVC] with LiTFSI. *Measurement, 46*, 1650-1656.

Ramesh, S., & Ling, O.P. (2010). Effect of ethylene carbonate on the ionic conduction in poly(vinylidenefluoride-hexafluoropropylene) based solid polymer electrolytes. *Polymer Chemistry, 1*, 702-707.

Ramesh, S., Liew, C.-W., & Arof, A.K. (2011). Ion conducting corn starch biopolymer electrolytes doped with ionic liquid 1-butyl-3-methylimidazolium hexafluorophosphate. *Journal of Non-Crystalline Solids, 357*, 3654-3660.

Ramesh, S., Shanti, R., & Morris, E. (2012). Studies on the thermal behavior of CS:LiTFSI:[Amim] Cl polymer electrolytes exerted by different [Amim] Cl content. *Solid State Sciences, 14*, 182-186.

Ramesh, S., Winie, T., & Arof, A.K. (2007). Investigation of mechanical properties of polyvinyl chloride-polyethylene oxide (PVC-PEO) based polymer electrolytes for lithium polymer cells. *European Polymer Journal, 43*, 1963-1968.

Ramesh, S., Yahaya, A.H., & Arof, A.K. (2002). Dielectric behaviour of PVC-based polymer electrolytes. *Solid State Ionics, 152-153*, 291-294.

Ramly, K., Isa, M.I.N., & Khiar, A.S.A. (2011). Conductivity and dielectric behaviour studies of starch/PEO+*x* wt-% NH_4NO_3 polymer electrolyte. *Materials Research Innovations, 15*, S82-S85.

Ramya, C.S., Selvasekarapandian, S., Hirankumar, G., Savitha, T., & Angelo, P.C. (2008). Investigation on dielectric relaxations of PVP-NH_4SCN polymer electrolyte. *Journal of Non-Crystalline Solids, 354*, 1494-1502.

Ramya, R., Sudha, P.N., & Mahalakshmi, J. (2012). Preparation and characterization of chitosan binary blend. *International Journal of Scientific and Research Publications, 2*(10). Retrieved from http://www.ijsrp.org/research-journal-1012.php

Rao, M., Geng, X., Liao, Y., Hu, S., & Li, W. (2012). Preparation and performance of gel polymer electrolyte based on electrospun polymer membrane and ionic liquid for lithium ion battery. *Journal of Membrane Science, 399-400*, 37-42.

Ravi, M., Kumar, K.K., Mohan, V.M., & Rao, V.V.R.N. (2014). Effect of nano TiO_2 filler on the structural and electrical properties of PVP based polymer electrolyte films. *Polymer Testing, 33*, 152-160.

Reddy, M.J., Kumar, J.S., Rao, U.V.S., & Chu, P.P. (2006). Structural and ionic conductivity of PEO blend PEG solid polymer electrolyte. *Solid State Ionics, 177*, 253-256.

Rodrigo (2012, December 11). *How does biodegradable polymer upset the balance of the environment compared to synthetic polymer?*. Retrieved from http://writepass.com/journal/2012/12/how-biodegradable-polymer-upset-the balance-of-the-environment-compare-to-synthetic-polymer/

Roobottom, H.K., Jenkins, H.D.B., Passmore, J., & Glasser, L. (1999). Thermochemical radii of complex ions. *Journal of Chemical Education, 76*, 1570-1572.

Roscher, M.A., Bohlen, O., & Vetter, J. (2011). OCV hysteresis in Li-ion batteries including two-phase transition materials. *International Journal of Electrochemistry, 2011*, 984320.

Rosli, N.H.A., Chan, C.H., Subban, R.H.Y., & Winie, T. (2012). Studies on the structural and electrical properties of hexanoyl chitosan/polystyrene-based polymer electrolytes. *Physics Procedia, 25*, 215-220.

Rotta, J., Minatti, E., & Bareto, P.L.M. (2011). Determination of structural and mechanical properties, diffractometry, and thermal analysis of chitosan and hydroxypropylmethylcellulose (HPMC) films plasticized with sorbitol. *Ciencia e Technologia de Alimentos, 31*, 450-455.

Saaid, S.I.Y., Kudin, T.I.T., Ali, A.M.M., Ahmad, A.H., & Yahya, M.Z.A. (2009). Solid state proton battery using plasticised cellulose-salt complex electrolyte. *Materials Research Innovations, 13*, 252-254.

Sadhukhan, S. (2011). *Preparation and characterization of polymer electrolytes* (Master's thesis, National Institute of Technology Rourkela, Rourkela, Odisha, India). Retrieved from http://ethesis.nitrkl.ac.in/2698

Saikia, D., Pan, Y.-C., & Kao, H.-M. (2012). Synthesis, multinuclear NMR characterization and dynamic property of organic–inorganic hybrid electrolyte membrane based on alkoxysilane and poly(oxyalkylene) diamine. *Membranes, 2*, 253-274.

Sajilata, M.G., Singhal, R.S., & Kulkarni, P.R. (2006). Resistant starch - A review. *Comprehensive Reviews in Food Science and Food Safety, 5*, 1-17.

Salleh, E, & Muhamad, I.I. (2010). Starch-based antimicrobial films incorporated with lauric acid and chitosan. *AIP Conference Proceedings, 1217*, 432-436.

Salleh, E., Muhamad, I.I., & Khairuddin, N. (2009). Structural characterization and physical properties of antimicrobial (AM) starch-based films. *World Academy of Science, Engineering and Technology, 3*, 392-400.

Samar, M.M., El-Kalyoubi, M.H., Khalaf, M.M., & El-Razik, M.M.A. (2013). Physicochemical, functional, antioxidant and antibacterial properties of chitosan extracted from shrimp wastes by microwave technique. *Annals of Agricultural Science, 58*, 33-41.

Samsudin, A.S., Khairul, W.M., & Isa, M.I.N. (2012). Characterization on the potential of carboxy methylcellulose for application as proton conducting biopolymer electrolytes. *Journal of Non-Crystalline Solids*, *358*, 1104-1112.

Samsudin, A.S., Lai, H.M., & Isa, M.I.N. (2014). Biopolymer materials based carboxymethyl cellulose as a proton conducting biopolymer electrolyte for application in rechargeable proton battery. *Electrochimica Acta, 129*, 1-13.

Sasaki, H., Bala, P.K., Yoshida, H., & Ito, E. (1995). Miscibility of PVDF/PMMA blends examined by crystallization dynamics. *Polymer, 36*, 4805-4810.

Schaefer, J.L., Lu, Y., Moganty, S.S., Agarwal, P., Jayaprakash, N., & Archer, L.A. (2012). Electrolytes for high-energy lithium batteries. *Applied Nanoscience, 2*, 91-109.

Schreiber, S.B., Bozell, J.J., Hayes, D.G., & Zivanovis, S. (2013). Introduction of primary antioxidant activity to chitosan for application as a multifunctional food packaging material. *Food Hydrocolloids, 33*, 207-214.

Sekhar, P.C., Kumar, P.N., & Sharma, A.K. (2012a). Role of salt concentration on conductivity and discharge characteristics of PMMA based polymer electrolyte system. *International Journal of Scientific and Research Publications, 2*.

Sekhar, P.C., Kumar, P.N., & Sharma, A.K. (2012b). Effect of plasticizer on conductivity and cell parameters of (PMMA+$NaClO_4$) polymer electrolyte system. *IOSR Journal of Applied Physics, 2*, 1-6.

Selvasekarapandian, S., Baskaran, R., & Hema, M. (2005). Complex AC impedance, transference number and vibrational spectroscopy studies of proton conducting PVAc-NH_4SCN polymer electrolytes. *Physica B, 357*, 412-419.

Selvasekarapandian, S., Hema, M., Kawamura, J., Kamishima, O., & Baskaran, R. (2010). Characterization of PVA-NH_4NO_3 polymer electrolyte and its application in rechargeable proton battery. *Journal of the Physical Society of Japan, 79*, 163-168.

Sengwa, R.J., Dhatarwal, P., & Choudhary, S. (2015). Effects of plasticizer and nanofiller on the dielectric dispersion and relaxation behaviour of polymer blend based solid polymer electrolytes. *Current Applied Physics, 15*, 135-143.

Sharma, P., Kanchan, D.K., & Gondaliya, N. (2012). Effect of nano-filler on structural and ionic transport properties of plasticized polymer electrolyte. *Open Journal of Organic Polymer Materials, 2*, 38-44.

Shelton, D.R., & Lee, W.J. (2000). Cereal carbohydrates. In K. Kulp, & J.G. Ponte Jr. (Eds.), *Handbook of cereal science and technology, Second edition, Revised and expanded* (pp. 385-416). New York, NY: CRC Press.

Shibayama, M., Uenoyama, K., Oura, J.-I., Nomura, S., & Iwamoto, T. (1995). Miscibility and crystallinity control of nylon 6 and poly(*m*-xylene adipamide) blends. *Polymer, 36*, 4811-4816.

Shuhaimi, N.E.A. (2011). *Ionic conductivity and related studies in methyl cellulose based polymer electrolytes and application in supercapacitors* (Master's thesis, University of Malaya, Kuala Lumpur, Malaysia). Retrieved from http://studentsrepo.um.edu.my/1978

Shuhaimi, N.E.A., Alias, N.A., Kufian, M.Z., Majid, S.R., & Arof, A.K. (2010). Characteristics of methyl cellulose-NH_4NO_3-PEG electrolyte and application in fuel cells. *Journal of Solid State Electrochemistry, 14*, 2153-2159.

Shuhaimi, N.E.A., Alias, N.A., Majid, S.R., & Arof, A.K. (2008). Electrical double layer capacitor with proton conducting κ-carrageenan-chitosan electrolytes. *Functional Materials Letters, 1*, 195-201.

Shuhaimi, N.E.A., Majid, S.R., & Arof, A.K. (2009). On complexation between methyl cellulose and ammonium nitrate. *Materials Research Innovations, 13*, 239-242.

Shuhaimi, N.E.A., Teo, L.P., Woo, H.J., Majid, S.R., & Arof, A.K. (2012). Electrical double-layer capacitors with plasticized polymer electrolyte based on methyl cellulose. *Polymer Bulletin, 69*, 807-826.

Shukur, M.F., & Kadir, M.F.Z. (2015). Electrical and transport properties of NH_4Br-doped cornstarch-based solid biopolymer electrolyte. *Ionics, 21*, 111-124.

Shukur, M.F., Azmi, M.S., Zawawi, S.M.M., Majid, N.A., Illias, H.A., & Kadir M.F.Z. (2013). Conductivity studies of biopolymer electrolytes based on chitosan incorporated with NH_4Br. *Physica Scripta*, *T157*, 014049.

Shukur, M.F., Ibrahim, F., Majid, N.A., Ithnin, R., & Kadir, M.F.Z. (2013). Electrical analysis of amorphous corn starch-based polymer electrolyte membranes doped with LiI. *Physica Scripta, 88*, 025601.

Shukur, M.F., Ithnin, R., & Kadir, M.F.Z. (2014). Electrical characterization of corn starch-LiOAc electrolytes and application in electrochemical double layer capacitor. *Electrochimica Acta, 136*, 204-216.

Shukur, M.F., Ithnin, R., Illias, H.A., & Kadir, M.F.Z. (2013). Proton conducting polymer electrolyte based on plasticized chitosan-PEO blend and application in electrochemical devices. *Optical Materials, 35*, 1834-1841.

Shukur, M.F., Sonsudin, F., Yahya, R., Ahmad, Z., Ithnin, R., & Kadir, M.F.Z. (2013). Electrical properties of starch based silver ion conducting solid biopolymer electrolyte. *Advanced Materials Research, 701*, 120-124.

Silva, M.M., Barros, S.C., Smith, M.J., & MacCallum, J.R. (2004). Characterization of solid polymer electrolytes based on poly(trimethylenecarbonate) and lithium tetrafluoroborate. *Electrochimica Acta, 49*, 1887-1891.

Sim, L.N., Majid, S.R., & Arof, A.K. (2014). Effects of 1-butyl-3-methyl imidazolium trifluoromethanesulfonate ionic liquid in poly(ethyl methacrylate)/poly(vinylidenefluoride-co-hexafluoropropylene) blend based polymer electrolyte system. *Electrochimica Acta, 123*, 190-197.

Singh, N., Singh, J., Kaur, L., Sodhi, N.S., & Gill, B.S. (2003). Morphological, thermal and rheological properties of starches from different botanical sources. *Food Chemistry, 81*, 219-231.

Sinha, V.R., Singla, A.K., Wadhawan, S., Kaushik, R., Kumria, R., Bansal, K., & Dhawan, S. (2004). Chitosan microspheres as a potential carrier for drugs. *International Journal of Pharmaceutics, 274*, 1-33.

Song, X., & Cheng, L. (2014). Chitosan/kudzu starch/ascorbic acid films: Rheological, wetting, release, and antibacterial properties. *African Journal of Agricultural Research, 9*, 3816-3824.

Speight, J.G. (2002). *Chemical process and design handbook*. United States: McGraw Hill Professional.

Srivastava, N., & Chandra, S. (2000). Studies on a new proton conducting polymer system: poly(ethylene succinate) + NH_4ClO_4. *European Polymer Journal, 36*, 421-433.

Srivastava, N., Chandra, A., & Chandra, S. (1995). Dense branched growth of $(SCN)_x$ and ion transport in the poly(ethyleneoxide) NH_4SCN polymer electrolyte. *Physical Review B, 52*, 225-230.

Stephan, A.M., Thirunakaran, R., Renganathan, N.G., Sundaram, V., Pitchumani, S., Muniyandi, N., … Ramamoorthy, P. (1999). A study on polymer blend electrolyte based on PVC/PMMA with lithium salt. *Journal of Power Sources, 81-82*, 752-758.

Stygar, J., Zukowska, G., & Wieczorek, W. (2005). Study of association in alkali metal perchlorate-poly(ethylene glycol) monomethyl ether solutions by FT-IR spectroscopy and conductivity measurements. *Solid State Ionics, 176*, 2645-2652.

Su'ait, M.S., Ahmad, A., Hamzah, H., & Rahman, M.Y.A. (2011). Effect of lithium salt concentrations on blended 49% poly(methyl methacrylate) grafted natural rubber and poly(methyl methacrylate) based solid polymer electrolyte. *Electrochimica Acta, 57*, 123-131.

Subban, R.H.Y., & Arof, A.K. (2003a). Impedance spectroscopic studies on a binary salt poly(vinyl chloride) based electrolyte. *Ionics, 9*, 375-381.

Subban, R.H.Y., & Arof, A.K. (2003b). Experimental investigations on PVC-$LiCF_3SO_3$-SiO_2 composite polymer electrolytes. *Journal of New Materials for Electrochemical Systems, 6*, 197-203 .

Subban, R.H.Y., & Arof, A.K. (2004). Plasticiser interactions with polymer and salt in PVC-$LiCF_3SO_3$-DMF electrolytes. *European Polymer Journal, 40*, 1841-1847.

Subbu, C., Mathew, C.M., Kesavan, K., & Rajendran, S. (2014). Electrochemical, structural and optical studies on poly(vinylidene chloride-co-acrylonitrile) based polymer blend membranes. *International Journal of Electrochemical Science, 9*, 4944-4958.

Subramaniam, R.T., Chiam-Wen, L., Yee, L.P., & Morris, E. (2012). Characterization of high molecular weight poly(vinyl chloride) - lithium tetraborate electrolyte plasticized by propylene carbonate. In M. Luqman (Ed.), *Recent advances in plasticizers* (pp. 165-190). Hampshire, England: InTech.

Subramanian, V., Zhu, H., & Wei, B. (2008). Nanostructured manganese oxides and their composites with carbon nanotubes as electrode materials for energy storage devices. *Pure and Applied Chemistry, 80*, 2327-2343.

Sudhakar, Y.N., & Selvakumar, M. (2012). Lithium perchlorate doped plasticized chitosan and starch blend as biodegradable polymer electrolyte for supercapacitors. *Electrochimica Acta, 78*, 398-405.

Suljovrujic, E., Micic, M., & Milicevic, D. (2013). Structural changes and dielectric relaxation behavior of uniaxially oriented high density polyethylene. *Journal of Engineered Fibers and Fabrics, 8*, 131-143.

Suryanarayana, C. (2004). *Mechanical alloying and milling*. Boca Raton: CRC Press.

Suthanthiraraj, S.A., & Vadivel, M.K. (2012). Effect of propylene carbonate as a plasticizer on $(PEO)_{50}AgCF_3SO_3$:SnO_2 nanocomposite polymer electrolyte. *Applied Nanoscience, 2*, 239-246.

Syahidah, S.N., & Majid, S.R. (2013). Super-capacitive electro-chemical performance of polymer blend gel polymer electrolyte (GPE) in carbon-based electrical double-layer capacitors. *Electrochimica Acta, 112*, 678-685.

Takami, N., Sekino, M., Ohsaki, T., Kanda, M., & Yamamoto, M. (2001). New thin lithium-ion batteries using a liquid electrolyte with thermal stability. *Journal of Power Sources, 97-98*, 677-680.

Tamilselvi, P., & Hema, M. (2014). Conductivity studies of $LiCF_3SO_3$ doped PVA: PVdF blend polymer electrolyte. *Physica B, 437*, 53-57.

Tan, H.W., Aziz, A.R.A., & Aroua, M.K. (2013). Glycerol production and its applications as a raw material: A review. *Renewable and Sustainable Energy Reviews, 27*, 118-127.

Teo, L.P., Buraidah, M.H., Nor, A.F.M., & Majid, S.R. (2012). Conductivity and dielectric studies of Li_2SnO_3. *Ionics, 18*, 655-665.

Teoh, K.H. (2012). *Effect of doping fillers towards corn starch based green polymer electrolytes* (Master's thesis, University of Malaya, Kuala Lumpur, Malaysia). Retrieved from http://studentsrepo.um.edu.my/4175

Teoh, K.H., Ramesh, S., & Arof, A.K. (2012). Investigation on the effect of nanosilica towards corn starch-lithium perchlorate-based polymer electrolytes. *Journal of Solid State Electrochemistry, 16*, 3165-3170.

Teramoto, N., Motoyama, T., Mosomiya, R., & Shibata, M. (2003). Synthesis, thermal properties, and biodegradability of propyl-etherified starch. *European Polymer Journal, 39*, 255-261.

Thenmozhi, N., Gomathi, T., & Sudha, P.N. (2013). Preparation and characterization of biocomposites: Chitosan and silk fibroin. *Der Pharmacia Lettre, 5*, 88-97.

Tiwari, T., Srivastava, N., & Srivastava, P.C. (2013). Ion dynamics study of potato starch + sodium salts electrolyte system. *International Journal of Electrochemistry, 2013*, 670914.

Tripathi, S., Mehrotra, G.K., Tripathi, C.K.M., Banerjee, B., Joshi. A.K., & Dutta, P.K. (2008). Chitosan based bioactive film: Functional properties towards biotechnological needs. *Asian Chitin Journal, 4*, 29-36.

Ubwa, S.T., Abah, J., Asemave, K., & Shambe, T. (2012). Studies on the gelatinization temperature of some cereal starches. *International Journal of Chemistry, 4*, 22-28.

Ulaganathan, M., Nithya, R., Rajendran, S., & Raghu, S. (2012). Li-ion conduction on nanofiller incorporated PVdF-co-HFP based composite polymer blend electrolytes for flexible battery applications. *Solid State Ionics, 218*, 7-12.

Vani, C.V., Thanikaikarasan, S., Mahalingam, T., Sebastian, P.J., Verea, L.E., & Shajan, X.S. (2014). Effect of X-ray irradiation on dielectric properties of polymer electrolytes complexed with $LiCF_3SO_3$. *Journal of New Materials for Electrochemical Systems, 17*, 139-145.

Vanysek, P. (2011). Electrochemical series. In W.M. Haynes (Ed.), *Handbook of Chemistry and Physics 92nd Edition* (pp. 5-80). Boca Raton: CRC Press.

Varshney, P.K., & Gupta, S. (2011). Natural polymer-based electrolytes for electrochemical devices: A review. *Ionics, 17*, 479-483.

Vieira, D.F., Avellaneda, C.O., & Pawlicka, A. (2007). Conductivity study of a gelatin-based polymer electrolyte. *Electrochimica Acta, 53*, 1404-1408.

Vijaya, N., Selvasekarapandian, S., Hirankumar, G., Karthikeyan, S., Nithya, H., Ramya, C.S., & Prabu, M. (2012). Structural, vibrational, thermal, and conductivity studies on proton-conducting polymer electrolyte based on poly (*N*-vinylpyrrolidone). *Ionics, 18*, 91-99.

Vijaya, N., Selvasekarapandian, S., Malathi, J., Iwai, Y., Nithya, H., & Kawamura, J. (2013). ^1H NMR study on PVP-NH_4Cl based- proton conducting polymer electrolyte. *Indian Journal of Applied Research, 3*, 506-510.

Viswanathan, S., & Dadmun, M.D. (2002). Guidelines to creating a true molecular composite: Inducing miscibility in blends by optimizing intermolecular hydrogen bonding. *Macromolecules, 35*, 5049-5060.

Wagner, J.B., & Wagner, C. (1957). Electrical conductivity measurements on cuprous halides. *Journal of Chemical Physics, 26*, 1597-1601.

Wang, C.Y., Sun, J., Liu, H.K., Dou, S.X., MacFarlace, D., & Forsyth, M. (2005). Potential application of solid electrolyte P11OH in Ni/MH batteries. *Synthetic Metals, 152*, 57-60.

Wang, Z., Yang, K., Brenner, T., Kikuzaki, H., & Nishinari, K. (2014). The influence of agar gel texture on sucrose release. *Food Hydrocolloids, 36*, 196-203.

Winie, T., & Arof, A.K. (2004). Dielectric behaviour and AC conductivity of $LiCF_3SO_3$ doped H-chitosan polymer films. *Ionics, 10*, 193-199.

Winie. T., & Arof, A.K. (2006). Transport properties of hexanoyl chitosan-based gel electrolyte. *Ionics, 12*, 149-152.

Winie, T., Ramesh, S., & Arof, A.K. (2009). Studies on the structure and transport properties of hexanoyl chitosan-based polymer electrolytes. *Physica B*, *404*, 4308-4311.

Wongsaenmai, S., Ananta, S., & Yimnirun, R. (2012). Effect of Li addition on phase formation behavior and electrical properties of $(K_{0.5}Na_{0.5})NbO_3$ lead free ceramics. *Ceramics International, 38,* 147-152.

Woo, H.J. (2013). *Ionic conductivity and related studies of polymer electrolytes based on poly(ε-caprolactone)* (Doctoral thesis, University of Malaya, Kuala Lumpur, Malaysia). Retrieved from http://studentsrepo.um.edu.my/4751

Woo, H.J., Majid, S.R., & Arof, A.K. (2011a). Conduction and thermal properties of a proton conducting polymer electrolyte based on poly (ε-caprolactone). *Solid State Ionics, 199-2000*, 14-20.

Woo, H.J., Majid, S.R., & Arof, A.K. (2011b). Transference number and structural analysis of proton conducting polymer electrolyte based on poly(ε-caprolactone). *Materials Research Innovations, 15*, S49-S54.

Woo, H.J., Majid, S.R., & Arof, A.K. (2012). Dielectric properties and morphology of polymer electrolyte based on poly(ε-caprolactone) and ammonium thiocyanate. *Materials Chemistry and Physics, 134*, 755-761.

Woo, H.J., Majid, S.R., & Arof, A.K. (2013). Effect of ethylene carbonate on proton conducting polymer electrolyte based on poly(ε-caprolactone) (PCL). *Solid State Ionics, 252*, 102-108.

Wu, Q.X., & Zhang, L.N. (2001). Structure and properties of casting films blended with starch and waterbone polyuretane. *Journal of Applied Polymer Science, 79*, 2006-2013.

Xi, J., Qiu, X., Li, J., Tang, X., Zhu, W., & Chen, L. (2006). PVDF-PEO blends based microporous polymer electrolyte: Effect of PEO on pore configurations and ionic conductivity. *Journal of Power Sources, 157*, 501-506.

Xu, Y., & Hanna, M.A. (2005). Physical, mechanical, and morphological characteristics of extruded starch acetate foams. *Journal of Polymers and the Environment, 13*, 221-230.

Xu, Y.X., Kim, K.M., Hanna, M.A., & Nag, D. (2005). Chitosan-starch composite film: preparation and characterization. *Industrial Crops and Products, 21*, 185–192.

Yahya, M.Z.A., & Arof, A.K. (2003). Effect of oleic acid plasticizer on chitosan-lithium acetate solid polymer electrolytes. *European Polymer Journal, 39*, 897-902.

Yan, S., Zeng, S., Su, X., Yin, H., Xiong, Y., & Xu, W. (2011). H_3PO_4-doped 1,2,4-triazole-polysiloxane proton conducting membrane prepared by sol–gel method. *Solid State Ionics, 198*, 1-5.

Yap, K.S. (2012). *Characteristics of PMMA-grafted natural rubber polymer electrolytes* (Doctoral thesis, University of Malaya, Kuala Lumpur, Malaysia). Retrieved from http://studentsrepo.um.edu.my/3815

Yap, S.C., & Mohamad, A.A. (2007). Proton batteries with hydroponics gel as gel polymer electrolyte. *Electrochemical and Solid State Letters, 10*, A139-A141.

Yin, J., Luo, K., Chen, X., & Khutoryanskiy, V.V. (2006). Miscibility studies of the blends of chitosan with some cellulose ethers. *Carbohydrate Polymers, 63*, 238-244.

Yu, L., Dean, K., & Li, L. (2006). Polymer blends and composites from renewable resources. *Progress in Polymer Science, 31*, 576-602.

Yusof, Y.M., Illias, H.A., & Kadir, M.F.Z. (2014). Incorporation of NH_4Br in PVA-chitosan blend-based polymer electrolyte and its effect on the conductivity and other electrical properties. *Ionics, 20*, 1235-1245.

Zain, N.M., & Arof, A.K. (1998). Structural and electrical properties of poly(ethylene oxide)-cadmium sulphate complexes. *Materials Science and Engineering B, 52*, 40-46.

Zainal, N., Mohamed, N.S., & Idris, R. (2013). Properties of ENR-50 based electrolyte system. *Sains Malaysiana, 42*, 481-485.

Zakaria, Z., Izzah, Z., Jawaid, M., & Hassan, A. (2012). Effect of degree of deacetylation of chitosan on thermal stability and compatibility of chitosan-polyamide blend. *Bioresources, 7*, 5568-5580.

Zarillo, S., Pearsall, D.M., Raymond, J.S., Tisdale, M.A., & Quon, D.J. (2008). Directly dated starch residues document early formative maize (*Zea mays* L.) in tropical Ecuador. *Proceedings of the National Academy of Sciences of the United States of America, 105*, 5006-5011.

Zeng, X., Wu, D., Fu, R., & Lai, H. (2008). Structure and EDLC characteristics of pitch-based carbon aerogels. *Materials Chemistry and Physics, 112*, 1074-1077.

Zhai, M., Zhao, L., Yoshii, F., & Kume, T. (2004). Study on antibacterial starch/chitosan blend film formed under the action of irradiation. *Carbohydrate Polymers, 57*, 83-88.

Zhang, J.F., & Sun, X. (2004). Mechanical properties of poly(lactic acid)/starch composites compatibilized by maleic anhydride. *Biomacromolecules, 5*, 1446-1451.

Zivanovic, S., Li, J., Davidson, P.M., & Kit, K. (2007). Physical, mechanical, and antibacterial properties of chitosan/PEO blend films. *Biomacromolecules, 8*, 1505-1510.

Zong, Z., Kimura, Y., Takahashi, M., & Yamane, H. (2000). Characterization of chemical and solid state structures of acylated chitosans. *Polymer, 41*, 899-906.

LIST OF PUBLICATIONS AND PAPERS PRESENTED

List of Publications Which are Related to the Thesis:

1) **Shukur, M.F.**, Ithnin, R., & Kadir, M.F.Z. (2014). Electrical properties of proton conducting solid biopolymer electrolytes based on starch-chitosan blend. *Ionics, 20*, 977-999.

2) **Shukur, M.F.**, & Kadir, M.F.Z. (2015). Hydrogen ion conducting starch-chitosan blend based electrolyte for application in electrochemical devices. *Electrochimica Acta, 158*, 152-165.

List of Other Publications:

1) **Shukur, M.F.**, Azmi, M.S., Zawawi, S.M.M., Majid, N.A., Illias, H.A., & Kadir, M.F.Z. (2013). Conductivity studies of biopolymer electrolytes based on chitosan incorporated with NH_4Br. *Physica Scripta, T157*, 014049.

2) **Shukur, M.F.**, Yusof, Y.M., Zawawi, S.M.M., Illias, H.A., & Kadir, M.F.Z. (2013). Conductivity and transport studies of plasticized chitosan-based proton conducting biopolymer electrolytes. *Physica Scripta, T157*, 014050.

3) **Shukur, M.F.**, Majid, N.A., Ithnin, R., & Kadir, M.F.Z. (2013). Effect of plasticization on the conductivity and dielectric properties of starch-chitosan blend biopolymer electrolytes infused with NH_4Br. *Physica Scripta, T157*, 014051.

4) **Shukur, M.F.**, Ithnin, R., Illias, H.A., & Kadir, M.F.Z. (2013). Proton conducting polymer electrolyte based on plasticized chitosan-PEO blend and application in electrochemical devices. *Optical Materials, 35*, 1834-1841.

5) **Shukur, M.F.**, Ibrahim, F.M., Majid, N.A., Ithnin, R., & Kadir, M.F.Z. (2013). Electrical analysis of amorphous corn starch-based polymer electrolyte membranes doped with LiI. *Physica Scripta, 88*, 025601.

6) **Shukur, M.F.**, Ithnin, R., & Kadir, M.F.Z. (2014). Electrical characterization of corn starch-LiOAc electrolytes and application in electrochemical double layer capacitor. *Electrochimica Acta, 136*, 204-216.

7) **Shukur, M.F.**, & Kadir, M.F.Z. (2015). Electrical and transport properties of NH_4Br-doped cornstarch-based solid biopolymer electrolyte. *Ionics*, *21*, 111-124.

8) **Shukur, M.F.**, Ithnin, R., & Kadir, M.F.Z. (2014). Protonic transport analysis of starch-chitosan blend based electrolytes and application in electrochemical device. *Molecular Crystals and Liquid Crystals, 603*, 52-65.

List of Papers Presented at International Conferences:

1) **Shukur, M.F.**, Kadir, M.F.Z., Ahmad, Z., & Ithnin, R., *Dielectric studies of proton conducting polymer electrolyte based on chitosan/PEO blend doped with NH_4NO_3*. Paper presented at the 2nd International Conference on Key Engineering Materials (ICKEM 2012), Singapore, 26-28 February 2012.

2) **Shukur, M.F.**, Kadir, M.F.Z., Yahya, R., & Ithnin, R., *Application of plasticized starch/chitosan biopolymer blend based electrolyte membrane doped with $LiClO_4$ in supercapacitor*. Paper presented at the 16th International Meeting on Lithium Batteries (IMLB 2012), Jeju, South Korea, 17-22 June 2012.

3) **Shukur, M.F.**, Azmi, M.S., Zawawi, S.M.M., Majid, N.A., Illias, H.A., & Kadir, M.F.Z., *Conductivity studies of biopolymer electrolytes based on chitosan incorporated with NH_4Br*. Paper presented at the 3rd International Conference on the Physics of Optical Materials and Devices (ICOM 2012), Belgrade, Serbia, 3-6 September 2012.

4) **Shukur, M.F.**, Yusof, Y.M., Zawawi, S.M.M., Illias, H.A., & Kadir, M.F.Z., *Conductivity and transport studies of plasticized chitosan-based proton conducting biopolymer electrolytes*. Paper presented at the 3rd International Conference on the Physics of Optical Materials and Devices (ICOM 2012), Belgrade, Serbia, 3-6 September 2012.

5) **Shukur, M.F.**, Majid, N.A., Ithnin, R., & Kadir, M.F.Z., *Effect of plasticization on the conductivity and dielectric properties of starch-chitosan blend biopolymer electrolytes infused with NH_4Br*. Paper presented at the 3rd International Conference on the Physics of Optical Materials and Devices (ICOM 2012), Belgrade, Serbia, 3-6 September 2012.

6) **Shukur, M.F.**, Ithnin, R., & Kadir, M.F.Z., *Protonic transport analysis of starch-chitosan blend based electrolytes and application in electrochemical device*. Paper presented at the 12th International Conference on Frontiers of Polymers and Advanced Materials (ICFPAM 2013), Auckland, New Zealand, 8-13 December 2013.